UNIVERSITY OF TRENTO

Doctoral School in Civil, Environmental and
Mechanical Engineering

Curriculum 2. Mechanics, Materials, Chemistry and Energy

Gabriele Greco

Experimental nanomechanics of natural or artificial spider silks and related systems

2020 Doctoral thesis

UNIVERSITY OF TRENTO - Italy
Department of Civil, Environmental and Mechanical Engineering

Doctoral School in Civil, Environmental and Mechanical Engineering
Topic 2. Mechanics, Materials, Chemistry and Energy - XXXII Cycle (2016/2019)

Doctoral Thesis - January 2020

Gabriele Greco

Experimental nanomechanics of natural or artificial spider silks and related systems

Supervisors
Nicola Maria Pugno: University of Trento
Barbara Mazzolai: Center for Micro-BioRobotics@SSSA

Credits of the cover image: Maria Bonati

University of Trento
Doctoral School in Civil, Environmental and Mechanical Engineering
http://web.unitn.it/en/dricam
Via Mesiano 77, I-38123 Trento
Tel. +39 0461 282670 / 2611 - *dicamphd@unitn.it*

To all the teachers of my life

INDEX

1. SUMMARY

Spider silks are biological materials that have inspired the humankind since its beginning. From raising the interest of ancient philosophers to the practical outcomes in the societies, spider silks have always been part of our culture and, thus, of our scientific development. They are protein-based materials with exceptional mechanical and biological properties that from liquid solutions passes to the solid fibres once extruded from the body of the spiders.

Spider silks have deeply been investigated in these decades for their possible outcomes in biomedical technology as a supporting material for drugs delivery or tissues regeneration.

Furthermore, spiders build webs with the support of different types of silks to create mechanically efficient structures, which are currently under investigation as models for metamaterials and fabrics with superior mechanical properties. This diversity in materials and structures makes spider silks scientific outcomes potentially infinite.

In this work, we present some of the outputs of these three years of PhD. We explored the properties of the native material across different aspects (different species and glands) and trying to find possible derived applications (tissue engineering). Then we explored the mechanical behaviour of the natural structures (such as orb webs or attachment discs) coupled with their biological functions.

In order to develop to an industrial level this material, we tried to understand and improve the physical properties of artificial spider silk, which helps also in understanding the ones of the native materials.

2. LIST OF PUBLICATIONS

The following papers have been published in peer reviewed journals:

1. Gabriele Greco, Federico Bosia, Francesca Tramacere, Barbara Mazzolai, Nicola M. Pugno, *The role of hairs in the adhesion of octopus suckers: a hierarchical peeling approach.*, 2020, *Bioinspir. Biomim.* **15** 035006
2. Alessandra Dellaquila & Gabriele Greco, Elisabetta Campodoni, Mauro Mazzocchi, Barbara Mazzolai, Anna Tampieri, Nicola M. Pugno, Monica Sandri, *Optimized production of a high-performance hybrid biomaterial: biomineralized spider silk for bone tissue engineering*, J. APPL. POLYM. SCI. 2019, doi: 10.1002/APP.48739
3. Yuejiao Yang & Gabriele Greco, Devid Maniglio, Barbara Mazzolai, Claudio Migliaresi, Nicola Pugno, Antonella Motta, *Spider (Linothele megatheloides) and silkworm (Bombyx mori) silks: Comparative physical and biological evaluation*, Materials Science and Engineering: C, 2019, doi: 10.1016/j.msec.2019.110197
4. Hamideh Mirbaha, Parviz Nourpanah, Paolo Scardi, Mirco D’incau, Gabriele Greco, Luca Valentini, Silvia Bittolo Bon, Shahram Arbab and Nicola Pugno, *The Impact of Shear and Elongational Forces on Structural Formation of Polyacrylonitrile/Carbon Nanotubes Composite Fibers during Wet Spinning Process*, Materials, 2019, 12, 2797; doi:10.3390/ma12172797
5. Gabriele Greco, Maria F. Pantano, Barbara Mazzolai & Nicola M. Pugno, *Imaging and mechanical characterization of different junctions in spider orb webs*, Scientific Reports, (2019) 9:5776, DOI: 10.1038/s41598-019-42070-8
6. Roberto Guarino, Gabriele Greco, Barbara Mazzolai, Nicola M. Pugno; *Fluid-structure interaction study of spider’s hair flow-sensing system*, materialstoday: Proceedings, Volume 7, Part 1, 2019, Pages 418-42, DOI: 10.1016/j.matpr.2018.11.104
7. Meng Xu, Sayantan Pradhan, Francesca Agostinacchio, Ramendra K. Pal, Gabriele Greco, Barbara Mazzolai, Nicola M. Pugno, Antonella Motta, and Vamsi K. Yadavalli; *Easy, Scalable, Robust, Micropatterned Silk Fibroin Cell Substrates*, Adv. Mater. Interfaces 2019, 1801822, DOI: 10.1002/admi.201801822

8. Kundanati, Greco, Pugno, 2017; *Ingegneria Bio-Ispirata a coleotteri e ragni (Bioinspired engineering from Beetles and Spiders)*, 2017, Entomata, 5, 10-13

The following papers have been submitted in peer reviewed journals and are now under the second cycle of revision:

1. Gabriele Greco, Jonas Wolff, Nicola M. Pugno, *Stronger and tougher silk for resilient attachment discs: the mechanical properties of the Cupiennius salei (Keyserling, 1877) piriform silk.*
2. Gabriele Greco, Nicola M. Pugno, *The mechanical properties of unknown spider silk at different fibre lengths and related Weibull scaling laws on the fracture strength.*

3. INTRODUCTION

3.1. The Bio-inspired approach

Since the beginning of humankind, humanity has always been fascinated by Nature, especially for its smart solutions to overcome challenges. Some of these challenges share common traits with the challenges that humans undertake. This is precisely the reason why scientists (or better intellectuals) around the world and from every age started looking at Nature as a source of inspiration.

3.1.1 To learn, not to copy

Nature spends almost 4.5 billion of years in trying to overcome particular challenges and prosper, by spreading the living organisms all around the globe. This process, which one can call evolution, has been longer with respect to the evolution of humanity. For this reason, Nature uses optimized technical solution that are more efficient than ours. All of these have marvellous and elegant structures that have always inspired the mind of scientists.

Although the term “Biomimetic” has been recently coined[1], humankind has always taken inspiration from Nature to develop technologies, especially when the challenges were in common (for example flying). Often, the term “Biomimetic” is confused with men’s copying of Nature in its structures to create new technologies.

Although this could be fascinating from certain points of view, it is very far from reality[2]. For example, although the flight of birds and our airplanes share similarities, a few differences persist (the plane does not flap its wings). Accordingly, one can now discover a more accurate meaning of biomimicry. First and foremost, one must understand the concepts that rule the natural phenomenon that could be able to solve one of our problems. Then, one works towards the development of the same concept, but in a easier way possible, as e means to scale the concept one has developed to an industrial level.

Understanding the concept that is under the phenomenon is not always straightforward. Sometimes, this is the most difficult challenge.

As an example, one might consider the adhesion of the octopi’s suckers. These incredible structures allowed octopuses to efficently adhere to any kind of surfaces[3]. It is natural that scientists tried to develop adhesives that were able to adhere to many surfaces in various and even extreme conditions[4,5]. In order to do so, they tried to model the mechanism underneath the adhesion of the suckers[6,7], but the efficiency of the developed technology was still not comparable to the one of the animal[8]. This is probably caused by the fact that the adhesion mechanism is tremendously complex and hard to model, especially under water. In this context, the discovery of the hairs in the suckers' wall has pointed out that the model had to be changed[9] (Figure 3-1). In one of our works, we addressed this aspect by modifying the previous model[10] by inserting hairs according to the Gao's approach[11]. For more details in this regard, the reader can check the paper in Appendix D.

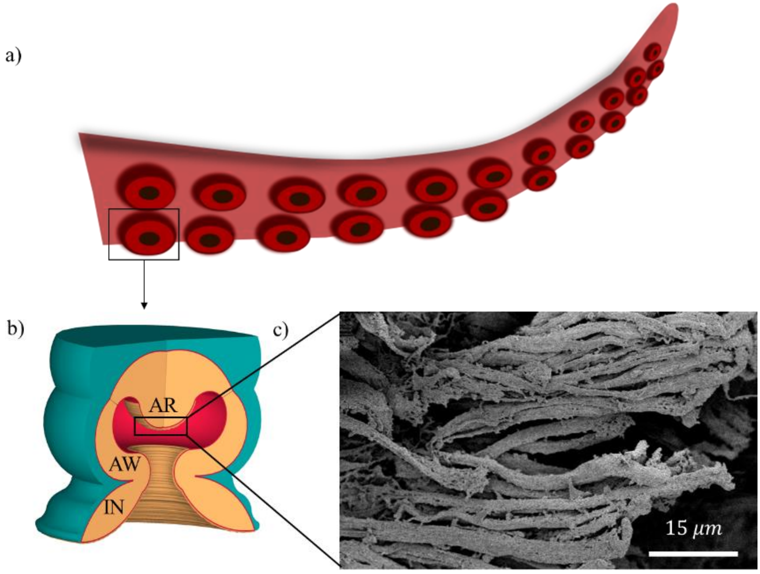

Figure 3-1: a) Schematic of an octopus' arm. b) Schematic of an octopus sucker with a c) focus of the hairs that are present in the acetabulum roof (AR). (Appendix II D)

3.1.2. What can we learn from spiders?

Being a spiders' enthusiast, it is impossible for me to not mention spiders in this chapter. They are amazing creatures that have evolved in about 400 million years.

Looking at them, one might be fascinated by their ability in climbing smooth surfaces, perceiving the small air flows to "see" in the dark, staying dry in wet environments and, of course, dangling around with their silk.

As one individual can be fascinated by them, of course so are scientists.

In these decades, scientists have tried to understand the mechanisms that underlay under these spiders' features in order to develop smart technologies.

Starting from the hair-like structures that spiders use to detect air flows in the dark[12], scientists have tried to develop bio-inspired airflow sensors[13,14] to be applied in soft robotics (Figure 3-2). In this regard, we investigated the interaction between hair-like structures in spiders with airflows. By measuring the mechanical properties of the “hairs” and with the support of simulations, we noticed that after a certain spacing between the hairs (ca 1.5-2 cm), the hairs do not interact one with each other, optimizing the sensing[15]. For more details on this behalf, the reader might check the paper in Appendix A.

Other hair-like aspects that make spiders interesting are their hydrophobicity[16]. The production of superhydrophobic surfaces has interested scientists in these decades[17]. The study of the hydrophobicity of spiders could be thus helpful in discovering new possible surfaces, especially if one considers those spiders that live totally under water[18]. Moreover, hair-like structures are essential to spiders for climbing smooth surfaces even in the presence of high humidity rates[19,20]. This has been an important source of inspiration, as the geckos[11], for developing and designing smart adhesives systems and possible futuristic suits[21,22].

Furthermore, the venom of spiders is considered a very powerful source of inspiration for developing smart technologies. Despite the toxicity of some of these arachnids, not as high as one may easily think, their complex venom has some nice features able to overcome some of our medical challenges. For example, the venom of the *Nephila clavipes* is studied for developing insecticides[23]. The venom of some Theraphosidae is deeply studied for pain treatment, anaesthetic and anticancer drugs [24,25]. Finally, the venom of some of the most dangerous spiders (*Phoneutria sp.*, *Atrax sp.*) is currently under investigation as a potential source of drugs against cardiovascular and neurodegenerative diseases[26].

Another interesting features that spiders present is the mechanical efficiency of their bite. Able to penetrate the steel, the morphology and the mechanics of the fang of spiders has attracted the attention of many scientists interested in developing bio-inspired needles[27,28].

These are just some examples on what spiders have still to teach us in regards to technology. It has to be mentioned that the lab of Prof. Pugno has gained expertise in studying spiders and other arthropods[28] (for more details on the activity of this lab, check paper in Appendix C). I have not mentioned silk by purpose, since the entire thesis is devoted to it.

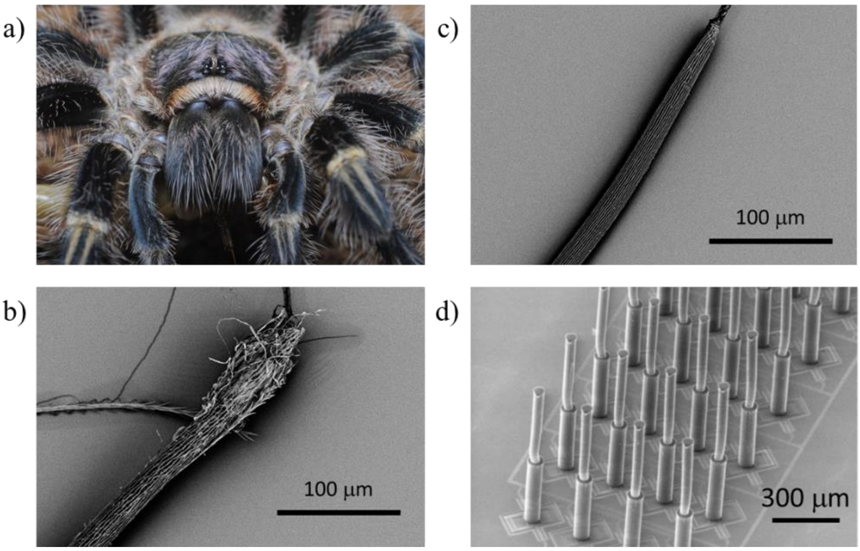

Figure 3-2: a) The spider Grammostola pulchripes (courtesy of Aracnofilia). b-c) SEM pictures of the hairs like structures used by spiders to sense air flows[15]. *d) Bio-inspired air flows sensors, adapted from*[13].

3.1.3. Spider silks and their applications: the Bio-inspired approach

During these three years we have mainly studied spider silks. As many scientists, we have been fascinated by the incredible variety of remarkable properties and uses that spider silks have both for the animal and human point of view. Our path in discovering this material is peculiarly adequate to the bio-inspired context. By describing it, I advise the reader to refer to Figure 3-3.

Being interested in applying spider silk to solve technological challenges, we had to start by understanding the material itself. We then looked at what the materials has meant in pasts ages and how it is seen today. The presence of spider silk in our culture is so deep that one can follow its scent till ancient Greece.

After that, we looked at the properties of the materials, e.g. mechanical and biological ones. In this context it is tremendously important to understand how spiders use silks to perform different functions (from mating to webs building). Understanding the functions of such structures or materials in Nature means learn from them smart ways to solve problems. Once we had in mind that, we explored several possible applications that can be achieved by using spider silk as a supporting material for developing composites or just as a basic material for tissue engineering.

At that point we faced the first difficulty: spiders cannot produce a large amount of silk. For this reason, we looked at different solutions to produce it at an industrial level. Artificial production seems to be the best solutions to this problem and for this reason we started looking at artificial fibres and their properties.

In doing this, we faced another difficulty: the poor properties of artificial spider silk. These were not comparable with the native ones, for the fact that we are simply not able to barely copy Nature in its processes, i.e. spider silk spinning. Moreover, we discovered that artificial spider silk presents some problems in maintaining stability under different environmental conditions (as the native material). In order to remove them, we were forced to look back at the natural spider silk in order to understand the causes of these instabilities (e.g. supercontraction).

Aiming to produce bio-inspired technologies, we were then forced several times to pay back attention to the natural material.

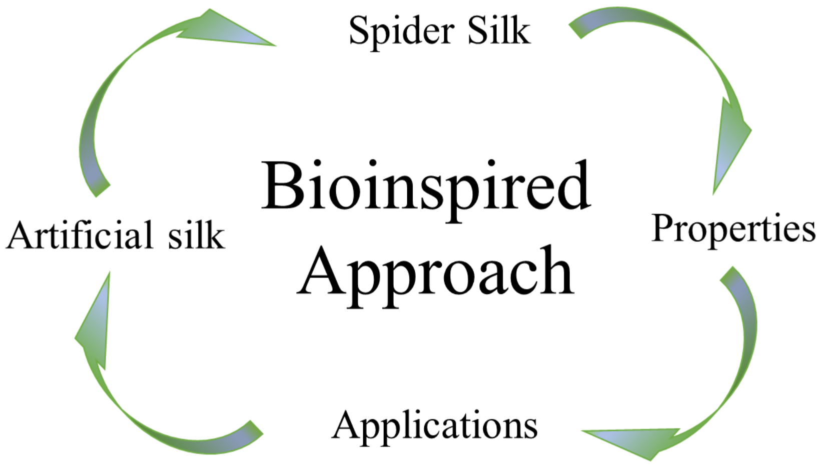

Figure 3-3: The bioinspired approach applied to spider silk. The schematic of these three years of PhD.

3.2. Spider Silks and Spider Webs: an overview

3.2.1. Spiders and Silks

Spiders belong to the class of Arachnids and we can count more than 48000 species around the world[29]. They spread in almost all the possible habitats, with the exception of open sea, glaciers and highest mountains[30]. This must give an idea of how much these creatures have adapted themselves to various environments, by developing incredible strategies and structures to overcome the natural challenges.

Among them, spider silk represents an important aspect that strongly contributed to spider’s evolution, being actually one of the features that defines spiders. It is in fact possible to state that the first spiders evolved when it started to spin silk, i.e. 400 million years ago[31,32].

Spiders store liquid silks in their glands and when they need it, they spin into solid fibres. In particular, a single spider is able to produce different types of silk (from 2 to 7), from different glands[33]. Each one of these, presents different properties and functions. Considering the 48000 species of spiders, it is possible to estimate around 150000 different types of spider silks[34]. From these numbers we understand the incredible biological variability of these materials, which leads to an incredible physical and chemical variability.

Figure 3-4: a) A spider that is showing the typical display during ballooning (adapted from[35]*). b) Cocoon of a Steatoda pakulliana spider (courtesy of Aracnofilia). c) Argiope bruennichi and its web decorations (courtesy of Aracnofilia).*

Being central in their life, spider silks have been used for many purposes. Listing all of them is impossible, however we report here some of the most peculiar. In these, we selectively removed the production of webs and lining for safety reason (discussed later).

- *Ballooning.* (Figure 3-4a) One of the reasons of the wide spreading of spiders around the world is surely the possibility to perform ballooning once they hatch from the eggs. This occurs when the spiders are in an apical part of a plant or a flower. Once then, the animals start to spin a single silk thread and, because of the wind and electrical fields that are generated that pull it, it flies[35–37]. It is thought that the first scientist who observed this phenomenon and took notes of it was Charles Darwin while travelling on the Beagle, who observed this incredible phenomenon. Literarly (p.233 of[38]): "*The ship was sixty miles distant from the land, in the direction of a steady, though light, breeze. Vast numbers of a small spider, about one-tenth of an inch in length, and of a dusky red colour, were attached to the webs. There must have been, I should suppose, some thousands on the ship. The little spider, when first coming in contact with the rigging, was always seated on a single thread, and not on the flocculent mass. This latter seems merely to be produced by the entanglement of the single threads….The little aeronaut as soon as it arrived on board was* *very active, running about, sometimes letting itself fall, and then reascending the same thread; sometimes employing itself in making a small and very irregular mesh in the corners between the ropes.*”

- *Cocoons*. (Figure 3-4b) Spiders lay eggs. For protection, they cover them with a thick layer of silk, usually produced by both aciniform and tubuliform glands and take care of it till the hatch of the slings[30]. It is necessary that the silk of the cocoon protect the eggs inside and for this reason it has to be very tough. Interestingly, very far in time from the development of the equipment necessary to investigate the mechanical properties of the silk and very far from the discovery of the toughness of the egg sac silk of spiders, the fact that the toughness of the cocoon silk is the highest was postulated by E. White in 1952 in his book Charlotte’s Web[39], where Charlotte (the spider) was talking about its cocoon:” *…"Yes, it is pretty," replied Charlotte, patting the sac with her two front legs. "Anyway, I can guarantee that it is strong. It's made out of the toughest material I have. It is also waterproof. The eggs are inside and will be warm and dry."* “(Page 124).
- *Mating and courtship.* Spiders use their silk during mating and courtship behaviours[40]. By neglecting the passive uses of silk, i.e. transmission of vibration or chemical signals, it is interesting to point out some active behaviours that involve silk. In the spider *Pisaura mirabilis* the male spins a pack of silk to wrap a killed prey. This, then, is given to the female as a nuptial gift in order to make her “mating friendly”. Curiously, some Thomisidae spiders wrap the female in a silk “bondage” in order to make her unable to move till they have finished the mate.
- *Decorations*. (Figure 3-4c) Some spiders decorate their webs with aciniform silk[41,42]. These are quite visible in the structure and normally are laid at the centre of the orb web. Their functions are still controversial. However, the main hypothesis are that they are important in avoiding the impact of birds on the web and at the same time attract flying insects.

3.2.2. The spider silk: major ampullate silk

As previously said, 150000 is the number of estimated types of spider silks on Earth. Among them, we know pretty well only one type: the dragline. This represents almost the 95% of the scientific literature that deals with spider silk. It is produced to secure spiders to surfaces (Figure 3-5a), to balloon and as a main structural component in the webs[30]. Even if it can be composed by more than one single fibre[43], the main component of it is the silk produced by the major ampullate gland, which represents the most investigated silk.

To pinpoint some of the features that could represent spider silks, we refer to this type, but not all the properties of silks are conserved among different types.

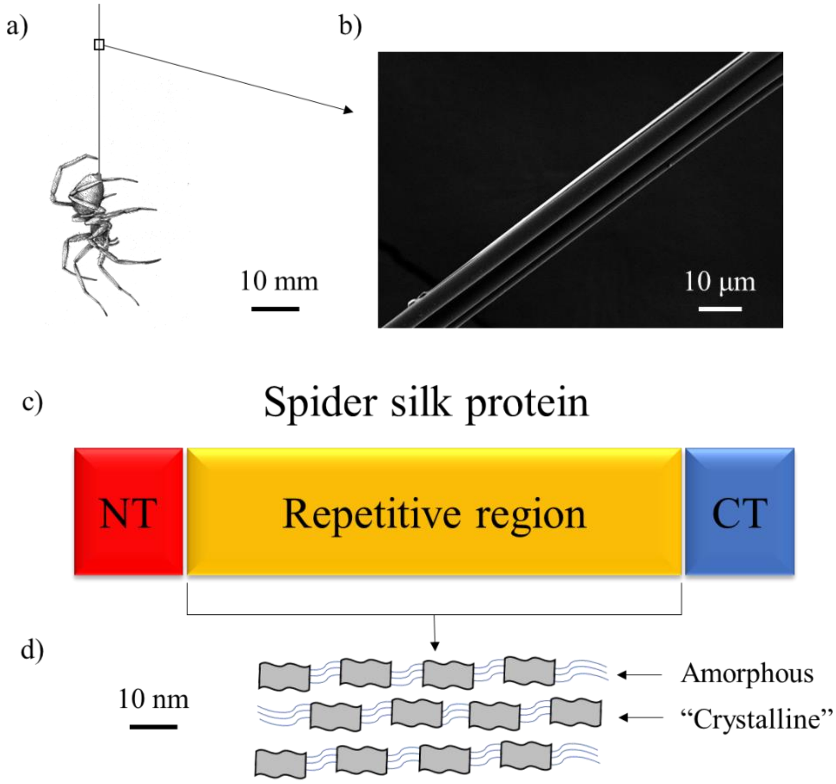

Figure 3-5: a) A spider spins the silk from its spinneret (placed in the opistosoma); b) the dragline has a typical diameter of some micrometres and it is composed by two or three threads; c) the typical spider silk protein is composed by a repetitive region (yellow) sandwiched between the NT and the CT terminal domains. d) The repetitive regions have a peculiar secondary structure that consists in amorphous and semi-crystalline structures with different phases.

The typical dimension of a major ampullate fibre is around 3-10 µm (Figure 3-5b). This fibre has a hierarchical structure composed by several layers[44] where the most external ones are composed by glycoproteins and lipids. It is still not fully understood what are the functions of these layers, since it seems that they are not involved in the interaction with water and in the definition of the mechanical properties of the fibres[45]. The most important part, in fact, is the core of the fibre that is constituted by different proteins, which are usually named MaSp1, MaSp2 and so on (spidroins). These proteins tend to be very high in molecular weight, which for each monomer can be up to 350 kDa[46]. Normally the major part of these proteins is constituted by a repetitive region (Figure 3-5c) that is constituted by the repetition of modular units, which account almost the 90% of the amino acids that compose the protein. At the sides of this, there are two terminal domains (Figure 3-5c) that are composed by at least 100 amino acids and whose sequence seems to be conserved among different spider species and silk types[47]. These terminal domains are essential for spider silk solution storage in glands and their spinning throughout the ducts[48]. The repetitive region, on the other hand, is fundamental for the mechanical properties of the silk and it consists in modular units that have 40-200 amino acids each[49]. In these, the most abundant are Glycine and Alanine. Several of these modular units build the core region of the protein. Through several techniques, such as NMR, it has been shown that there are polyalanine regions that re likely to form nanosized crystals packed together in β-sheets[50] (Figure 3-5d). There are strongly non covalently crossed linked and are supposed to are the main cause of the silk's strength. The regions rich in Glycine, on the other hand, are less understood even if they are likely to form amorphous regions (e.g. β-turns, α-helix), which are likely the main cause of the great deformability of silk. It has to be noticed that both these two main categories of structures, the amorphous and crystalline ones, can occur in different phases or states[51]. The mechanics of these structures will be discussed later.

Table 3-1: Typical silks glands of spiders and their abbreviation[30,33,43,52–54].

Gland / Structure	**Abbreviation**
Major Ampullate	MA
Minor Ampullate	MiA
Piriform	Pi
Aggregate	Ag

Aciniform	Ac
Flagelliform	Fl
Tubuliform	Tu
Cribellum	Cr
Mygalomorphae	Anc

3.2.3. The other spider silks

There are several typologies of spider silks, each one produced by a different gland placed in the abdomen of a spider. Each gland is connected by means of a duct with the spigot from which the silk is extruded as a solid fibre.

Each silk that is produced by the spiders looks different with respect to the other in term of morphology, chemical and physical properties. It is commonly accepted to abbreviate the name of the glands that produce certain typologies of silk to facilitate the usage of these terms. Table 3-1 shows the known spider silks and the gland that produces them. Many of the glands that are typical in certain spiders, for example the major ampullate one, can occur in different shapes (e.g. flat spigots[54]) that affect the mechanical properties and the function of the silk.

In such a variety of spiders, is thus straightforward to imagine a much bigger variety of different types of silk with respect to the actual one. There are, for examples, some families of spiders (such as Dipluridae) that are under investigated from the silk point of view and whose material could be an important source of innovation in new emergent technologies[55].

The knowledge on these kinds of new silks is also crucial in understanding their role in the building process of spider's webs and their mechanical efficiency

3.2.4. From spider silks to spider webs

The huge variability in spider silks types is reflected also in the huge variability among spider's webs structures, morphologies and functions (Figure 3-6).

When a spider builds a web, it does in a synergistic way that optimize the mechanical efficiency of the structure (discussed later in chapter 4). Even if there is still debate on this, it seems that this incredible optimization is achieved not from a learning process, but from the genetic encode of each animal[56,57].

The efficiency is of course dependent on the function that the web is supposed to achieve. For example, orb webs are perfect structures to stop flying prey, 3d cobweb are perfect structures to provide solidity to the spider den and also capability in stopping ground animals.

The variability of the webs is also improved by the fact that there are many species of spiders on earth and almost every day a new one is described. For this reason, also new types of webs could be found, as it has been happened recently for the leaf web of the spiders of the genus *Emblyna*[58].

Moreover, spiders use many types of silks to build their webs. For ecribellate orb weaver, for example, we can count at least five different typologies of silks in a single orb web build by an adult female[43]. This is not valid for the ancient infraorder mygalomorphae whose spiders possess only two types of silk glands. One is designed for the production of the web and the other for the production of the cocoon[30].

It is thus impossible to state something general about webs especially by considering that in scientific literature only orb webs are deeply investigated. This is probably due to the fact that they are very simple in geometry, to model, and to farm spiders that can produce them in a lab[59,60]. For example, is not easy to investigate and study the 3d cobweb from Theridiidae. Their shape is irregular and thus very hard to model[61]. Moreover, the structure is not rebuilt by spiders every day. They in facts add every day new threads, making almost impossible to recognise the main mechanisms that lead to their efficiency. Fortunately, in a recent work a scanning technique has been developed to investigate these peculiar types of webs, giving hope to their modelling[62].

Figure 3-6: The variety of spider webs. Here we report just few examples of typical web structures for different spiders to illustrate their variety. Courtesy of Aracnofilia (Italian Association of Arachnology)

3.3. Spier Silks and Humans

The concepts related to spider silks are intrinsically weighty in our society. Because of their properties, symbols and representations, spider silks have influenced the human culture in arts, technologies, rituals and fear or deep restlessness.

Is thus important to give an idea of how these materials permeate the evolution of our knowledge, leading us to a better awareness of the field in which we are trying to contribute.

This paragraph deals with the continuity of spider silks in affecting our culture. From the ancient Greeks and Romans to today, I will show small examples of the importance of spider silks in culture.

Moreover, it is always interesting to compare the way in which these materials were seen in the past and now.

As Thucydides said (431-404 B.C): “We must know the past to understand the present and guide the future”.

3.3.1. Spider silk in ancient Greece and Rome

We find several evidences of the presence of spider silks and webs in the culture of ancient Rome and Greece. It is interesting to notice the modernity of the thoughts and descriptions that the ancient philosophers or thinkers wrote on these materials and structures.

Observation and interest to spiders can be traced back to one of the first literary work which have survived until today, namely Homer’s Odissey. The spider web is mentioned twice in it. The first reference entails a metaphor which implies that spiders weave in abandoned places: Od. 16.34-5 “[…] *and the couch of Odysseus, for want of sleepers, perhaps lies full of foul spider webs*”. Transl. Murray 1995, 121[63]). The second reference, on the other hand, concerns a more elaborate image, since it is related to one of the most famous episodes of Greek mythology: the adultery love between Ares, the god of war, and Aphrodite, goddess of love. They make love illicitly, hidden in the house of Hephaistos, husband of Aphrodite. When Hephaistos finds out what happened, furious for the deceit, he arranges a trap in case they want to do that again, and this trap is designed as a spider web for its thinness and difficulty to be seen (Od. 8.272-81, esp. 279-81 “*and many (bonds), too, were hung from above, from the roofbeams, fine as spiders’ webs, so that no one even of the blessed gods could see them, so cunningly they were fashioned*”. Transl. Murray 1995, 293[64]).

Another interesting examples can be given by Aristotle and Pliny the elder. In this paragraph, we are going just to quote two parts of their book, to be kept in mind during the whole read of the work as an evidence of the modernity of the observations. Aristotle describes for the first time (*HA* 8.623a) the act of weaving of the spider, out of embellished literary metaphors or mythological accounts:

“It weaves by first stretching thread to the extremities in every direction, then it lays down the radii from the middle (it takes the middle with fair accuracy) and on these lays down the woof, so to speak, and then weaves them together. Now the bed and storage she arranges elsewhere, but she does her hunting at the centre where she keeps watch. Then when something has fallen in and the centre has been moved, first she binds it round and enwraps it with webs until she has made it helpless, then she lifts it up and carries it away ...”* (Transl. Balme 1991, 329-31[65]).

Pliny the Elder, on the other hand, was surprise on the incredible mechanical efficiency of spiders’ web. The following quotation describes it (*Naturalis Historia* 11.28,83–4):

“*Then its (i.e. the web’s) strength – when is it broken by the winds? What quantity of dust weighs it down? When the spider is practising its art and learning to weave, the breadth of the web often reaches between two trees and the length of the thread stretches down from the top of the tree and there is a quick return right up the thread from the ground, and the spider goes up and brings down the threads simultaneously. But when a catch falls into the web, how watchfully and alertly it runs to it! Although it may be clinging to the edge of the net, it always runs to the middle, because in* *that way it entangles the prey by shaking the whole*" (Transl. Rackham 1940, 483).

These are just examples, but the most well-known (and most continuative from the temporal point of view) artistic expression that sees as a main character a spider is Arachne's myth. The most detailed expression of it, even if it is a Greek myth, can be found in latin literature: Ovid's *Metamorphoses* (VI). Arachne was the shepherd daughter who started weaving when very young. She acquired soon a great ability in weaving that led her to boast herself as a better weaver than Athena, by refusing the fact that was because of the goddess that she has her talent. Athena got offended and challenged the young girl. Athena's work represented four different competitions between mortals and gods where gods punished the mortals because they dared to put themselves at the same level of the gods. Arachne's one, on the other hand, represented scenes where gods fooled and abused the mortals, where Zeus was the most representative since he abused and seduced many women.

When Athena understood that not only the work of Arachne insulted the gods but also that her work was better than hers, she destroyed, moved by envy, the work of the young girl and hit her temple three times. Arachne, moved by the desperation, took a noose and was going to hang herself when Athena stopped her. Although the psychological implications of Arachnes' myth have been across times, the story has always been very permeating in the western culture and it stimulated and inspired several artistic expressions. To mention a representative one, Gustave Dorè depicted Arachne's transformation in an intense painting inspired by Dante's *Purgatory* XII (Figure 3-7).

Even if these are just examples of how spider silk and webs were clear concepts in ancient societies, they give an idea of how much the silks and webs related concepts were already rooted in the culture.

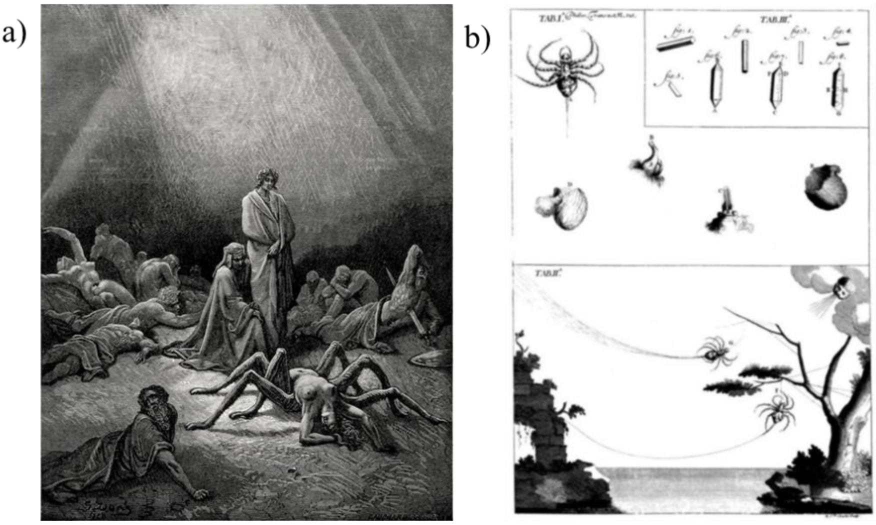

Figure 3-7: Gustave Doré "Arachné au purgatoire" (Paris, Hachete, 1868). b) Illustration of the treatise of M. Bon (Figure1-2), adapted from[66].

3.3.2. Spider silk after the copyright

The birth of the copyright (1710) has affected our way of doing science and that is why I explicitly selected it as a key moment.

One of the first journals that published scientific papers under the copyright was, of course, the Philosophical Transactions of the Royal Society. The reader might also be interested in the fact that one of the first papers published in that occasion was about spider silk (Phil. Trans. 1710-1711 27, 2-16, published 1 January 1710) by Monsieur Bon (Figure 3-7b). THE interest in spider silk was already present. In this ground-braking paper, M. Bon elucidated the different possible applications that spider silk might have not only in fabrics, but also in medical practices.

Even if not in the scientific community, from historical sources we have learned that spider silk was present in many societies around the world.

Let us then consider what happened in the Solomon Islands, where some fishermen of the Melanesian population were used to use spider webs as a support in fishing activities in the lagoons. In one of his remarkable work, the anthropologist Alfred Gell described these techniques in the border between technology and magic[67]: "*From this kite, which hovered over the water, there descended a further string to which was attached a ball of spider's webs, which dangled just on the surface of the water. Fish in the lagoon would see the sparkling spider's web ball and mistake it for an insect but when they bit into it the sticky spider's web would cause their jaws to adhere to one another, so that they could not let go. At this point the fisherman would reel in the whole contraption and take the fish.*"

(Alfred Gell, Technology and Magic, 1988). From this quotation two roles of the spider silk/webs arise: as a bait and as the main structural element for making the fish uncapable of escape. For the latter, it is unlikely that a big fish would have been captured and thus this hypothesis tends to be not considered as true[68]. More likely, under the light spider silks created a visive bait where a fisherman can eventually hide the hook. This debate is still ongoing and the truth far from be discovered, but what is sure is that Melanesian people knew what were spider silks and their potential as useful materials.

Another example of the uses of spider silks is the "Smothering hood" of the nimangki population in south of Malakula (one of the islands of Vanatu). This was a special suit made entirely by spider silk (probably from *Nephila sp.*). A recent PhD work[69] associated this hood as a symbol of higher hierarchical level in the previous mentioned society. Among many reasons about the choice of spider silk, people of high hierarchy were likely to wear this uncomfortable suit as also a symbol of the robustness and endurance of the material.

In the premodern society, however, one of the most representative examples of the role of spider silk is given by Non Songer. During the second World War, the demand of telescopic sight of guns and periscopes was high. The use of spider silk as a thread for producing optical instruments was not a novelty[70], and to fulfil this needs this young lady created a farm of about 10000 black widows (*Latrodectus sp.*) spiders in United States (Figure 3-8a)[69]. In one of her articles, Non Songer illustrated her products by drawing a target that was produced by a spider to pinpoint a tiger (Figure 3-8b). The meaning of this was the fact that a spider can kill a tiger, and its intrinsic nature as predator was on human being side, aiding the kill.

Interestingly, even if these examples seem to be far from our culture, the effect that spiders and spider silks have had in our culture never vanished, but perhaps changed in the modern world. Nowadays, fortunately, we do not need any more to use spiders to build weapons.

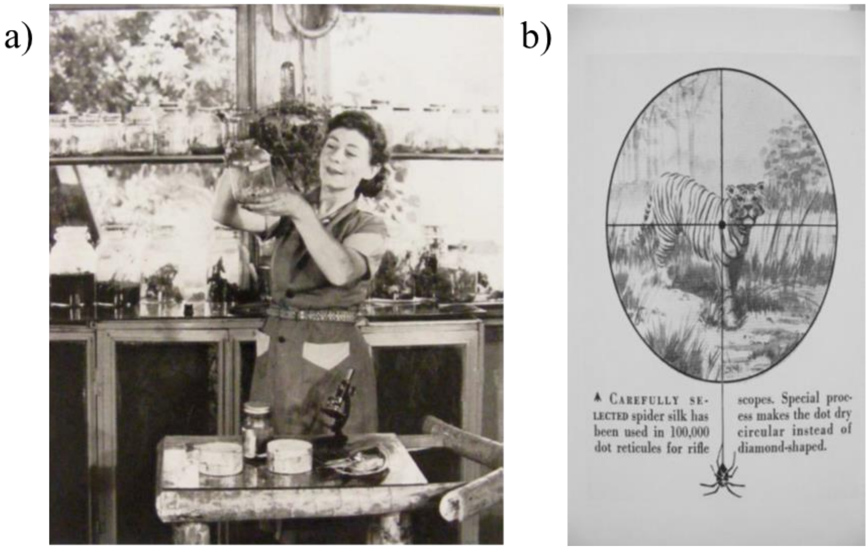

▲ Carefully selected spider silk has been used in 100,000 dot reticules for rifle scopes. Special process makes the dot dry circular instead of diamond-shaped.

Figure 3-8: a) Nan Songer. Photo: Paramount Pictures. b) Drawing from Songer's article. Nan Songer Hook, "Spiders for Profit, "Natural History Magazine (November 1955): 456-461.

3.3.3. Spider silk in the modern world

In this context, we consider modern world everything that is after the XXI century. In our culture, spiders can have a huge effect and the affected areas span from the arts to literature (not considering science and technology that are better discussed later on).

In term of an artistic point of view, Thomas Saraceno and his webs in the dark, or the chain webs of James Hodges are terrific examples. We cannot also neglect the inspiration from spiders that Marvel® took in order to create the character of Spiderman.

Moreover, we cannot neglect the effect that the spiders have on most of the youngster creating strong emotions, such as fear. For this reason, there are books entirely devoted to spiders. As an example, since we have already discussed about "Charlotte's Web" in the previous paragraph, let us consider the recent Italian book "Rebecca dei ragni" (Spiders' Rebecca). In this, the author uses spiders and their webs making as an excuse to create a noir environment and a context to raise tension and fear in the young reader.

These animals have a such high capacity on affecting our culture that there are several examples of companies that use spiders and their silks to create marketing. Is there any better figure to represent solidity than a spider's web? Nowadays, of course, it is almost impossible to use native spider silks to create product (better discussed later), but with the support of genetic engineering it is possible to create spider silk-like materials.

Bolt Threads (https://boltthreads.com/) (Figure 3-9b), for example, is a recent company that uses spider silk as a material to create commercial fashion products such as ties, which can costs several hundred dollars.

These examples aim to show to the reader the influence that spiders and their silks can have on our culture.

Used as excuses, as a source of fear or as a source of inspiration spider silks and webs have been always capable to stimulate our mind (from the ancient Greece to the modern world). The reasons of this can be many, but for sure the materials properties have had an important role in showing the remarkability of such materials.

Figure 3-9: a) Front page of "Rebecca dei Ragni", a book for child recently published in Italy. b) Spider silk's tie produced by the company Bolt Threads (boltthreads.com).

3.4. The mechanical properties

In this paragraph we will concentrate on the mechanical properties of the dragline, since they are the main source of the interest in spider silk. Because of the combination of strength and ductility, major ampullate silk represents today one of the best materials in term of mechanical properties (Figure 3-10). It outperforms most of the high efficiency man-made fibres (see appendix B).

At the moment, there is a great interest in exploring different types of spider silk, but very little is known about them.

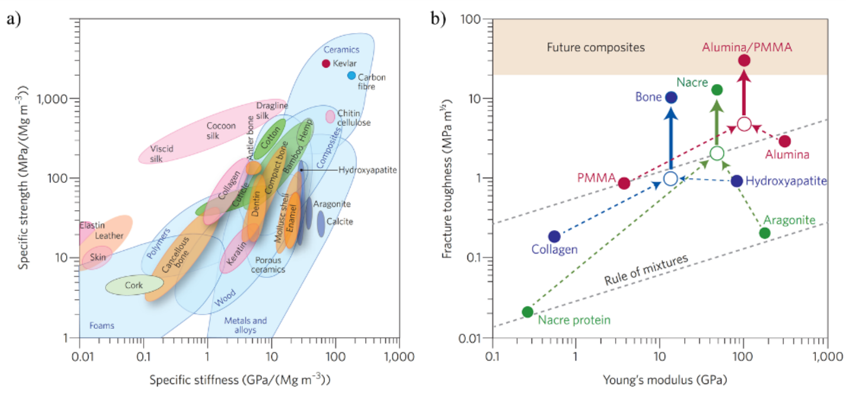

Figure 3-10: a) Ashby plot of the specific values (that is, normalized by density) of strength and stiffness (or Young's modulus) for both natural and synthetic materials. b) Many natural composite materials, as exemplified by bone and nacre, have toughness values that far exceed those of their constituents and their homogeneous mixtures (as indicated by the dashed lines), and are able to sustain incipient cracking by utilizing extensive extrinsic toughening mechanisms. Reprinted with permission from [71] *(License number: 4702701384129)*

3.4.1. The nanomechanics of spider silk

The secondary structure of major ampullate silk is the reason of its peculiar mechanical properties (Figure 3-11). We summarise here the main features of the nanomechanics of these secondary structures (e.g. β-sheets, and amorphous regions). Most of this information, come from simulation and numerical approaches. What really determines the mechanical properties of the silk is the chemical bonding between the secondary structures[72]. In particular, the hydrogen bonds occur in a denser state in the crystalline region and less dense state in the amorphous one.

Keten et al.[73] have worked on the mechanical response of these structures under load. In general, polyalanine and the adjacent poly-alanine-glycine regions represent the stiffer crystal part while the glycine rich region is typically associated to the amorphous and more extensible region. The outstanding mechanical properties of the silk derives mainly from this, namely a balance between extensibility and strength given by these two regions. In particular, the β-turns provide the hidden length that gives to the silk its extraordinary extensibility and toughness. The rupture occurs at the crystalline region when hydrogen bonds break.

Talking about the stress strain curve of the silk, we recognise four typical regimes. The first linear regime (initial rigidity till the yielding point) occurs when the amorphous region is initially stretched and the H-bonds inside break. Then, there is the unfolding of the entropic β-turns structures that provides extensibility (nonlinear elastic regime) under relatively low stress. While the amorphous strands begin to align each other, there is a formation of additional H-bonds providing the stiffening and thus the load is transferred to the crystals. In the end, the failure occurs when the H-bonds in the crystalline regions break and the stick-slip (sliding of the β-sheets crystals) mechanism occurs.

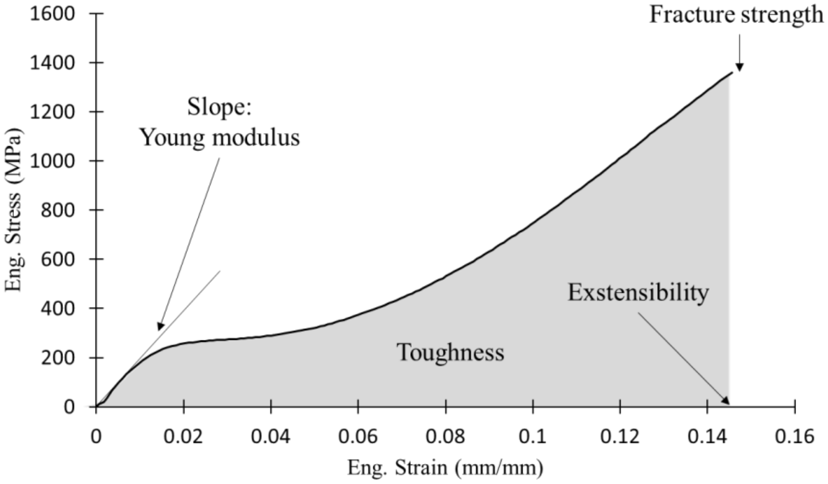

Figure 3-11: The stress-strain curve of a typical spider silk fibre. Young modulus, Toughness modulus, Extensibility and Fracture strength are the common mechanical properties obtained from the curve.

<u>How to measure the mechanical properties of silk</u>

This is one of the biggest problems in spider silk mechanical properties standardization.

The simplest approach to investigate the mechanical properties of spider silk fibres is to perform tensile tests (apply a load or a strain on the fibre). From them, what is typically obtained is a stress-strain curve (Figure 3-11). The slope of the initial elastic part of the curve (before the yielding point) represents the Young's modulus of the material. The fracture strength and the extensibility (strain at break) are simply obtained with the last points of the curve prior to fracture. Finally, the toughness is calculated by integrating the stress-strain curve.

Measuring silk's mechanical properties by means tensile tests is practically simple, but it requires some precautions. These derive from the fact that silk is a viscoelastic polymer and it is extremely reactive to environmental conditions.

For example, humidity has a strong impact on spider silk mechanical properties[74] (with a certain variation among different species[75]). It is thus essential to test the silk under controlled conditions. Fortunately, the same cannot be stated for temperature, which has an effect on silk's mechanical properties only at high variations[76].

After the spinning, additional tensional states on silk change the mechanical properties of the material (viscoelasticity)[74]. The spinning itself can affect a lot the mechanical properties. In fact, being a result of both the contribution of pH and shear forces, other forces applied to the fibres would result in modified tensional states. It is experimentally proved that spinning at different velocities (from spiders) means change mechanical properties[77–79]. The ageing of the silk is also very important, which results in a stiffening over the time with the consequent reduction in toughness[80,81], probably because of the drying and crystals reorientation.

Furthermore, the life history of the spider itself is very important. In particular, the diet of the spider (especially the protein content) affects the mechanical properties of the silk[82]. Although it is not yet demonstrated, the age of the spider could affect the mechanical properties, as it does with its brain volume and behaviours[83]. This could be related to the fact that the mechanical properties of the silk depend on the mass of the spider[84,85] and, thus, its age.

Finally, the strain rate at which the fibres are tested affects the mechanical properties of the silk. During the pulling of the silk, giving time to it means allowing it to relax and thus change its mechanical configuration [86].

An important aspect to take under consideration while measuring mechanical properties of spider silk through tensile tests is the measure of the diameter of the fibres (used to calculate the section and thus the stress). Two common techniques are Scanning Electron Microscopy and Optical Microscopy. The former is powerful and allows the scientist to have images at high resolution and discover fine details on the external structure. The latter is less powerful, but it is more user-friendly and less time consuming.

Although the first one seems to be better in studying the morphology of spider silk, it has several aspects that make it not preferential in measuring the diameter of the fibres.

The first one is the repeatability. It is known that spider silk, along a single thread, could vary the diameter[87]. This is a reason of the fact that silk displays tremendous variability in mechanical properties of samples prepared at the same moment[88]. Measuring the diameter under SEM is thus partially informative, since it concentrates only on a few samples. Moreover, the SEM sample preparation required specific techniques in order to not ruin the sample under this invasive methodology. One of these is making the sample as much conductive as possible and dehydrating for its insertion in high vacuum chambers[89,90]. For all the reasons that we stated before, it is thus clear that this procedure could affect the shape and morphology of the studied samples. A study compared the mechanical properties and the morphology obtained through these two microscopy's techniques[87]. It revealed that, because of all the processes involved in SEM technique, there is an underestimation of the diameter of the fibres (with a consequent overestimation of the mechanical properties). Moreover, it does not consider the intrinsic variability of each tested fibres, producing more scattering and statistically weaker data. In terms of other possible techniques, AFM could be used as well to investigate the diameter of the fibres. However, it requires a deep handling of the fibres that could affect the mechanical properties (added to the fact that is time consuming). Fortunately, it can provide useful information such as the topography and morphology of the fibres (Figure 3-12).

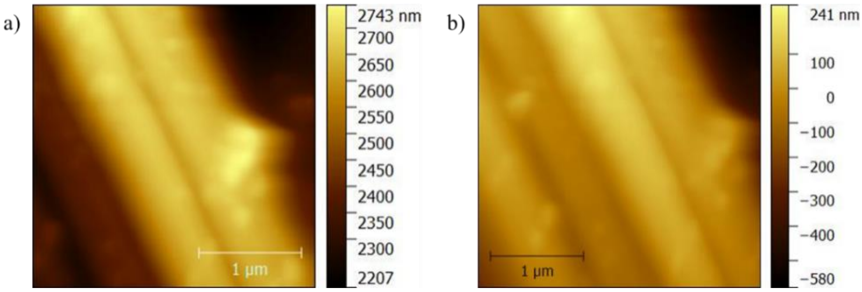

Figure 3-12: AFM pictures of a bundle of fibres that form the dragline. The fibres are pretty smooth, but with different diameters. The experimental details in[55]

In this work, we obtained the diameter with an optical microscope.

The engineering stress is thus obtained by dividing the force by the cross-section area, which is supposed to be constant during the tests.

In math

$$\sigma = \frac{F}{A_0}$$

The engineering strain, on the other hand, is obtained by dividing the displacement by the gauge length. In math

$$\epsilon = \frac{\Delta l}{l_o}$$

Another interesting possibility to study the mechanical properties of spider silk is through nanoindentation (performed with an AFM or a NanoIndenter, where the former is more complicated than the latter).

This technique is tricky if not performed on standard materials, but also very powerful. Its main advantage is the fact that it allows the experimentalist to perform tests directly on the sample on specific locations. It is, thus, possible to extrapolate local information on the mechanical properties of the material.

Another important aspect is that, for certain testing conditions, it allows the scientist to not modify the sample. For example, spider attachment discs are directly produced by a spider on a flat surface[91]. By giving the possibility to the spider to spin the anchorage on a rigid surface, it is immediately possible to obtain a perfect sample for nanoindentation. In this way, there is no need to touch or modify the sample that would, since its viscoelastic nature, affect tremendously its mechanical properties (see chapter 5). A recent study performed on spiders orb web demonstrated the validity of this approach[92].

The nanoindentation technique consists basically in a tip (in nanoindenters typically made of diamond) that is forced to penetrate the material by a strain or load gauge[93]. The machine usually measures the response of the material (by means of the elastic or plastic force) and thus obtain the load displacement curve (Figure 3-13a).

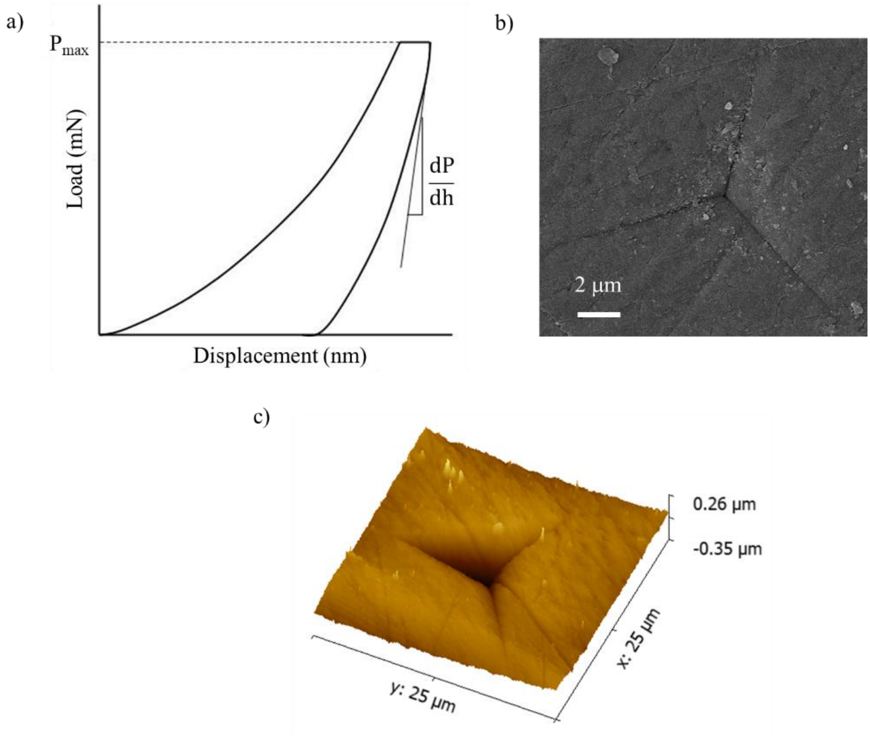

Figure 3-13: a) Typical load displacement curve of a nanoindentation test. b) SEM image of an indentation hole on chitin (spider teeth tissue). c) AFM image of the same indent depicted previously.

By means of this and through the theory developed by Oliver and Pharr[94] it is possible to obtain the hardness and the Young's modulus of the material.

The former can be obtained through

$$H = \frac{P_{max}}{A}$$

where H is the hardness (GPa), P_{max} is the maximum load in the force displacement curve and A is the contact area between the tip (probe) and the material.

The latter, Young's modulus, can be obtained in the following way by the combination of the two formulas

$$\frac{1}{E_r} = \frac{1-\nu^2}{E} + \frac{1-\nu_i^2}{E_i}$$

and

$$S = \frac{dP}{dh} = \frac{2}{\sqrt{\pi}} E_r \sqrt{A}$$

where E_r stands for the reduced modulus, ν is the Poisson ratio of the material, E its Young's modulus, ν_i the Poisson ratio of the indenter, E_i its Young's modulus, S the stiffness (Figure 3-13a), P the load and h the depth. The validity of this model is limited in the case of the contact of the tip and the material is geometrically determined (A). For this reason, it is always imperative to double check the indentation points with the support of the SEM and AFM (Figure 3-13b,c). In particular, these two powerful techniques can also provide information about the roughness of the surface that is supposed to be indented, which affects the measurement[93].

Once the methodology for measuring the mechanical properties has been decided, the experimentalist has to keep in mind the fact that the mechanical properties of spider silk vary at the interspecific and intraspecific level.

Dragline

The mechanical properties of the dragline (mainly MA silk threads) were investigated deeply for the first time in the 1976 by Denny[84]. Since then, silk's community has characterized a huge number of spider silks. We report some of them in Table 3-2. It is possible to notice how these properties vary across species.

Try to list all the mechanical properties of the dragline is a challenge, but we can have a rough idea about the material that we are dealing with. Thus, we are going to list some of the most peculiar ones of major ampullate silk. Being a viscoelastic material, testing spider silk at high strain rate speeds means to increase its Young's modulus and strength, but decrease its deformability and toughness[84,95]. This could be related to the fact that a viscoelastic material that is able to relax (and thus has time for it) can eventually decrease the tensional states in it and thus restore some reversible states in crystallinity[51,96]. This crystallinity can also be changed during the fibre spinning, which means that forcing silk formation or changing the spinning condition will affect the mechanical properties of the silk itself[78].

The crystallinity can also be changed by means of the temperature, which actually changes the mobility of the molecules. Testing spider silk at different temperature has demonstrated that it is tougher at cryogenic temperature[76]. Low temperature, on the contrary with respect to high temperature, also improve the strength of the silk.

Spider silk is a good material in term of capability to bear hysteresis cycles both as a fibre and as a bundle[97,98].

Spider	**Exstensibility (mm/mm)**	**Strength (MPa)**	**Young’s modulus (GPa)**	**Toughness (MJ/mm^3)**	**Reference**
Dysdera crocata	0.18	545	8.0	48	Swanson et al. 2006[99]
Schizocosa mccooki	0.24	553	4.6	60	Swanson et al. 2006[99]
Hypochilus pococki	0.17	945	10.9	96	Swanson et al. 2006[99]
Agelenopsis aperta	0.18	958	12.1	101	Swanson et al. 2006[99]
Peucetia viridans	0.18	1089	10.1	108	Swanson et al. 2006[99]
Nephila clavipes	0.17	1215	13.8	111	Swanson et al. 2006[99]
Plectreurys tristis	0.24	829	16.1	112	Swanson et al. 2006[99]
Metella simoni	0.28	765	8.6	114	Swanson et al. 2006[99]
Holocnemus pluchei	0.15	1244	14.3	115	Swanson et al. 2006[99]
Argiope trifasciata	0.21	1137	9.2	115	Agnarsson et al. 2008[81]
Phidippus ardens	0.19	975	14.2	116	Swanson et al. 2006[99]
Argiope argentata	0.18	1463	8.2	116	Swanson et al. 2006[99]
Latrodectus geometricus	0.31	764	10.2	117	Agnarsson et al. 2008[81]
Metepeira grandiosa	0.24	1049	10.6	121	Swanson et al. 2006[99]
Deinopis spinosa	0.19	1345	10.4	124	Agnarsson et al. 2008[81]
Uloborus diversus	0.23	1078	9.1	129	Swanson et al. 2006[100]
Latrodectus hesperus	0.22	959	9.5	132	Agnarsson et al. 2008[81]
Kukulcania hibernalis	0.22	1044	22.2	132	Swanson et al. 2006[99]
Mastophora hutchinsoni	0.27	1137	9.4	140	Swanson et al. 2006[100]
Araneus gemmoides	0.24	1414	8.6	164	Agnarsson et al. 2008[81]

Gasteracantha cancriformis	0.30	1315	8.0	178	Swanson et al. 2006[99]
Scytodes sp.	0.36	1179	10.7	230	Swanson et al. 2006[99]
Caerostris darwini	0.52	1652	11.5	354	Agnarsson et al. 2010[101]
Araneus diadematus	0.25	660	8.5	270	This work
Ancylometes	0.24	900	22	180	This work
Cupiennius salei	0.29	720	11	120	This work
Nuctenea umbratica	0.21	1200	10	140	This work
Phoneutria fera	0.32	940	27	200	This work
Zygiella x-notata	0.19	280	4.9	36	This work
Steatoda triangulosa	0.42	205	1.7	50	This work
Steatoda pakulliana	0.26	409	3.9	49	This work
Latrodectus tredecimguttatus	0.34	218	4.0	62	This work

Table 3-1: Mechanical properties of the dragline (MA silk) of different species.

As all materials, spider silk is affected by scaling laws[102,103]. This means that increasing the length of the spider silk fibre means decreasing its strength. We tested spider silk fibres at different length keeping the same relative speed (1% of the gauge length per second). Figure 3-14a is shown the strength of spider silk as a function of the tested length. In order to understand better this we used Weibull statistics, which represents a good tool in order to understand fracture mechanics and scaling laws[104]. The importance of this statistics is mainly due to its versatility in describing different phenomena and the possibility to obtain scaling laws of the analyzed material. The most used distribution of this kind is the two parameters Weibull distribution, which is defined by its cumulative density function

$$F(x) = 1 - e^{-\left(\frac{l}{l_0}\right)^d \left(\frac{x}{x_0}\right)^m} \qquad (1)$$

where, in our case, x is the fracture strength of the material, m is the shape parameters, where x_0 is the scale parameter associated to the strength, l is the length of the sample, l_0 is the minimal length containing a defect and d is the Weibull dimension. This expresses how energy is dissipated during fracture, namely if it is dissipated along the volume (d=3), the section (d=2) or the length (d=1). Equally, it represents the dimension of the dispersion of defects in the material. Commonly, $b = x_0 \left(\frac{l}{l_0}\right)^{-\frac{d}{m}}$ (2) is identified as a parameter that can be computed experimentally and that contains information on scale parameter and scaling law. Thus $F(x)$ represents the probability of the fracture strength to be equal to or less than x. The scaling laws are defined by the variation of the scale parameter with respect to the size of the material. In this case the variation of the scale parameter was introduced by Weibull with his theory[104], for which the fracture strength of a material decreases with the increase in size of the test specimen, because of the higher statistical presence of defects. This theory is also based on the fact that the shape parameter (m) is constant during the variation of the length. In the case of spider silk, we assume that the fractal dimension d is between 1 and 3.

In this work, we estimated Weibull parameters using the linear regression method. By applying to equation (1) the double logarithm we obtain

$$\ln\left(\ln\left(\frac{1}{1-F(x)}\right)\right) = mln(x) - mln(b) \qquad (3)$$

where x is the experimental value. After the organization of the values from the lowest to the biggest, $F(x)$ was computed with estimator median rank[105,106]

$$\hat{F}(x_i) = \frac{i-0.3}{n+0.4} \qquad (4)$$

where n is the number of data point in the set.

Thus, it was possible to know the value of the cumulative density function associated to each value of ultimate stress only by considering its relative position. The equation (3) was plotted for each set of data. From equation (3) the shape parameter (Weibull modulus m) was simply computed as the slope of the plot and we used the following relation for the constant associated to the scale parameter (b)

$$b = e^{-\left(\frac{\gamma}{m}\right)} \qquad (5)$$

where γ is the intercept on the vertical axis (namely $-mln(b)$).

We performed the Kolmogorov Smirnov test to verify that for each set of data we could applied Weibull statistics with the obtained parameters. An acceptance value of 95% was taken (Matlab®). To evaluate the scaling laws and the Weibull dimension of the silk of the species *Cupiennius salei*, we used five sizes: 0.55 cm, 0.75 cm, 1.0 cm, 1.2 cm and 1.4 cm. The shape parameter m and the constant b were computed for each data set. The analysis of the scaling law was performed using equation (2). In this case, we applied the logarithm to the equation (2) and obtain

$$\ln(b) = -\frac{d}{m}\ln(l) + \ln\left(\sigma_0 l_0^{\frac{d}{m}}\right) \qquad (6)$$

from where we can obtain directly the value of d from the slope of the logarithm plot and by knowing the value of the shape parameter m that is constant by changing the length of the sample.

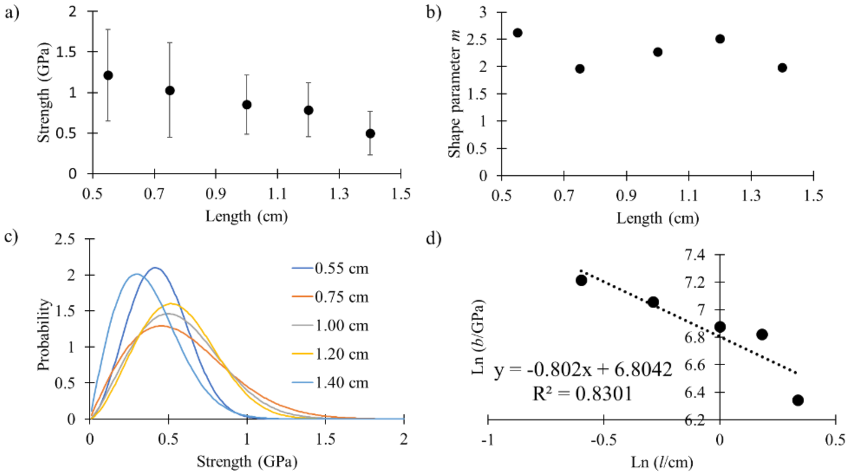

Figure 3-14: a) Plot of the mean strength versus length sample. b) Plot of the Weibull modulus versus length, mainly constant during the variation of the length. c) The different distributions of the different thread lengths for the Cupiennius salei. d) Linear plot of the shape parameter versus sample length.

Figure 3-14b shows that the obtained shape parameters were constant along all the tested dimensions, confirming the validity of Weibull statistics to our material. Weibull distributions themselves were very similar across all the length, showing that the statistical behavior is consistent (Figure 3-14c). Moreover, in Figure 3-14d is depicted the plot of equation (6), from which we can obtain *d* of spider silk that in this case is 1.8. This result highlights the necessity to modify Weibull statistics for spider silk, in order to consider the defects propagation also in the transversal direction (i.e. within the cross section of the fiber). This is a confirmation of the fact that Weibull dimension of the spider silk is between 1 and 3. It may therefore be argued that spider silk dissipates energy before fracture along the longitudinal and transversal direction of the thread, giving thus a volumetric dissipative effect of the silk. This could be a reason why dragline is so effective in absorbing kinetic energy[107]. This type of silk is also very efficient in bearing torsional moments, because of its peculiar secondary structure[108]. In particular, the torsional response is mainly mediated by the amorphous regions.

3.5. Spider silks applications

Spider silks are remarkable materials in term of mechanical properties. In addition, they present also other physical properties that could be useful in the design of possible technological applications (e.g. thermal insulation[109], piezoelectrical properties[110]).

Among all, the properties that make this material even more interesting are the biological ones. The ability of cells in adhering and proliferating on spider silk dragline was already discovered in the earlier XI centuries[111]. Moreover, spider silk seems to be strong in resisting bacteria proliferation[112]. In this regards, a recent work proposed the hypothesis that is the absence of nutrition that stops bacteria proliferation[113].

Coupled with the mechanical ones, these two driving properties led spider silks on top of the list of possible biological materials in biomedical technologies.

3.5.1. Biomedical technologies

Looking beyond the uses of fibres, in these decades several techniques have allowed scientists to explore the biomedical applications of spider silk in other forms. All of these, usually start from a spider silk solution (the strong solvent is commonly HFIP, less commonly water). With this and usually through a chemical treatment it is possible to produce nanospheres or nanoparticles. They can be used as tools for drug delivery and cancer therapy[114], as well as in hybrid composites[115,116].

Films[117], hydrogels[118], bioinks[119] and foams[120] are other typical products to produce technologies with similar purposes.

Spider silk solutions can also be used as a coating to functionalize and improve the biological properties of 3d materials[121–123]. For example, they can reduce the bacteria activity[124] or act as a bio-shield[125].

Moreover, hybrid composites with spider silk for tissue engineering have been produced with silica[126], collagen[127] and magnetosome[128].

If we classify as a biomedical technology the one that aims to prevent the degradation of food, spider silk coating has been demonstrated to be a good tool to improve the durability of specific fruits, such as apricots[129].

3.5.2. The other applications

The features of spider silks allow them to be considered for many purposes. Although the mechanical properties are terrific and major ampullate silk has been proposed as a possible substitute against Kevlar® in body armours[130], it is not an ideal material for this application because of its deformability that would lead to a huge deformation of the armour before the actual stop of the bullet. Fortunately, the mechanical properties of spider silk are still desirable for reinforcing composites[131].

Reinforcement apart, spider silk’s fibres can be used for producing sensors for airflows[132] and in music technology as violin’s strings[133].

Moreover, the mechanical properties can be optimized or improved by producing composites. It has been demonstrated, indeed, that the strength of spider silk can be improved by mixing it with metals[134] or graphene or carbon nanotubes[135].

The addition of these kind of materials (e.g. nanomaterials), usually leads to an improvement of the electrical properties[136,137], which are pretty poor in native silk[110]. This allows silk to be used as a material for developing sensors, e.g. humidity one[138].

This is especially true if one considers the incredible sensitivity of spider silk to polar chemical species, such as water[139].

Moreover, spider silks are considered useful bioindicators. Being able to interact with almost everything, they are pretty sensible to the presence of pollutants in the air. Studies monitored spider webs and checked the presence of pollutants on them[140,141].

Finally, in order to avoid to be invaded by ants, the silk of certain spiders has been selected to be ant's repellent[142].

From spider webs to technology

Spiders webs are not only interesting because of the materials that compose them. Their mechanical efficiency (e.g. stopping flying prey) could be a source of inspiration for developing technologies that are far from the mere use of the material.

For example, it is known that spiders attach their webs and dragline with specific attachment discs produced by the piriform silk[143]. Thanks to these structures, spiders webs are able to bear high wind loads[144], reduce the damage after impacts[145], and improve the capability of stopping high kinetic objects[146]. It is, thus, interesting to investigate the possibility to produce attachment devices or adhesives inspired to these structures[147,148].

Trying to learn from the geometry of spiders web sometimes can give nice tips to improve the efficiency of chemical or electrical membranes, which are designed for catching chemical pollutants[149,150]. Moreover, the same geometries can be applied in aerospace engineering, to develop catching nets for wandering objects in the space[151].

Nowadays, the metamaterials research's topic is receiving huge attention. Spiders web play an important role also here, where their geometries are currently under investigation for developing acoustic metamaterials[152,153].

The droplets of water captured in the web after the rain are always fascinating. Some scientists, used the ability of orb webs to capture water to create bio-inspired membranes in order to harvest water in those places where it is scarce (such as deserts)[154].

Some spiders are good decorators of their webs (as it has been written previously). These decorations, whose function is still to be fully determined, play a role in avoiding the impact of birds in the orb webs. The Ornlux company (http://www.ornilux.com/) noticed few years ago that almost 1 billion of birds die every year in the state of New York because of the impact with glasses (most frequently windows). They decided to insert the spider's webs decorations inside the glasses, by making them invisible to humans but visible to birds. Although the results are not known in term of bird's safety, the company treated several hundred million of building.

Another example of how spider webs structure inspire scientists could be the MART of Rovereto (Italy), the museum of the modern art. The famous architect Mario Botta maybe took inspiration in designing the ceiling like an orb web (perhaps as a symbol of structural solidity). Other architects, on the other hand, used the bell webs of *Argyroneta aquatica* to design a pavilion in Stuttgart at the congress centre[155].

Spider Silk in technology: but when?

In terms of numbers, nowadays we do have 9670 patents related to spider silk, where the first was recorded in 1942 for dental health care. These reflect the more of 17000 scientific papers that have been published in silk's topic, getting light on the importance that silks have in scientific community.

Nowadays we are still far from the huge use of spider silk-based technologies in industry. However, there are promising example that give hope to the potentiality of these materials. Bolt Threads, which has been mentioned previously in the thesis, represents just an example.

There is still a lot of work to do. Improving the efficiency of the artificial spinning, improving the mechanical properties of the artificial fibres are just examples of points that have to be addressed if we really want to apply spider silk at the industrial level.

We might say, fortunately, that the advances in silk technologies are so far fast that the fact of wearing a tie made of spider silk is no more a pure fantasy.

3.6. References

1. Vincent, J.F.V.; Bogatyreva, O.A.; Bogatyrev, N.R.; Bowyer, A.; Pahl, A.K. Biomimetics: Its practice and theory. J. R. Soc. Interface 2006, 3, 471–482.
2. George, A. ADVANCES IN BIOMIMETICS; 2011; ISBN 9789533071916.

3. Smith, A.M. Cephalopod sucker design and the physical limits to negative pressure. J. Exp. Biol. 1996, 199, 949–58.
4. Laschi, C.; Mazzolai, B.; Mattoli, V.; Cianchetti, M.; Dario, P. Design of a biomimetic robotic octopus arm. Bioinspiration and Biomimetics 2009, 4.
5. Hou, J.; Wright, E.; Bonser, R.H.C.; Jeronimidis, G. Development of Biomimetic Squid-Inspired Suckers. J. Bionic Eng. 2012, 9, 484–493.
6. Tramacere, F.; Beccai, L.; Kuba, M.; Gozzi, A.; Bifone, A.; Mazzolai, B. The Morphology and Adhesion Mechanism of Octopus vulgaris Suckers. PLoS One 2013, 8.
7. Tramacere, F.; Pugno, N.M.; Kuba, M.J.; Mazzolai, B.; Tramacere, F.; Mazzolai, B. Unveiling the morphology of the acetabulum in octopus' suckers and its role in attachment. J. R. Soc. Interface 2015, 5, 1–5.
8. Sareh, S.; Althoefer, K.; Li, M.; Noh, Y.; Tramacere, F.; Sareh, P.; Mazzolai, B.; Kovac, M. Anchoring like octopus: biologically inspired soft artificial sucker. J. R. Soc. Interface 2017, 14, 20170395.
9. Tramacere, F.; Appel, E.; Mazzolai, B.; Gorb, S.N. Hairy suckers: The surface microstructure and its possible functional significance in the octopus vulgaris sucker. Beilstein J. Nanotechnol. 2014, 5, 561–565.
10. Afferrante, L.; Carbone, G.; Demelio, G.; Pugno, N. Adhesion of elastic thin films: Double peeling of tapes versus axisymmetric peeling of membranes. Tribol. Lett. 2013, 52, 439–447.
11. Gao, H.; Wang, X.; Yao, H.; Gorb, S.; Arzt, E. Mechanics of hierarchical adhesion structures of geckos. Mech. Mater. 2005, 37, 275–285.
12. Barth, Spiders world: senses and behaviour; Springer, Ed.; Heildeberg, 2002; Vol. 133; ISBN 9783642083624.
13. Droogendijk, H. Bio-inspired MEMS Flow and Inertial Sensors, 2014.
14. Humphrey, J.A.C.; Barth, F.G. Medium Flow-Sensing Hairs : Biomechanics and Models; 2008; Vol. 34; ISBN 9780123737144.
15. Guarino, R.; Greco, G.; Mazzolai, B.; Pugno, N.M. Fluid-structure interaction study of spider ' s hair flow-sensing system. Mater. Today Proc. 2019, 7, 418–425.
16. Suter, R.B.; Stratton, G.E.; Miller, P.R. TAXONOMIC VARIATION AMONG SPIDERS IN THE ABILITY TO

REPEL WATER : SURFACE ADHESION AND HAIR DENSITY. J. Arachnol. 2004, 32, 11–21.

17. Ghio, S.; Paternoster, G.; Bartali, R.; Belluti, P.; Boscardin, M.; Pugno, N.M. Fast and large area fabrication of hierarchical bioinspired superhydrophobic silicon surfaces. J. Eur. Ceram. Soc. 2016, 36, 2363–2369.
18. Mammola, S.; Cavalcante, R.; Isaia, M. Ecological preference of the diving bell spider Argyroneta aquatica in a resurgence of the Po plain (Northern Italy) (Araneae: Cybaeidae). Fragm. Entomol. 2016, 48, 9.
19. Kesel, A.B.; Martin, A.; Seidl, T. Adhesion measurements on the attachment devices of the jumping spider Evarcha arcuata. J. Exp. Biol. 2003, 2733–2738.
20. Wolff, J.O.; Gorb, S.N. The influence of humidity on the attachment ability of the spider Philodromus dispar (Araneae , Philodromidae) Subject collections The influence of humidity on the attachment ability of the spider Philodromus dispar. Proc. R. Soc. B 2011.
21. Pugno, N.M. Spiderman gloves. Nano Today 2008, 3, 35–41.
22. Pugno, N.M. Towards a Spiderman suit: Large invisible cables and self-cleaning releasable superadhesive materials. J. Phys. Condens. Matter 2007, 19.
23. Jin, L.; Fang, M.; Chen, M.; Zhou, C.; Ombati, R.; Hakim, A.; Mo, G.; Lai, R.; Yan, X.; Wang, Y. An insecticidal toxin from Nephila clavata spider venom. Amino Acids 2017, 49, 1237–1245.
24. Andreev-andrievskiy, A.; Lagereva, E.; Osipov, D.; Berkut, A.; Grishin, E.; Vassilevski, A. Pharmacological analysis of Poecilotheria spider venoms in mice provides clues for human treatment. Toxicon 2017, 138.
25. Wu, T.; Wang, M.; Wu, W.; Luo, Q.; Jiang, L.; Tao, H.; Deng, M. Spider venom peptides as potential drug candidates due to their anticancer and antinociceptive activities. J Venom Anim Toxins incl Trop Dis 2019, 1–13.
26. Nentwig, W. Spider ecophysiology; 2013; ISBN 9783642339899.
27. Politi, Y.; Priewasser, M.; Pippel, E.; Zaslansky, P.; Hartmann, J.; Siegel, S.; Li, C.; Barth, F.G.; Fratzl, P. A spider’s fang: How to design an injection needle using chitin-based composite material. Adv. Funct. Mater. 2012, 22, 2519–2528.
28. Lakshminath Kundanati, Gabriele Greco, N.P. Ingegneria bio-ispirata a coleotteri e ragni. Entomata 2017, 5, 10–13.

29. Murray, A.T. Homer Odissey. Vol. II.; London, 1995;
30. Murray, A.T. Homer Odissey. Vol. I.; London, 1995;
31. Blame, D.M. Aristotle. History of Animals; (Mass.), C., Ed.; London, 1991;
32. Bon, M. A discourse upon the Usefulness of the Silk of Spiders. Phil. Trans. 1710, 27, 2–16.
33. Gell, A. Technology and Magic. Anthropol. Today 1988, 4, 6–9.
34. Barton, G.; Dietrich, S. The Ingenious and Singular Apparatus: Fishing Kites of the Indo-Pacific: Illustrated with Figures of the Things Defcrib'd; Demand, B.– B. on, Ed.; Heildeberg, 2009; ISBN 3839168740, 9783839168745.
35. Morgan, E. Making with spider silk: the entangled processes of human and nonhuman animals, University College London, 2013.
36. Morgan, E. Gossamer Dyas; Press, S.A., Ed.; London, 2016; ISBN 978-1-907222-35-9.
37. Bern, N.H.M. World Spider Catalog.
38. Foelix, R. Biology of Spiders; 2011; Vol. 53; ISBN 9788578110796.
39. Craig, L.B. and C.L. Spider Silk Evolution and 400 Million Years of Spinning, Waiting, Snagging, and Mating; Press, Y.U., Ed.; London, 2012;
40. SHEAR, W.A.; PALMER, J.M.; CODDINGTON, J.A.; BONAMO, P.M. A Devonian Spinneret: Early Evidence of Spiders and Silk Use. Science (80-.). 1989, 246, 479–481.
41. Vollrath, F.; Knight, D.P. Liquid crystal spinning of spider silk. Nature 2001, 410, 541–548.
42. Basu, A. Advances in Silk Science and Technology; The Textile Institute: Boston, 2015; ISBN 9781782423119.
43. Morley, E.L.; Robert, D. Electric Fields Elicit Ballooning in Spiders. Curr. Biol. 2018, 28, 2324-2330.e2.
44. Suter, R.B. Ballooning: Data From Spiders in Freefall indicate the Importance of Posture. J. Arachnol. 1992, 20, 107–113.
45. Reynolds, A..; Bohan, D..; Bell, J.. Ballooning dispersal in arthropod taxa with convergent behaviours: dynamic properties of ballooning silk in turbulent flows. Biol. Lett. 2006, 2, 371–373.
46. Darwin, C. The Voyage of the Beagle; wordsworth.; 1839;
47. White, E.B. Charlotte's Web. Book 2007, 1–157.
48. Scott, C.E.; Anderson, A.G.; Andrade, M.C.B. A review of the mechanisms and functional roles of male silk use in spider courtship and mating. J. Arachnol. 2018, 46, 173–206.

49. Craig, C.L.; Bernard, G.D.; Bernard2, G.D. Insect Attraction to Ultraviolet-Reflecting Spider Webs and Web Decorations. Source Ecol. Ecol. 1990, 71, 616–623.
50. Herberstein, M.E.; Craig, C.L.; Coddington, J.A.; Elgar, M.A. The functional significance of silk decorations of orb-web spiders: a critical review of the empirical evidence. Production 2000, 649–669.
51. Greco, G.; Pantano, M.F.; Mazzolai, B.; Pugno, N.M. Imaging and mechanical characterization of different junctions in spider orb webs. Sci. Rep. 2019, 9, 5776.
52. Sponner, A.; Vater, W.; Monajembashi, S.; Unger, E.; Grosse, F.; Weisshart, K. Composition and hierarchical organisation of a spider silk. PLoS One 2007, 2.
53. Yazawa, K.; Malay, A.D.; Masunaga, H.; Numata, K. Role of Skin Layers on Mechanical Properties and Supercontraction of Spider Dragline Silk Fiber. Macromol. Biosci. 2018, 19, 1–7.
54. Ayoub, N.A.; Garb, J.E.; Tinghitella, R.M.; Collin, M.A.; Hayashi, C.Y. Blueprint for a High-Performance Biomaterial: Full-Length Spider Dragline Silk Genes. PLoS One 2007, 2.
55. Rising, A.; Hjalm, G.; Ngstro, W.; Johansson, J. N-Terminal Nonrepetitive Domain Common to Dragline , Flagelliform , and Cylindriform Spider Silk Proteins. Biomacromolecules 2006, 2, 3120–3124.
56. Andersson, M.; Chen, G.; Otikovs, M.; Landreh, M.; Nordling, K.; Kronqvist, N.; Westermark, P.; Jörnvall, H.; Knight, S.; Ridderstråle, Y.; et al. Carbonic Anhydrase Generates CO2and H+That Drive Spider Silk Formation Via Opposite Effects on the Terminal Domains. PLoS Biol. 2014, 12, 1–15.
57. Eisoldt, L.; Smith, A.; Scheibel, T. Decoding the secrets of spider silk. Mater. Today 2011, 14, 80–86.
58. Hijirida, D.H.; Do, K.G.; Michal, C.; Wong, S.; Zax, D.; Jelinski, L.W. 13C NMR of Nephila clavipes major ampullate silk gland. Biophys. J. 1996, 71, 3442–3447.
59. Holland, G.P.; Lewis, R. V.; Yarger, J.L. WISE NMR Characterization of Nanoscale Heterogeneity and Mobility in Supercontracted Nephila clavipes Spider Dragline Silk. J. Am. Chem. Soc. 2004, 126, 5867–5872.
60. Eberhard, W.G.; Hazzi, N.A. Web construction of Linothele macrothelifera (Araneae: Dipluridae). J. Arachnol. 2013, 41, 70–75.

61. Swanson, B.O.; Anderson, S.P.; DiGiovine, C.; Ross, R.N.; Dorsey, J.P. The evolution of complex biomaterial performance: The case of spider silk. Integr. Comp. Biol. 2009, 49, 21–31.
62. Koebley, S.R.; Vollrath, F.; Schniepp, H.C. Toughness-enhancing metastructure in the recluse spider’s looped ribbon silk. Mater. Horiz. 2017, 4, 377–382.
63. Yang, Y.; Greco, G.; Maniglio, D.; Migliaresi, C.; Pugno, N.; Motta, A. Spider (Linothele megatheloides) and silkworm (Bombyx mori) silks: Comparative physical and biological evaluation. Mater. Sci. Eng. C 2019, 110197.
64. Witt, P.N.; Rawlings, J.O.; Reed, C.F. Ontogeny of Web-building Behavior in Two Orb-weaving Spiders. AM. Zool. 1972, 12, 445–454.
65. Reed, C.F.; Scarboro, M.B.; Carolina, N.; Peakall, D.B. Experience and the Orb Web. Dev. Psychobiol. 1970, 3, 251–265.
66. Eberhard, W.G. Leaf webs of Emblyna sp . and Mallos hesperius (Araneae : Dictynidae). Arachnology 2019, 18, 260–269.
67. Lin, L.H.; Edmonds, D.T.; Vollrath, F. Structural engineering of an orb-spider’s web. Nature 1995, 373, 146–148.
68. Zschokke, S.; Herberstein, M.E. Laboratory Methods for Maintaining and Studying Web-Building Spiders. J. Arachnol. 2005, 33, 205–213.
69. Blackledge, T.A.; Coddington, J.A.; Gillespie, R.G. Are three-dimensional spider webs defensive adaptations? Ecol. Lett. 2003, 6, 13–18.
70. Krell, A.; Su, I.; Qin, Z.; Bisshop, A.; Buehler, M.J.; Bisshop, A.; Mj, B.; Buehler, M.J. Imaging and analysis of a three-dimensional spider web architecture. 2018.
71. Wegst, U.G.K.; Bai, H.; Saiz, E.; Tomsia, A.P.; Ritchie, R.O. Bioinspired structural materials. Nat. Mater. 2015, 14, 23–36.
72. Heim, M.; Römer, L.; Scheibel, T. Hierarchical structures made of proteins. The complex architecture of spider webs and their constituent silk proteins. Chem. Soc. Rev. 2010, 39, 156–164.
73. Keten, S.; Xu, Z.; Ihle, B.; Buehler, M.J. Nanoconfinement controls stiffness, strength and mechanical toughness of Β-sheet crystals in silk. Nat. Mater. 2010, 9, 359–367.
74. Liu, Y.; Shao, Z.; Vollrath, F. Relationships between supercontraction and mechanical properties of spider silk. Nat. Mater. 2005, 4, 901–905.

75. Boutry, C.; Blackledge, T.A. Evolution of supercontraction in spider silk: structure-function relationship from tarantulas to orb-weavers. J. Exp. Biol. 2010, 213, 3505–3514.
76. Yang, Y.; Chen, X.; Shao, Z.; Zhou, P.; Porter, D.; Knight, D.P.; Vollrath, F. Toughness of spider silk at high and low temperatures. Adv. Mater. 2005, 17, 84–88.
77. Ortlepp, C.S.; Gosline, J.M. Consequences of forced silking. Biomacromolecules 2004, 5, 727–731.
78. Vollrath, F.; Madsen, B.; Shao, Z. The effect of spinning conditions on the mechanics of a spider's dragline silk. Proc. R. Soc. B Biol. Sci. 2001, 268, 2339–2346.
79. Perez-Rigueiro, J. The effect of spinning forces on spider silk properties. J. Exp. Biol. 2005, 208, 2633–2639.
80. Lepore, E.; Isaia, M.; Mammola, S.; Pugno, N. The effect of ageing on the mechanical properties of the silk of the bridge spider Larinioides cornutus (Clerck, 1757). Sci. Rep. 2016, 6.
81. Agnarsson, I.; Boutry, C.; Blackledge, T.A. Spider silk aging: Initial improvement in a high performance material followed by slow degradation. J. Exp. Zool. Part A Ecol. Genet. Physiol. 2008, 309, 494–504.
82. Craig, C.L.; Riekel, C.; Herberstein, M.E.; Weber, R.S.; Kaplan, D.; Pierce, N. Evidence for diet effects on the composition of silk proteins produced by spiders. Mol. Biol. Evol. 2000, 17, 1904–1913.
83. Pasquet, A.; Toscani, C.; Anotaux, M. Influence of aging on brain and web characteristics of an orb web spider. J. Ethol. 2018, 36, 85–91.
84. Denny, M.W. the Physical Properties of Spider'S Silk and Their Role in the Design of Orb-Webs. J. Exp. Biol. 1976, 65, 483–506.
85. Brandwood, A. Mechanical properties and factors of safety of spider drag lines. J. Exp. Biol. 1985, 116(0), 141–152.
86. Gosline, J.M.; Guerette, P.A.; Ortlepp, C.S.; Savage, K.N. The mechanical design of spider silks: from fibroin sequence to mechanical function. J. Exp. Biol. 1999, 202, 3295–3303.
87. Blackledge, T.A.; Cardullo, R.A.; Hayashi, C.Y. Polarized light microscopy, variability in spider silk diameters, and the mechanical characterization of spider silk. Invertebr. Biol. 2005, 124, 165–173.
88. Prez-Rigueiro, J.; Elices, M.; Llorca, C. V. Tensile properties of Argiope trifasciata drag line silk obtained from the spider's web. J. Appl. Polym. Sci. 2001, 82, 2245–2251.

89. Echlin, P. Handbook of Sample Preparation for Scanning Electron Microscopy and X-Ray Microanalysis; Springer, Ed.; New York, 2009; ISBN 9780387857305.
90. Maugel, T.K.; Goldstein, J.I.; Yakowitz, H. Practical Scanning Electron Microscopy; 2006; Vol. 95; ISBN 9781461344247.
91. Grawe, I.; Wolff, J.O.; Gorb, S.N. Composition and substrate-dependent strength of the silken attachment discs in spiders. J. R. Soc. Interface 2014, 11, 20140477–20140477.
92. Das, R.; Kumar, A.; Patel, A.; Vijay, S.; Saurabh, S.; Kumar, N. Biomechanical characterization of spider webs. J. Mech. Behav. Biomed. Mater. 2017, 67, 101–109.
93. C.Fisher-Cripps, A. Nano-indentation; 2005; Vol. 36; ISBN 1574-0684.
94. Oliver, W.C.; Pharr, G.M.; Introduction, I. An improved technique for determining hardness and elastic modulus using load and displacement sensing indentation experiments. J. Mater. Res. 1992, 7.
95. WORK, R.W. Viscoelastic behaviour and wet supercontraction of major ampullate silk fibres of certain orb-web-Building Spiders (Araneae). J. Exp. Biol. 1985, 118, 379 LP – 404.
96. Shaw, M.T.; Macknight, W.J. Introduction to Polymer Viscoelasticity; Interscience, W.-, Ed.; New Jersey, 2005; ISBN 0471740454.
97. Vehoff, T.; Glišović, A.; Schollmeyer, H.; Zippelius, A.; Salditt, T. Mechanical properties of spider dragline silk: Humidity, hysteresis, and relaxation. Biophys. J. 2007, 93, 4425–4432.
98. Hennecke, K.; Redeker, J.; Kuhbier, J.W.; Strauss, S.; Allmeling, C.; Kasper, C.; Reimers, K.; Vogt, P.M. Bundles of Spider Silk, Braided into Sutures, Resist Basic Cyclic Tests: Potential Use for Flexor Tendon Repair. PLoS One 2013, 8.
99. Swanson, B.O.; Blackledge, T.A.; Summers, A.P.; Hayashi, C.Y. Spider Dragline Silk: Correlated and Mosaic Evolution in High-Performance Biological Materials. Evolution (N. Y). 2006, 60, 2539.
100. Swanson, B.O.; Blackledge, T.A.; Beltrán, J.; Hayashi, C.Y. Variation in the material properties of spider dragline silk across species. Appl. Phys. A Mater. Sci. Process. 2006, 82, 213–218.
101. Agnarsson, I.; Kuntner, M.; Blackledge, T.A. Bioprospecting finds the toughest biological material: Extraordinary silk from a giant riverine orb spider. PLoS One 2010, 5, 1–8.

102. Yao, H.; Gao, H. Reprint of “Multi-scale cohesive laws in hierarchical materials” [In. J. Solids Struct. 44 (2007) 8177-8193]. Int. J. Solids Struct. 2008, 45, 3627–3643.
103. Carpinteri, A.; Pugno, N. Are scaling laws on strength of solids related to mechanics or to geometry? Nat. Mater. 2005, 4, 421–423.
104. Weibull, W. A Statistical Theory of the Strength of Materials. Ingeniorsvetenskapsakademiens 1939, 151, 1–45.
105. Barbero, E.; Fernandez-Saez, J.; Navarro, C. Statistical analysis of the mechanical properties of composite materials. Compos. Part B 2000, 31, 375–381.
106. Dirikolu, M.; Aktas, a; Birgoren, B. Statistical analysis of fracture strength of composite materials using Weibull distribution. Turk. J. Eng. Environ. Sci 2002, 26, 45–48.
107. Sensenig, A.T.; Lorentz, K.A.; Kelly, S.P.; Blackledge, T.A. Spider orb webs rely on radial threads to absorb prey kinetic energy. J. R. Soc. Interface 2012, 9, 1880–1891.
108. Liu, D.; Yu, L.; He, Y.; Peng, K.; Liu, J.; Guan, J.; Dunstan, D.J. Peculiar torsion dynamical response of spider dragline silk. Appl. Phys. Lett. 2017, 111.
109. Xing, C.; Munro, T.; White, B.; Ban, H.; Copeland, C.G.; Lewis, R. V. Thermophysical properties of the dragline silk of Nephila clavipes spider. Polym. (United Kingdom) 2014, 55, 4226–4231.
110. Karan, S.K.; Maiti, S.; Kwon, O.; Paria, S.; Maitra, A.; Si, S.K.; Kim, Y.; Kim, J.K.; Khatua, B.B. Nature driven spider silk as high energy conversion efficient bio-piezoelectric nanogenerator. Nano Energy 2018, 49, 655–666.
111. Allmeling, C.; Jokuszies, A.; Reimers, K.; Kall, S.; Vogt, P.M. Use of spider silk fibres as an innovative material in a biocompatible artificial nerve conduit. J. Cell. Mol. Med. 2006, 10, 770–777.
112. Roozbahani, H.; Asmar, M.; Ghaemi, N.; Issazadeh, K. Evaluation of Antimicrobial Activity of Spider Silk Pholcus Phalangioides Against Two Bacterial Pathogens in Food Borne. Int. J. Adv. Biol. Biomed. Res. 2014, 2, 2197–2199.
113. Zhang, S.; Piorkowski, D.; Lin, W.; Lee, Y.; Liao, C.; Wang, P. Nitrogen inaccessibility protects spider silk from bacterial growth. J. Exp. Biol. 2019.
114. Jastrzebska, K.; Florczak, A.; Kucharczyk, K.; Lin, Y.; Wang, Q.; Mackiewicz, A.; Kaplan, D.L.; Dams-Kozlowska, H. Delivery of chemotherapeutics using spheres made of

bioengineered spider silks derived from MaSp1 and MaSp2 proteins. Nanomedicine 2018, 13, 439–454.

115. Lucke, M.; Mottas, I.; Herbst, T.; Hotz, C.; Römer, L.; Schierling, M.; Herold, H.M.; Slotta, U.; Spinetti, T.; Scheibel, T.; et al. Engineered hybrid spider silk particles as delivery system for peptide vaccines. Biomaterials 2018, 172, 105–115.

116. Kucharczyk, K.; Rybka, J.D.; Hilgendorff, M.; Id, M.K.; Slachcinski, M.; Mackiewicz, A.; Giersig, M.; Dams-, H.; Id, K. Composite spheres made of bioengineered spider silk and iron oxide nanoparticles for theranostics applications. 2019, 1–20.

117. Agostini, E.; Winter, G.; Engert, J. Water-based preparation of spider silk films as drug delivery matrices. J. Control. Release 2015, 213, 134–141.

118. Thamm, C.; DeSimone, E.; Scheibel, T. Characterization of Hydrogels Made of a Novel Spider Silk Protein eMaSp1s and Evaluation for 3D Printing. Macromol. Biosci. 2017, 17, 1–9.

119. DeSimone, E.; Schacht, K.; Pellert, A.; Scheibel, T. Recombinant spider silk-based bioinks. Biofabrication 2017, 9, 0–4.

120. Schacht, K.; Vogt, J.; Scheibel, T. Foams Made of Engineered Recombinant Spider Silk Proteins as 3D Scaffolds for Cell Growth. ACS Biomater. Sci. Eng. 2016, 2, 517–525.

121. Chouhan, D.; Lohe, T.; Thatikonda, N.; Naidu, V.G.M.; Hedhammar, M.; Mandal, B.B. Silkworm silk scaffolds functionalized with recombinant spider silk containing a fibronectin motif promotes healing of full-thickness burn wounds Silkworm silk scaffolds functionalized with recombinant spider silk containing a fibronectin motif promotes h. ACS Biomater. Sci. Eng. 2019.

122. Gustafsson, L.; Jansson, R.; Hedhammar, M.; van der Wijngaart, W. Structuring of Functional Spider Silk Wires, Coatings, and Sheets by Self-Assembly on Superhydrophobic Pillar Surfaces. Adv. Mater. 2018, 30, 1–8.

123. Chouhan, D.; Thatikonda, N.; Nilebäck, L.; Widhe, M.; Hedhammar, M.; Mandal, B.B. Recombinant Spider Silk Functionalized Silkworm Silk Matrices as Potential Bioactive Wound Dressings and Skin Grafts. ACS Appl. Mater. Interfaces 2018, 10, 23560–23572.

124. Franco, A.R.; Fernandes, E.M.; Rodrigues, M.T.; Fernando, J.; Gomes, M.E.; Leonor, I.B.; Kaplan, D.L.; Reis, R.L. Antimicrobial coating of spider silk to prevent bacterial attachment on silk surgical sutures. Acta Biomater. 2019.

125. Zeplin, P.H.; Maksimovikj, N.C.; Jordan, M.C.; Nickel, J.; Lang, G.; Leimer, A.H.; Römer, L.; Scheibel, T. Spider silk coatings as a bioshield to reduce periprosthetic fibrous capsule formation. Adv. Funct. Mater. 2014, 24, 2658–2666.
126. Kumari, S.; Bargel, H.; Scheibel, T. Recombinant Spider Silk – Silica Hybrid Scaffolds with Drug- Releasing Properties for Tissue Engineering Applications. Macromol. Rapid Commun. 2019, 1900426.
127. Pawar, K.; Welzel, G.; Haynl, C.; Schuster, S.; Scheibel, T. Recombinant Spider Silk and Collagen-Based Nerve Guidance Conduits support Neuronal Cell Differentiation and Functionality in vitro Recombinant Spider Silk and Collagen-Based Nerve Guidance Conduits Support Neuronal Cell Differentiation and Functionality . ACS Appl. Bio Mater. 2019.
128. Mickoleit, F.; Borkner, C.B.; Toro-Nahuelpan, M.; Herold, H.M.; Maier, D.S.; Plitzko, J.M.; Scheibel, T.; Schüler, D. In vivo coating of bacterial magnetic nanoparticles by magnetosome expression of spider silk-inspired peptides. 2018.
129. Tahir, H.M.; Pervez, N.; Nadeem, J.; Khan, A.A.; Hassan, Z. Esculent coating of spider silk enhanced the preservation and shelf life of apricot. Braz. J. Biol. 2019, 6984, 1–7.
130. Sharma, A.; Dwivedi, V.K. Replacement of Kevlar With Spider Silk in Body armour. World J. Technol. Eng. Res. 2018, 3, 44–52.
131. Shah, D.U.; Porter, D.; Vollrath, F. Can silk become an effective reinforcing fibre? A property comparison with flax and glass reinforced composites. Compos. Sci. Technol. 2014, 101, 173–183.
132. Zhou, J.; Miles, R.N. Sensing fluctuating airflow with spider silk. Proc. Natl. Acad. Sci. 2017, 2017, 201710559.
133. Osaki, S. Spider silk violin strings with a unique packing structure generate a soft and profound timbre. Phys. Rev. Lett. 2012, 108, 1–5.
134. Lee, S.M.; Pippel, E.; Gösele, U.; Dresbach, C.; Qin, Y.; Chandran, C.V.; Bräuniger, T.; Hause, G.; Knez, M. Greatly increased toughness of infiltrated spider silk. Science (80-.). 2009, 324, 488–492.
135. Lepore, E.; Bonaccorso, F.; Bruna, M.; Bosia, F.; Taiolo, S.; Garberoglio, G.; Ferrari, A.; Pugno, N.M. Silk reinforced with graphene or carbon nanotube spun by spiders. 2D Mater. 2017, 64, 897–905.

136. Steven, E.; Saleh, W.R.; Lebedev, V.; Acquah, S.F.A.; Laukhin, V.; Alamo, R.G.; Brooks, J.S. Carbon nanotubes on a spider silk scaffold. Nat. Commun. 2013, 4, 1–8.
137. Kiseleva, A.; Kiselev, G.; Kessler, V.; Seisenbaeva, G.; Gets, D.; Rumyantseva, V.; Lyalina, T.; Fakhardo, A.; Krivoshapkin, P.; Krivoshapkina, E. Optically Active Hybrid Materials Based on Natural Spider Silk. ACS Appl. Mater. Interfaces 2019.
138. Li, X.; Zong, L.; Wu, X.; You, J.; Li, M.; Li, C. Biomimetic engineering of spider silk fibres with graphene for electric devices with humidity and motion sensitivity. J. Mater. Chem. C 2018, 6, 3212–3219.
139. Hey Tow, K.; Chow, D.M.; Vollrath, F.; Dicaire, I.; Gheysens, T.; Thevenaz, L. Exploring the use of native spider silk as an optical fibre for chemical sensing. J. Light. Technol. 2017, 8724, 1–8.
140. Rachwał, M.; Rybak, J.; Rogula-Kozłowska, W. Magnetic susceptibility of spider webs as a proxy of airborne metal pollution. Environ. Pollut. 2018, 234, 543–551.
141. Rybak, J.; Spówka, I.; Zwoździak, A.; Fortuna, M.; Trzepla-Nabagło, K. Evaluation Of The Usefulness Of Spider Webs As An Air Quality Monitoring Tool For Heavy Metals. Ecol. Chem. Eng. S 2015, 22, 389–400.
142. Zhang, S.; Koh, T.H.; Seah, W.K.; Lai, Y.H.; Elgar, M.A.; Li, D. A novel property of spider silk: chemical defence against ants. Proc. R. Soc. B Biol. Sci. 2012, 279, 1824–1830.
143. Wirth, M.; Wolff, J.O.; Appel, E.; Gorb, S.N. Ultrastructure of spider thread anchorages. J. Morphol. 2019, 280, 534–543.
144. Pugno, N.M.; Cranford, S.W.; Buehler, M.J. Synergetic material and structure optimization yields robust spider web anchorages. Small 2013, 9, 2747–2756.
145. Cranford, S.W.; Tarakanova, A.; Pugno, N.M.; Buehler, M.J. Nonlinear material behaviour of spider silk yields robust webs. Nature 2012, 482, 72–76.
146. Meyer, A.; Pugno, N.M.; Cranford, S.W. Compliant threads maximize spider silk connection strength and toughness. J. R. Soc. Interface 2014, 11, 20140561–20140561.
147. Wolff, J.O.; Herberstein, M.E. Three-dimensional printing spiders: Back-and-forth glue application yields silk anchorages with high pull-off resistance under varying loading situations. J. R. Soc. Interface 2017, 14.

148. Wolff, J.O.; Van der Meijden, A.; Herberstein, M.E. Distinct spinning patterns gain differentiated loading tolerance of silk thread anchorages in spiders with different ecology. Proc. R. Soc. B Biol. Sci. 2017, In Press.
149. Zhu, Q.; Tang, X.; Feng, S.; Zhong, Z.; Yao, J.; Yao, Z. ZIF-8@SiO 2 composite nanofiber membrane with bioinspired spider web-like structure for efficient air pollution control. J. Memb. Sci. 2019, 252–261.
150. Liao, J.; Yang, M.; Zhang, W.; Zeng, D.; Ning, C.; Yuan, H. Spider silk-inspired universal strategy : directional patching of one-dimensional nanomaterial-based flexible transparent electrodes for smart flexible electronics. Chem. Eng. J. 2019, 123663.
151. Xu, B.; Yang, Y.; Yan, Y.; Zhang, B. Bionics design and dynamics analysis of space webs based on spider predation. Acta Astronaut. 2019, 159, 294–307.
152. Miniaci, M.; Krushynska, A.; Movchan, A.B.; Bosia, F.; Pugno, N.M. Spider web-inspired acoustic metamaterials. Appl. Phys. Lett. 2016, 109.
153. Krushynska, A.O.; Bosia, F.; Miniaci, M.; Pugno, N.M. Spider web-structured labyrinthine acoustic metamaterials for low-frequency sound control. New J. Phys. 2017, 19, 1–12.
154. Huang, Z.X.; Liu, X.; Wu, J.; Wong, S.C.; Qu, J.P. Electrospinning water harvesters inspired by spider silk and beetle. Mater. Lett. 2018, 211, 28–31.
155. Knippers, J.; Nickel, K.G.; Speck, T. Biomimetic research for Architecture and Building Construction: Biological Design and Integrative Structures; Springer, Ed.; 2016; ISBN 9783319463728.

3.7. Content of the chapters

Chapter 4:
Chapter 4 explores the mechanical properties of different types of silk junctions among threads in the spider orb webs. Through imaging and tensile tests, it illustrates how the superior mechanical efficiency of spider webs is achieved.

Chapter 5:
Chapter 5 explores the mechanical properties of the piriform silk produced by the species *Cupiennius salei*. This silk plays a crucial role in spider

attachment’s discs and threads’ junctions. With the support of a simple analytical model, the mechanical properties of the single fibre are related with the mechanical properties of the whole membrane.

Chapter 6:

Chapter 6 reports the characterization of the unknown silk of *Linothele megatheloides*, which is better than the silkworm silk in terms of biological properties. This spider is able to produce large amount of silk and with a comparative approach we show that this new material gives promising perspectives on tissue engineering.

Chapter 7:

Chapter 7 deals with the characterization of hybrid materials composed by spider silk and hydroxyapatite (which has been biomimetically mineralized on the silk) with the aim of bones tissue regeneration. In this chapter the optimization of the production process is described as well as the obtained composite characterization.

Chapter 8:

Chapter 8 describes a simple protocol to develop and design biomedical devices based on silk. The promising mechanical properties and the capability to tune the biological ones are here presented as a key for future investigation on similar spider’s silk related systems.

Chapter 9:

Chapter 9 explores the mechanical properties of artificial spider silk under different conditions. With the aim to improve such properties, the effects of humidity on these fibres is reported and analysed together with a protocol to reduce such effects. Moreover, the effects of incubating the fibres longer in the spinning buffer are reported.

4. CHARACTERIZATION OF DIFFERENT JUNCTIONS IN SPIDER ORB WEBS

This chapter is based on the paper published in Scientific Reports (volume 9, Article number: 5776, 2019, DOI: 10.1038/s41598-019-42070-8) and deals with the mechanics of the junctions (produced by different glands and silks) in the orb web of the spider *Nuctenea umbratica*. For the sake of shortness, the reader may find the supplementary information in the original paper.

Goal of the chapter: This chapter aims to explore the mechanical properties of different types of silk junctions among threads in the spider orb webs. Through imaging and tensile tests, we illustrate how the superior mechanical efficiency of spider webs is achieved. In this way, spider orb webs are seen as inspiration to develop fabrics and related bio-inspired systems.

4.1. Abstract

Spider silk and spider orb webs are among the most studied biological materials owing to their outstanding mechanical properties. A key feature that contributes significantly to the robustness and capability to absorb high kinetic energy of spider webs is the presence of junctions connecting different silk threads. Surprisingly, in spite of their fundamental function, spider web junctions have never been characterized. Herein, through mechanical characterization and imaging, we show for the first time that spider orb webs host two different types of junction, produced by different silk glands, which have different morphology, and load bearing capability. These differences can be explained in view of the different roles they play in the web, i.e. allowing for a localized damage control or anchoring the whole structure to the surrounding environment.

4.2. Introduction

Spider silk is a unique protein-based material produced by the silk glands of spiders [1-3]. Owing to its outstanding mechanical properties, which have been investigated in depth [4-8], spider silk is currently under consideration for a variety of applications, ranging from engineering to medicine[9-13]. During their evolution, spiders have used their silk for a variety of purposes, including production of egg sacs, mating behavior, self-defense and prey capture [1,2,14]. For the capture of prey, the orb-web

(Figure 4-1a) is one of the most effective structures developed by nature [15].

From a mechanical point of view, the behavior of the orb-web under external loads due to wind and impacts has been studied mainly through a numerical approach [16]. It was found that the spider's web can resist extreme wind conditions owing to the presence of specific anchorages that securely fix it to a surface [17]. From a structural point of view, these anchorages, or attachment discs, consist of very thin (~ tens of nanometers in diameter) fibers embedded in a matrix with an unknown chemical composition [18-20] (Figure 4-1b). The mechanical properties of such discs were intensively investigated through both theoretical and experimental studies. In particular, their mechanical behavior was studied through the theory of multiple peeling and its numerical implementation [21-22]. More recently, experiments were performed in order to derive the peeling force required to detach spider silk anchorages from different substrates (Figure 4-1b-d) [23-25].

Besides anchorages, other important features contribute significantly to the performances of the spider's web. These are the junctions connecting different threads to one another (Figure 4-1e) [26] within the same web (Figure 4-1a). At junctions, web threads interact in a synergistic fashion that provides the whole structure with its unique capability of minimizing the area damaged by the impact of an object, e.g. flies [27]. However, despite their fundamental role, spider web junctions have never been deeply characterized. Thus, herein we focus specifically on the role played by these structural elements and we give special attention to their morphology and mechanical properties.

In the literature, it is commonly accepted that junctions result from localized deposition of a silk-secretion produced by the piriform glands of spiders [2], which are the same glands that produce the silk used for the attachment discs (Figure 4-1b,e). However, the experimental evidence of this work, in agreement with Vasanthavada et al. [28], shows that aggregate glands, which are normally used to produce the glue droplets in the catching spiral threads [29] (Figure 4-2a-b), are involved, too.

Finally, in order to explain the need for the presence of two different junctions in the orb web, we performed, for the first time, both morphological analyses and mechanical characterization tests.

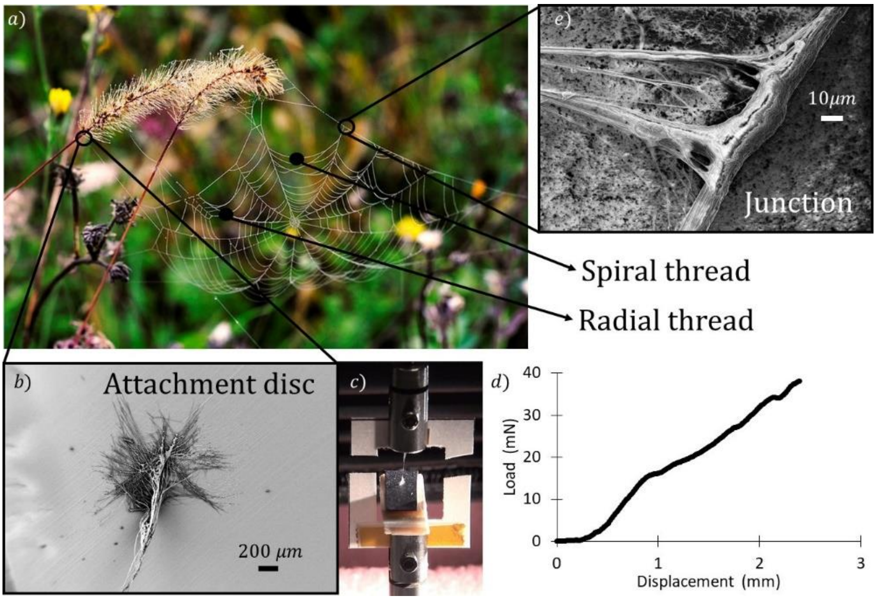

Figure 4-1: a) Picture of an orb-web structure (courtesy of Federica Fabietti), including radial and spiral threads, as indicated by the arrows. Adjacent threads are held together at junction points. The whole web structure is fixed to the ground by attachment discs; b) SEM picture of an attachment disc, produced by Nuctenea umbratica that anchors the web to a substrate; c) A web anchorage under mechanical characterization through a nanotensile testing machine. Here a dangling silk fiber connected to the disc is pulled until the disc is completely detached from its paper substrate, providing the load-displacement curve reported in (d). e) SEM picture of a junction connecting a spiral and a radial thread isolated from an orb web produced by the species Nuctenea umbratica; the junction was not metalized.

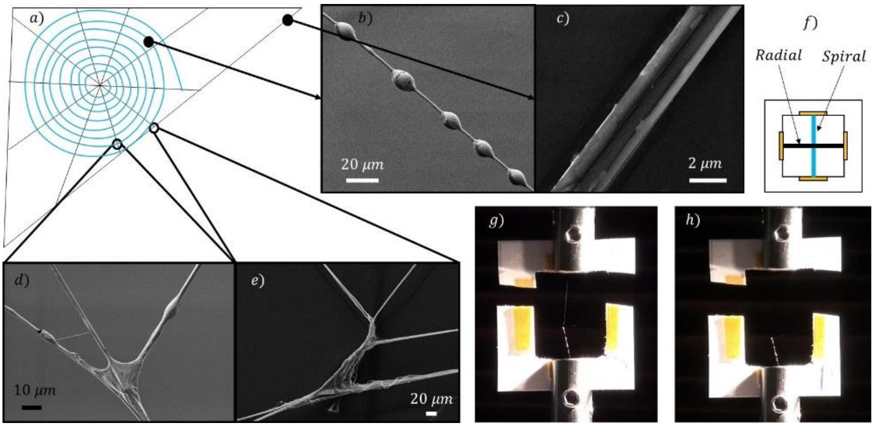

Figure 4-2: a) Schematic of an orb web, consisting of spiral (b) and radial (c) threads. d) SEM picture of a junction involving two spiral threads and one radial thread. e) SEM picture of a junction between two radial threads. Significant difference can be observed between the two types of junction. f) Schematic of a web sample mounted on a paper frame to test junction structural properties. g) Junction sample under mechanical characterization through a nanotensile testing machine and h) the remaining structure after junction failure.

4.3. Results

In the web structure we can identify two kinds of junction according to the type of the involved threads (either spiral or radial, Figure 4-2b-c). If we compare their morphology (Figure 4-2d-e, Figure 4-3), several differences emerge. Junctions between radial threads, which are those occurring along the edges of the web (Figure 4-2e) or where this is fixed to the substrate, have a multiple fibril shape. This morphology is similar to that of the attachment disc (Figure 4-1b) and could be thus produced by the piriform glands as well [2]. On the other hand, junctions that involve both radial and spiral threads look completely different (Figure 4-2d). Indeed, they consist of a glue drop that looks like the droplets in catching spiral threads (Figure 4-2b, Figure 4-3a-c). Thus, similarly to these latter, they can be expected to be produced by aggregate glands, too. The role of the aggregate glands in the production of this kind of junctions in orb web has never been reported, but only observed in 3D cob web by Vasanthavada et al. [28]

In order to evaluate the mechanical properties of all the orb web junctions, we isolated from the orb web five different samples, each involving a specific number of junctions and silk threads (Figure 4-3): (a) T-shaped spiral-to-radial junction (TSR), (b) Cross-shaped spiral-radial junction (CSR), (c) Net-shaped spiral-to-radial junction (NSR), (d) T-shaped radial-to-radial junction (TRR), and radial-to-surface junction (RFS, here reported for the sake of comparison with the literature). The first tested configuration (a) consists of a spiral thread joined nearly perpendicular to a radial thread by aggregate silk glue (Figure 4-3a). The second (b) is similar to the previous one, but with another spiral thread that is arranged normal to the radial thread, thus resulting in a cross shape with aggregate glue at the middle (Figure 4-3b). The third tested configuration (c) belongs to a more complex web structure, composed of a supporting radial thread that crosses four perpendicular spiral threads that are connected through aggregate silk (Figure 4-3c). The fourth tested configuration (d) has a T shape that differs from type (a), as it consists of only radial threads joined together by a multifibril structure that recalls the piriform silk morphology (Figure 4-3d). The fifth sample (Figure 4-1b-d) is the whole attachment disc of the web as produced by the piriform gland.

In order to investigate the mechanical properties, ten replications for each sample were considered, where either a spiral or radial thread was pulled out of its junction (Figure 4-2f-h, Figures S1-S6, Tables S1-S5). We found that the mean force necessary to break TSR junctions (type a) was 0.4 ± 0.2 mN, with dissipated energy of 1.5 ± 1.1 μJ and mean displacement at break of 9 ± 4 mm (Figure 4-2). We noticed that after failure the supporting radial thread remained undamaged (Figure S2). For the CSR junctions (type b), we found that the mean force at break was 0.9 ± 0.2 mN, its dissipated energy was 3.4 ± 1.8 μJ and its mean displacement at break was 10 ± 5 mm (Figure 4-4). The supporting structure resulted unbroken after the break of the junction also in this case (Figure S3). The NSR sample (type c) showed an average force at break of 1.3 ± 0.5 mN, dissipated energy of 7.4 ± 5.5 μJ with the corresponding mean displacement at break being 19 ± 5 mm (Figure 4-4). After the rupture of the junction linked to the spiral thread where the force was applied, the remaining structure resulted undamaged (Figure S4). The mean maximum load that the TRR junction (type d) can withstand was 9 ± 2 mN, its dissipated energy was 19 ± 8μJ with a corresponding displacement at break of 5 ± 1 mm (Figure 4-4). The supporting radial thread resulted undamaged after the junction failure (Figure S5). Finally, the anchorage sample showed an average force at break of 18 ± 10 mN, dissipated energy of 26 ± 10 μJ, with the corresponding mean displacement at break being 2.9 ± 1.2 mm (Figure 4-4). The initial length of the pulled thread was 0.5 cm in all the tested specimens.

In order to interpret the differences among the force values recorded for each junction sample, we performed both ANOVA and Weibull Statistics analysis (Tables S1-S5, S9, Supporting Figures S6-S11). In particular, junction separation forces differed significantly across all junction types (ANOVA, p~0, all post-hoc pairwise comparisons p<0.05). Interestingly, the highest p-value (~0.02) was observed for CSR and NSR junctions (Table S9). Indeed, the Weibull distributions obtained from the data available for CSR and NSR samples are very similar, while the distributions corresponding to the samples that involve radial threads show a huge difference with respect to those that involve spiral threads.

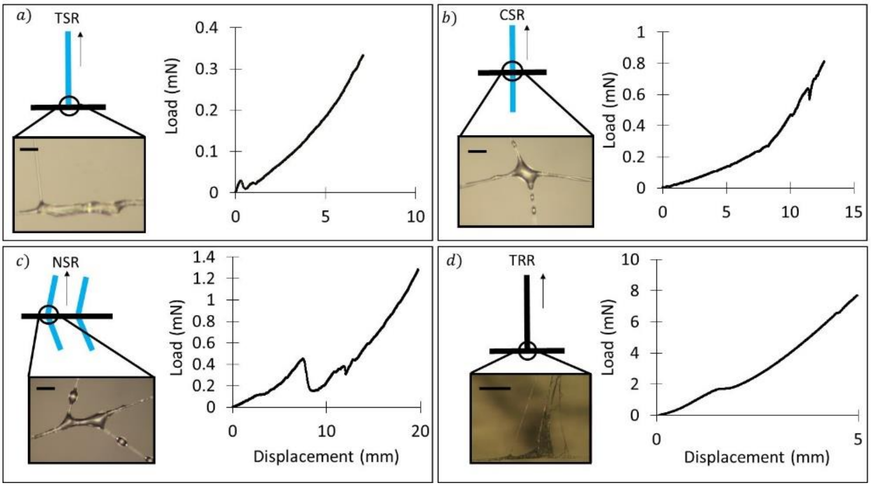

Figure 4-3: Example Load/Displacement curves derived from testing different web samples, each involving a different number/type of silk threads and junctions. These curves were obtained by pulling until complete detachment: a) a spiral thread from a radial thread; b) a spiral thread from a radial thread connected to another spiral thread; c) a spiral thread form a complex system with more than one spiral thread connected to a single radial thread; d) a radial thread from a radial thread. Images reveal that junctions involving either spiral and radial threads or only radial threads are characterized by different morphology. Scale bar:10 µm.

Type of junction	**Failure mode**	**Force at break**	**Displacement at break**	**Energy dissipated at break**
a) Spiral from Radial (TSR) ⊥	—	0.4 ± 0.2 mN	9 ± 4 mm	1.5 ± 1.1 µJ
b) Spiral from Radial (CSR) ┼	┬	0.9 ± 0.2 mN	10 ± 5 mm	3.4 ± 1.8 µJ
c) Spiral from Radial (NSR) 		1.3 ± 0.5 mN	19 ± 5 mm	7.4 ± 5.5 µJ
d) Radial from Radial (TRR) ⊥	—	9 ± 2 mN	5 ± 1 mm	19 ± 8 µJ
e) Radial from a surface (RFS) 		18 ± 10 mN	2.9 ± 1.2 mm	26 ± 10 µJ

Figure 4-4: Maximum load/displacement and toughness obtained after testing different web samples. All displacements are referred to an initial length of 0.5 cm. The second column reports what is left after the sample failure: in all the tested configurations, the supporting structure resulted unbroken after the junction failure (i.e., complete detachment of the pulled thread). The toughness was computed by calculating the area under the load-displacement curves.

4.4. Discussion

Two features common to all the tested samples are concerned with the maximum force, which is recorded when the pulled thread detaches completely from its junction (Figures S2-S5), and the shape of the sample after the mechanical test, whose structure (consisting of either another thread or a more complex architecture) looks the same as before the test, except for the pulled thread. This indicates the ability of the web structure to localize the damage regardless the size of its analyzed portion.

Regarding the structural properties collected in Figure 4-3 and Figure 4-4, we can immediately see that junctions involving only radial threads, such as TRR or RFS configurations, which are mainly composed of piriform silk, are much stronger (23 times and 46, respectively, compared to TSR) yet tougher (with a dissipated energy of 13 and 26 times bigger than that of TSR sample, respectively) than those involving spiral threads, which are mainly composed of aggregate silk. Such result is also supported by the statistical analysis of the breaking force (Tables S1-S5, S8, Figures S6-S11). This can be easily explained by recalling the different position that such junctions occupy within the web structure. In particular, junctions between radial threads, which are located at the edge of the web, must support higher loads (e.g. high-speed wind) in comparison to the region embedded within the boundary of the web that has mainly the function to stop preys. In this region, aggregate silk joins the spiral threads to radial threads, providing the spider's web with its classical orb shape. Spiral-radial thread junctions act as filters for choosing the appropriate prey for the spider and for avoiding useless damage of the cobweb. As big loads could be fatal to the structure, causing an extended and irreversible damage, high kinetic energy objects are allowed to pass through the web by producing a localized rupture, e.g. of a single junction (that thus behaves as a sacrificial element). The existence of two different types of junction becomes thus necessary, with one (i.e., pyriform based junction) for sustaining high loads and holding the structure as a whole and the other one (i.e., aggregate based junction) for catching preys without compromising the integrity of the entire structure and allowing spiders to save energy in rebuilding the web after an impact [27]. Finally, it can be observed from our tests that when we pull a radial thread out of a spiral-radial thread junction, the stiffness of the supporting structure plays a role in determining the mechanical properties of the web sample. Indeed, moving from TSR to CSR and NSR, the increase of structural complexity and stiffness, given by the addition of one or more spiral threads connected to the same radial thread, leads to an increase of the maximum force, and also an increase of displacement at break and dissipated energy (Tables S6-S8). This agrees also to what found for configuration TRR, that is stiffer and tougher than TSR sample. Radial threads are themselves stiffer than spiral ones, with a Young's modulus of ~1 GPa, that is one order of magnitude bigger than that of spiral threads (~ 0.1 GPa). By referring to the force increase in CSR (2.4) and NSR (3.3) with respect to TSR samples

(Table S5), this tends to saturate with the increase of complexity (e.g., stiffness) of the structure itself (the force at break of NSR is only 1.4 bigger than that for CSR in spite of the addition of a number of threads). This suggests that after a certain number of threads added to the anchor, there is no more increase in the junction load bearing capacity.

4.5. Conclusion

A 400 million years evolution has designed the orb web as a structure simultaneously able to stop flying prey, localize damage after impacts and withstand high loads. The interaction among the threads and their anchorages to the substrate could provide an explanation to the mechanical efficiency of the orb webs. This interaction is mediated by the presence of junctions that connect threads to each other or to the surrounding environment. In this work, we observed that two different types of junction exist and we measured the force necessary to break them in different configurations. The first type results to be made of aggregate silk that is used by spiders for joining radial and spiral threads as well as to provide spiral threads with sticky droplets. The second type results to be composed of pyriform silk that is mainly used for joining either radial threads together and/or radial threads with the substrate. The first type of junction showed a lower breaking force with respect to the second type, even if an increase in both the force and displacement at break was observed as associated to an increased structural complexity. This difference in terms of breaking force can be explained by considering the different roles that these kinds of junction play in the orb web. Indeed, junctions between two radial threads and between radial threads and surfaces have to withstand higher loads since these supports the whole web structure, while junctions involving spiral threads have to guarantee damage localization (e.g., web robustness), thus breaking at lower loads.

The achievements of our work could provide new information that shed light on the mechanical behavior of spider’s orb web that can be used for the design of new bio-inspired nets and fabrics with superior mechanical properties.

4.6. Methods

4.6.1. Spiders care and web production

The spider under study was *Nuctenea umbratica* (Clerck 1876), common nocturnal spider that usually builds its web during the night. We kept three individuals in glass terrarium of about 30x30x40 cm. All spiders were adult females and fed with a weekly diet of *Blaptica dubia* that were breed in the “Laboratory of Bio-inspired and Graphene Nanomechanics” and fed weekly with carrots and fish food. All terrariums were set in the same way with three long sticks covered with paper attached to the wall of the terrarium. Each terrarium was provided with a small refuge, made of paper, in the right corner of the cage to allow the spider to feel protect and live without stress during the day. Each spider produced its orb web after a few days.

4.6.2. Sample preparation

The tested samples were prepared by following the same procedure reported by Blackledge et al. [30] and Grawe et al. [23] we stuck the web samples on a paper frame provided with a square window of 1 cm side. The web sample was fixed to the paper frame with a double-sided tape. We checked the direction of the spinning process before collecting web samples. By referring to the anchorages, we stuck black paper on the terrarium walls where the spider spins the attachment disc. Then we cut the portion of the paper containing the anchorage and fix it on a wood block (2x0.5x0.5 cm^3). This block was fixed on the previous paper support by attaching the radial thread on the upper part of the frame.

4.6.3. Optical and SEM images

For the morphology characterization, we used an Optical microscope (Jenavert) with a 20x enlargement lens. The microscope was provided with a camera (Canon) connected to a computer for remote control.

For the SEM characterization, we used a Zeiss – 40 Supra. The metallization was made by using a sputtering machine Q150T and the sputtering mode was Pt/Pd 80:20 for 5 minutes. For the Figure 1b we did not metalize the sample and the picture was taken at 2.0 kV, 1300 Magnification with secondary electron detector. For the Figure 1c the picture was taken at 2.0 kV, 103 Magnification and with secondary electron detector. With reference to figures 2b-e the pictures were taken at 2.0 kV, 15 kV, 2.0 kV and 15.0 kV, 1290, 5580, 2520 and 641 magnifications, respectively, with the secondary electron detector in all cases.

4.6.4. Mechanical characterization

For the mechanical characterization, we used a nanotensile machine (Agilent technologies T150 UTM) with a cell load of 500 mN. The displacement speed was 10 μm per second with the frequency load at 20 Hz. The samples were mounted in order to pull a spiral or radial thread out (depending on the sample) in the opposite direction to spider spinning. The declared sensitivity of the machine is 10 nN for the load and 1 Å for the displacement in the dynamic configuration. The tests were recorded with a Sony Camera. Six to ten samples were tested for each configuration.

4.7. References

1. Foelix, R. Biology of Spider. Oxford University Press 53, (2011).

2. Nentwig, W. Spider ecophysiology. Spider Ecophysiology (2013). doi:10.1007/978-3-642-33989-9
3. Madsen, B., Shao, Z. Z. & Vollrath, F. Variability in the mechanical properties of spider silks on three levels: Interspecific, intraspecific and intraindividual. Int. J. Biol. Macromol. 24, 301–306 (1999).
4. Plaza, G. R., Guinea, G. V., Pérez-Rigueiro, J. & Elices, M. Thermo-hygro-mechanical behavior of spider dragline silk: Glassy and rubbery states. J. Polym. Sci. Part B Polym. Phys. 44, 994–999 (2006).
5. Das, R. et al. Biomechanical characterization of spider webs. J. Mech. Behav. Biomed. Mater. 67, 101–109 (2017).
6. Plaza, G. R. et al. Relationship between microstructure and mechanical properties in spider silk fibers: identification of two regimes in the microstructural changes. Soft Matter 8, 6015 (2012).
7. Guinea, G. V., Elices, M., Pérez-Rigueiro, J. & Plaza, G. Self-tightening of spider silk fibers induced by moisture. Polymer (Guildf). 44, 5785–5788 (2003).
8. Perez-Rigueiro, J. The effect of spinning forces on spider silk properties. J. Exp. Biol. 208, 2633–2639 (2005).
9. Vollrath, F. Biology of spider silk. Int. J. Biol. Macromol. 24, 81–88 (1999).
10. Cetinkaya, M., Xiao, S., Markert, B., Stacklies, W. & Gräter, F. Silk fiber mechanics from multiscale force distribution analysis. Biophys. J. 100, 1298–1305 (2011).
11. Kluge, J. A., Rabotyagova, O., Leisk, G. G. & Kaplan, D. L. Spider silks and their applications. Trends Biotechnol. 26, 244–251 (2008).
12. Vollrath, F. & Porter, D. Spider silk as archetypal protein elastomer. Soft Matter 2, 377 (2006).
13. Lewis, R. V. Spider Silk : Ancient Ideas for New Biomaterials Spider Silk : Ancient Ideas for New Biomaterials. 106, 3762–3774 (2006).
14. Eisoldt, L., Smith, A. & Scheibel, T. Decoding the secrets of spider silk. Mater. Today 14, 80–86 (2011).
15. Boutry, C. & Blackledge, T. A. Wet webs work better: humidity, supercontraction and the performance of spider orb webs. J. Exp. Biol. 216, 3606–3610 (2013).
16. Asakura, T. & Miller, T. Biotechnology of Silk. 5, (2014).

17. Pugno, N. M., Cranford, S. W. & Buehler, M. J. Synergetic material and structure optimization yields robust spider web anchorages. Small 9, 2747–2756 (2013).
18. Blasingame, E. et al. Pyriform spidroin 1, a novel member of the silk gene family that anchors dragline silk fibers in attachment discs of the black widow spider, Latrodectus hesperus. J. Biol. Chem. 284, 29097–29108 (2009).
19. Kovoor, J. & Zylberberg, L. FINE STRUCTURAL ASPECTS OF SILK SECRETION DlADEMATUS). IN THE. Tissue Cell 12, 547–556 (1980).
20. Kovoor, J. & Zylberberg, L. Fine structural aspects of silk secretion in a spider. Tissue Cell 14, 519–530 (1982).
21. Pugno, N. M. The theory of multiple peeling. Int. J. Fract. 171, 185–193 (2011).
22. Brely, L., Bosia, F. & Pugno, N. M. Numerical implementation of multiple peeling theory and its application to spider web anchorages. Interface Focus 5, 20140051 (2015).
23. Grawe, I., Wolff, J. O. & Gorb, S. N. Composition and substrate-dependent strength of the silken attachment discs in spiders. J. R. Soc. Interface 11, 20140477–20140477 (2014).
24. Wolff, J. O., Van der Meijden, A. & Herberstein, M. E. Distinct spinning patterns gain differentiated loading tolerance of silk thread anchorages in spiders with different ecology. Proc. R. Soc. B Biol. Sci. In Press, (2017).
25. Wolff, J. O., Grawe, I., Wirth, M., Karstedt, A. & Gorb, S. N. Spider's super-glue: thread anchors are composite adhesives with synergistic hierarchical organization. Soft Matter 11, 2394–2403 (2015).
26. Meyer, A., Pugno, N. M. & Cranford, S. W. Compliant threads maximize spider silk connection strength and toughness. J. R. Soc. Interface 11, 20140561–20140561 (2014).
27. Cranford, S. W., Tarakanova, A., Pugno, N. M. & Buehler, M. J. Nonlinear material behaviour of spider silk yields robust webs. Nature 482, 72–76 (2012).
28. Vasanthavada, K. et al. Spider glue proteins have distinct architectures compared with traditional spidroin family members. J. Biol. Chem. 287, 35985–35999 (2012).
29. Opell, B. D. & Schwend, H. S. Adhesive efficiency of spider prey capture threads. Zoology 112, 16–26 (2009).
30. Blackledge, T. A. Quasistatic and continuous dynamic characterization of the mechanical properties of silk from the

cobweb of the black widow spider Latrodectus hesperus. J. Exp. Biol. 208, 1937–1949 (2005).

5. STRONGER AND TOUGHER SILK FOR RESILIENT ATTACHMENT DISCS: THE MECHANICAL PROPERTIES OF THE PIRIFORM SILK

The complete model of spider orb web is still lacking. Among all the difficulties, the mechanical characterization of all the silks that compose it is maybe one of the hardest to solve. In this chapter, which is based on a paper recently submitted and now under revision, we explore the mechanical properties of the piriform silk and what role it plays in attachment discs as a membrane. For the sake of shortness, the reader may find the supplementary information in the original paper.

Goal of the chapter: This chapter aims to explore the mechanical properties of the piriform silk produced by the species *Cupiennius salei*. This silk has never been investigated in depth and it plays a crucial role in spider attachment's discs. For this reason, we explore its mechanical properties and we relate them with the mechanical properties of the whole membrane. This will help the understanding of these complex systems and will give an inspiration to design new efficient adhesives.

5.1. Abstract

Spiders are able to produce different types of silk with different mechanical and biological properties. Piriform silk is produced to secure spiders and their webs to surfaces by using a multi-fibrils system embedded in a cement-like matrix. Although the efficiency of the attachment discs produced by spiders has been uncovered, the mechanical properties of this membrane-like silk products are mostly unknown. Herein we report an investigation of the mechanical properties of the piriform silk of the species *Cupiennius salei*. Through nanoindentation and nanotensile techniques and with the support of a simple theoretical model, we estimated the mechanical properties of this silk and those of the whole membrane. These results elucidate the mechanical properties of the piriform silk as well as could help the design of more efficient bio-inspired adhesives and fabrics.

5.2. Introduction

Silk is produced by spiders to fulfil various functions such as for hunting, locomotion and to build robust cocoons and webs [1]. In 400 million years of evolution the optimization of the properties of the spider silk has been achieved through the diversification of this protein-based material[31]. Each one of the different silk types is equipped with a unique combination of physical, chemical and biological properties [2]. In particular, the outstanding mechanical and biological properties of the dragline [3,4] (mainly produced by the ampullate glands) have been intensely studied in the last two decades, inspiring and developing novel technologies [5,6].

Although the dragline silk is in the main focus of the applied silk science, it is only one representative of the silk family among the huge variety of silk types that exist. If the amount of species of spiders on Earth (more than 48,000[30]) and the fact that each one is able to spin from 2 to 7 types of silk [7] are considered, 150,000 different types of spider silk can be counted on the planet, each one with different properties [8]. Among them, the silk produced by the piriform gland has been the least studied, although it is one of the most common types of spider silk with a fundamental function: the substrate attachment of silk threads.

The first studies that report a histological analysis of the piriform glands were conducted by Kovoor et al. [9,10]. In these, the shapes and the dimensions of these glands were reported by highlighting their position close to the spinnerets that also host the duct of the major ampullate gland. In comparison to the latter, the piriform glands are much smaller and numerous.

Blasingame et al. [11] associated the protein of the piriform gland to the silk family thanks to the revealed conservation in the non-repetitive C-terminal region. The predicted aminoacidic composition of the piriform silk (the fibrous component) revealed an impressive amount of Alanine by considering the other type of the silk produced by the same spider [11,12]. However, the content of Alanine in the lumen of the *Latrodectus hesperus* showed less amount of this amino acid. Alanine can be associated with crystal-forming polyalanine chains, which contribute to a high Young's modulus and strength of the silk material [13]. Moreover, a recent study [14] predicted the molecular weight of the PySp1 (the main protein of the piriform fibres) to be 578 kDa, greater with respect to the one of the dragline (between 200 and 300 kDa [7]). The molecular weight has been demonstrated to be correlated with the strength of fibres both in native and artificial silks [15,16].

Piriform silk is used by spiders to create robust and efficient anchorages and adhesive systems that have been optimized during the evolution of spiders [17]. These glue the dragline to a surface, securing in this way the arachnid in the event of a fall [1,18] (Figure 51a-c). Moreover, they are used to anchor the supporting threads of a cobweb to a surface or to join ampullate silk threads inside a web [1,8,18,19]. The attachment discs are spun very fast (often completed in under a second) and create a durable, efficient adhesive [20].

The adhesive membrane (‘attachment disc’) is composed of a multi-fibril system embedded in a cement-like matrix (Figure 1d-f) that create a structure able to bear high loads [11,21]. Spiders can adjust the morphology of the attachment disc and thus its overall mechanical behaviour. For example, the attachment discs used to secure the cob webs to surfaces are different with respect to the ones used to secure wandering spiders while walking or hunting [22]. Moreover, it has been demonstrated that spiders spin larger attachment discs if their weight is experimentally manipulated [23].

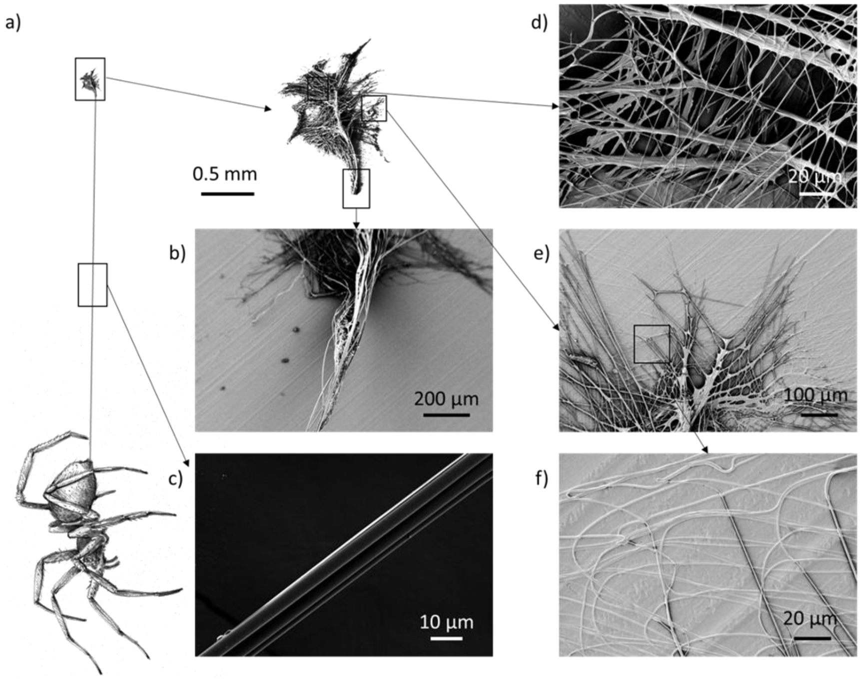

Figure 5-1: a) Schematic of a spider that spins its dragline, anchored to the substrate by means of an attachment disc. b) The initial part of the dragline is composed by more threads than the c) distal part of the dragline. d) SEM picture of the median part of the attachment disc, e) the lateral part and f) an enlargement of the lateral part, which shows fibrils attached to the surface.

A recent study [24] revealed that the relative proportion of the cement-like glue and the fibre content of the attachment discs differ between spiders of different ecology and evolutionary history; and it demonstrated that the piriform fibres and the dragline are not in contact with the substrate. Accordingly, are not directly involved in the attachment disc’s adhesion, yet the embedded fibres may affect the mechanical properties of the glue layer. Whereas the ultrastructure of the piriform fibres is rather constant across species, the ultrastructure of the glue is very different [24].

In order to understand the mechanical behaviour under load of these fascinating systems, several approaches have been used. The multiple peeling theory [25] has been used as a key model in order to explain the structure and material optimization to improve the adhesive's efficiency of the attachment discs and anchorages [26-28]. From the experimental point of view, the load to detach these membranes from surfaces has been measured by varying the surface's conditions, demonstrating a strong dependence on the type of used substrate [29].

All these aspects, both together with the structural hierarchical analysis that has been done on the piriform attachment discs [24,30], could be used for the development and the design of bio-inspired adhesives with superior mechanical performances [31].

However, several knowledge gaps have to be covered in the modelling and characterization of the piriform silk and the attachment discs before achieving possible bio-inspired solutions, such as artificial spinning of attachment discs or adhesives. Among these, there is the need for an understanding of the effects of attachment disc geometry on its load bearing capabilities [32]. Moreover, the understanding of the mechanical properties of the piriform silk is crucial in order to model the mechanical behaviour of the membrane. The first tensile tests of piriform silk have been performed on isolated piriform silk fibres (including their glue layer) of a hunting spider (*Drassodex* sp.) that were carefully peeled off an anti-adhesive polymer substrate [33]. In this work, an extensibility of 0.51 ± 0.26 mm/mm, a strength of 511.0 ± 123.6 MPa, a toughness 140.7 ± 74.3 MPa, and a Young's modulus of 5.59 ± 1.75 GPa were measured. However, in attachment discs single piriform fibres are not used in isolation, but it is their assembly into a multi-fibre compound material that make up its full-scale properties. It is therefore indispensable to generate a model to understand the mechanical properties of attachment discs on multiple hierarchical levels.

In this work, we determined empirically the mechanical properties of the single piriform silk fibre and of the whole attachment disc of the species *Cupiennius salei* through nanoindentation and nanotensile techniques. We developed a simple model in order to explain the overall behaviour of the membrane composed by piriform silk and the dragline. With this work, we aim to create a comprehensive understanding of the mechanical properties of piriform silk and its spinning product (the attachment disc), also helping the possibility to develop and design bio-inspired adhesives with superior properties.

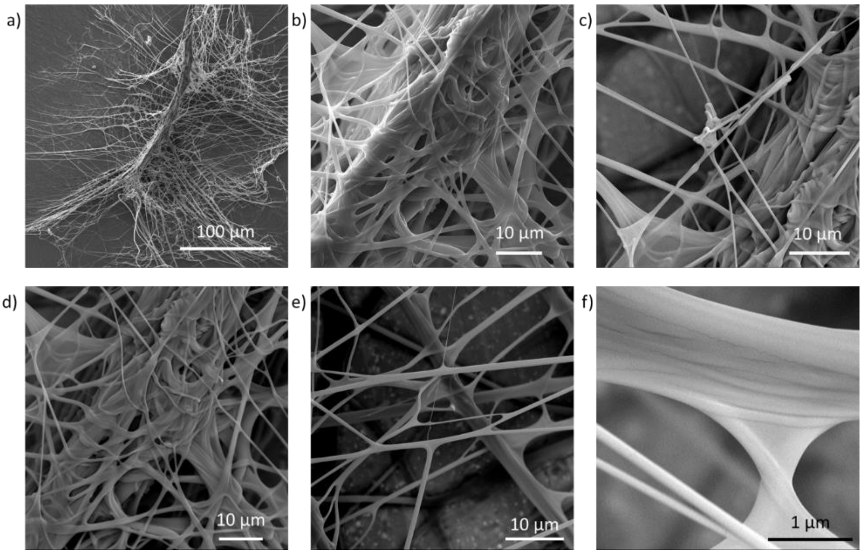

Figure 5-2: Figure 2: SEM images of an attachment disc of Cupiennius salei. a) The structure is composed of a dragline thread that is suspended in a network of glue-coated fibrils. b-f) different details of the piriform silk network in the attachment disc.

5.3. Analytical model

5.3.1. Evaluating the spacing among fibrils

Determining the mechanical properties of piriform silk from attachment disc membranes creates difficulties due to the chaotic distribution of the fibres in the membrane (Figure 5-2). This means the membrane cannot be modelled as an isotropic material with a homogeneous stress distribution as commonly done in tensile testing experiments. Based on the observation that piriform fibres form a layered network in the attachment disc (Figures 5-1, 5-2), we model the silk membrane as a lattice of a glue-fibre material (Figure 5-3). The spacing between the fibres, (i.e. the porosity of the membrane), is one of the key aspects to take into consideration to model the mechanical behaviour of the piriform membrane. We have evaluated it indirectly (the direct SEM measurement is not accurate) by considering the mean mass of the membranes, which can be precisely measured through a TGA system. Based on the work of Wirth et al.[26], we can estimate that the thickness of the glue (the third phase) that envelops the fibres is around 20 nm, which is small compared to the diameter of the fibre. Thus, for the sake of simplicity, we do not consider the presence of the glue in the calculation of the volume.

We assume that the density of the piriform silk is similar to that of major ampullate silk ($\rho_p \sim \rho_{silk} \sim 1.3\,\frac{\mathrm{g}}{\mathrm{cm}^3} = \rho$). The nominal volume of the membrane V_n ($= w \cdot l \cdot t$) multiplied for the mean density of the membrane (ρ_m) is equal to the mass m of the membrane:

$$\rho_m V_n = m$$

from which we can obtain the mean density of the membrane. The membrane mass is also given by the real density of the silk multiplied by the real volume of the silk fibrils in the membrane. By following the schematic in Figure 5-3 we can thus write:

$$\rho_m V_n = \rho V \Rightarrow \frac{\rho_m}{\rho} = \frac{A_d l + \frac{2A_p wtl}{s^2}}{wtl} \Rightarrow$$

$$\Rightarrow s = \sqrt{\frac{2A_p wtl}{\frac{\rho_m}{\rho} wtl - A_d l}} \quad (1)$$

where A_d is the cross-sectional area of the dragline fiber of length l and A_p is the cross-sectional area of the piriform fibril network with fibrils of length l and spacing s (Figure 5-3).

Equation (1) can be then used to compute the mean spacing between the fibres in the piriform membrane.

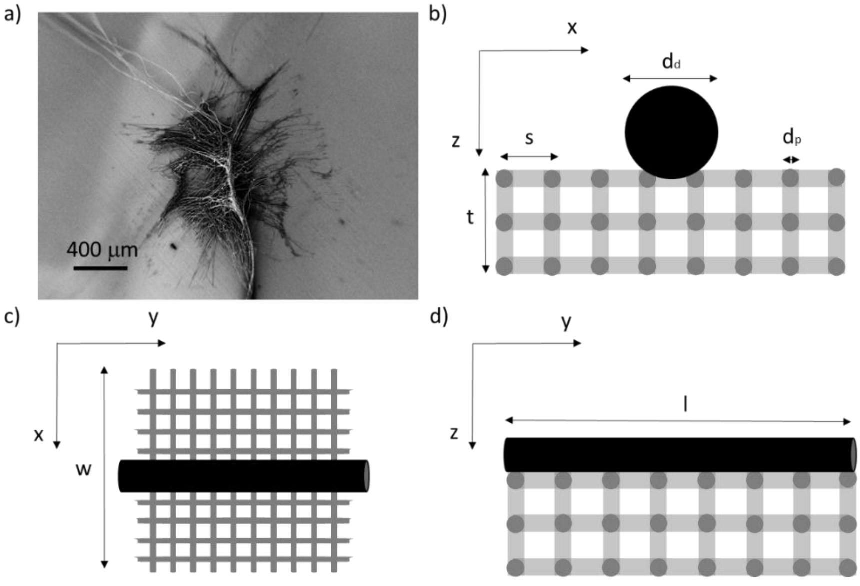

Figure 5-3: a) SEM picture of an attachment disc. b-d) Schematic model in the three volume directions used to compute the mechanical properties of the membrane.

5.3.2. Evaluation of the stress in the fibrils

By referring to Figure 3 we can also estimate the engineering stress applied to the membrane through the measure of the load applied to it and section involved. In this approach, we neglect the layered structure of piriform silk, but integrate across its glue and fibre fraction.

Along the y direction we have

$$\sigma_y = \frac{F_y}{A_y} = \frac{F_y}{A_d + \frac{A_p w t}{s^2}} \quad (2)$$

On the other hand, along the x direction we have

$$\sigma_x = \frac{F_x}{A_x} = \frac{F_x}{\frac{A_p t l}{s^2}} \quad (3)$$

Is thus possible to compute the engineering stress on the membrane.

Interestingly, if we consider the force applied to the membrane in one of the two directions, we find in the y direction that

$$F_y = F_d + F_p \Rightarrow \sigma_y = \frac{\sigma_d A_d}{A_d + \frac{t w A_p}{s^2}} + \frac{\frac{\sigma_p A_p w t}{s^2}}{A_d + \frac{t w A_p}{s^2}} \quad (4)$$

whereas in the x direction that

$$F_x = F_p \Rightarrow \sigma_x = \sigma_p \quad (5)$$

This means that the stress computed along the x direction gives exactly the stress on the piriform silk.

Equation 4 represents also a relation between the strength of the dragline (σ_d), the strength of the piriform silk (σ_p), and the strength of the whole membrane (in this case σ_y). Thus, knowing the strength of the piriform silk measured with equation 5, there is the possibility to check the strength of the dragline through equation 4 as a control.

5.3.1. Evaluation of the Young's modulus of the fibrils

In order to estimate the Young's modulus of the whole membrane we can consider again topology expressed in Figure 5-3.

We consider the membrane composed by piriform fibrils with Young's modulus E_p.

The relation between the Young modulus (E) and the spring constant (k) under tensile longitudinal load is given by:

$$k = \frac{EA}{d} \quad (6)$$

where A is the section of the fibre, and d its length.

During loading along the direction of the dragline (y direction) thread we have n fibrils in series, N and N' in parallel (x and z direction) that can be obtained by:

$$n = \frac{l}{l_p}$$
$$N = \frac{t}{s}$$
$$N' = \frac{w}{s}$$

where l_p is the mean length of the fibril.

Thus the stiffness of the piriform fibrils along y is predicted to be:

$$k_{eql}' = \frac{k_p}{n} NN'$$

where $k_p = E_\mathrm{p} A_\mathrm{p} / l_\mathrm{p}$ is the spring constant of the piriform fibril. Moreover, in the y direction we have to consider also the contribution of the dragline. This is in parallel to the membrane and thus the total membrane stiffness is predicted to be:

$$k_{eqy} = \frac{k_p}{n}\, NN' + \frac{E_d A_d}{l_d}$$

where E_d is the Young's modulus of the dragline, and l_d its length.

From this we can estimate the Young's modulus of the whole membrane through equation 6 and by assuming $l \approx l_d$ as:

$$E_{eqy} = \frac{\pi}{4}\left(\frac{E_p d_p^2}{s^2} + \frac{E_d d_d^2}{tw}\right) \quad (7)$$

where d_p is the diameter of the piriform fibres and d_d is the diameter of the dragline.

On the other hand, if we consider the membrane pulled along x direction, we have n' fibrils in series along x direction, N and N'' in parallel (y and z direction), namely:

$$n' = \frac{w}{l_p}$$
$$N'' = \frac{l}{s}$$

The equivalent membrane stiffness along the x direction is thus:

$$k_{eqx} = \frac{k_p}{n'} NN''$$

and from this we can estimate the Young's modulus of the whole membrane along the x direction by using equation 6, i.e.:

$$E_{eqx} = E_p \frac{\pi d_p^2}{s^2 4} \quad (8)$$

Finally, it is possible to notice that equation (7) and (8) differ only for the contribution of the dragline, which increases the equivalent Young's modulus of the membrane along y with respect to x.

5.4. Materials and Methods

5.4.1. Spiders

The spiders under study were adult females of *Cupiennius salei* (Keyserling 1877). They were kept in different plastic box and fed with a weekly diet of *Blaptica dubia* or *Acheta domestica (*feed with carrots and fish food). All the plastic boxes were set in a room with controlled environmental parameters. Each terrarium was provided with a refuge by considering the need of the spider to allow the animal to feel protected and live without stress, according to the Italian regulation on animal protection and EU Directive 2010/63/EU for animal experiments.

5.4.2. SEM pictures

SEM characterization was performed using a Zeiss – 40 Supra for the Figure 5-1 and 5-2. For Figure 5-1b we used EHT at 2.00 kV, WD 8.1 mm, 236x with secondary electrons detector. For the Figure 5-1c we used EHT at 5.00 kV, WD 6.1 mm, 3000x with secondary electrons detector. For the Figure 5-1d we used EHT at 2.00 kV, WD 8.2 mm, 1490x with secondary electrons detector. For the Figure 5-1e we used EHT at 2.00 kV, WD 8.4 mm, 347x with secondary electrons detector. For the Figure 5-1f we used EHT at 2.00 kV, WD 8.4 mm, 2010x with secondary electrons detector. For the Figure 5-2a we used EHT at 2.00 kV, WD 8.1 mm, 104x with secondary electrons detector. Figure 5-3 was taken with the support of a desktop SEM Phenom PRO. The used parameters are for the Figure 5-3a EHT 15kV, 290x, WD 0.9 mm and secondary electrons detector, for the Figure 3b EHT 15 kV, 4500x, WD 59 μm and secondary electrons detector, for the Figure 5-3c EHT 15 kV, 5800x, WD 46 μm and backscattered electron detector, for the Figure 5-3d EHT 15 kV, 4500x, WD 59 μm and backscattered electrons detector, for the Figure 5-3e EHT 15 kV, 5400x, WD 49 μm and backscattered electrons detector, for the Figure 5-3f EHT 15 kV, 16500x, WD 16 μm and backscattered electrons detector. For the Figure 5-2a EHT 2 kV, 104x, WD 8.1 mm and secondary electrons detector.

The metallization was made by using a sputtering machine Q150T and the sputtering mode was Pt/Pd 80:20 for 5 minutes.

5.4.3. Measurement of attachment disc mass

The measurement of the mass of the membranes was performed by using a TGA ANALYSIS TA Q5000. We measured the mass of 13 membranes and then the mass of 14 membranes for 3 minutes (to get stable values). The difference among these values represent the average mass of a membrane.

5.4.4. Measurement of attachment disc length

We used the pictures obtained through an optical microscope (Zeiss Axiotech and Axiovert) and analysed through ImageJ [34] software analysis. In this way we obtained the mean length and the width of the membranes. The thickness was measured through a calibre by sandwiching the membrane between its jaws. An optical microscope was used to validate these results. For each measurement, one hundred samples were measured.

5.4.5. Nanoindentation tests

The tested samples were prepared by letting the spider walk on a quartz substrate and let it spin the attachment discs. This quartz substrate was mounted on an iNano®Nanoindenter (Nanomechanics Inc.). The declared sensitivity of the machine is 3 nN for the load and 0.001 nm for the displacement.

The used mapping method (Nanoblitz 3d, Nanomechanics Inc.) involved a 200 μm × 200 μm square with 400 indentation points inside (each for a maximum of 0.05 mN loads for the piriform and 5 mN for the dragline). On the other hand, the standard indentation to load method was used in at two different maximum loads: 0.05 mN for the piriform, and 5 mN for the dragline. We used a Berkovich tip with a tip radius of about 20 nm for the experiments.

5.4.6. Tensile tests

The dragline samples were prepared by cutting the dragline from the attachment disc. Specimens were stuck on a paper holder provided with a window of 1 cm x 1 cm and fixed with a double-sided tape. The diameters of the fibres that compose the dragline were measured with an optical microscope (Zeiss Axiotech and Axiovert). The membranes were obtained by detaching them from the substrate (commercial braplast plastic box, www.braplast.com). The test samples of piriform silk were prepared by fixing the attachment discs (up to the considered pulling direction, e.g. x or y) on a paper frame provided with a rectangular window with 1 mm height. The sample was fixed to the paper frame with a double-sided tape and by using Loctite super glue [35]. For the y direction, the dragline was included in the membrane.

The tests were performed with the support of the nanotensile machine Agilent UTM T150 (Keysight technology) with a cell load of 500 mN. The displacement speed was 1% of the gauge length per second. The declared sensitivity of the machine is 10 nN for the load and 1 Ȧ for the displacement in the dynamic configuration. The tests were recorded with a Sony Camera.

5.4.7. ANOVA Analysis

Analysis of variance was performed to compare the mean values of the strain at break, strength, Young's modulus and toughness from x- and y-stress tests (i.e. attachment discs pulled by fibril direction and by dragline direction).

The parameters used to verify the null hypothesis, i.e. all the data sets come from the same distribution and have the same mean value, were:

$$SSQ_a = \sum_{g=1}^{G} n_g\left(m_g - m\right)^2$$

$$SSQ_e = \sum_{g=1}^{G}\sum_{j=1}^{n_g}\left(x_{gj} - m_g\right)^2$$

where G is the number of different samples under consideration, n_g is the number of tests of the same sample, m is the mean value of all the data, m_g is the mean value within the group (i.e., sample), and x is the single force value. These sums of squares were used to compute the T value:

$$T = \frac{\frac{SSQ_a}{G-1}}{\frac{SSQ_e}{n-G}}$$

that has been compared with the ideal value of the Fisher function F with a significance level of 5%. If $T>F$ we reject the null hypothesis and thus we can consider the difference among the data set as significant (i.e., the difference is due to intrinsic differences among the samples and not a consequence of internal variance). The *p*-value was computed in MatLab®.

5.4.8. Weibull statistics

In order to analysis the fracture strength distribution we used Weibull statistics. Weibull cumulative density function is defined by the following relation (we omit the scaling effects here):

$$F(x, m, x_0) = 1 - e^{-\left(\frac{x}{x_0}\right)^m} \quad (9)$$

where x is the fracture strength m is the shape parameter and x_0 the scale parameter. F represents the probability that the sample break at the strength x.

In order to obtain the relative probability density distributions of the different samples (i.e. $f(x, m, x_o) = \frac{m}{x_0^m} x^{m-1} e^{-\left(\frac{x}{x_0}\right)^m}$) we obtained the Weibull shape and scale parameter by using the linear regression method. By applying the double logarithm to (9) we obtain the following equation

$$\ln\left(\ln\left(\frac{1}{1-F(x)}\right) = mln(x) - mln(x_0)\right.$$

where F could be estimated through the median rank estimator

$$\hat{F}(x_i) = \frac{i-0.3}{n+0.4}$$

where n is the number of tested specimen and i is the order of the considered one (after the organization of the samples from the weakest till the strongest). Kolmogorov Smirnov and R square tests were performed to each set of data to verify (under the 95% of acceptance, MatLab®) that Weibull statistics could be applied to data set.

5.5. Results

When a spider walks, it produces attachment discs where it secures the dragline (Figure 5-1a). Close to the attachment disc, the dragline is composed by more fibres (Figure 5-1b) than in its distal portion (i.e. close to the spinnerets, Figure 5-1c). The attachment discs are complex structures composed of multiple fibres with a mean diameter of 1.2 ± 0.5 µm and coated with a glue (Figure 5-1,5-2). The thickness, the width and the length of the membranes are respectively 5 ± 1 µm, 1.8 ± 0.4 µm, 3.3 ± 0.6 µm (Figure S1). The mass of the membranes (Figure S2) has been measured as around 5 µg, which gives us (by equation (1)) the mean fibrils spacing around 4.6 µm (Table S1).

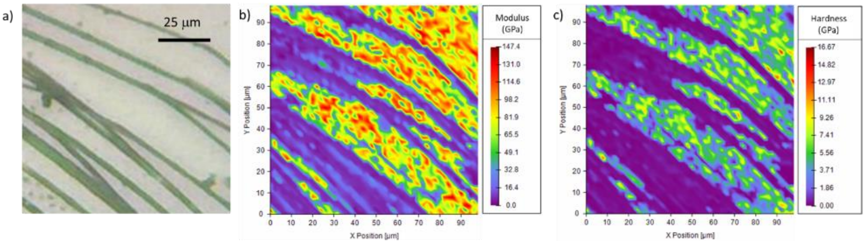

Figure 5-4: the nanoindentation mapping of the mechanical properties obtained for the analysis of the piriform silk on the border of the attachment disc.

5.5.1. Nanoindentation tests

In order to measure the mechanical properties of the piriform silk, we used nanoindentation and nanotensile tests.

We performed a series of control experiments regarding the Young's modulus obtained with the nanoindentation technique with respect to the one obtained through tensile tests [36,37].

The tests on the dragline on the attachment discs revealed consistent values between the two considered techniques. In particular, with the nanoindentation (Figure S3, Table S2) we measured a Young's modulus of 4.2 ± 0.8 GPa, which was confirmed also through the mapping method (Figure S4). These were confirmed by the tensile tests (Table S3), which gave us a Young's modulus of 5.2 ± 4.8 GPa (computed by taking the slope of the fitting regression line in the steepest part of the stress-strain curve), the strain at break of 0.27 ± 0.09 mm/mm, the mean strength of 365 ± 290 MPa, and the mean toughness of 61 ± 47 MJ/m^3. From nanoindentation we obtained a hardness of 0.33 ± 0.10 GPa for the dragline.

The investigation of the piriform silk through nanoindentation was performed by using the single indentation method and mapping method. The single indentation method was performed on different positions along the membrane (Figure S5). The obtained Young's modulus of the single fibre was 3.9 ± 1.4 GPa (Table S4), whereas the hardness was 0.09 ± 0.05 GPa. The Young's modulus values are not that different in comparison to the ones of the dragline. These observations were confirmed also by the mapping method applied to the attachment disc (Figure 5-4, Figure S6-S7). The results were consistent with the indentation depth (Figure S8), which was kept less than the 10% of the thickness of the fibres [38,39].

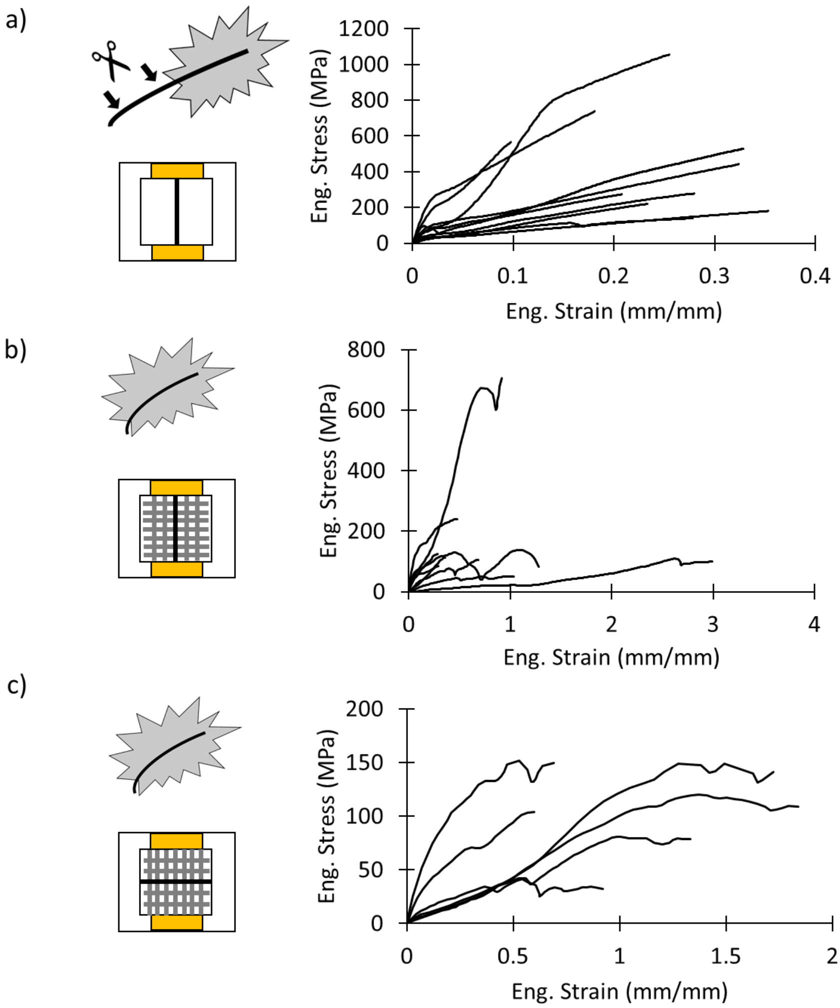

Figure 5-5: a) Schematics of test sample and stress-strain curves of dragline samples. b) Schematics of test sample and stress-strain curves of the attachment disc pulled in the dragline direction (y direction). c) Schematics of test sample and stress-strain curves of the attachment disc pulled in the fibrils direction (x direction).

5.5.2. Tensile tests

In order to measure the overall mechanical properties of the structures we performed nanotensile tests on different structures: the dragline, the whole membrane pulled along the y direction (Figure 5-3b), and the whole membrane pulled along the x direction (Figure 5-3d). The obtained stress-strain and load-displacement (for the last type of test) curves are depicted in Figure 5-5. The stress on the membrane was computed by using equations (2) and (3) and values in the Table S1.

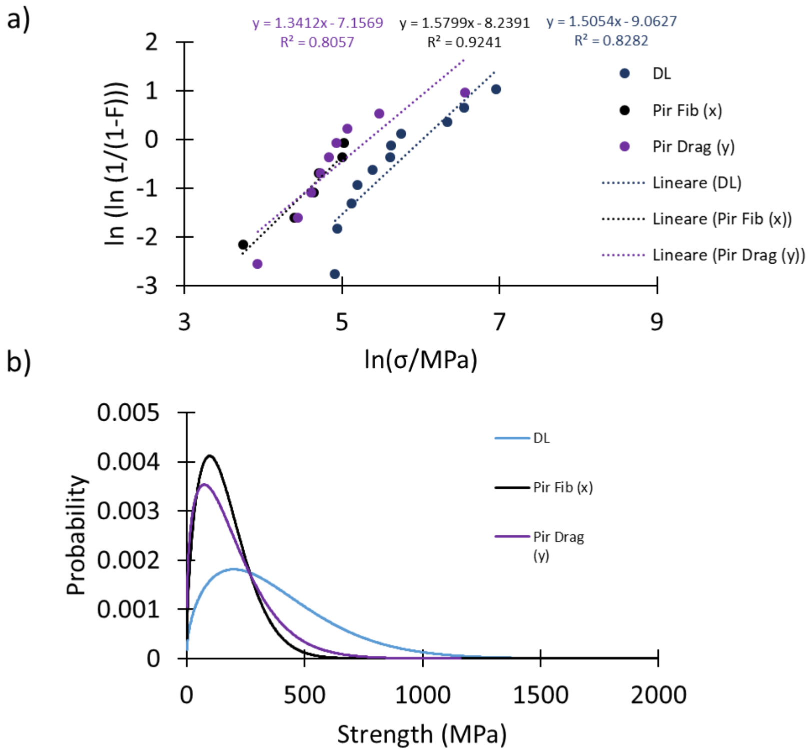

Figure 5-6: a) Linear regression plots of the different sets of samples to compute the Weibull parameters used to plot b) the Weibull probability density distributions of the strength of the tested samples.

There was no significant difference in mechanical properties between the x- and y-mounting of attachment disc samples (Table S5-S6). The strain at break, the strength, the Young's modulus and the toughness were for the x and y direction respectively 1.18 ± 0.53 and 0.93 ± 0.85, 106 ± 42 MPa and 190 ± 180 MPa, 0.19 ± 0.10 MPa and 0.33 ± 0.18 MPa, 87 ± 53 MJ/m^3 and 97 ± 90 MJ/m^3.

In order to evaluate the difference of the mechanical properties between attachment discs and the dragline we performed a one-way ANOVA test (Table S7). Only the strength of the dragline and the membrane pulled along the x direction resulted to be statistically different (p = 0.00487, all post-hoc pairwise comparisons p<0.05). This suggests that the dragline is stronger than the piriform silk membrane.

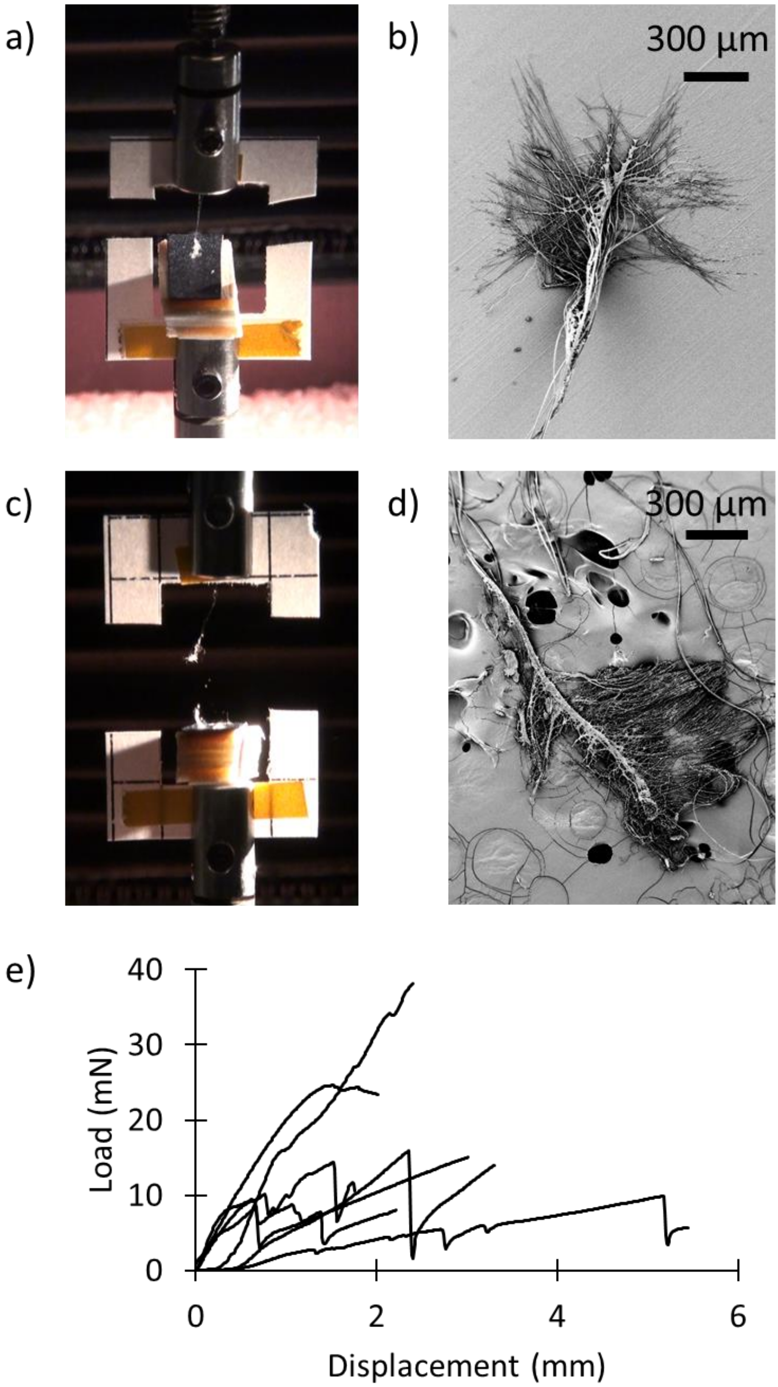

Figure 5-7: a) The attachment disc pulled on the dragline during the test; b) SEM image of an attachment disc; c) Failure mode of the attachment discs. d) SEM image reveals that the membrane detaches completely from the substrate by failing on the piriform silk level,

keeping the attachment disc almost intact. e) Load displacement curves of the detachment of the attachment disc.

A better understanding of the difference between the strength of the analysed sampled can be given by looking at Weibull statistics. In this case, the linear regression method was used to compute the Weibull parameters (Figure 5-6a, Table S8) and these were used to plot the strength's probability density distributions of the tested samples (Figure 5-6b). The narrower shape of the strength probability distribution of the membranes relative to the dragline indicated their more homogeneous fracture behaviour.

In order to evaluate the detachment behaviour of the whole membrane from the substrate we performed peeling tests of the whole structure (Figure 5-7). Table S9 reports all the values obtained for the displacement at fracture, force at fracture and stiffness at fracture, which have the mean values respectively of 2.9 ± 1.2 mm, 18 ± 10 mN, and 6.8 ± 5.8 N/m. These data are similar to the ones reported in literature [20,29,30,32,33,40]. Moreover, the failure of the attachment discs occurs mainly at the level of the piriform silk (Figure 5-7c) in our setup, instead of at the dragline's level. In this way, the attachment disc remains almost intact (Figure 5-7d) after the detachment from the surface, indicating that the adhesion was measured and not the fracture of the attachment disc.

Table 5-1: Values of the mechanical properties of all types of tested samples obtained in the experimental and theoretical study, compared with literature values (from another species).

Sample	The value is obtained with:	Strain at break (mm/mm)	Strength (MPa)	Young's modulus (GPa)	Toughness (MJ/m^3)
Dragline (near the disc)	Tensile exp	0.26 ± 0.09	365 ± 290	5.2 ± 4.8	60.9 ± 46.6
	Nanoindentation			4.2 ± 0.8	
	Equation		425 equation 4	6.1 equation 7	
Piriform silk fibre	Tensile exp	0.51 ± 0.26 [33]	511 ± 124 [33]	5.59 ± 1.75 [33]	141 ± 74 [33]
	Nanoindentation			3.9 ± 1.4	
	Equation		128 equation 4	3.45 equation 8	
Membrane pulled by x direction	Tensile exp	1.18 ± 0.53	106 ± 42	0.19 ± 0.10	87 ± 53
	Equation		128 equation 4	0.21 equation 8	
Membrane pulled by y direction	Tensile exp	0.93 ± 0.85	190 ± 180	0.33 ± 0.18	97 ± 90
	Equation		174 equation 4	1.19 equation 7	

Comparison with the model

Table 5-1 reports all the values of the quantities measured in this work, the comparison among them and the values obtained from literature and our theoretical approach. The Young's modulus estimated with the support of equations (7) and (8) is similar to the one measured by nanoindentation. The values obtained for the piriform silk are similar to those present in the work of Wolff et al. [33]. Equation (7) was also used as a control for estimating the Young's's modulus of the dragline, which is similar to the one obtained experimentally.

Equation (4) gives us the possibility to estimate the strength of the dragline by knowing the measured strength of the membrane along the x and y direction and the strength of the piriform silk. The obtained value is very similar to the one measured through tensile tests, confirming the validity of our simple model.

It is essential to understand how the spacing distance *s* can affect the results. We thus plot (Figure S7) the theoretical values obtained with equations (4), (7) and (8) as functions of the spacing distance *s* in the measured range. From this, it is possible to notice that our results fit well with respect to the obtained *s* values.

5.6. Discussion

Due to the adhesive nature of piriform silk, it is difficult to obtain native fibre samples for tensile tests. Here, we used a whole-membrane approach, in combination with a numerical model to determine the mechanical properties of piriform silk. When collecting samples, the detachment of the attachment discs from the carrier substrate may create damage or induce a pre-stress that could affect the measurements [41,42]. We therefore backed up our test results by a nanoindentation approach that has been proven a good solution in order to measure *in loco* the mechanical properties of native attachment discs without the requirement of sample manipulation [36]. The combined results from these different approaches are consistent. The nanoindentation tests revealed that the piriform silk of *Cupiennius salei* has a Young's modulus comparable to its dragline.

The simple theoretical model expressed by equations gave us results in agreement with the ones obtained through tensile tests and taken from literature [33]. Moreover, it gave us the possibility to relate the mechanical properties of the single fibres with the ones of the whole membranes along the different pulling directions. The results were checked also by comparison with the tensile results on the dragline and on the single piriform fibres found in the work by Wolff et al. [33]. The effect of the measure of the spacing parameter *s* in the equation has been investigated with the support of the plot in Figure S6, which reveals a good agreement and accuracy of our results.

Another important aspect to consider about the strength of materials is their dimensions. Increasing the length of a material (or in general its dimension) usually leads to a decrease in term of strength [43]. This is valid also for spider silk (unpublished data on Weibull scaling laws). Piriform silk is composed by numerous small fibres each one with a mean length of few tens of microns. This could increase the strength of each fibre and then the strength of the whole membrane.

Regarding the overall mechanical behaviour of the membrane, the complexity of the structure and its random shape could be an important cause for the remarkable mechanical properties of attachment discs, as randomization in a system could improve its toughness and ductility [44].

5.7. Conclusion

Hundreds of million years have selected attachment systems of spiders to bear high loads[17]. Despite their fundamental role, these anchorages are still poorly understood due to the practical difficulties in sample preparation, the complexity of the system and the high variation of attachment disc structures.

In this context, knowledge of the mechanical properties of the attachment disc material (piriform silk) is essential in order to understand the overall mechanical behaviour of the whole membrane.

With this work we delivered the required information of piriform silk properties, that will help to generate a better understanding of the adhesion performance of attachment discs. This will stimulate the design of bio-mimetic super adhesives, contribute to the bioprospecting of novel silk materials for biotechnological applications and contribute to the understanding of spider web function.

5.8. References

1. Foelix, R. Biology of Spider. Oxford University Press 53, (2011).
2. Craig, L. B. and C. L. Spider Silk Evolution and 400 Million Years of Spinning, Waiting, Snagging, and Mating. (2012).
3. Lepore, E. et al. Silk reinforced with graphene or carbon nanotube spun by spiders. 2D Mater. 64, 897–905 (2017).
4. Agnarsson, I., Kuntner, M. & Blackledge, T. A. Bioprospecting finds the toughest biological material: Extraordinary silk from a giant riverine orb spider. PLoS One 5, 1–8 (2010).

5. Eisoldt, L., Smith, A. & Scheibel, T. Decoding the secrets of spider silk. Mater. Today 14, 80–86 (2011).
6. Wolff, J. O., Wells, D., Reid, C. R. & Blamires, S. J. Clarity of objectives and working principles enhances the success of biomimetic programs Clarity of objectives and working principles enhances the success of biomimetic programs. Bioinspir. Biomim. 12, (2017).
7. Vollrath, F. & Knight, D. P. Liquid crystal spinning of spider silk. Nature 410, 541–548 (2001).
8. Basu, A. Advances in Silk Science and Technology. (The Textile Institute, 2015).
9. Kovoor, J. & Zylberberg, L. FINE STRUCTURAL ASPECTS OF SILK SECRETION DlADEMATUS). IN THE. Tissue Cell 12, 547–556 (1980).
10. Kovoor, J. & Zylberberg, L. Fine structural aspects of silk secretion in a spider. Tissue Cell 14, 519–530 (1982).
11. Blasingame, E. et al. Pyriform spidroin 1, a novel member of the silk gene family that anchors dragline silk fibers in attachment discs of the black widow spider, Latrodectus hesperus. J. Biol. Chem. 284, 29097–29108 (2009).
12. Geurts, P. et al. Synthetic spider silk fibers spun from pyriform spidroin 2, A glue silk protein discovered in orb-weaving spider attachment discs. Biomacromolecules 11, 3495–3503 (2010).
13. Yarger, J. L., Cherry, B. R. & Van Der Vaart, A. Uncovering the structure-function relationship in spider silk. Nat. Rev. Mater. 3, (2018).
14. Chaw, R. C., Saski, C. A. & Hayashi, C. Y. Complete gene sequence of spider attachment silk protein (PySp1) reveals novel linker regions and extreme repeat homogenization. Insect Biochem. Mol. Biol. 81, 80–90 (2017).
15. Bowen, C. H. et al. Recombinant Spidroins Fully Replicate Primary Mechanical Properties of Natural Spider Silk. Biomacromolecules 19, 3853–3860 (2018).
16. Xia, X.-X. et al. Native-sized recombinant spider silk protein produced in metabolically engineered Escherichia coli results in a strong fiber. Proc. Natl. Acad. Sci. 107, 14059–14063 (2010).
17. Wolff, J. O. et al. Evolution of aerial spider webs coincided with repeated structural optimization of silk anchorages. Evolution (N. Y). 73, 2122–2134 (2019).
18. Asakura, T. & Miller, T. Biotechnology of Silk. 5, (2014).

19. Greco, G., Pantano, M. F., Mazzolai, B. & Pugno, N. M. Imaging and mechanical characterization of different junctions in spider orb webs. Sci. Rep. 9, 5776 (2019).
20. Wolff, J. O. & Gorb, S. N. Attachment Structures and Adhesive Secretions in Arachnids. Comparative Contact Mechanics 7, (2016).
21. Cranford, S. W., Tarakanova, A., Pugno, N. M. & Buehler, M. J. Nonlinear material behaviour of spider silk yields robust webs. Nature 482, 72–76 (2012).
22. Sahni, V., Harris, J., Blackledge, T. A. & Dhinojwala, A. Cobweb-weaving spiders produce different attachment discs for locomotion and prey capture. Nat. Commun. 3, 1106–1107 (2012).
23. Wolff, J. O., Jones, B. & Herberstein, M. E. Plastic material investment in load-bearing silk attachments in spiders. Zoology 131, 45–47 (2018).
24. Wirth, M., Wolff, J. O., Appel, E. & Gorb, S. N. Ultrastructure of spider thread anchorages. J. Morphol. 280, 534–543 (2019).
25. Pugno, N. M. The theory of multiple peeling. Int. J. Fract. 171, 185–193 (2011).
26. Pugno, N. M., Cranford, S. W. & Buehler, M. J. Synergetic material and structure optimization yields robust spider web anchorages. Small 9, 2747–2756 (2013).
27. Brely, L., Bosia, F. & Pugno, N. M. Numerical implementation of multiple peeling theory and its application to spider web anchorages. Interface Focus 5, 20140051 (2015).
28. Liprandi, D., Bosia, F. & Pugno, N. M. A theoretical-numerical model for the peeling of elastic membranes. J. Mech. Phys. Solids (2019). doi:10.1016/j.jmps.2019.103733
29. Grawe, I., Wolff, J. O. & Gorb, S. N. Composition and substrate-dependent strength of the silken attachment discs in spiders. J. R. Soc. Interface 11, 20140477–20140477 (2014).
30. Wolff, J. O., Grawe, I., Wirth, M., Karstedt, A. & Gorb, S. N. Spider's super-glue: thread anchors are composite adhesives with synergistic hierarchical organization. Soft Matter 11, 2394–2403 (2015).
31. Jain, D., Sahni, V. & Dhinojwala, A. Synthetic adhesive attachment discs inspired by spider's pyriform silk architecture. J. Polym. Sci. Part B Polym. Phys. 52, 553–560 (2014).
32. Wolff, J. O., Van der Meijden, A. & Herberstein, M. E. Distinct spinning patterns gain differentiated loading tolerance of silk

thread anchorages in spiders with different ecology. Proc. R. Soc. B Biol. Sci. In Press, (2017).

33. Wolff, J. O., Řezáč, M., Krejčí, T. & Gorb, S. N. Hunting with sticky tape: functional shift in silk glands of araneophagous ground spiders (Gnaphosidae). J. Exp. Biol. 220, 2250–2259 (2017).
34. Schneider, C. A., Rasband, W. S. & Eliceri, K. W. NIH Image to ImageJ: 25 years of image analysis. Nat. Methods 9, 671–675 (2012).
35. Blackledge, T. A., Cardullo, R. A. & Hayashi, C. Y. Polarized light microscopy, variability in spider silk diameters, and the mechanical characterization of spider silk. Invertebr. Biol. 124, 165–173 (2005).
36. Das, R. et al. Biomechanical characterization of spider webs. J. Mech. Behav. Biomed. Mater. 67, 101–109 (2017).
37. Denny, M. W. the Physical Properties of Spider'S Silk and Their Role in the Design of Orb-Webs. J. Exp. Biol. 65, 483–506 (1976).
38. C.Fisher-Cripps, A. Nano-indentation. 36, (2005).
39. Hay, J. L., O'Hern, M. E. & Oliver, W. . The importance of contact radius for substrate independent property measurement of thin films. Mat. Res. Soc. Symp. Proc. 522, 27–32 (1998).
40. Wolff, J. O. & Herberstein, M. E. Three-dimensional printing spiders: Back-and-forth glue application yields silk anchorages with high pull-off resistance under varying loading situations. J. R. Soc. Interface 14, (2017).
41. Garrido, M. A., Elices, M., Viney, C. & Pérez-Rigueiro, J. The variability and interdependence of spider drag line tensile properties. Polymer (Guildf). 43, 4495–4502 (2002).
42. Perez-Rigueiro, J. The effect of spinning forces on spider silk properties. J. Exp. Biol. 208, 2633–2639 (2005).
43. Carpinteri, A. & Pugnø, N. Are scaling laws on strength of solids related to mechanics or to geometry? Nat. Mater. 4, 421–423 (2005).
44. Cranford, S. W. Increasing silk fibre strength through heterogeneity of bundled fibrils. J. R. Soc. Interface 10, (2013).

6. SPIDER (*LINOTHELE MEGATHELOIDES*) AND SILKWORM (*BOMBYX MORI*) SILKS: COMPARATIVE PHYSICAL AND BIOLOGICAL EVALUATION

This chapter is based on a paper that we published on Materials Science and Engineering: C (volume 107, 110197, 2020, DOI: 10.1016/j.msec.2019.110197). For the sake of shortness, the reader may find the supplementary information in the original paper.

Goal of the chapter: New typologies of spider silks must be investigated in order to find new possible materials for biomedical applications.

We report here for the first time the biological evaluation of the silk of *Linothele megatheloides*, which are better than the silkworm silk ones. Being able to produce large amount of silk, we strongly believe in the potential industrial application of this silk. A comparative approach is here developed to state that this new material gives promising perspectives on tissue engineering.

6.1. Abstract

Silks, in particular silkworm silks, have been studied for decades as possible candidate materials for biomedical applications. Recently, great attentions have been paid to spider silks, mainly due to their unique and remarkable mechanical properties. Both materials express singular interactions with cells through specific biorecognition moieties on the core proteins making up the two silks. In this work, the silk from a Colombia spider, *Linothele megatheloides* (LM), which produces a single type of silk in a relatively large amount, was studied in comparison with silk from *Bombyx mori* silkworm, before and after degumming, with the evaluation of their chemical, mechanical and biological properties. Unexpected biological features in cell culture tests were found for the LM silk already at very early stage, so suggesting further investigation to explore its use for tailored biomedical applications.

6.2. Introduction

Silk fibers produced by silkworms [1] and spiders [2] have aroused great interests among researchers during the past decades due to their unique properties [3, 4]. The natural silk fiber produced by silkworm has been deeply studied and used/proposed for biomedical applications such as tissue engineering, prosthetic material and drug delivery [5-9]. Also spider silk nowadays is taken into consideration for biomedical applications [10]. Spiders use silk to build robust cobwebs [11, 12] and also for making egg sacks [13], lifting heavy objects [14] and even flying [15]. For each specific function, composition and properties of the silk filaments are different and this is a crucial difference with respect to the silkworm silk, which has single chemical composition and properties [16]. Among the different types of spider silk that exist on Earth (which are estimated to be 150,000), only dragline silk (mainly from *Nephila clavipes*), which composes the main frame of the web, has been intensively studied and characterized in terms of physical, chemical and biological properties [17].

Allmeling C. et al [18] used the dragline silk of the spider of the genus *Nephila* to make constructs that were seeded with Schwann cells and were investigated as sciatic nerve conduits in rats. They concluded that native dragline silk is a viable material for Schwann cell migration and proliferation for peripheral nerve regeneration. Vollrath F. et al [19] proved the biocompatibility of major ampullate dragline silk reeled from *Nephila clavipes*, native silk reeled from a *Brachypelma sp.* spider, and native silk taken from this spider's web, implanted subcutaneously in pigs. In these works, after the epicutaneous application of the material, a rapid healing process was observed superficially and after 14 days histopathological analysis revealed no difference between the original and the newborn tissue. However, the main challenge of applying native dragline silk in tissue engineering is the low scale production and the spiders' cannibalistic behaviour [20] that make it difficult farming spiders and harvesting their silk. Production of spider silk-like fiber through modified organisms has been investigated for decades, with genetically modified plants [21], mammals [22], silkworm [23], yeast and bacteria, to have alternative more exploitable sources of this remarkable protein [24]. With all investigated methods, however, silks structurally similar but with inferior properties with respect to the ones spun by the spiders were obtained [25].

Recent improvement in spinning technology has been achieved thanks to the work of Rising and Johannson [26, 27]. In particular, they produced a large-scale amount of spider silk-like fibers by using a biomimetic apparatus with pH gradient and shear forces, as it occurs in the natural spinning dope of spiders. However, the mechanical properties of these fibers were still poor with respect to the natural ones. In this regard, the work of Bowen et al [25] demonstrated that is possible to improve the mechanical properties of spider artificial silk by increasing the molecular weight of the spun proteins. However, in spite of the many brilliant results, we are still far from scalability of these materials with properties close to those of the native spider silk. For this reason, a further and deeper investigation on new possible raw silks has to be done. Then, solutions or alternative to the artificial spinning, with better scalability and properties could be discovered and explored.

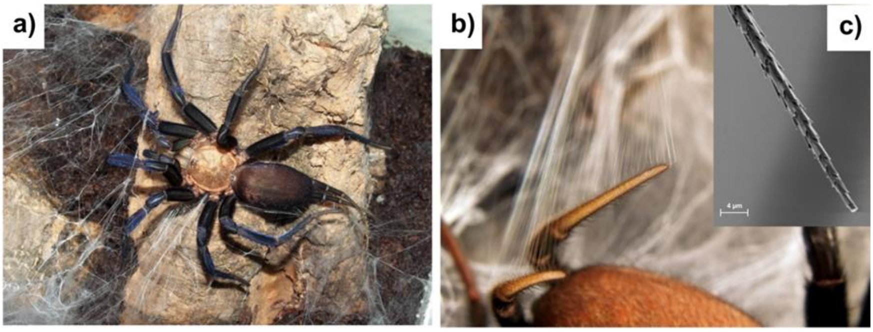

Figure 6-1: Linothele megatheloides spider (LM) and its spigots. a) The Colombian spider Linothele megatheloides (frontal view, Courtesy of Enrico Simeon); b) The spinneret of LM spider (Courtesy of Enrico Simeon); c) Field Emission Scanning Electron Microscopy (FE-SEM) image of the spigots on spinnerets of LM spider. The scale bar in figure c is equivalent to 4 μm.

In this work, we studied for the first time the silk produced by one of the largest Dipluridae spiders original from Colombia, *Linothele megatheloides* (Paz & Raven, 1990) [28] (Figure 6-1a). The peculiarity of these spider is in its two 2 cm long spinnerets, the large up to 60 mg amount of silk produced in a week, and the easiness to farm with respect to other orb weaver spiders (Figure 6-1b) [29]. Furthermore, this species produces only one type of silk, this leading to a simplification of the silk-harvesting process (Figure 6-1c) [30]. Mechanical properties, fiber morphology, protein structure and amino acid composition of *Linothele megatheloides* spider (LM) silk were characterized and compared with silk from *Bombyx mori* cocoon before (SC) and after degumming (DS). Preliminary biocompatibility aspects of natural networks made by different types of silk mentioned above were studied by imaging cell (NIH 3T3 fibroblast) adhesion with confocal microscopy, and assessing cells metabolic activity and proliferations. Competitive cell adhesion test was assessed by directly comparison of LM silk and *Bombyx mori* silk (before and after degumming).

6.3. Materials and methods

6.3.1. Materials

Spiders under study were adult females of *Linothele megatheloides* (Aranae, Paz & Raven, 1990). One of the reasons to choose this specie was that the easy possibility to extract the silk without damaging it. They were kept in different glass or plastic terrariums and fed with a weekly diet of insects (mainly *Blaptica dubia* or *Acheta domestica*). All the terrariums were set in a room with controlled environmental parameters. Each terrarium was provided with a small refuge by considering the need of the spider to feel protect and live without stress, according to the Italian regulation on animal protection and EU Directive 2010/63/EU for animal experiments. *Bombyx mori* (polyhybrid) cocoons, produced in a controlled environment, were kindly provided by Chul Thai Silk Co., Ltd. (Petchaboon province, Thailand). Undegummed and degummed fibers were considered. For degumming, cocoons were cut in to pieces and then treated in two 98°C distilled (DI) water baths of Na_2CO_3 (Sigma, USA, 1.1g/L and 0.4 g/L, respectively), 1.5 hours each, 10 g per liter. Then they were rinsed thoroughly with warm DI water to remove the salt and completely dried at room temperature in a laminar flow hood.

6.3.2. Sample preparation

For cell proliferation and metabolic activity tests, round samples 1.5 cm diameter were isolated from the original silk net of the spider and from a thin layer separated from the middle part of the cocoon, without (SC) and after (DS) degumming.

For cell adhesion test, fibers were isolated from the net samples and competitively tested in couples fixed on a polymethylmethacrylate frame (Figure S1).

6.3.3. Field Emission Scanning Electron Microscopy (FE-SEM) observations

Samples with cells were first fixed in 4% glutaraldehyde in 0.1 M Cacodylate buffer for 1h at room temperature, followed by washing in 0.1 M cacodylate buffer (three times) and then dried at room temperature. All samples were observed with a field emission-scanning electron microscope (FE-SEM, Supra 40/40VP, Zeiss, Germany), in dry state and after coating with Pt/Pd in a reduced argon atmosphere.

6.3.4. Mechanical properties

The tested samples were prepared by following the same procedure reported by Blackledge et al [31]. We stuck the silk samples on a paper frame provided with a square window of 1 cm side. The silk sample was fixed to the paper frame with a double-sided tape. For silkworm silk it was sufficient to collect the single thread spun by the spider. On the other hand, for the silk of *Linothele megatheloides* we stimulate directly the spinneret of the spider to stimulate the spinning of the silk. For the mechanical characterization, we used a nanotensile machine (Agilent technologies T150 UTM) with a cell load of 500 mN. The imposed strain rate was 1%/s. Before mounting the samples, we measured their diameter with an optical microscope. The declared sensitivity of the machine is 10 nN for the load and 0.1 nm for the displacement in the dynamic configuration. Ten samples were tested for each silk type and we report the mean value and standard deviation. The tensile tests were performed at a temperature of 21°C and relative humidity of 35-39%. In this work we did not tested the silks at different humidity rates. Moreover, a quite recent work on supercontraction (effect of humidity on spider silk mechanical and structural properties) on suborder of Mygalomorphae spiders suggested that the effect of humidity on their silks is minimal when compared to those of orb weavers [32].

6.3.5. Atomic Force Microscopy (AFM)

The AFM used to obtain the images, topography and force curves on the samples is a NT-MDT Smena scanner. The environmental conditions at which we operated were controlled and with a temperature of 24°C and relative humidity of 71%. We used different cantilevers and operational modalities to obtain topography and force curves respectively. The former was measured in semi-contact mode, by using a NT-MTD NSG-11B tip (10 nm nominal tip radius, resonance frequency of 181 kHz and force constant between 2.5 and 10 N/m). The latter were obtained by using a contact mode tip (NT-MTD, CSG-11B, 10 nm nominal tip radius, 428 kHz resonance frequency and force constant between 0.01 and 0.08 N/m).

The threads of the different silks type were stuck in a Double-Sided Bonding tape on the sapphire AFM sample holder. AFM data were analyzed with the support of Gwyddion and IA_P9 application. The roughness values were computed both for the average (Ra) and mean root square (Rq) value, following British standard ISO 4287:2000.

The current/tip-deflection response curve of the cantilever was calculated starting from the current/distance curves collected on a silicon chip surface and was estimated to be equal to 0.006 A/m. The adhesion force values where obtained by using the nominal elastic constant of the used cantilevers and by measuring the jump out current of the tip from the surfaces of the silk. Ten curves were obtained for each type of silk. Mean and standard deviation of the snap-out current values were then computed.

6.3.6. Fourier Transformation Infrared spectroscopy (FTIR)

Fourier transformation infrared spectroscopy (FTIR) analysis was performed directly on LM silk in attenuated total reflectance (ATR) mode (FTIR–ATR, Spectrum One, PerkinElmer, USA) equipped with Zinc

Selenide crystal on ATR. The spectrum collected in the range from 650 to 4000 cm^{-1} with 64 scans at the resolution of 4 cm^{-1}. Secondary structures analysis of protein structure were determined by Fourier transform infrared spectroscopy (FTIR) in attenuated total reflectance (ATR) mode (FTIR–ATR, Spectrum One, PerkinElmer, USA) equipped with Zinc Selenide crystal on ATR. The spectra processing was performed by Origin 2016 software (peak analyzer mode). The spectra were baseline corrected, smoothed with the Savitsky-Golay method (10 points). A Fourier self-deconvolution (FSD, parameter setting: Gamma 5 and Smoothing Factor 0.2) was used to enhance of the infrared spectra in the Amide I region (1600 - 1700 cm^{-1}) [31]. Then the peaks assigned to different secondary structures [31] were determined using a second order derivative and fitted using Gaussian function to minimize χ^2. Especially in β-sheet secondary structure, intermolecular (centered around 1616-1627 cm^{-1} and 1697-1703 cm^{-1}) and intramolecular (centered around 1628-1637 cm^{-1}) β-sheet were calculated separately. The area of each peak has been taken as measure of the specific structure.

6.3.7. Amino acid composition

The amino acid composition of LM silk, silk cocoon and degummed silk was determined with the Waters AccQ-Fluor™ Reagent Kit using the AccQ-Tag™ amino acid analysis method (Waters Corp., Milford, MA, USA). For each sample, 4 mg was hydrolysed by 6 M HCl at 120 ± 2 °C in a silicone oil bath for 24 h. The air-dried hydrolysates were reconstituted with 20mM HCl and then mixed with Waters AccQ-Fluor Reagent to obtain stable amino acids. The amino acid composition was determined by reverse phase high performance liquid chromatography (RP-HPLC) using an AccQ-Tag™ column (3.9 ×150 mm, Waters Corp., Milford, MA, USA) with a gradient of Waters AccQ-Tag™ Eluent A, Milli-Q water, and Acetonitrile (HPLC grade). The amino acids were detected with the Jasco UV-1570 detector set (Jasco, Bouguenais, France) at 254 nm. The chromatograms obtained were compared with Waters Amino Acid Hydrolysate Standards.

6.3.8. Cell culture

Murine embryo fibroblast (NIH 3T3, ATCC number: CRL-1658) cell line was cultured in Dulbecco's modified Eagle's medium (DMEM), with 10% fetal bovine serum (FBS), 1 mM sodium pyruvate, 2 mM l-glutamine and 1% antibiotic/antimycotic in a humidified atmosphere of 5% CO_2 at 37 °C with changing the medium every third day. Cells (at passage number 8) were collected by trypsin and were seeded in a 24-well plate (3×10^4 cells/well in 1.0 ml medium) with samples inside and cultured in standard NIH 3T3 medium. Before all the biological tests, samples were sterilized with aqueous ethanol solution 70% (v/v) for 2 h. After washed carefully to remove ethanol solution, samples were dried under a sterile hood at room temperature.

6.3.9. Cell morphology, distribution and immunofluorescence staining

Cell morphology and distribution were visualized by Rodhamine phalloidin and 4’6-diamidino-2-phenylindole (DAPI) staining. Rodhamine phalloidin stains actin filaments of cytoskeleton resulting in red fluorescence while DAPI stains nuclei resulting in blue fluorescence. At day 1 and day 2, the cell seeded samples were fixed with 4% paraformaldehyde, washed three times with PBS and then were permeabilized using 0.2% Triton X-100 PBS solution for 30 min. After washing in PBS for 3 times (15 min each time), cells were incubated with Rodhamine phalloidin (5.0 µl/well) and DAPI (1.0 ml/well, 5.4µl dilute in 25.0 ml PBS) for 1 h at room temperature. After three rinses with PBS, samples were observed using Zeiss LSM 510 Meta confocal laser scanning microscope (CLSM).

6.3.10. Cell proliferation by DNA quantification (PicoGreen assay)

To evaluate cell proliferation on the different netwroks, a PicoGreen® DNA quantification assay (Quant-iT PicoGreen® dsDNA Assay, Invitrogen™, Carlsbad, USA) was used. After 1 and 2 days culture, the culture medium was removed and the samples were washed with PBS. Samples were then covered with 300 µl of 0.05% Triton-X in PBS, and the supernatants were collected and stored in single tubes (Eppendorf) at -20°C until analysis. Before analysis, tubes were thawed at room temperature, and sonicated for 10 seconds with a Hielscher ultrasonic homogenizer (UP400S, 400 watt-24 kHz, cycle 1, amplitude 40%, from Hielscher Ultrasonics, Teltow, Germany). Extracts of 100 µl were subsequently placed in a black 96-well plate, and mixed with 100 µl of PicoGreen® working solution, prepared following the manufacturer’s instructions. Four independent samples were analyzed for each experimental condition. Fluorescence intensity was measured with a Tecan Infinite 200 microplate reader (Tecan Group, Männedorf, Switzerland) using excitation wavelength 485 nm and emission wavelength 535 nm. A calibration curve was created using a double-stranded DNA standard provided by the kit and was used for the calculation of the DNA content. Finally, the approximate number of cells per sample was determined from DNA content by the conversion factor of 7.7 pg DNA per cell.

6.3.11. Cell metabolic activity (AlamarBlue assay)

Cells viability after 1 and 2 days of culture was determined with AlamarBlue® Cell Viability assay (Invitrogen™, Carlsbad, USA), that quantifies cellular metabolic activity and in turn determines the concentration of viable cells in a given sample. AlamarBlue® reagent was added directly to each well 10% of the cell culture medium volume. Then, the well plates were incubated at 37°C in a humidified atmosphere with 5% CO_2 for 45 minutes. A volume 100 μl of solution was collected from each well and the fluorescence signal was measured with a Tecan Infinite 200 microplate reader (Tecan Group, Männedorf, Switzerland) with an excitation wavelength of 560 nm and an emission wavelength of 590 nm. Four replicates were considered for each experimental condition.

6.3.12. Statistics

In order to analysis the fracture strength distribution we used Weibull statistics. It is defined by the following relation

$$F(x, m, x_0) = 1 - e^{-\left(\frac{x}{x_0}\right)^m} \quad (1)$$

where x is the fracture strength m is the shape parameter and x_0 the scale parameter. F represents the probability that the sample break at the strength x.

In order to obtain the relative probability density distributions of the four different silk types (i.e. $f(x, m, x_o) = \frac{m}{x_0^m} x^{m-1} e^{-\left(\frac{x}{x_0}\right)^m}$) we obtained the Weibull shape and scale parameter by using the linear regression method. By applying the double logarithm to (1) we obtain the following equation

$$\ln\left[\ln\left(\frac{1}{1 - F(x)}\right)\right] = m\ln(\mathrm{x}) - m\ln(\mathrm{x}_0) \qquad (2)$$

where F could be estimated through the median rank estimator

$$\hat{F}(x_i) = \frac{i - 0.3}{n + 0.4} \quad (3)$$

where n is the number of tested specimen and i is the order of the considered one (after the organization of the samples from the weakest till the strongest). Kolmogorov Smirnov test was performed to each seat of data to verify (under the 95% of acceptance, MatLab®) that Weibull statistics could be applied to data set.

For chemical characterizations, statistical evaluation was carried out using Origin Pro 2016 and Microsoft Office Excel 2010. Data were expressed as mean ± standard deviation (SD).

The *in vitro* NIH 3T3 cell proliferation and differentiation tests were performed on four replicates for each group. All quantitative data were expressed as mean standard ± deviation (SD). Statistical analyses were performed using GraphPad Prism 6 (GraphPad Software, La Jolla, CA, USA). The quantitative biological results were compared using a two-way analysis of variance (ANOVA). A significance level of 95% with a p value of 0.05 was used in all statistical tests performed.).

6.4. Results

6.4.1. Composition and structural characterization

The results of amino acid composition analysis (mol %) of all samples (Table S1) showed remarkable differences between the composition of LM and silkworm silk, before (SC) and after (DS) degumming. In particular, LM silk presented much more Serine (23.0% vs. 11.2/11.7%) and much less Glycine (16.9% vs. 44.5/45.4%) and the presence of two amino acids, Asparagine (5.0%) and Glutamine (1.4%) are not found in the silkworm silk. By classifying amino acids into short chain (Gly, Ala and Ser) and long chain (Asp, Glu, Tyr, Arg, Leu, Val, Pro, Lys, Ile, Phe, Thr, Cys, His and Met) residues [33], LM presented more long chain residues (36.9% vs. 16.9/16.3%) and less short chain residues (63.0% vs. 83.1/83.7%).

Molecular structure of LM, SC and DS was characterized by Fourier Transform Infrared Spectroscopy (FTIR) (Figure 6-2a). The peaks related to Amide A (3280 cm^{-1}), Amide I (1623 cm^{-1}), Amide II (1515 cm^{-1}) and Amide III (1230 cm^{-1}) were centered at the same wavelength[34]. In all silk samples, the peaks centered at around 1623 cm^{-1} (Amide I) and 1515 cm^{-1} (Amide II) indicated a significant amount of β-sheet structure[35]. A peak related to the presence of β-polyalanines was detected at 964 cm^{-1} just in LM spectra [36]. In order to better elucidate the structure of protein in different samples, a secondary structure analysis was performed by analyzing the Amide I region (1600-1720 cm^{-1})[37], and the results were summarized in Figure 6-2b and 6-2c. LM fiber showed the lowest β-sheet (39.8% in total, 22.4% for intermolecular bonding) and α-helix (12.2%) structures with the highest random coils presence (27.6%). Among the other samples, DS showed the highest β-sheet (55.1%) content and lowest β-turn (13.5%).

6.4.2. Silk fibers morphology

Fibers morphology of different silks was observed by Field Emission Scanning Electron Microscopy (FE-SEM) (Figure 6-3). FE-SEM images showed different surface morphologies and dimensions of the studied silks. LM silk (Figure 6-3c) presented an irregular roughness that could be better seen at higher resolution in Figure 6-3d. The fiber size calculated on FE-SEM images of SC and DS was in between 10-20 µm (Figure 6-3a and 6-3b, respectively), while for LM silk (Figure 6-3c) resulted less than 1 µm. The spontaneous assembling of silk filaments is also quite different, with isolable single fibers for SC and DS silks and regions of irregular assembling in LM filaments (Figure 6-3c and 6-3d). Worth nothing is however the typical spigots of the *Linothele megatheloides* spider that are covered by scales, as shown in Figure 6-1c.

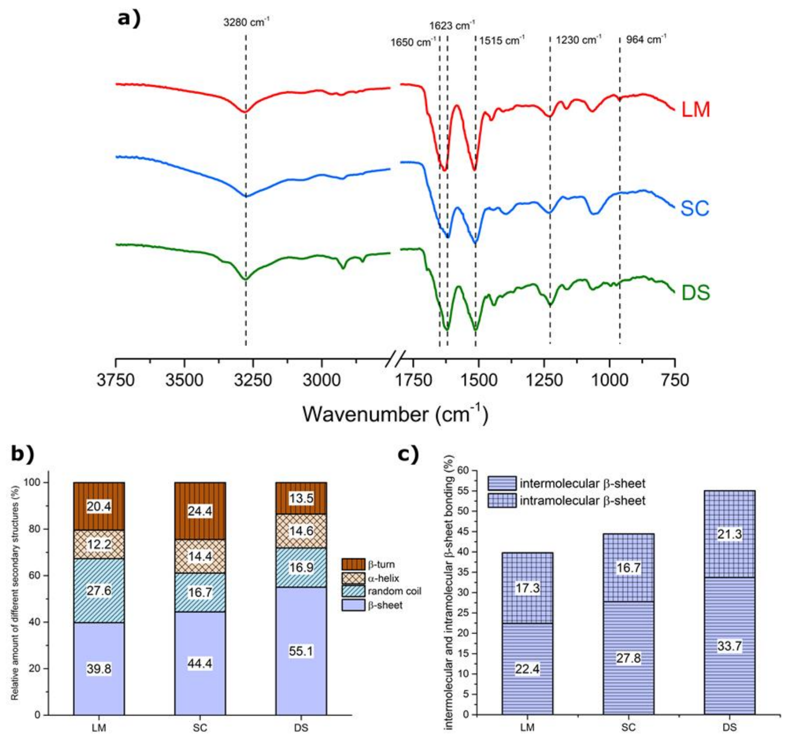

Figure 6-2: Molecular structure analyses. a) Samples FTIR spectra; b) FTIR secondary structure analysis on Amide I of different silks (based on related structure peak areas); c)

Ratio of intermolecular and intramolecular bonds detected on different silks (based on related intermolecular and intramolecular β-sheet areas). LM: Linothele m. silk; SC: Bombyx m. silk; DS: degummed Bombyx m. silk.

6.4.3. Mechanical properties

Figure 6-4 and Table S2 compare the tensile mechanical properties of the investigated silks. The mechanical properties of LM silk are very different from those of SC and DS (Figure 6-4 and Table S2), with an elastoplastic behavior, a plastic onset at very small levels of stress and a failure that occurs with a progressive decrease of stress (Figs. 6-4a and 6-4b). The energy at break of LM silk was quite high, even if the smallest among the investigated fibers when normalized with respect to the volume (toughness: 4± 3 MJ/m^3 (LM), 82 ± 60 MJ/m^3 (SC), 55± 20 MJ/m^3 (DS)) (Table S2). On the other hand, by considering the computed Weibull parameters of these silks (Figure 6-4c) and their relative distributions (Figure 6-4d), we noticed huge differences in term of statistical behavior. In Weibull distributions of the strength (Figure 6-4d), the narrower distribution highlights the more homogeneous behavior of this silk, untypical in spider silk that usually presents broader distributions.

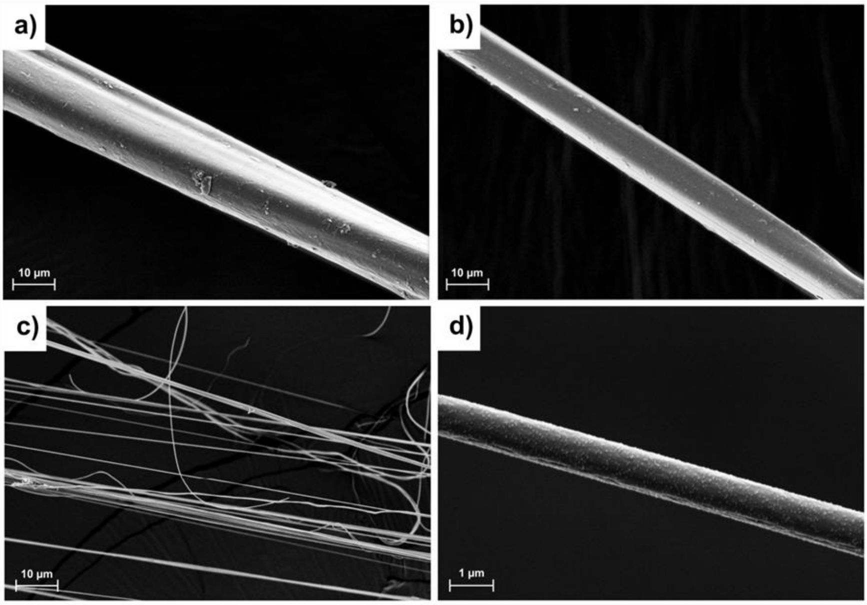

Figure 6-3: FE-SEM images of silk fibers. a) Silkworm cocoon silk from Bombyx mori before (SC) and b) after degumming (DS); c) and d) Linothele megatheloides spider silk (LM) in different magnifications. The scale bars in figure a, b and c are equivalent to 10 µm and the scale bar in figure d is equivalent to 1 µm.

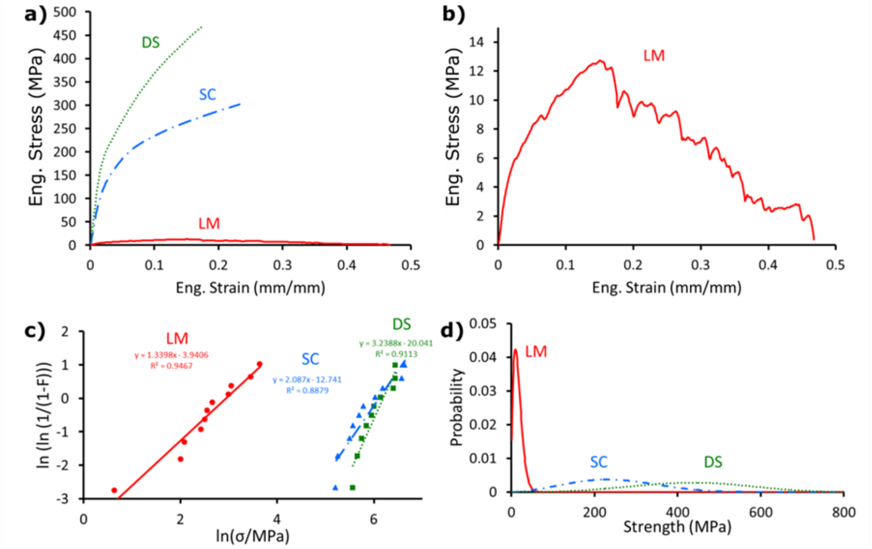

Figure 6-4: Mechanical behaviors of samples. a) the tested different silks; b) LM silk. c) Linear regression method used to compute the Weibull parameters and d) Weibull probability distribution of the strength of the tested silks. LM: Linothele m. silk; SC: Bombyx m. silk; DS: degummed Bombyx m. silk.

6.4.4. Atomic Force Microscopy (AFM)

Atomic Force Microscopy (AFM) images obtained on the tested silks are reported in Figure S2. In particular, *Linothele megatheloides* silk was the only one presenting submicrometric fibers diameter. The roughness data obtained from AFM images (Table S3) showed that LM presents the highest roughness (4.4 nm for Ra and 5.4 nm for Rq), confirming FE-SEM images. SC and DS had respectively the intermediate values of 1.9 / 2.6 nm, and 2.1 / 2.8 nm. All the tested fibers showed rather homogeneous surfaces with the exception of DS, in which numerous relief islands were visible and were probably due to presence of residual sericin spots (Figure S2d).

Furthermore, AFM force/distance curves were used in order to measure adhesion of the cantilever tip on the silk surface, that, since the measurements were performed in air and were mainly influenced by the capillary forces, so, the tract where the tip detaches from the sample, can be considered a qualitative indicator of the surface wettability (Figure S3). The shapes of the curves were significantly different among the samples and the values of the adhesion force necessary to detach the tip from silk surfaces (snap-out) are reported in Table S4. In particular, since the z travel range of the used scanner was limited to 4 µm, for LM silk type it was not able to finalize the snap-out of the tip from the surface. This sets the sample at the highest level of adhesion force among all the others. The high standard deviation obtained on DS with respect to the other samples could be correlated with the presence of highly hydrophilic sericin spots (Figure S3d) that could strongly scatter the adhesion values.

6.4.5. Cell proliferation and metabolic activity on different natural networks

To investigate the early stage of interaction of the investigated silks with cells, NIH 3T3 cell line were seeded on the network naturally produced by spider (LM) and derived from the silk of the silkworm cocoon (SC and DS), prepared as reported in the materials paragraph. Cell proliferation studies were performed at day 1 and day 2, using PicoGreen® DNA quantification assay. According to the results (Figure 6-5a), cell number of each sample increased gradually at each time point. However, LM silk had the largest number of adhered cells during two days' cell culture; while the increasing of the cells in day 2 was not as significant as SC and DS. These results were in well agreement with the confocal images (Figure 6-5g – 6-5l) that evidenced a larger cell growth for LM silk network than for other networks. It was obvious from Figure 6-5g – 6-5l that cells adhered on LM silk maintained the regular spindle shaped cellular morphology and were well connected to each other after 2 days culture in comparison to as in SC and DS.

Figure 6-5b and 6-5c reports the NIH 3T3 cells metabolic activity, measured by AlamarBlue® assay. For LM silk, the total cellular metabolic activity was significantly higher than other samples, but showed no sensible increment from day 1 to day 2. DS promoted a continuous increasing of cell metabolic activity while SC showed a decrease. Total cell metabolic activity was also normalized to total DNA content previously determined using the PicoGreen® DNA quantification assay (Figure 6-5c). Cells seeded on LM silk showed a higher specific activity when compared to others in all time points. Nevertheless, SC showed a lower normalized activity than DS in day 2.

6.4.6. Cell adhesion, morphology and distribution on different silk fibers

Single fiber competitive combinations of LM silk with SC and DS, arranged as indicated in Figure 6-6, were set for NIH 3T3 adhesion tests. Confocal microscopy images (Figure 6-6) clearly indicated that already at day 1 the LM silk filaments were fully covered by well spread cells, forming clusters, with only a few or no cells adhering to the other samples, even after two days culture. The findings are confirmed by FE-SEM images of Figure 6-6, moreover indicating a high degree of spreading of cells on LM fibers and the presence after two days of a continuous cell monolayer, in particular when in competition with SC fibers (Figure 6-6l).

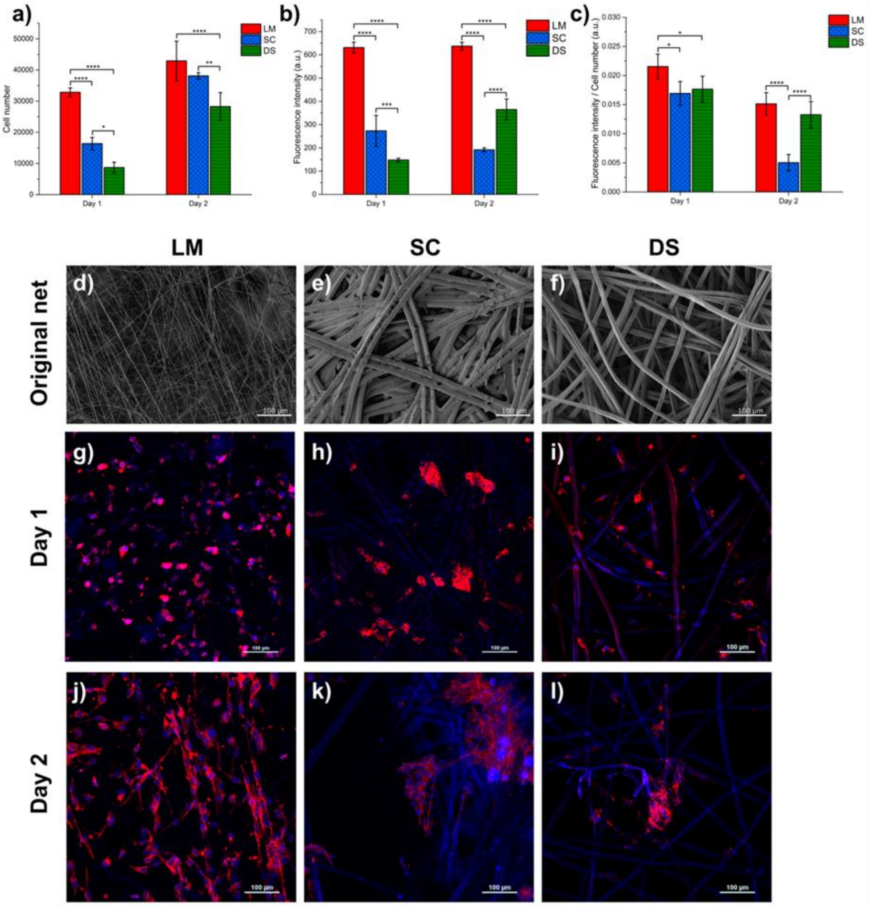

Figure 6-5: Cell adhesion, proliferation and metabolic activity for NIH 3T3 cell line cultured for 1 and 2 days on different silk network. a) cell number derived from total DNA content measured by PicoGreen assay; b) total metabolic activity determined by AlamarBlue assay; c) metabolic activity normalized with respect to DNA content. d) - f) FE-SEM images of different original silk networks (without cells), and g) - l) confocal microscopy images of samples seeded with NIT 3T3 after day 1 and day 2 of culture. LM: Linothele m. silk; SC: Bombyx m. silk; DS: degummed Bombyx m. silk. The Scale bars in the figures are equivalent to 100 µm.

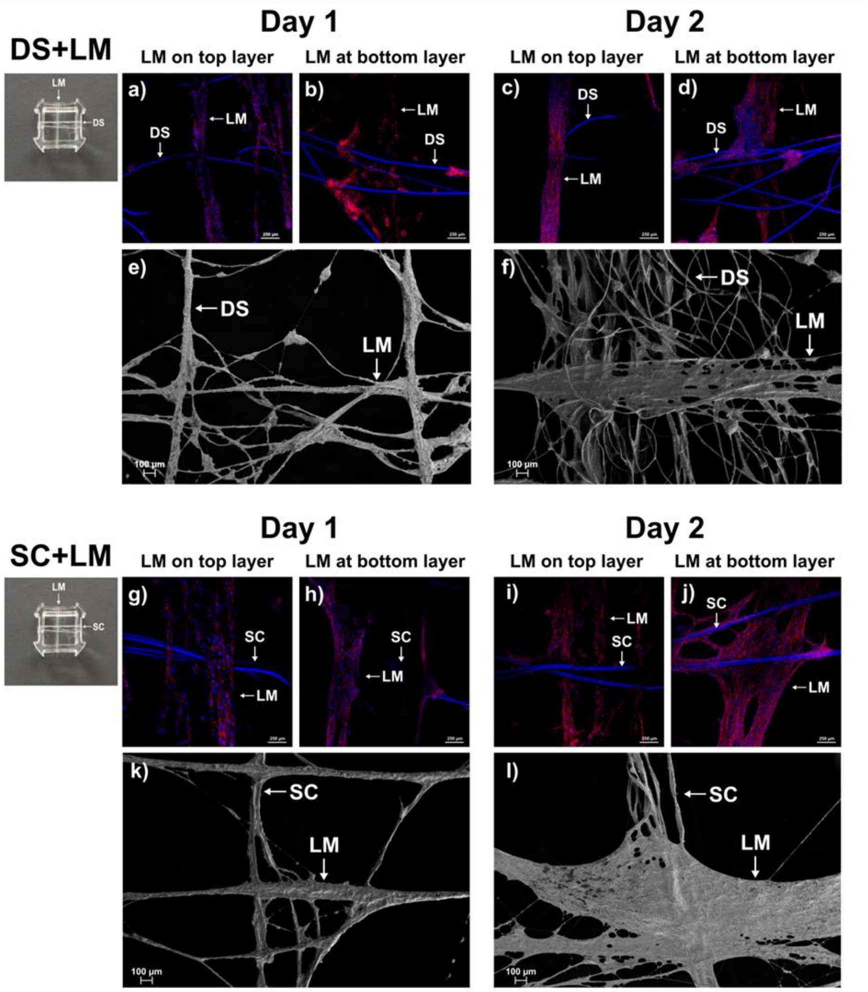

Figure 6-6: Cell adhesion, morphology and distribution on different silk fibers. a) - d) and g) - j) Confocal images of NIH 3T3 cells adhesion on different silks samples at day 1 and day 2 of culture. The scale bars in the figures are equivalent to 250 µm. e) - f) and k) – l) FE-SEM images of cell adhesion on different silks samples after day 1 and day 2 of culture. The scale bars in these figures are equivalent to 100 µm. LM: Linothele m. silk; SC: Bombyx m. silk; DS: degummed Bombyx m. silk.

6.5. Discussion

Silks are a family of proteins, that can be produced by several organisms like Lepidoptera and Arthropods [38]. Depending on source, silks can be very different in terms of chemistry, molecular structure and mechanical properties [16]. The domestic silkworm *Bombyx mori* silk has been deeply studied, worldwide used for making fabrics, employed in surgery already in the past as suture thread and more recently proposed for the repair of tendons and ligaments and for the fabrication of tissue engineering scaffolds [5-9]. Nowadays, also spider silk is draining the attention of scientists working in biomedical field [4].

In our work, for the first time, we have characterized physical and biological properties of *Linothele megatheloides* (LM) spider, produces a single type of silk in a relatively quite large quantity (60 mg / week), which partially overcomes the limitations of silk procurement from other types of spiders. LM silk was compared with the already deeply investigated silk filament of *Bombyx mori* silkworm. Samples were evaluated in terms of chemical (amino acid composition, FTIR and secondary analysis) and physical (AFM, tensile test and morphology observation) properties. Finally, cell adhesion, metabolic activity and purification were investigated by culturing NIH 3T3 cells on the different silk fibers and networks. The results were assessed by imaging (confocal microscopy and FE-SEM) and quantitative analysis (AlamarBlue and PicoGreen assay).

Amino acid composition is one of the most important aspects considering the impact on secondary structure, molecular water interaction and, as a consequence, on mechanical properties. Results demonstrated a remarkable difference in amino acid composition between LM silk and the other samples. Gly, Ala and Ser were the most abundant amino acids in all considered silks types, and all were involved in β-sheet secondary structure formations [33]. However, it was observed that the composition of different types of silk differ mainly in the relative percentages of individual residues, and also, in the presence/absence of specific residues (rich in Glu and Asp). By classifying protein residues into short chain (S) and long chain (L), it is worth noticing that the lowest percentage of S residues increases the ratio of L/S in LM silk. The lowest amount of short side residues, together with the lowest content of Gly makes LM silk fibers less able to structure in β-sheets. In fact, the lowest content of β-sheet was detected in LM silk together with highest random coils conformations. This conformation defined a more flexible material with a higher extensibility (Figure 6-4) with respect of the other samples. In addition, intramolecular bonding (stabilize the secondary structure of the chain) and intermolecular bonding (forces between chains holding in a substance) also effect the mechanical properties. As expected from the amino acid composition, LM silk fiber had the lowest content of intermolecular bonds, due to the lowest percentage of Gly, which also played a role on tensile behavior (Figure 4a).

Under tensile testing, LM silk behaves in a different way with respect to other typical silks, with a more softening rather than stiffening constitutive law (Table S2). The softening - often associated to stress drops - is correlated to the failure of single fibers within the thread sample[39], which in this case is basically a bundle of fibers. This result was also in well agreement with the results of secondary structure analysis: the lower amount of β-sheets (low intermolecular bonding) present in LM silk, leads to a lower strength (16 ± 10 MPa) and toughness (4 ± 3 MJ/m^3) of the material. The group of fibers that composed a single sample did not simultaneously break under load (Figure 6-4b) and the stress drop was progressive and not catastrophic as in the other cases (when break occurs). The surface roughness was observed by FE-SEM imaging (Figure 6-3) and confirmed by AFM analyses. The highest roughness of LM silk could be attributed to a different way of fiber production by the three considered animals. *Linothele megatheloides* spins many tiny and sticky fibers per time (Figure 6-1b and 6-3c), leading to a high difficulty in isolating a single thread without damaging it.

To evaluate the bioactivities of different silks in terms of cell adhesion, proliferation and metabolism, natural networks were taken into consideration firstly. The cells adhered on LM network demonstrated a significant enhancement of cell number, a higher cellular proliferation and metabolic activity comparing to other samples. This trend was confirmed also by normalized metabolic activity. Interestingly, cells adhered on DS showed a slower proliferation and activation compare with LM in day 1, but after 2 days became comparable. The different cell behavior was observed on SC and DS due to the release of sericin from SC, which was already seen to promote fast cell adhesion and with a mitogenic effect on cells (for example, corneal epithelial cells and retinal cell [40]). These results were in well agreement with cell adhesion morphology. In general, cell behavior was not affected by the position of silk in the samples (LM on top or bottom), but mainly by the silk type. Well spared and regular spindle shaped cellular morphology were observed on LM silk in comparison to lower affinity globular clusters. The preliminary NIH 3T3 cell adhesion evaluation clearly showed the highest cell adhesion ability on LM silk fibers.

Cell adhesion is a complex mechanism, driven by several aspects, mostly controlled by hydrophilicity, surface chemistry and material morphology, and depending on the adhesion mechanisms, different cell activities can be triggered[41]. Environment stored fibers contained alike amount of water,

in the range 7-8.5%, as determined by thermogravimetric analysis (data not reported here). This can suggest that they will take comparable amount of water when immersed in the culture medium, that would be however impossible to measure without introducing artifacts in the experiment.
The LM fibers lowest relative amount of β-sheet (intermolecular bonding) and the highest amount of random coils together with a very high roughness, can well explain the fast cell adhesion observed. Furthermore, a contribution on early adhesion could come from the different fiber size in the nets [42]. We have demonstrated that LM silk stimulated NIH 3T3 cells proliferation after one day and two days of *in vitro* culture. It was confirmed the faster cell adhesion and activation on LM when compared with *Bombyx m.* silk, in particular in the early stage (1 day). The results suggested that the silk of *Linothele megatheloides* can induce a faster cell adhesion and activation in comparison to the other tested fibers. Considering that *Linothele megatheloides* produces a single type of silk, with high homogeneity and relatively high production rate, it can be considered as a potential source for developing novel spider silk based materials from nature.

6.6. Conclusion

Chemical, mechanical and *in vitro* biological properties of *Linothele megatheloides* spider (LM) silk were determined in comparison with *Bombyx mori* silkworm silk, before and after degumming. LM silk is characterized by the fact that it produces for the network just one type of filament at a relatively high production rate when compared to other spiders, this making easier the collection and evaluation of this silk for potential applications also in medicine. With respect to the *Bombyx mori* silkworm silk (before and after degumming), LM silk presented higher amount of serine in amino acid composition, lower amount of β-sheet and α-helix secondary structure and higher random coils units. Moreover LM fibers were thinner (less than 1μm diameter), rougher, and resulted to have the highest level of adhesion force among all the tested samples. NIH 3T3 cells were used to evaluate the early stage of cell adhesion *in vitro* biological properties of the investigated silks. A first used specific setup with couples of fibers arranged in competitive arrays, demonstrated the highest early time cell adhesion of the LM silk. These results have been confirmed by cell culture tests on samples made from the nets or from the cocoons, where again faster cellular proliferation together with a more proficuous metabolic activity was confirmed for LM silk samples. The noticeable biological behavior of LM silk found in these preliminaty tests justifies further and deeper investigations in order to outline hypotheses on the its potential use for applications in biomedicine and namely in the field of tissue engineering.

6.7. References

1. Z. Shao, F. Vollrath, Nature, 418 (2002) 741.
2. S.W. Cranford, A. Tarakanova, N.M. Pugno, M.J. Buehler, Nature, 482 (2012) 72.
3. O. Hakimi, D.P. Knight, F. Vollrath, P. Vadgama, Composites Part B: Engineering, 38 (2007) 324-337.
4. H.M. Tahir, K. Zahra, A. Zaheer, K. Samiullah, Punjab Univ. J. Zool, 32 (2017) 143-154.
5. P. Bhattacharjee, B. Kundu, D. Naskar, H.-W. Kim, T.K. Maiti, D. Bhattacharya, S.C. Kundu, Acta biomaterialia, 63 (2017) 1-17.
6. D. Jao, X. Mou, X. Hu, Journal of functional biomaterials, 7 (2016) 22.
7. C. Migliaresi, A. Motta, Scaffolds for tissue engineering: Biological design, materials, and fabrication, Pan Stanford, 2014.
8. T. Yucel, M.L. Lovett, D.L. Kaplan, Journal of Controlled Release, 190 (2014) 381-397.
9. K. Numata, D.L. Kaplan, Advanced drug delivery reviews, 62 (2010) 1497-1508.
10. K. Gellynck, P. Verdonk, R. Forsyth, K.F. Almqvist, E. Van Nimmen, T. Gheysens, J. Mertens, L. Van Langenhove, P. Kiekens, G. Verbruggen, Journal of Materials Science: Materials in Medicine, 19 (2008) 2963-2970.
11. N.M. Pugno, S.W. Cranford, M.J. Buehler, Small, 9 (2013) 2747-2756.
12. A. Meyer, N.M. Pugno, S.W. Cranford, Journal of The Royal Society Interface, 11 (2014) 20140561.
13. O. Hakimi, D.P. Knight, M.M. Knight, M.F. Grahn, P. Vadgama, Biomacromolecules, 7 (2006) 2901-2908.
14. N.M. Pugno, Meccanica, 53 (2018) 1105-1114.
15. R.B. Suter, Journal of Arachnology, (1992) 107-113.
16. T. Asakura, T. Miller, Biotechnology of silk, Springer, 2014.
17. A. Basu, Advances in Silk Science and Technology, Woodhead Publishing, 2015.

18. C. Allmeling, A. Jokuszies, K. Reimers, S. Kall, C. Choi, G. Brandes, C. Kasper, T. Scheper, M. Guggenheim, P. Vogt, Cell proliferation, 41 (2008) 408-420.
19. F. Vollrath, P. Barth, A. Basedow, W. Engström, H. List, In vivo (Athens, Greece), 16 (2002) 229-234.
20. M.C. Andrade, Behavioral Ecology, 9 (1998) 33-42
21. J. Scheller, U. Conrad, Molecular Farming: Plant-made Pharmaceuticals and Technical Proteins, 11 (2006) 1.
22. A. Salazar, M. Keusgen, J. von Hagen, Amino acids, 48 (2016) 1161-1171.
23. F. Teulé, Y.-G. Miao, B.-H. Sohn, Y.-S. Kim, J.J. Hull, M.J. Fraser, R.V. Lewis, D.L. Jarvis, Proceedings of the national academy of sciences, 109 (2012) 923-928.
24. H. Chung, T.Y. Kim, S.Y. Lee, Current opinion in biotechnology, 23 (2012) 957-964.
25. C.H. Bowen, B. Dai, C.J. Sargent, W. Bai, P. Ladiwala, H. Feng, W. Huang, D.L. Kaplan, J.M. Galazka, F. Zhang, Biomacromolecules, 19 (2018) 3853-3860.
26. A. Rising, J. Johansson, Nature chemical biology, 11 (2015) 309.
27. M. Andersson, Q. Jia, A. Abella, X.-Y. Lee, M. Landreh, P. Purhonen, H. Hebert, M. Tenje, C.V. Robinson, Q. Meng, Nature chemical biology, 13 (2017) 262.
28. N. Paz, R.J. Raven, Journal of Arachnology, (1990) 79-86.
29. W.G. Eberhard, N.A. Hazzi, The Journal of Arachnology, 41 (2013) 70-75.
30. F. Vollrath, International Journal of Biological Macromolecules, 24 (1999) 81-88.
31. T.A. Blackledge, J.E. Swindeman, C.Y. Hayashi, Journal of Experimental Biology, 208 (2005) 1937-1949.
32. C. Boutry, T.A. Blackledge, Journal of Experimental Biology, 213 (2010) 3505-3514.
33. S.J. Lombardi, D.L. Kaplan, Journal of Arachnology, (1990) 297-306.
34. E. Metwalli, U. Slotta, C. Darko, S. Roth, T. Scheibel, C. Papadakis, Applied Physics A, 89 (2007) 655-661.
35. E. Cooper, K. Knutson, Fourier transform infrared spectroscopy investigations of protein structure, in: Physical methods to characterize pharmaceutical proteins, Springer, 1995, pp. 101-143.
36. K. Spiess, R. Ene, C.D. Keenan, J. Senker, F. Kremer, T. Scheibel, Journal of Materials Chemistry, 21 (2011) 13594-13604.
37. X. Hu, D. Kaplan, P. Cebe, Macromolecules, 39 (2006) 6161-6170.

38. C.L. Craig, Annual review of entomology, 42 (1997) 231-267.
39. N.M. Pugno, T. Abdalrahman, Nanoscience and Nanotechnology Letters, 3 (2011) 882-884.
40. Z. Wang, Y. Zhang, J. Zhang, L. Huang, J. Liu, Y. Li, G. Zhang, S.C. Kundu, L. Wang, Scientific reports, 4 (2014) 7064.
41. H.-I. Chang, Y. Wang, Cell responses to surface and architecture of tissue engineering scaffolds, in: Regenerative medicine and tissue engineering-cells and biomaterials, InTech, 2011.
42. A.T. Nguyen, S.R. Sathe, E.K. Yim, Journal of Physics: Condensed Matter, 28 (2016) 183001.

7. BIOMINERALIZED SPIDER SILK FOR BONE TISSUE ENGINEERING

This chapter is based on the paper that we published in the Journal of Applied Polymer Science (48739, 2019, DOI: 10.1002/APP.48739). This paper is here reprinted with the permission of © 2019 WILEY-VCH Verlag GmbH & Co. KGaA, Weinheim (License number: 4718800675311).

Goal of the chapter: The chapter deals with the production of hybrid materials composed by spider silk and hydroxyapatite (which has been biomimetically mineralized on the silk). Finding new hybrid materials with desirable mechanical and biological properties is always challenging. In this case, the produced material is suitable for bone tissue regeneration applications.

7.1. Abstract

Silks have been widely used as biomaterials due to their biocompatibility, biodegradability, and excellent mechanical properties. In the present work, native spider silk was used as organic template for controlled nucleation of hydroxyapatite (HA) nano-coating that can act as biomimetic interface. Different bio-inspired neutralization methods and process parameters were evaluated to optimize the silk functionalization. The morphology and chemical composition were investigated by scanning electron microscopy, energydispersive X-ray spectroscopy, Fourier transform infrared spectroscopy, and X-ray diffraction analysis and mechanical properties were studied through tensile tests. Results showed that the optimized protocol enabled a controlled and homogeneous nucleation of apatite nano-crystals while maintaining silk mechanical performances after mineralization. This study reports the optimization of a simple and effective bio-inspired nucleation process for precise nucleation of HA onto spider silk templates, suitable to develop high-performance hybrid interfaces for bone tissue engineering.

7.2. Introduction

Silks are fibrous protein polymers spun by some species of *Lepidoptera* (as butterflies and silkworms) and *Arachnida*, i.e. spiders [177]. These biological polymers have been extensively studied in the past decades because of its biocompatibility, biodegradability, non-toxicity and excellent mechanical properties, such as tensile strength and toughness [49,178,179].

Silk from silkworms, usually fibroin from *Bombix mori,* has been employed as suture material for centuries [180] and it's currently the main silk type used in biomedical field due to its availability and ease of commercial production [178]. Silk-based biomaterials are used for tissue engineering (TE) applications in form of scaffolds [181], hydrogels [182], films or fibers [183] as well as nanoparticles in drug delivery systems [184,185]. Moreover, silk-based devices have been successfully designed and developed for regeneration of different tissues, such as bone, tendon, ligament, skin and nerve [186]. Li *et al.* developed silk fibroin-based scaffolds incorporating nanoparticles of hydroxyapatite (HA) and bone morphogenic protein 2 (BMP-2) by electrospinning of silk fibers for bone TE [187]. Their results revealed an improved bone formation and osteogenesis process *in vitro.* Shi *et al.* produced knitted meshes of silk functionalized with low crystallinity HA for regeneration of the bone/ligament interface, demonstrating cells proliferation and differentiation *in vitro* and recovery of mechanical strength and tissue regeneration *in vivo* [188].

Spider silk, particularly draglines spun by major ampullate (MA) gland, has become of great interest in bio-engineering in the past decades due to the outstanding mechanical properties, higher biocompatibility and lower immunogenicity compared to silkworm silk [55,145,189]. Nevertheless, native spider silk use is limited because of low production yields and difficulty in spiders farming [183,190]. A feasible solution is to produce engineered synthetic genes and recombinant proteins encoding spider silk. Hardy *et al.* [191] developed films made of mineralized biodegradable polyesters and recombinant spider silk proteins (eADF4(C16)), capable to enhance bone tissue formation *in vitro.* Although the encouraging results from genetic engineering [192,193], a close mimicry of the complex structure and mechanical behavior of spider silk remains an ambitious target.

Chemical, biological and mechanical properties ensure that silks can be successfully used in bone tissue engineering; furthermore it represents a suitable template for HA nucleation through biomineralization processes, enhancing bone formation and osteointegration [194,195]. The mechanism of bone biomineralization consists of simultaneous nucleation of nanoHA crystals on self-assembling collagen matrix and it has been replicated *in vitro* successfully [196]. Other processes [197,198] for the mimesis of this natural process are based on the use of proteins, natural or synthetic polymers or organoapatites [199], as well as organic templates, such as silks [187], while the inorganic phase (hydroxyapatite) is usually synthesized from salts-mediated reactions, acid-base (neutralization) syntheses or by using synthetic body fluids (SBF) [200]. Cao *et al.* [201] mineralized spider dragline silks through immersion in a HA precursor solution for up to 10 days, demonstrating the possibility of nucleating HA crystals with a preferred orientation. Dmitrović *et al.* [202] produced spider silk coated with calcite via a salt-mediated biomineralization process from calcium chloride and ammonium carbonate. Their data revealed formation of regular rhombic crystals along the fibers, with a potential application as bone grafts.

In this study, bio-inspired HA neutralization synthesis has been optimized to effectively functionalize native silk draglines from *Cupiennius salei* (Keyserling 1877). As a first step, the effect of reagents concentration, reagents pouring order and HA maturation time was investigated to obtain a controlled nucleation of inorganic phase. The mineralized silks were then evaluated in terms of coating morphology, chemical composition and mechanical properties and results were compared to untreated and supercontracted silks and to HA crystals deposition from a precursor solution. The goal of the present work is to define a simple and reproducible bio-inspired mineralization protocol to precisely nucleate a HA nano-coating on silk organic templates in order to produce a hybrid biomaterial with potential applications in bone tissue engineering.

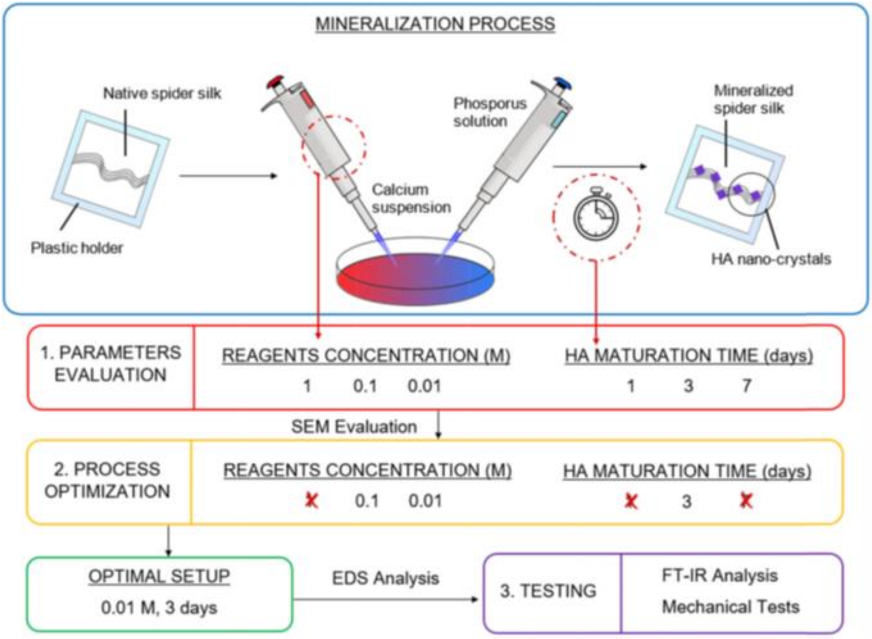

Figure 7-1: Process overview: parameter evaluation, process optimization, and testing for the three mineralization processes.

7.3. Experimental

7.3.1. Materials

The spiders under study were adult females of *Cupiennius salei* (Keyserling 1877). They were kept in different glass terrarium and fed with a weekly diet of *Blaptica dubia* or *Acheta domestica.* All the terrariums were set in the same room with controlled environmental parameters. Each terrarium was provided with a small refuge by considering the need of the spider to allow the animal to feel protected and live without stress, according to the Italian regulation on animal protection and EU Directive 2010/63/EU for animal experiments.

Phosphoric acid (H_3PO_4, purity 85 wt %) and calcium hydroxide ($Ca[OH]_2$, purity 95 wt %) were purchased from Sigma Aldrich (St. Louis, Missouri, USA). Synthetic HA powder was obtained from Riedel-de Haën (Seelze, Germany).

7.3.2. Silk sampling

Segment of dragline were collected from the spider *Cupiennius salei*, which produces it continuously during its walking around the terrarium. The dragline is a thread composed by two or three fibres and it is used by the spiders in order to not fall down from surfaces [43]. Silk samples were prepared by following the procedure reported by Blackledge *et al.* [203]. Briefly, specimens were stuck on a plastic holder provided with a window of 1cmx1cm and fixed with a double-sided tape.

7.3.3. Mineralization of Spider Silk

Each plastic holder containing the silk fibers was fixed on the bottom of a well in a 6-multiwell culture plate (Corning Costar, Corning, New York, USA) with masking tape. A basic suspension and an acidic solution were prepared by, respectively, dispersing $Ca(OH)_2$ and H_3PO_4 in milli-Q water (ASTM Type I ultrapure water, arium comfort; Sartorius GmbH, Göttingen, Germany) and kept under magnetic stirring. Reagent solutions with 1, 0.1, and 0.01 M concentration were prepared to perform three different reactions (Figure 7-1). For the HA deposition (1), used as control, the acidic and the basic solutions were mixed together under gentle magnetic stirring and let to stand for 30 min to initiate the HA crystal nucleation; the precursor solution was then poured into the well containing the silk fiber. In the biomineralization synthesis (2), silk fiber was covered with the $Ca(OH)_2$ suspension and the phosphoric solution was immediately added dropwise. The reversal biomineralization process (3) was performed by inverting the reagents order compared to process (2), thus dropping the basic suspension over the silk, previously immersed in the acidic solution. All the syntheses were performed at room temperature, and the reagent volume (5 mL) was calculated to ensure a Ca/P ratio of 1.67, typical of stoichiometric HA. The reaction product was kept under low mechanical shaking at 37 °C in incubator (M250-RH, MPM Instruments s.r.l., Bernareggio, Italy) for different maturation times (1, 3, or 7 days, Figure 7-1). The mineralized silk was subsequently removed from the well and washed with milli-Q water for two consecutive times to eliminate any synthesis debris and dried in stove (FP 53, Binder GmbH, Tuttlingen, Germany) at 40 °C for 1 h.

7.3.4. Morphological and Chemical Characterization of Mineralized Spider Silks

Silks surface morphology was examined by Scanning Electron Microscopy (SEM-FEI, Quanta 200, UK) operating at 5 kV. The evaluation of the crystals dimension was performed using an image processing software (Fiji, ImageJ)[204]. The elliptical shape of the crystals has been taken into account by measuring both the major and minor axis dimensions, with a minimum number of measurement n=30 per each image. Three different images for each mineralization process have been analyzed for the calculation of the average dimensions. Quantitative chemical microanalysis of the mineral phase was performed by Energy Dispersive X-ray Analysis (EDS-INCA Suite, Oxford Instruments, UK) with an accelerating voltage of 8 kV and working distance of 8 mm. All samples were coated with a layer of gold (18 nm of thickness, 60s, 20 mA) (Sputter Coater Q150TES, Quorum, Italy).

Fourier transform infrared spectrometer (FT-IR, Nicolet™ iS™5, Thermo Scientific™, USA) equipped with a monolithic diamond for attenuated total reflectance detection (iD7 ATR Thermo Scientific™, USA) was used to collect mid-IR spectra (400 to 4000 cm^{-1}, resolution of 4 cm^{-1}). Spectra analysis (Omnic™ Spectra Software, Thermo Scientific™, USA) were performed on (a) mineralized silks, (b) the residues of hydroxyapatite after biomineralization, (c) the raw spider silk and (d) a commercial hydroxyapatite powder, used as reference material.

The phase analysis of the synthesized HA was conducted by using an X-ray diffractometer (XRD, Bruker D8 Advance, Karlsruhe, Germany) equipped with a Lynx-eye position-sensitive detector (Cu Kα radiation, α = 1.54178 Å). XRD spectra were recorded at a step size (2θ) of 0.02◦ from 20° to 80◦ and a scan speed of 0.5 s.

7.3.5. Mechanical Tests

Tensile tests were carried out on silks produced with the optimized setup parameters using a nanotensile machine (T150 UTM, Agilent Technologies, Santa Clara, California, USA) with a cell load of 500 mN, nominal declared sensitivity of 10 nN for the load in the dynamic configuration. The displacement speed was 10 μm/s with a frequency load of 20 Hz. Before mounting the samples, the number of threads and the diameters of each specimen were measured with an optical microscope in order to compute the area of the total cross section involved. Sample holder was mounted between the clamps to keep the silk fibers parallel to the clamps and cut before the trials. At least 10 samples were tested for each silk type and the mean values (± SD) of strength (MPa), strain at break (mm/mm), toughness (MJ/m^3), and Young's modulus (GPa) were calculated from the stress–strain curves.

7.3.6. Statistical methods

Weibull statistics was performed for each set of data to obtain Weibull parameters, namely scale and shape parameters, through the maximum likelihood method [205]. Analyses were carried out using Mathematica® as processing software. Once the parameters were obtained, their relative probability distributions were plotted.

7.4. Results and Discussion

In the present study, two bio-inspired mineralization processes were performed to grow HA nano-crystals on native spider draglines and to develop a biomimetic hybrid material suitable for bone tissue regeneration. The process and the experimental parameters were optimized to achieve a controlled HA nucleation and a homogeneous coating. Due to the low availability and the reduced dimensions of the raw material (few μm in diameter), all steps required a fine control during the dragline manipulation. Reagent concentration and HA maturation time were evaluated, since they are known to affect crystal nucleation, size, morphology, orientation, as well as chemical composition and coating Homogeneity [33]–[36].

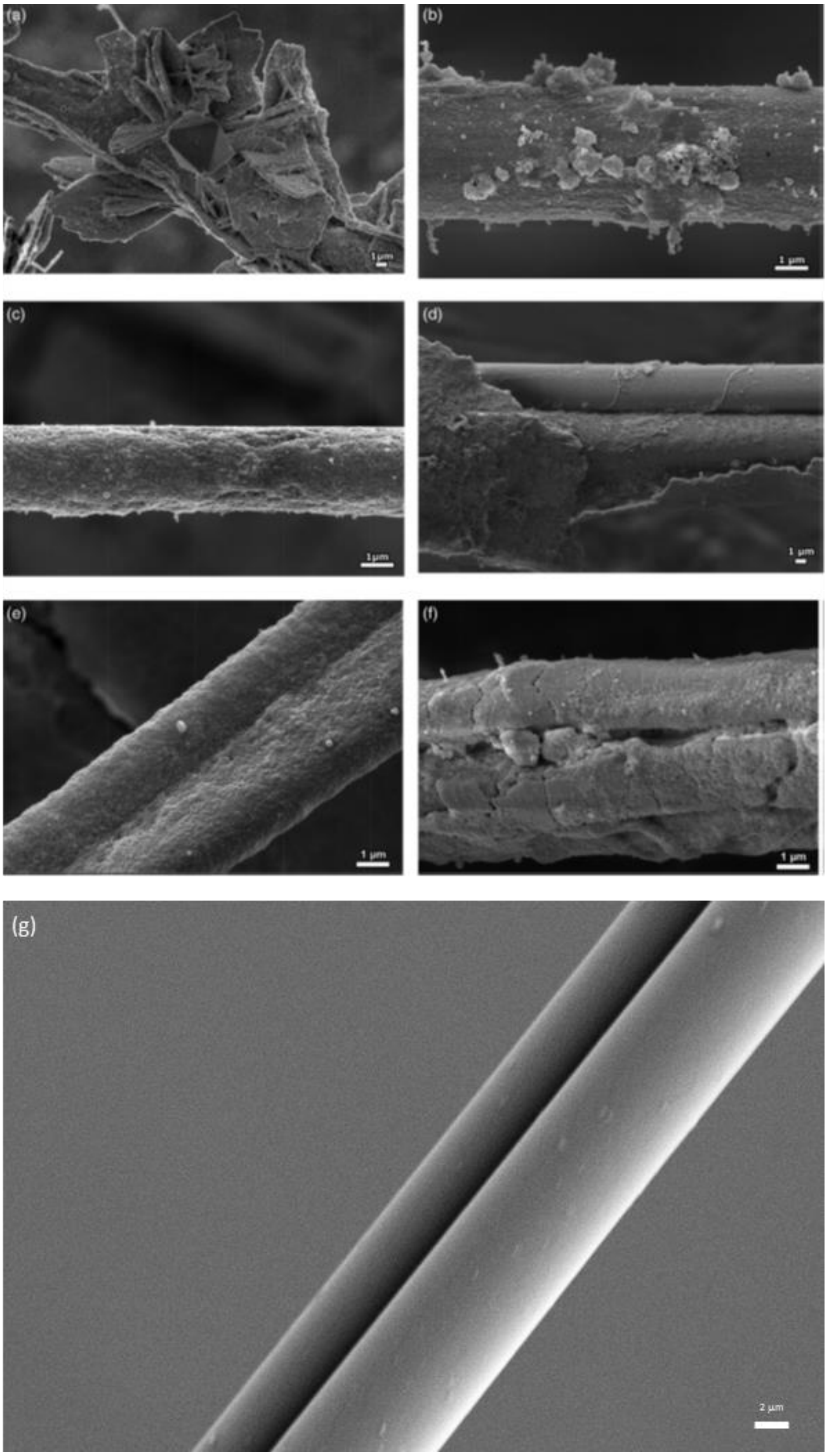

Figure 7-2: SEM images of spider silks mineralized using different process parameters. Silks mineralized by varying the reagent concentrations: (a) 1 M of reagent concentrations

(1 day of HA maturation, biomineralization protocol); (b) 0.1 M; and (c) 0.01 M (3 days of HA maturation time, reversal biomineralization). Silks mineralized by varying the HA maturation time: (d) 1 day (0.1 M of reagent concentrations, biomineralization), (e) 3 days and (f) 7 days (0.01 M of reagent concentrations, reversal biomineralization). (g) Native dragline of spider silk that was not treated.

7.4.1. *Evaluation of the Effect of Reagent Concentration, HA Maturation Time, and Mineralization Process on Silk Coating*

SEM was used to evaluate the coating homogeneity and the HA crystal features, confirming that the HA crystal nucleation depends on the concentration of free ions in the reaction medium and the incubation period. A reagent concentration of 1 M suddenly produced macroscopic HA aggregates on the well bottom after mixing the reagents and resulted in a nucleation of nonconfined micrometric calcium phosphate flakes [Figure 7-2(a)] due to the rapid consumption of calcium and phosphate ions from the reagent solution [38-40]. The aggregates resulted to be hard to wash and led to a breaking of specimens at any maturation time. Mineralized silks produced with 0.1 M of reagent concentration were characterized by local HA aggregates with a typical “cauliflower-like” morphology (dimension of a hundred of nanometers to few micrometers) and grape-like aggregates that determine a nonhomogeneous morphology [Figure 7-2(b)]. A reagent concentration of 0.01 M led to a homogeneous formation of HA nano-crystals over the entire fiber length, with crystals length lower than 100 nm [Figure 7-2(c)]. Analysing the effect of different incubation time (1, 3, and 7 days), SEM images after 1 day revealed the formation of a discontinuous layer of inorganic phase with partially melted crystals and the presence of micrometric aggregates while large parts of the silks remained completely bare [Figure 7-2(d)]. Three days resulted to be a sufficient incubation time to obtain a complete and homogeneous apatite layer over the fiber [Figure 7-2(e)] while an increase of the incubation time up to 7 days caused the growth of clusters of inorganic phases [Figure 7-2(f)].

Reagent concentrations of 0.1 and 0.01 M and 3 days of samples incubation were thus chosen as suitable variables to have uniform mineralization and minimize the formation of large inorganic aggregates. The morphological analysis performed on samples treated for 3 days with a 0.01 M reagent concentration showed that the 3 treatments produced a uniform inorganic coating composed of partially fused nano-crystals with rod-like shape and homogeneous thickness of few hundred micrometers [Figure 7-3(a,b)]. The calculated crystal average dimension resulted to be 61 ±13 nm, 46 ± 8 nm, and 62 ± 18 nm for HA deposition, biomineralization, and reversal biomineralization, respectively, with no statistically significant differences among the three methods [Figure 7-3(c)].

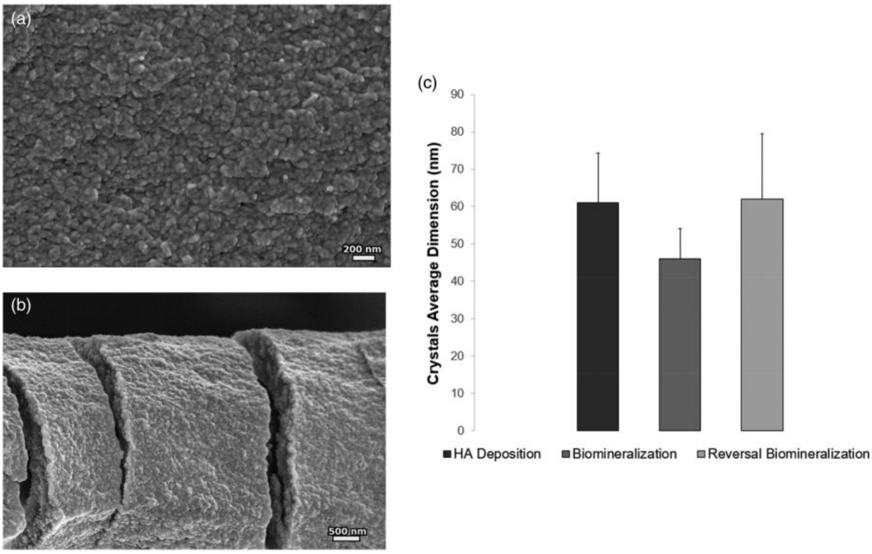

Figure 7-3: SEM images of mineralized silk (reversal biomineralization, reagent concentrations of 0.01 M, 3 days of HA maturation) show (a) the nucleation of a nanometric uniform coating and (b) its thickness in correspondence with the coating fracture. (c) Crystal average dimension has been calculated for the three mineralization processes.

Table 7-1: EDS Results of Ca/P Ratios for Mineralized Spider Silks (Reagent Concentrations of 0.1 and 0.01 M and HA Maturation Time of 3 days).

	Concentration	
	0.1 *M*	0.01 *M*
Process	Ca/P mean (atomic %)	
HA deposition	1.69 ± 0.12	1.68 ± 0.30
Biomineralization	1.81 ± 0.16	1.78 ± 0.30
Reversal biomineralization	1.63 ± 0.23	1.56 ± 0.12

7.4.2. EDS, FTIR ATR, and XRD Analyses

Elemental analyses were used to assess the calcium phosphate phase formation for silks processed with reagent concentrations of 0.1 and 0.01 M (3 days of HA maturation) via the three processes (Table 7-1). Results showed that the HA deposition leads to formation of a stoichiometric HA phase, confirmed by a Ca/P of about 1.67 for both the reagent concentrations tested while the biomineralization process induces the formation of a mineral phase with a Ca/P ratio biased toward the calcium (Ca/P higher than 1.67), revealing a preferential and faster binding of Ca^{2+} ions by the spider draglines [29,41,42].

Although no significant differences of crystal morphologies and sizes between the biomineralization and the reversal process were found (Figure 7-3), data from EDS analyses revealed that the reversal process entails a reduction of the calcium uptake from the silk, leading to a Ca/P ratio typical of nonstoichiometric, biomimetic calcium-deficient HA (with a Ca/P ratio of 1.50–1.67) [39,43].

FTIR ATR spectra of both commercial HA powder (control) and HA residues from the biomineralization process [Figure 7-4(a), spectra a and b] showed peaks at 600 cm^{-1}, typical of PO_4^{3-} bending mode, and peaks at about 960, 1000, and 1090 cm^{-1}, assigned to the PO_4^{3-} stretching mode, confirming the highly crystalline HA phase of the synthesis residues. The native spider spectrum [spectrum c in Figure 7-4(a)] revealed the presence of amide III (1230 cm^{-1}), amide II (1500–1560 cm^{-1}), amide I (1620–1690 cm^{-1}), and amide A (at about 3280 cm^{-1}). The presence of the characteristic apatite peaks in the mineralized silk spectra proved that a successful nucleation of HA occurred for all the mineralization processes [44–46] [Figure 7-4(a), spectra d, e and f]. According to the EDS analyses, the biomineralization and reversal biomineralization processes led to a broadening of the apatite peaks compared to both HA residues and HA deposition spectra, suggesting the role of spider silk as a template for the growth of a biomimetic low-crystalline HA coating. The remaining bands are ascribed to spider silk, as shown by the raw material spectrum [47-49].

To confirm the chemical composition of the mineral phase, XRD analysis was performed on the reaction powders obtained from the biomineralization process (0.01 M reagent concentration) after 1 day of maturation. The XRD pattern exhibited a scarcely crystalline profile of the mineral phase, with broad undulations and few discrete peaks, in good agreement with EDS and FTIR results [Figure 7-4(b)]. The diffraction peaks resulted to be typical of a calcium phosphate HA according to the main lattice reflections of the JCPDS-ICDD file (Card # 09-0432).

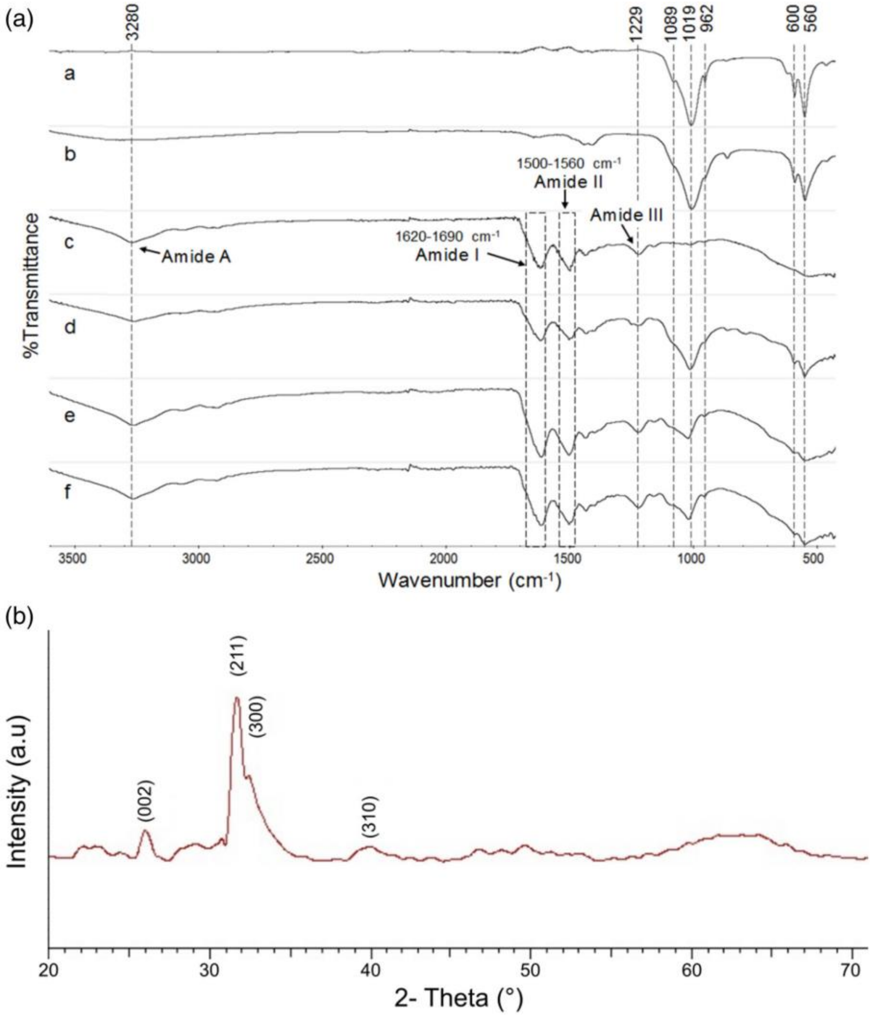

Figure 7-4: (a) FTIR spectra of (a) commercial HA powder, (b) HA residue of synthesis, (c) raw material (native spider silk dragline), (d) silks mineralized by HA deposition, (e) silks mineralized by biomineralization (neutralization process), and (f) silks mineralized by reversal biomineralization. (b) XRD pattern of HA powder nucleated by biomineralization.

Table 7-2: Measured and Computed Mechanical Properties of Raw Spider Silk, Supercontracted Spider Silk, and Mineralized Spider Silk (0.01 M of Reagent Concentrations, 3 days of HA Maturation).

Process	Strength (MPa)	Strain at break (mm/mm)	Toughness (MJ/m^3)	Young's modulus (GPa)	Weibull scale parameter (MPa)	Weibull shape parameter
Raw material	580 ± 520	0.27 ± 0.03	110 ± 120	8.5 ± 7.1	620	1.2
Supercontracted	190 ± 190	0.41 ± 0.25	57 ± 59	2.9 ± 4.6	162	1.4
HA deposition	160 ± 100	0.32 ± 0.17	38 ± 23	2.5 ± 1.7	156	1.4
Biomineralization	150 ± 120	0.44 ± 0.27	57 ± 49	4.6 ± 2.7	161	1.4
Reversal biomineralization	120 ± 90	0.45 ± 0.25	41 ± 39	2.3 ± 1.5	135	1.5

7.4.3. Mechanical Properties

Uniaxial tensile tests were performed on specimens from all groups (silks treated by HA deposition, biomineralization, and reversal biomineralization), mineralized with a reagent concentration of 0.01 M and 3 days of HA maturation. Raw material (untreated spider silk) and supercontracted silk, obtained by maintaining the samples in wet conditions overnight at room temperature and 100% of saturated humidity, were used as controls. The data revealed that mineralization of spider silks leads to a reduction of the strength, toughness, and Young's modulus and to an increase of strain at break compared to the raw material, a behavior that can be mainly attributed to the silk supercontraction (Table 7-2, Figure 7-5).

The strength of silks, that is, the stress just before thread's fracture, resulted in a reduction from 580 ± 520 MPa of the untreated silk to less than 200 MPa for supercontracted and mineralized silks, with similar values for the three mineralization processes. The interaction with water is responsible for silk supercontraction, a phenomenon that affects the morphological, physical, and mechanical properties of spider silk [50-52], with a reduction of strength caused probably by the annihilation and reorganization of silk hydrogen bonds in contact with water molecules [53,54]. The presence of an inorganic coating could also contribute in reducing the strength because of an increase of the fiber diameter compared to the raw material.

Supercontraction is also responsible for the increase of strain at break and the reduction of Young's modulus. This is due to the fact that during hydrogen bond annihilation, there is an increase of entropic elasticity, which increases the tangle status of the molecules [55,56]. This trend was similar for HA deposition and reversal biomineralization. In fact, silk shrinking determines the formation of more elastic fibers [57] while apatite is a ceramic material characterized by a brittle mechanical behavior, with low toughness and low resistance to load bearing in comparison with flexible materials [58-60].

The analysis of the Weibull statistics shown that the mineralization process leads to a homogenization of the fracture behavior [Figure 7-5(b)] that could be correlated to the recovery of fibers after the mineralization process [56,61–63]. Shape parameters between 1.4 and 1.5 were obtained for all the supercontracted and mineralized samples, with a narrower probability distribution compared to the raw material, so the fracture behavior is expected to be more deterministic. The reduction of the Weibull scale parameter indicates a decrease in strength according to the analysis of the stress–strain curves. Namely, the mineralization process reduces the scale parameter from 620 (native silk) to 156, 161, and 135 MPa for the

HA deposition, biomineralization, and reversal biomineralization, respectively.

Although the supercontraction affects notably the mechanical behavior of native silk, mineralized silks still present performances comparable to many natural and artificial fibers with remarkable mechanical properties [64]. Furthermore, the hybrid composite shows mechanical properties comparable to that of natural bone in terms of strength and elastic modulus [65] and superior to many natural and synthetic biomaterials used in bone TE [66,67].

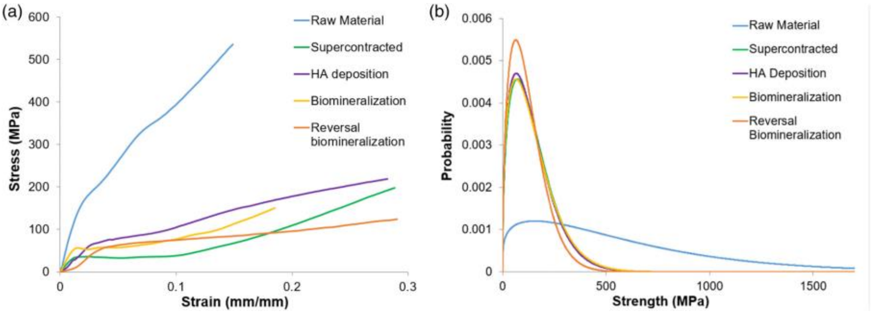

Figure 7-5: (a) Stress–strain curves and (b) Weibull probability distribution of the raw material, supercontracted silk, and mineralized spider silks.

7.5. Conclusion

This study demonstrated that native spider silk can be coated with a nanostructured mineral layer by tuning neutralization process parameters to get a reproducible and effective surface functionalization. Two different bio-inspired neutralization processes were performed, and the mineralized silks were compared to raw material, supercontracted silks, and samples produced by simple HA deposition. Morphological analyses revealed that the use of 0.01 M of reagent concentration and 3 days of apatite maturation led to a homogeneous and thin coating of HA nano-crystals. FTIR and XRD spectra confirmed the nucleation of a lowcrystalline HA phase onto spider silk, and data from EDS demonstrated that the reversal biomineralization conveyed the nucleation of biomimetic, poorly crystalline, and nonstoichiometric HA. Mechanical results revealed that silk supercontraction is mainly responsible for a reduction in elasticity, strength, and toughness of mineralized silks, nevertheless ensuring outstanding mechanical properties, comparable to those of human bone.

In summary, the fine tuning of biomineralization parameters led to the controlled nucleation of biomimetic HA onto native spider silk while maintaining good mechanical performances, making this hybrid biomaterial interesting for bone TE applications. Biological in vitro tests and the design of scaffolds that incorporate biomineralized spider silk for enhancing mechanical properties while providing a biomimetic interface will be pursued in future studies.

7.6. References

1. Kaplan, D. L.; Lombardi, S. J.; Muller, W. S.; Fossey, S. A. Biomaterials; Palgrave Macmillan UK: London, UK, 1991; p. 53.
2. Altman, G. H.; Diaz, F.; Jakuba, C.; Calabro, T.; Horan, R. L.; Chen, J.; Lu, H.; Richmond, J.; Kaplan, D. L. Biomaterials. 2003, 24, 401.
3. Mirahmadi, F.; Tafazzoli-Shadpour, M.; Shokrgozar, M. A.; Bonakdar, S. Mater. Sci. Eng. C. 2013, 33, 4786.
4. Eisoldt, L.; Smith, A.; Scheibel, T. Mater. Today. 2011, 14, 80.
5. Mackenzie, D. Med. Hist. 1973, 17, 158.
6. Dhandayuthapani, B.; Yoshida, Y.; Maekawa, T.; Kumar, D. S. Int. J. Polym. Sci. 2011, 2011, 290602.
7. Kim, U.-J.; Park, J.; Li, C.; Jin, H.-J.; Valluzzi, R.; Kaplan, D. L. Biomacromolecules. 2004, 5, 786.
8. Vepari, C.; Kaplan, D. L. Prog. Polym. Sci. 2007, 32, 991.
9. Kundu, J.; Chung, Y.-I.; Kim, Y. H.; Tae, G.; Kundu, S. C. Int. J. Pharm. 2010, 388, 242.
10. Elsner, M. B.; Herold, H. M.; Müller-Herrmann, S.; Bargel, H.; Scheibel, T. Biomater. Sci. 2015, 3, 543.
11. Jao, D.; Mou, X.; Hu, X. J. Funct. Biomater. 2016, 7, 22.
12. Kim, H. J.; Kim, U.-J.; Kim, H. S.; Li, C.; Wada, M.; Leisk, G. G.; Kaplan, D. L. Bone. 2008, 42, 1226.
13. Shi, P.; Teh, T. K. H.; Toh, S. L.; Goh, J. C. H. Biomaterials. 2013, 34, 5947.
14. Rising, A.; Widhe, M.; Johansson, J. Cell. Mol. Life Sci. 2011, 68, 169.
15. Cranford, S. W.; Tarakanova, A.; Pugno, N. M.; Buehler, M. J. Nature. 2012, 482, 72.
16. Yang, Y.; Greco, G.; Maniglio, D.; Migliaresi, C.; Pugno, N.; Motta, A. Mater. Sci. Eng. C. 2019, 107, 110197.
17. Schacht, K.; Scheibel, T. Curr. Opin. Biotechnol. 2014, 29, 62.
18. Hardy, J. G.; Torres-Rendon, J. G.; Leal-Egaña, A.; Walther, A.; Schlaad, H.; Cölfen, H.; Scheibel, T. R. Materials (Basel). 2016, 9, 560.
19. Rising, A.; Johansson, J. Nat. Chem. Biol. 2015, 11, 309.

20. Andersson, M.; Jia, Q.; Abella, A.; Lee, X.-Y.; Landreh, M.; Purhonen, P.; Hebert, H.; Tenje, M.; Robinson, C. V.; Meng, Q. Nat. Chem. Biol. 2017, 13, 262.
21. Bhattacharjee, P.; Kundu, B.; Naskar, D.; Kim, H.-W.; Maiti, T. K.; Bhattacharya, D.; Kundu, S. C. Acta Biomater. 2017, 63, 1.
22. Yang, M.; He, W.; Shuai, Y.; Min, S.; Zhu, L. J. Polym. Sci. Part B Polym. Phys. 2013, 51, 742.
23. Thavornyutikarn, B.; Chantarapanich, N.; Sitthiseripratip, K.; Thouas, G.; Chen, Q. Prog. Biomater. 2014, 3, 61.
24. Tampieri, A.; Celotti, G.; Landi, E.; Sandri, M.; Roveri, N.; Falini, G. J. Biomed. Mater. Res. Part A. 2003, 67, 618.
25. Stevens, B.; Yang, Y.; Mohandas, A.; Stucker, B.; Nguyen, K. T. J. Biomed. Mater. Res. Part B Appl. Biomater. 2008, 85, 573.
26. Palmer, L. C.; Newcomb, C. J.; Kaltz, S. R.; Spoerke, E. D.; Stupp, S. I. Chem. Rev. 2008, 108, 4754.
27. Stupp, S. I.; Ciegler, G. W. J. Biomed. Mater. Res. Part A. 1992, 26, 169.
28. Nayak, A. K. Int. J. ChemTech Res. 2010, 2, 903.
29. Cao, B.; Mao, C. Langmuir. 2007, 23, 10701.
30. Dmitrovic, S.; Jokic, B.; Prekajski, M.; Pantic, J.; Zmejkoski, D.; Zarubica, A.; Matovic, B. Process. Appl. Ceram. 2016, 10, 37.
31. Greco, G.; Pantano, M. F.; Mazzolai, B.; Pugno, N. M. Sci. Rep. 2019, 9, 5776.
32. Blackledge, T. A.; Swindeman, J. E.; Hayashi, C. Y. J. Exp. Biol. 2005, 208, 1937.
33. Schindelin, J.; Arganda-Carreras, I.; Frise, E.; Kaynig, V.; Longair, M.; Pietzsch, T.; Preibisch, S.; Rueden, C.; Saalfeld, S.; Schmid, B.; Tinevez, J. Y.; White, D. J.; Hartenstein, V.; Eliceiri, K.; Tomancak, P.; Cardona, A. Nat. Methods. 2012, 9, 676.
34. Peterlik, H. J. Mater. Sci. 1972, 1995, 30.
35. Cazalbou, S.; Combes, C.; Eichert, D.; Rey, C.; Glimcher, M. J. J. Bone Miner. Metab. 2004, 22, 310.
36. Jongprateep, O.; Nueangjumnong, C., In Proceedings of the International Conference on Advanced Materials, Structures and Mechanical Engineering; 2016; pp 251.
37. Nancollas, G. H.; Mohan, M. S. Arch. Oral Biol. 1970, 15, 731.
38. Jin, Y.; Kundu, B.; Cai, Y.; Kundu, S. C.; Yao, J. Colloids Surfaces B Biointerfaces. 2015, 134, 339.
39. Dorozhkin, S. V. Materials (Basel). 2009, 2, 1975.
40. Lluch, A. V.; Ferrer, G. G.; Pradas, M. M. Colloids Surfaces B Biointerfaces. 2009, 70, 218.

41. Thiel, B. L.; Kunkel, D. D.; Viney, C. Biopolymers. 1994, 34, 1089.
42. Kino, R.; Ikoma, T.; Monkawa, A.; Yunoki, S.; Munekata, M.; Tanaka, J.; Asakura, T. J. Appl. Polym. Sci. 2006, 99, 2822.
43. Bohner, M. Injury. 2000, 31, D37.
44. Hooshmand, T.; Abrishamchian, A.; Najafi, F.; Mohammadi, M.; Najafi, H.; Tahriri, M. J. Compos. Mater. 2014, 48, 483.
45. Gheisari, H.; Karamian, E.; Abdellahi, M. Ceram. Int. 2015, 41, 5967.
46. Kede, M. L. F. M.; Mavropoulos, E.; da Rocha, N. C. C.; Costa, A. M.; da Silva, M. H. P.; Moreira, J. C.; Rossi, A. M. Surf. Coatings Technol. 2012, 206, 2810.
47. Papadopoulos, P.; Sölter, J.; Kremer, F. Eur. Phys. J. E. 2007, 24, 193.
48. Dong, Z.; Lewis, R. V.; Middaugh, C. R. Arch. Biochem. Biophys. 1991, 284, 53.
49. Slotta, U.; Tammer, M.; Kremer, F.; Koelsch, P.; Scheibel, T. Supramol. Chem. 2006, 18, 465.
50. Saravanan, D. J. Text. Apparel, Technol. Manag. 2006, 5, 1.
51. Work, R. W. Text. Res. J. 1977, 47, 650.
52. Boutry, C.; Blackledge, T. A. J. Exp. Biol. 2013, 216, 3606.
53. Tokareva, O.; Jacobsen, M.; Buehler, M.; Wong, J.; Kaplan, D. L. Acta Biomater. 2014, 10, 1612.
54. Nova, A.; Keten, S.; Pugno, N. M.; Redaelli, A.; Buehler, M. J. Nano Lett. 2010, 10, 2626.
55. Berardo, A.; Pantano, M. F.; Pugno, N. M. Interface Focus. 2016, 6, 20150060.
56. Liu, Y.; Shao, Z.; Vollrath, F. Nat. Mater. 2005, 4, 901.
57. Bell, F. I.; McEwen, I. J.; Viney, C. Nature. 2002, 416, 37.
58. Yan, W.-Q.; Nakamura, T.; Kawanabe, K.; Nishigochi, S.; Oka, M.; Kokubo, T. Biomaterials. 1997, 18, 1185.
59. Johnson, A. J. W.; Herschler, B. A. Acta Biomater. 2011, 7, 16.
60. Ramesh, N.; Moratti, S. C.; Dias, G. J. J. Biomed. Mater. Res. Part B Appl. Biomater. 2017, 106, 2046.
61. Pérez-Rigueiro, J.; Elices, M.; Guinea, G. V. Polymer (Guildf). 2003, 44, 3733.
62. Elices, M.; Plaza, G. R.; Pérez-Rigueiro, J.; Guinea, G. V. J. Mech. Behav. Biomed. Mater. 2011, 4, 658.
63. Agnarsson, I.; Dhinojwala, A.; Sahni, V.; Blackledge, T. A. J. Exp. Biol. 2009, 212, 1990.
64. Gosline, J.; Lillie, M.; Carrington, E.; Guerette, P.; Ortlepp, C.; Savage, K. Philos. Trans. R. Soc. B Biol. Sci. 2002, 357, 121.

65. Mow, V. C.; Huiskes, R. Basic Orthopaedic Biomechanics & Mechano-Biology; Lippincott Williams & Wilkins: Philadelphia, PA, USA, 2005.
66. Sabir, M. I.; Xu, X.; Li, L. J. Mater. Sci. 2009, 44, 5713. 67. Woodard, J. R.; Hilldore, A. J.; Lan, S. K.; Park, C. J.; Morgan, A. W.; Eurell, J. A. C.; Clark, S. G.; Wheeler, M. B.; Jamison, R. D.; Wagoner Johnson, A. J. Biomaterials. 2007, 28, 45.

8. LEARNING FROM SILKWORM SILK: EASY, SCALABLE, ROBUST, MICROPATTERNED SILK FIBROIN CELL SUBSTRATES

Spider silks are materials that are commonly associated to silkworm silk. The latter, is more common in silk community since its availability in large amount. Moreover, the practices in handling silkworms are easier with respect to the common practices in dealing with web building spiders[1]. This has led silkworm silk, during these decades, to practical outcomes that barely are thought for spiders silk[2]. In medicine, for example, the usability of silkworm silk has been continuously validated demonstrating its leading role in biomedical materials[3–5].

Thus, scientists have developed protocols and technologies that are not yet appliable on spider silk. Unfortunately, the ecologic impact of silkworm silk has to be improved[6] and this is why the production of spider silk from genetically modified organisms is needed[7].

Given a solution of silkworm silk, we have produced films for in-body applications. We hope that the technique developed in this work can be extended to spider silk.

This chapter is based, thus, on the paper that we published in Advanced Materials Interfaces (1801822, 2019, DOI: 10.1002/admi.201801822). This paper is here reprinted with the permission of © 2019 WILEY-VCH Verlag GmbH & Co. KGaA, Weinheim (License number: 4635440485608). For the sake of shortness, the reader may find the supplementary information in the original paper.

Goal of the chapter: The chapter aims to give a simple protocol to develop and design biomedical devices based on silk. The promising mechanical properties and the capability to tune the biological ones are here presented as a key for future investigation on similar spider silk related systems.

8.1. Abstract

Thin polymeric films are being explored for biomedical uses such as drug delivery, biofiltration, biosensors, and tissue regeneration. Of specific interest is the formation of mechanically flexible sheets, which can be formed with controllable thickness for sealing wounds, or as biomimetic cellular constructs. Flexible substrates with precise micro- and nanopatterns can function as supports for cell growth with conformal contact at the biointerface. To date, approaches to form free-standing, thin sheets are limited in the ability to present patterned architectures and

micro/nanotextured surfaces. Other materials have a lack of degradability, precluding their application as cellular scaffolds. An approach is suggested using biocompatible and biodegradable films fabricated from silk fibroin. This work presents the fabrication and characterization of flexible, micropatterned, and biodegradable 2D fibroin sheets for cell adhesion and proliferation. A facile and scalable technique using photolithography is shown to fabricate optically transparent, strong, and flexible fibroin substrates with tunable and precise micropatterns over large areas. By controlling the surface architectures, the control of cell adhesion and spreading can be observed. Additionally, the base material is fully degradable via proteolysis. Through mechanical control and directing the adherent cells, it is possible to explore interactions of cells and the microscale geometric topography.

8.2. Introduction

Thin polymeric films have long been used in industry for semiconductor applications, electronics packaging, as optical coatings, diffusion barriers, friction reduction, etc.[8] Recently, such films and sheets have been explored for biomedical uses such as drug delivery, biofiltration, biosensors, wound healing, and tissue regeneration.[9] Of specific interest are flexible, free-standing sheets, which can be formed with controllable thickness (ultrathin (tens of nanometers) to thin (few to tens of micrometers)). Sheets with mechanical flexibility and adhesiveness may be suitable for sealing wounds, or for the development of biomimetic cellular constructs. They can be stacked to form functional 3D tissues to form cell sheets as biomembranes or tissue/organ models.[10] They can also be used as substrates for wearable devices, soft robotics, and smart skins.[11] At the nanoscale thickness, such films can directly conform to the underlying surface, whereas at the microscale, adhesive layers may be needed for attachment to tissue.[12]

Integrating thin films as dynamic cell culture platforms is of great interest because of applications in biosensing, regenerative medicine, and soft robotics.[13] Cell culture substrates capable of physically supporting cell growth with topographical and spatial cellular control can provide insight into the dynamics of cell interactions, while forming scaffolds and cell-based biosensors.[13] A significant effort has been directed toward cellular micropatterning and organization.[14] Spatial positioning of cells has been achieved using different techniques including patterning nonfouling chemistries (or complementarily, patterning of cell-attachment chemistries[15]), plasma etching,[16] microfluidic patterning,[17] photolithography,[18] soft lithography,[19] inkjet printing,[20] and microcontact printing.[21] In addition, functionalization of the surface of substrates with proteins and enzymes has also been used to promote cell adhesion for orthopedic applications.[22] However, it is often challenging to adapt these approaches beyond rigid or stiff substrates to flexible, mechanically robust sheets. Flexible substrates with precise micro- and nanopatterns can function as supports for cell growth, resulting in ordered and functional cell sheets that may be implanted, with conformal contact at the biointerface.[23]

Flexible sheets may be formed using various techniques including casting elastomeric or intrinsically flexible materials, electrospinning, or by using spin coating or layer-by-layer assembly.[9c] Paper has also recently attracted attention due to its porosity and flexibility, while permitting modifications of physical and chemical properties.[24] Electrospinning to form micro- and nanofibrous architectures can form sheets (e.g., fiber mats) from a variety of synthetic and natural materials.[25] However, imparting the additional property of patterned architectures (micro/nanotextured surface) has been limited, particularly over large areas (e.g., centimeter).[26] Elastomers such as polydimethylsiloxane (PDMS) and polyurethanes have been used with favorable properties including high optical transparency, ability to form micropatterns, and control of stiffness.[27] Despite good biomimetic characteristics and tunable mechanical properties, these materials have high surface hydrophobicity, limited aqueous processing, and, importantly, a lack of degradability, which precludes their application as cellular scaffolds.

Recently, approaches toward forming flexible, micro- and nanopatterned substrates have been reported. Using pNIPAM as a sacrificial layer, thin polystyrene (PS) films were spin-coated and stamped with cell adhesive carbon nanotube–fibronectin composites using microcontact printing (μCP) to guide C2C12 skeletal myoblasts.[28] Ultrathin poly(methyl methacrylate) (PMMA) films were formed using a similar spin-coating procedure and micropatterned with cell-adhesive poly(l-lysine) using inkjet printing.[29] However, both PS and PMMA are nonbiodegradable polymeric materials, limiting their applications. Using degradable polymers such as poly(lactic acid) (PLA),[30] chitosan, and alginate,[31] free-standing films have been reported. An important report using self-assembled chitin nanofiber substrates micropatterned using replica molding for engineered cell sheets was shown.[32] These flexible substrates are biodegradable, mechanically strong, and can be manipulated into desired shapes. However, stamping procedures have limitations that can affect pattern resolution and reproducibility including deformation scalability over large areas, and ink mobility to unwanted regions.[33] Nonetheless, these interesting studies have shown the way for forming flexible, micropatterned sheets for various applications.

Herein, an approach is suggested using silk protein films. Silk as a natural biopolymer to fabricate various geometries to support the cell regeneration and tissue repair has been widely examined for the past few decades.[34] The silk protein fibroin possesses high mechanical strength and flexibility, optical transparency, biocompatibility, low immunogenicity, permeability to water and oxygen, and, importantly, biodegradability.[35] Fibroin, either by itself, or in conjunction with other materials, has been electrospun into films and mats for cell culture.[36] Micropatterned silk films prepared by molding were earlier reported.[37] In these experiments, different surface groove patterns were prepared from optically graded glass substrates followed by casting poly(dimethylsiloxane) replica molds. However, patterns that can be formed are not easily scalable and cannot recapitulate complex designs owing to the need to form transfer molds. In earlier work, our group reported the use of biochemically modified silk proteins (fibroin and sericin) that behave as negative tone photoresists for optical, electrochemical, and biomedical applications.[38] In these forms, silk proteins can be micropatterned using a facile, benchtop photolithographic technique, allowing the formation of microarchitectures on rigid or flexible substrates. High resolution at micro- and nanoscales, high throughput, and excellent reproducibility are achievable.

In this study, we demonstrate flexible, strong, micropatterned, and biodegradable 2D silk fibroin sheets for the adhesion and proliferation of cells. We show a rapid and scalable technique using photolithography to fabricate optically transparent, flexible fibroin substrates with tunable and precise micropatterns over large areas. To the best of our knowledge, this is the first report of a flexible, micropatterned cell culture substrate using photolithography combined with degradable natural or synthetic biopolymers. By controlling the surface architectures of these flexible sheets, the control of cell adhesion and spreading can be observed. The technique presented in this study is simple, requiring no clean room or strong reagents, and permits rapid engineering of mechanically robust sheets with a variety of topographic features and length scales. Since the structures are formed independently of the substrates, it is possible to form surface patterns of different mechanical properties from the underlying support. Additionally, since the base material is fully degradable via proteolysis, it provides a promising platform for the formation of cell sheets. Through mechanical control and directing the adherent cells, we can further explore the interactions of the cells and the microscale geometric topography.

8.3. Results and Discussion

8.3.1. Fabrication of Flexible, Micropatterned Fibroin Films

Mechanically flexible, biocompatible sheets present platforms for applications as surface biosensors, soft robotics, drug delivery vehicles, sealing of wounds, and tissue scaffolds. [9c] The presence of micropatterns can further provide opportunities to direct the behavior of cells or control cell morphology in situ.[39] To date, micropatterned films have been shown on rigid or supported formats (for instance, with an underlying glass or polystyrene substrate) or using flexible materials that are not degradable (e.g., PDMS). The development of flexible, and micropatterned films and membranes using degradable biopolymers has been limited.[31] In this work, microfabrication of flexible, silk fibroin films is realized using light-reactive conjugates and facile photolithographic techniques.[38] These conjugates can be used as stable, biodegradable, and biocompatible substrates on which patterns are formed. Previously, patterns of sericin were shown on flexible fibroin substrates, which could be accomplished since the two are soluble in different solvents (viz. sericin in water, fibroin in formic acid or HFIP). Here, we utilize fibroin as the material comprising both the substrate and the pattern. The use of photolithography provides a rapid route to form complex patterns that are not easily prepared using microcontact printing or molding.[37]

Initially, a solution of photo-crosslinkable silk fibroin in formic acid with a suitable photoinitiator was cast on a plain glass slide (1 cm2 area) and crosslinked by exposure under 365 nm UV light (Figure 8-1). The use of formic acid as a solvent allows us to form large scale, thin, flat, and stable fibroin films in an environmentally friendly process. [38b] These films are formed by crosslinking of the protein and not by a change in β-sheet conformation as shown in other works. [39,40] The UV crosslinked fibroin sheets formed are water insoluble and are stable in a wide range of solvents. Due to the absence of chemical linkage between the film and the glass support, the crosslinked fibroin sheet can be easily peeled off when immersed in water. The thickness of the film plays a defining role in its flexibility, and films ranging from hundreds of nanometers to tens of micrometers are easily formed by controlling the amount of fibroin/formic acid solution cast and the spin-coating speed. For example, 60 µL of fibroin solution cast on a plain glass slide of area 1 cm2 produces films with a thickness ≈10 µm at a spin speed of 800 rpm.

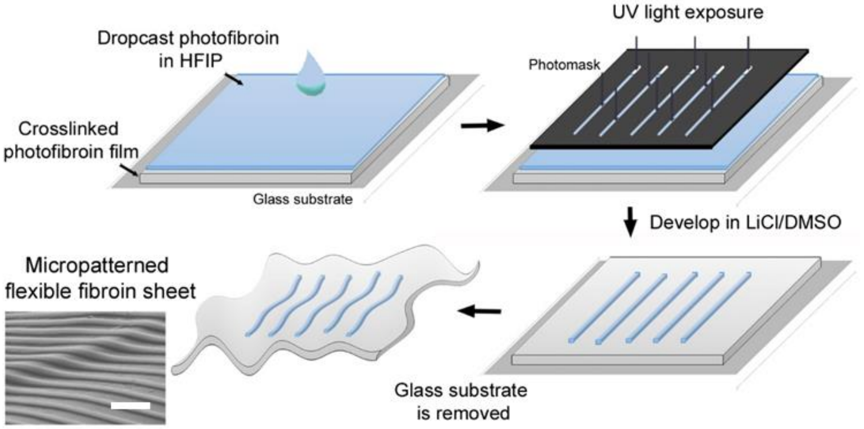

Figure 8-1: Fabrication of micropatterned flexible fibroin films via photolithography. Scale bars = 100 µm

To fabricate microarchitectures of silk fibroin photoresist on fibroin films, a 5% w/v solution in HFIP was cast on silk fibroin sheets prepared as described above. The presence of residual acrylate functional groups on the surface of the films enables the covalent attachment of patterns on them. This implies that the patterns do not delaminate when the film is subjected to mechanical deformation. Patterns are formed by exposure to 365 nm UV through a photomask (Figure 8-1). The area exposed by the UV light is crosslinked while, the unexposed areas dissolve when immersed in 1 m of LiCl in DMSO. A wide range of patterns with different shape, size, and complexity can be obtained depending on the nature of the photolithographic mask used. The use of a single material for the fabrication of the substrate and the patterns allows us to form microarchitectures of high stability due to the presence of the same chemistry. Due to the volatility of HFIP, a solution of photofibroin in HFIP can be cast on the fibroin films without disrupting the underlying film. This demands precise control over the amount of solution drop cast on the fibroin films and drying time prior to UV exposure for patterning. 30 μL of FPP/HFIP solution for a fibroin film of area 1 cm2 and a drying time of ≈5 min was found to be optimum for the results shown here. Once they are immersed for development, the entire structure can be delaminated from the glass support to form mechanically flexible films (Figure 8-2a). The images obtained from an optical microscope show the ability to form ordered patterns of various complexities over a large area (centimeter scale) of flexible fibroin sheet (Figure 8-2b,c). Thin, moist films can be applied to and readily conform to irregular surfaces (e.g., skin) without the need for any adhesive (Figure 8-2d). The films can also be attached in a dry condition to a curved surface (Figure S1, Supporting Information).

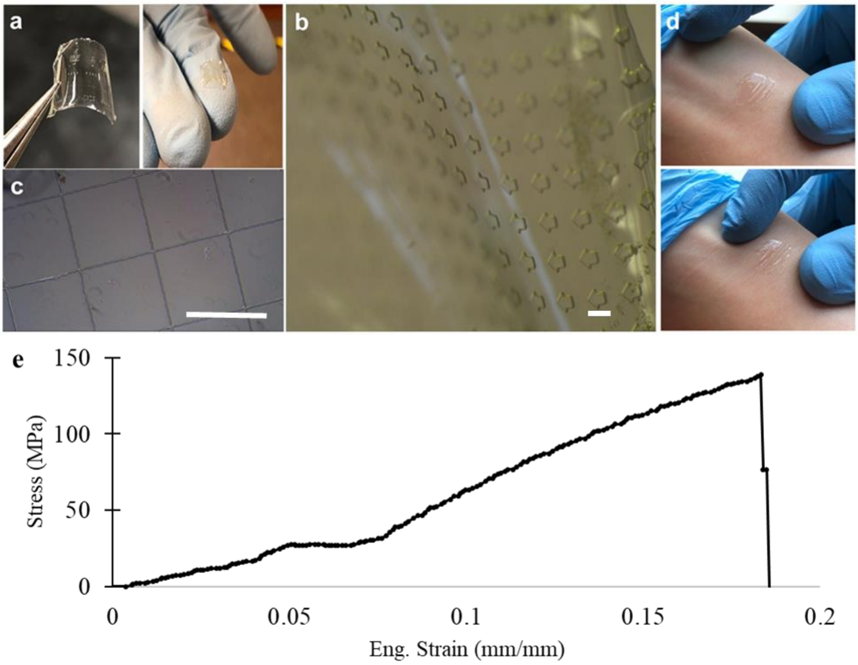

Figure 8-2: a) Mechanically stable micropatterned films formed by photolithography. Large area films can be patterned with microscale architectures b). c) Optical image of the films shown after sterilization with 70% ethanol. d) Ultrathin micropatterned films (<1 µm) can be easily applied to soft surfaces (e.g., skin) without any adhesive—shown in stretched and squeezed forms. e) Stress–strain curve of the substrate (dry condition), showing a strength >100 MPa. Scale bars = 500 µm

The micropatterned films are mechanically robust (strength > 100 MPa, Figure 8-2e) and can be held, rolled, or bent into various conformations numerous times without any loss in their chemical and physical properties. A video showing the tensile behavior of the films is provided in the Supporting Information. The films are stronger than the earlier reported micropatterned chitosan films.[32] To demonstrate the structural integrity and scalability at the microscale, optical and scanning electron microscopy (SEM) images were taken. The SEM images (Figure 8-3) depict the high fidelity and spatial and structural resolution of the micropatterns as lines or dots. Due to the vinyl linkage between the patterns and the substrate, a strong adhesion is observed at the interface and the structures are intact even in bent conditions. In Figure 8-3c,d, the film was examined before and after conducting several (≈10 times) extreme 180° bends. While some minor cracks may be seen on the film at the bend junction, the patterns themselves do not delaminate, demonstrating the high robustness of this system. This can be correlated to the differences in terms of Young’s modulus between the softer pattern and the stiffer substrate (Figure 8-4a–c) which are observed under nanoindentation. Under mechanical deformation, the former is thus more flexible with respect to the latter, adapting itself to the deformation of the substrate. The load–displacement curves obtained by nanoindentation of the patterned films and spatial distribution of the surface mechanical properties are presented in Table S1 and Figures S2 and S3 in the Supporting Information.

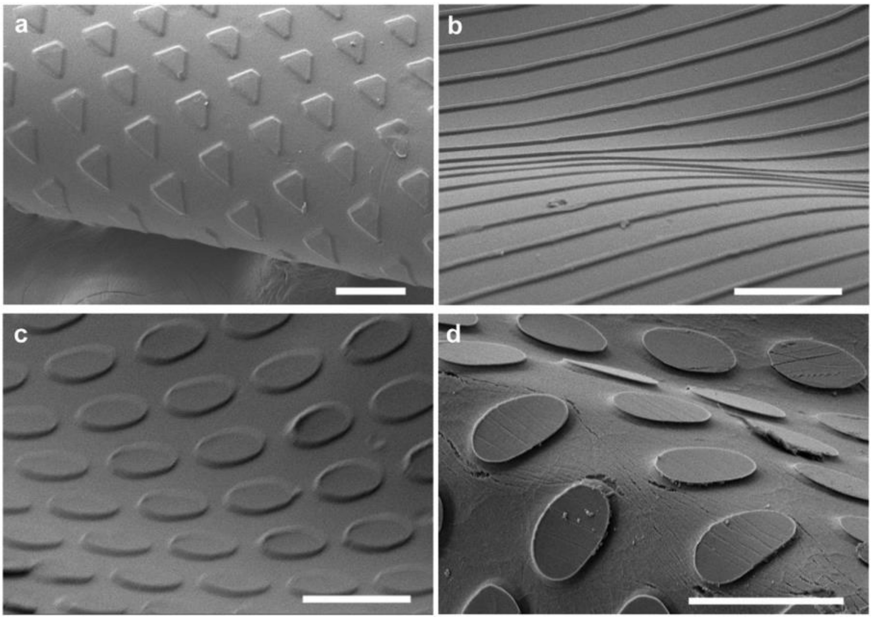

Figure 8-3: SEM images of the different forms of flexible microstructured films of silk fibroin fabricated by photolithography a) films can be fully rolled, b) different kinds of surface architectures are easily patterned using different photomasks. Image taken before c) and after d) repeated 180° bends shows nanoscale cracks but the film integrity is preserved and no delamination of features observed. Scale bar on all images = 100 µm.

AFM imaging of the films (Figure 8-4d,e) show that they are smooth at the nanoscale (both on the film and on the surface of the patterns) with a root mean square (RMS) roughness ≈5 nm over a 5 µm area. In this case, the films used for cell culture with patterns of 10–25 µm were imaged. In these films, the patterns were around 500 nm in height, fabricated via spin coating. Similar patterned films were used for cell culture as discussed below. The lines have a high structural fidelity and resolution demonstrating the accuracy of this photolithographic process to form micropatterns over large areas. Patterns down to ≈3 µm using benchtop lithography are easily formed (Figure S4, Supporting Information). Nanoscale patterning using electron beam lithography was previously demonstrated by our group and could potentially be extended to this system. Due to the optical transparency of the entire structure, they can also find their application in optics for the fabrication of soft and flexible optical systems.

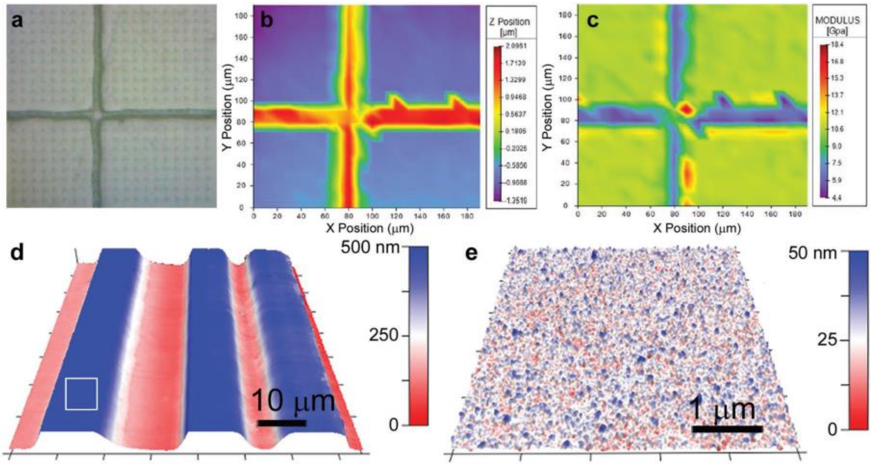

Figure 8-4: Spatial distribution of the localized mechanical property and imaging of the patterned surface. a) The optical microscope image of the surface following nanoindentation. b) Z-position of the indenter indicating the pattern height, and c) Young's modulus spatial distribution, showing the softer pattern on the stiffer underlying substrate (scales on all panels are same). d) AFM imaging of the fibroin micropatterns on fibroin films: 75 µm scan of 10 µm lines separated by 25 and 5 µm gaps. The patterns are 500 nm in height. e) Scan of a 5 × 5 µm area from the flat region of the line shows the flat nanosurface of the films (RMS roughness ≈ 5 nm over this area).

8.3.2. Proteolytic Degradation of Fibroin Substrates In Vitro

An advantage in using natural biopolymers is that devices fabricated based entirely on these materials can be degraded in physiological environments. The silk fibroin biomaterial used in this study enables controllable biodegradability of the flexible devices. Under the reaction of protease, the micropatterned sheets are degraded, ultimately leading to the loss of mass and structural integrity. An enzymatic biodegradation experiment was conducted on micropatterned films incubated in phosphate buffer saline (PBS) solution with or without protease (control) at 37 °C. The percentage of mass weight remaining (obtained as Wt/W0) was recorded to observe the overall decomposition of the films (n = 3) over time (Figure 8-5). No significant mass loss was observed when incubated in PBS over the 2 week period. Due to proteolytic biodegradation, a gradual loss of weight was observed and <40% of the weight remained after 14 days of incubation. After 14 days, the films incubated in the enzyme broke down, whereas the control samples maintained their integrity and flexibility. This was consistent with previously reported observations in which the biodegradability of fibroin based flexible devices can be tuned by controlling the degree of crosslinking and film thickness.[31,34] Therefore, devices with precisely engineered lifetimes can be fabricated using these micropatterned films, which can be useful as implantable bioelectronics and tissue scaffolds.

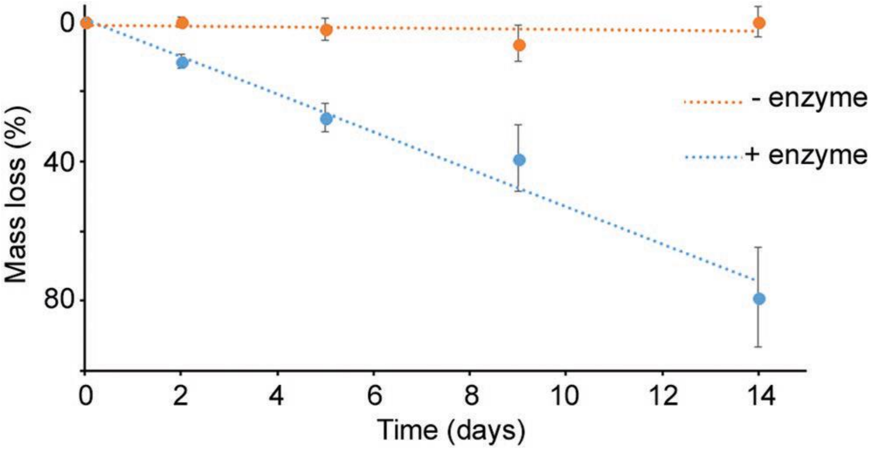

Figure 5: Proteolytic degradation of micropatterned fibroin films. The films are stable in buffers (solution containing no enzyme was used as the control denoted as −enzyme), but show significant mass loss in the presence of protease (+enzyme), ultimately breaking down completely within 3 weeks. (Sample size n = 3 films for each experiment)

8.3.3. Evaluation of Cell Adhesion

Unlike earlier reported cell patterning approaches, wherein cell adhesive regions are obtained by stamping, inkjet printing, proteins etc.,[15e,22,29] here spatial position is controlled through the use of surface micro/nanoarchitectures. To verify the impact of fibroin patterning on cell adhesion, human bone marrow-multipotent stromal cells (hBM-MSCs) were studied on the flexible fibroin sheets. The micropatterns and films are robust enough to withstand the sterilization procedure (Figure 8-2c). Three different conditions were explored on sheets micropatterned with square grids—unmodified sheets, preconditioning with expansion media, and coating with fibronectin. After 8 days of culture, the cytoskeleton was stained with Oregon Green and observed by confocal microscopy imaging. However, cells exhibited a low proliferation and nonspecific adhesion to unmodified sheets. In the case of pretreatment in expansion medium, films showed higher cell adhesion when compared with untreated sample, with preferential attachment to the fibroin patterns (Figure S5, Supporting Information) even if all sample surfaces were incubated in culture medium or fibronectin. At higher magnification, the alignment of the cytoskeleton on fibroin pattern coated with human fibronectin can be clearly seen. Note that multiple replicates (3–5 films for each condition) were performed. The results obtained on preconditioned with complete expansion medium and unmodified films were also useful, showing that despite the low adhesion, the films themselves are not cytotoxic.

Figure 8-6 shows cells on films coated with human fibronectin. DAPI was completely absorbed by the films and used only to show the underlying organization of the grid patterns. This condition had the highest proliferation rate and organization of the cells. The cells clearly align according to the design of the grid patterns. Most interestingly, in addition to the adhesion of the cells to the grid organization (Figure 8-6a), the cells were able to migrate from grid to grid eventually filling up the sheet (Figure S6, Supporting Information). Note that the height of the grids is ≈500 nm in these sheets. This data suggests a significant role of the fibronectin coating, that together with pattern organization is able to guide and enhance cellular growth and proliferation according to a specific designed order. It is clear that the topographical features of the fibroin pattern produced on a fibroin film still allow cell adhesion primarily along the patterns. The cells are therefore guided almost exclusively by the surface morphology, and to some extent, the stiffness differences between the pattern and the substrate. In these films, the patterns are less stiff in comparison to the substrate (Figure 8-2e). The ability to modulate the stiffness of the patterns is another advantage of this technique in comparison to molding techniques which form mechanically homogeneous films. Such flexible, cell culture sheets can therefore be used for fundamental studies of 3D tissue models and scaffolds, where the micropatterns can be used to guide cells initially, and the underlying sheets eventually degrade over time.

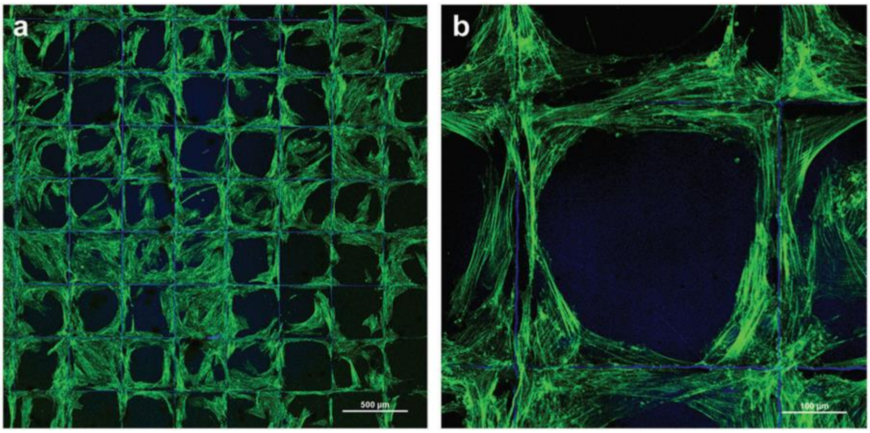

Figure 8-6: Figure 6. a) Contact guidance of fibroblasts on flexible fibroin films patterned with square grids (10 μm thick lines) as observed by confocal microscopy. The dark regions represent the film without any pattern. Images of hBM-MSCs cytoskeleton organization stained with Oregon Green 488 at day 8. Blue (DAPI) was completely absorbed by the films and used to show the grid-like shape pattern. Scale bar = 500 μm. b) Close-up showing the actin filaments attached to the underlying substrates. Scale bar = 100 μm.

8.4. Conclusions

In summary, here we demonstrate the facile fabrication of micropatterned, free-standing films of the silk protein fibroin that are flexible and can be used for controlling cellular organization. The films themselves are mechanically robust, can be formed at various thicknesses ranging from ultrathin (<1 μm) to thick (tens of micrometers), and can be controllably degradable. The surface of these films can be tailored by decorating with patterns of silk fibroin using a photolithographic technique, which permits the formation of complex, high resolution architectures at high throughput and scale (over several centimeters). Virtually any structural pattern can be easily and rapidly formed using light-assisted microfabrication. The cell-adhesive micropatterns were shown to spatially direct cells. In addition to the patterns, it is also possible to modulate the mechanical characteristics of the patterns. These results suggest that micropatterned silk sheets can provide a bioinspired and biodegradable structure toward the flexible cell culture platforms and devices.

8.5. Experimental Section

Synthesis of Photo-Crosslinkable Fibroin: Silk fibroin was extracted from silk cocoons using a standard protocol.[35] Fibroin protein photoresist (FPP) was prepared by the incorporation of photoreactive moieties to the fibroin structure as reported earlier.[30a] Briefly, pure fibroin was dissolved in 1 m LiCl/DMSO and reacted with 2-isocyanatoethyl methacrylate (IEM) in stoichiometric amounts for 5 h at 60 °C, while maintaining inert conditions using a constant flow of nitrogen. After the completion of the reaction, the product mixture was added to cold ethanol, and the methacrylated protein was obtained as the precipitate. The product was washed with a 1:1 ratio of cold ethanol and acetone followed by centrifugation and lyophilization for 24 h to obtain the fibroin protein photoresist (photofibroin) powder.

Fabrication of Flexible Micropatterned Fibroin Films: The flexible micropatterned substrate was fabricated by dissolving 7.5% w/v of photofibroin in formic acid (Acros Organics 98%). 2.5% w/v photoinitiator (Irgacure 2959, BASF) was added. The solution was drop cast on plain glass slides and air dried for 15–20 min in order to evaporate the excess solvent. The samples were exposed under a 365 nm UV lamp (Lumen Dynamics OmniCure 1000 system) for 3 s at 20 mW cm^{-2} for crosslinking. To create fibroin films, the samples were dipped in deionized (DI) water which facilitated the delamination from the glass. Micropatterns of silk fibroin were fabricated on these films using contact photolithography. Films prepared as discussed above were used as the substrates. A 5% w/v solution of FPP in 1,1,1,3,3,3-hexafluoro-2-propanol (HFIP, Sigma-Aldrich, St. Louis, MO) was drop casted on fibroin films. The samples were air dried for 5 min, allowing the HFIP to evaporate. Micropatterned structures were formed by placing a photolithographic mask with the desired array of patterns on the substrates and exposing it under UV irradiation for 1.6 s. Patterns were developed by immersing the samples in 1 m LiCl/DMSO solution for ≈2 h. The patterns were then rigorously cleaned with DI water to wash off any un-crosslinked material and excess LiCl/DMSO solution.

Proteolytic Degradation In Vitro: Micropatterned fibroin films can be proteolytically degraded over time in the presence of enzymes. In the present work, the degradation of fibroin microstructures on films in the presence of protease (Protease XIV from Streptomyces griseus, ≥3.5 U mg−1, Sigma Aldrich) was studied. Films (containing ≈2.5 mg fibroin) were incubated in 5 mL protease (1 U mg−1 of protein) at 37 °C and the degradation was studied over 2 weeks. Another set of samples were incubated in PBS buffer under the same environment, which served as the negative control (NC). The enzyme solution was replaced every 3 days to maintain the activity of protease. Samples from each set were taken out on different days, rinsed with DI water, dried under N2, and weighed to record their degradation over time. Degradation over time was characterized as a function of mass loss of the films.

In Vitro Cell Culture: Human bone marrow-multipotent stromal cells were cultured in expansion medium consisting of DMEM:F12 (Euroclone), supplemented with 10% fetal bovine serum (Euroclone), 1% antibiotic antimycotic (Euroclone). Cells were cultured in 75 cm2 flask at 37 °C and 5% CO2 in humidified atmosphere. Medium was changed twice per week and when at 80% confluence, were detached with trypsin-EDTA (Euroclone). For this study cells were used at passage 3.

Fibroin films prepared as discussed above were sterilized with 70% ethanol for 45 min and then washed twice with sterile distilled water to completely remove ethanol. To improve cell adhesion, one set of samples was preconditioned in complete expansion medium for 20 min at 37 °C, and the second set incubated in human fibronectin (Sigma) 10 µg mL−1 in PBS for 1 h at 37 °C. As a control, films without any treatment as well as cells seeded on tissue culture plate well (TCP) were used. Cells were seeded at 3 × 104 cells mL−1 on each sample. 1 mL of cell suspension was seeded. After seeding, cells were left to adhere for 1 h before adding fresh medium. Cells were then cultured up to 8 days.

Morphological Evaluation of Adhered Cells: Cell morphology and organization on patterned films were studied by imaging at day 8 after seeding using confocal microscopy. Prior to imaging, adhered cells were fixed with 4% PFA for 40 min, and then permeabilized with 0.2% Triton X-100 for 40 min. To investigate nuclear and cytoskeleton organization of cells on films, hBM-MSCs were stained with DAPI (Sigma-Aldrich) for nucleus and Oregon Green 488 (ThermoFisher) for actin filaments according to manufacturer's instructions for 15 min. Samples were examined using a Nikon A1 Confocal Laser Microscope.

Imaging and Nanoindentation: Imaging of the substrates was conducted using atomic force microscopy (AFM) via an MFP-3D AFM (Oxford Instruments, Santa Barbara, CA). Si3N4 cantilever (Olympus) with a nominal spring constant of k = 2 nN nm−1 was used for noncontact imaging in air. For mechanical characterization, nanoindentation was conducted using an iNano Nanoindenter (Nanomechanics Inc.) equipped with a Berkovich tip. The tested samples were prepared by affixing the film on a stub. The declared sensitivity of the machine was 3 nN for the load and 0.001 nm for the displacement. A mapping method (Nanoblitz 3d, Nanomechanics Inc.) was used, with a nanoindentation grid of 200 μm × 200 μm square with 400 indentation points inside and maximum load of 15 mN. The standard indentation method was used at 15, 30, and 45 mN maximum load to analyze the influence of the applied force. The standard indentation method with 45 mN maximum load was applied at different positions on the substrate to analyze the variation of the Young's modulus on the film surface. The comparison of the data (Figure 8-3c) was performed by using T-statistics and the taken quantile was 2.021 by considering more than 40 degrees of freedom.

Tensile Tests: Samples were prepared by fixing on a paper frame provided with a square window of 0.5 cm side. The sample was fixed to the frame using double-sided tape and a high-strength glue. For fracture tests, a MIDI 10 machine with a load cell of 10 N and imposed velocity of 0.1 mm s−1 (strain rate of 0.02 s−1) was used. The cyclic tests and the Young's modulus measurements were performed with the nanotensile machine Agilent UTM T150 (Keysight Technologies, CA), with a load cell of 500 mN and a displacement speed of 1 μm s−1. The tests were recorded with a Sony Camera (video showing the tensile test is provided in the Supporting Information).

Additional images of the microstructures, cellular spreading, mechanical testing data (load–displacement curves for indentation, Young's modulus distribution) as well as tensile stretching of the samples are provided in the Supporting Information.

8.6. References

1. Zschokke, S.; Herberstein, M.E. Laboratory Methods for Maintaining and Studying Web-Building Spiders. *J. Arachnol.* **2005**, *33*, 205–213.
2. Lalit Jajpura, A.R. The Biopolymer Sericin: Extraction and Applications. *J. Text. Sci. Eng.* **2015**, *05*, 1–5.
3. Altman, G.H.; Diaz, F.; Jakuba, C.; Calabro, T.; Horan, R.L.; Chen, J.; Lu, H.; Richmond, J.; Kaplan, D.L. Silk-based biomaterials. *Biomaterials* **2003**, *24*, 401–416.
4. Bhattacharjee, P.; Kundu, B.; Naskar, D.; Kim, H.-W.; Maiti, T.K.; Bhattacharya, D.; Kundu, S.C. Silk scaffolds in bone tissue engineering: An overview. *Acta Biomater.* **2017**.
5. Kundu, B.; Kurland, N.E.; Bano, S.; Patra, C.; Engel, F.B.; Yadavalli, V.K.; Kundu, S.C. Silk proteins for biomedical

applications : Bioengineering perspectives. *Prog. Polym. Sci.* **2014**, *39*, 251–267.

6. Astudillo, M.F.; Thalwitz, G.; Vollrath, F. Life cycle assessment of Indian silk. *J. Clean. Prod.* **2014**, *81*, 158–167.
7. Edlund, A.M.; Jones, J.; Lewis, R.; Quinn, J.C. Economic feasibility and environmental impact of synthetic spider silk production from escherichia coli. *N. Biotechnol.* **2018**, *42*, 12–18.
8. a) J. A. Forrest, K. Dalnoki-Veress, Adv. Colloid Interface Sci. 2001, 94, 167; b) C. M. Stafford, C. Harrison, K. L. Beers, A. Karim, E. J. Amis, M. R. VanLandingham, H.-C. Kim, W. Volksen, R. D. Miller, E. E. Simonyi, Nat. Mater. 2004, 3, 545.
9. a) S. Zhang, Y. Sunami, H. Hashimoto, Nanomaterials 2017, 7, 246; b) R. R. Costa, J. F. Mano, Chem. Soc. Rev. 2014, 43, 3453; c) T. Fujie, Polym. J. 2016, 48, 773.
10. Y. Haraguchi, T. Shimizu, T. Sasagawa, H. Sekine, K. Sakaguchi, T. Kikuchi, W. Sekine, S. Sekiya, M. Yamato, M. Umezu, T. Okano, Nat. Protoc. 2012, 7, 850.
11. a) S. J. Benight, C. Wang, J. B. H. Tok, Z. A. Bao, Prog. Polym. Sci. 2013, 38, 1961; b) L. Ricotti, T. Fujie, Bioinspiration Biomimetics 2017, 12, 021001.
12. a) D. H. Kim, N. S. Lu, R. Ma, Y. S. Kim, R. H. Kim, S. D. Wang, J. Wu, S. M. Won, H. Tao, A. Islam, K. J. Yu, T. I. Kim, R. Chowdhury, M. Ying, L. Z. Xu, M. Li, H. J. Chung, H. Keum, M. McCormick, P. Liu, Y. W. Zhang, F. G. Omenetto, Y. G. Huang, T. Coleman, J. A. Rogers, Science 2011, 333, 838; b) J. Sugano, T. Fujie, H. Iwata, E. Iwase, Jpn. J. Appl. Phys. 2018, 57, 06HJ04.
13. A. W. Feinberg, A. Feigel, S. S. Shevkoplyas, S. Sheehy, G. M. Whitesides, K. K. Parker, Science 2007, 317, 1366.
14. a) D. Falconnet, G. Csucs, H. M. Grandin, M. Textor, Biomaterials 2006, 27, 3044; b) A. P. Quist, S. Oscarsson, Expert Opin. Drug Discovery 2010, 5, 569.
15. a) R. Ogaki, M. Alexander, P. Kingshott, Mater. Today 2010, 13, 22; b) E. A. Cavalcanti-Adam, T. Volberg, A. Micoulet, H. Kessler, B. Geiger, J. P. Spatz, Biophys. J. 2007, 92, 2964; c) J. Huang, S. V. Gräter, F. Corbellini, S. Rinck, E. Bock, R. Kemkemer, H. Kessler, J. Ding, J. P. Spatz, Nano Lett. 2009, 9, 1111; d) A. I. Teixeira, G. A. Abrams, P. J. Bertics, C. J. Murphy, P. F. Nealey, J. Cell Sci. 2003, 116, 1881; e) M. Mrksich, Chem. Soc. Rev. 2000, 29, 267.
16. a) W. Srituravanich, N. Fang, C. Sun, Q. Luo, X. Zhang, Nano Lett. 2004, 4, 1085; b) M. Manso, P. Rossini, I. Malerba, A. Valsesia, L. Gribaldo, G. Ceccone, F. Rossi, J. Biomater. Sci., Polym. Ed. 2004, 15, 161.

17. a) E. Delamarche, A. Bernard, H. Schmid, A. Bietsch, B. Michel, H. Biebuyck, J. Am. Chem. Soc. 1998, 120, 500; b) S. Javaherian, K. A. O’Donnell, A. P. McGuigan, PLoS One 2011, 6, e20909.
18. a) I. S. Carrico, S. A. Maskarinec, S. C. Heilshorn, M. L. Mock, J. C. Liu, P. J. Nowatzki, C. Franck, G. Ravichandran, D. A. Tirrell, J. Am. Chem. Soc. 2007, 129, 4874; b) M. Shelly, S.-I. Lee, G. Suarato, Y. Meng, S. Pautot, Methods Mol. Biol. 2017, 1493, 321.
19. Y. Xia, G. M. Whitesides, Angew. Chem. 1999, 37, 551.
20. E. Roth, T. Xu, M. Das, C. Gregory, J. Hickman, T. Boland, Biomaterials 2004, 25, 3707.
21. a) J. L. Charest, M. T. Eliason, A. J. García, W. P. King, Biomaterials 2006, 27, 2487; b) A. Bernard, J. P. Renault, B. Michel, H. R. Bosshard, E. Delamarche, Adv. Mater. 2000, 12, 1067.
22. a) L. T. de Jonge, S. C. G. Leeuwenburgh, J. J. J. P. van den Beucken, J. G. C. Wolke, J. A. Jansen, Adv. Funct. Mater. 2009, 19, 755; b) C. Muderrisoglu, M. Saveleva, A. Abalymov, L. Van der Meeren, A. Ivanova, V. Atkin, B. Parakhonskiy, A. G. Skirtach, Adv. Mater. Interfaces 2018, 5, 1800452.
23. a) Y. Haraguchi, T. Shimizu, M. Yamato, T. Okano, RSC Adv. 2012, 2, 2184; b) Q. Ke, X. Wang, Q. Gao, Z. Wu, P. Wan, W. Zhan, J. Ge, Z. Wang, J. Tissue Eng. Regener. Med. 2011, 5, 138; c) M. Kawecki, M. Kraut, A. Klama-Baryła, W. Łabus´, D. Kitala, M. Nowak, J. Glik, A. L. Sieron´, A. Utrata-Wesołek, B. Trzebicka, A. Dworak, D. Szweda, J. Mater. Sci.: Mater. Med. 2016, 27, 111; d) A. Forghani, L. Kriegh, K. Hogan, C. Chen, G. Brewer, T. B. Tighe, R. Devireddy, D. Hayes, J. Biomed. Mater. Res., Part A 2017, 105, 1346.
24. K. Ng, B. Gao, K. W. Yong, Y. Li, M. Shi, X. Zhao, Z. Li, X. Zhang, B. Pingguan-Murphy, H. Yang, F. Xu, Mater. Today 2017, 20, 32.
25. a) J. L. Ifkovits, H. G. Sundararaghavan, J. A. Burdick, J. Visualized Exp. 2009, 32, 1589; b) C. Chen, B. T. Mehl, S. A. Sell, R. S. Martin, Analyst 2016, 141, 5311; c) X. M. Mo, C. Y. Xu, M. Kotaki, S. Ramakrishna, Biomaterials 2004, 25, 1883; d) X. Wang, B. Ding, B. Li, Mater. Today 2013, 16, 229.
26. a) H. Cao, T. Liu, S. Y. Chew, Adv. Drug Delivery Rev. 2009, 61, 1055; b) Q. Cheng, B. L. P. Lee, K. Komvopoulos, S. Li, Biomacromolecules 2013, 14, 1349.
27. a) A. Folch, B. H. Jo, O. Hurtado, D. J. Beebe, M. Toner, J. Biomed. Mater. Res. 2000, 52, 346; b) S. Halldorsson, E. Lucumi, R. Gómez-Sjöberg, R. M. Fleming, Biosens. Bioelectron. 2015, 63, 218; c) K. Kolind, K. W. Leong, F. Besenbacher, M. Foss, Biomaterials 2012, 33, 6626.

28. T. Fujie, S. Ahadian, H. Liu, H. X. Chang, S. Ostrovidov, H. K. Wu, H. Bae, K. Nakajima, H. Kaji, A. Khademhosseini, Nano Lett. 2013, 13, 3185.
29. T. Fujie, A. Desii, L. Ventrelli, B. Mazzolai, V. Mattoli, Biomed. Microdevices 2012, 14, 1069.
30. Y. Okamura, K. Kabata, M. Kinoshita, D. Saitoh, S. Takeoka, Adv. Mater. 2009, 21, 4388.
31. S. G. Caridade, C. Monge, F. Gilde, T. Boudou, J. F. Mano, C. Picart, Biomacromolecules 2013, 14, 1653.
32. P. Hassanzadeh, M. Kharaziha, M. Nikkhah, S. R. Shin, J. Jin, S. He, W. Sun, C. Zhong, M. R. Dokmeci, A. Khademhosseini, M. Rolandi, J. Mater. Chem. B 2013, 1, 4217.
33. A. Perl, D. N. Reinhoudt, J. Huskens, Adv. Mater. 2009, 21, 2257.
34. a) J. G. Hardy, L. M. Römer, T. R. Scheibel, Polymer 2008, 49, 4309; b) B. Kundu, N. E. Kurland, S. Bano, C. Patra, F. B. Engel, V. K. Yadavalli, S. C. Kundu, Prog. Polym. Sci. 2014, 39, 251.
35. G. H. Altman, F. Diaz, C. Jakuba, T. Calabro, R. L. Horan, J. Chen, H. Lu, J. Richmond, D. L. Kaplan, Biomaterials 2003, 24, 401.
36. H. J. Jin, S. V. Fridrikh, G. C. Rutledge, D. L. Kaplan, Biomacromolecules 2002, 3, 1233.
37. a) E. S. Gil, S. H. Park, J. Marchant, F. Omenetto, D. L. Kaplan, Macromol. Biosci. 2010, 10, 664; b) M. Hronik-Tupaj, W. K. Raja, M. Tang-Schomer, F. G. Omenetto, D. L. Kaplan, J. Biomed. Mater. Res., Part A 2013, 101, 2559.
38. a) N. E. Kurland, T. Dey, S. C. Kundu, V. K. Yadavalli, Adv. Mater. 2013, 25, 6207; b) A. Bucciarelli, R. K. Pal, D. Maniglio, A. Quaranta, V. Mulloni, A. Motta, V. K. Yadavalli, Macromol. Mater. Eng. 2017, 302, 1700110.
39. W. Ian, F. Arash, G. B. Alexander, J. Esmaiel, K. Ali, Nanotechnology 2011, 22, 212001.
40. H. J. Jin, J. Park, V. Karageorgiou, U. J. Kim, R. Valluzzi, D. L. Kaplan, Adv. Funct. Mater. 2005, 15, 1241.
41. R. K. Pal, A. A. Farghaly, C. Wang, M. M. Collinson, S. C. Kundu, V. K. Yadavalli, Biosens. Bioelectron. 2016, 81, 294.
42. D. N. Rockwood, R. C. Preda, T. Yucel, X. Q. Wang, M. L. Lovett, D. L. Kaplan, Nat. Protoc. 2011, 6, 1612.

9. ARTIFICIAL SPIDER SILK

This chapter is based on our research activity in collaboration with the group of Anna Rising at the Swedish University of Agricultural Sciences (Uppsala) and Karolinska Institutet (Stockholm). In particular, I would like to acknowledge Juanita Francis. Her precious work, in the part relative of the fibres that were kept longer in the bath, has been essential.

In this chapter, I will explore the state of the art of the work that we are currently doing on artificial spider silk.

The possible applications of spider silks (as we listed in the introduction) make it a desirable material for industry. But in order to apply it, a large amount of it is required. A possible solution to this is the spider under consideration in chapter 6 (*Linothele megatheloides*), which is now under investigation in our lab. Unfortunately, the possibility of harvesting silk directly from spiders is still not considered in industry since spiders are cannibalistic animals[1] and it is impossible to farm them all together.

There are, however, exceptions of spiders that can actually live in "society-like structures"[2], but the knowledge on them is so small that is almost impossible to think at the current stage to farm them and possibly obtain valuable silk. A possible solution to this could be, thus, the production of artificial spider silk.

Goal of the chapter: In this chapter, we focus on the different mechanical properties of artificial spider silk under different conditions. With the aim to improve such properties, the effects of humidity on these fibres is analysed together with a protocol to reduce them. Moreover, the effects of incubating the fibres longer in the spinning buffer are reported.

9.1. How to spin artificial spider silk?

As in the case of spiders, in order to spin these remarkable fibres scientists commonly start from the liquid solution (spider silk protein in water or more commonly strong solvents such as HFIP to solubilize silk proteins). Interestingly, keeping stable a solution of spider silk protein in water is a challenge per se, especially if we consider that in spider's gland the concentration of the solution can reach up to 30-50 % w/v[3]. In the pasts decades many attempts have been made to create this kind of solution with the support of genetically modified organisms. In particular, plants, yeast, bacteria, insects and even mammals have been modified with the aim to produce the protein broth from which fibres can be spun[4–8]. Unfortunately, it seems to be difficult to achieve the production of large amount of the material for all the mentioned technique apart for the yeast's and *Escherichia coli*'s ones[9]. For these, protocols to obtain the recombinant spider silk solutions have been developed.

Moreover, Alan et al.[10] explored the impact of the aforementioned production in the ecosystems. They explored the possibility to improve it (i.e. achieving better efficiencies in silk protein expressions) and demonstrated its greener impact with respect the common silkworm silk production[11].

In order to spin artificial spider silk we used the setup of Andersson et al.[12] and we used spider silk solution obtained from genetically modified *Escherichia coli*. The bacteria produce the spider silk protein, called NT2RepCT, and this is subsequently purified under non-denaturing conditions by using immobilized metal affinity chromatography. Finally, the protein is concentrated to 30-50% in an aqueous buffer at pH 8. The spinning apparatus consists in a syringe that injects at fixed (and controlled) flow rate the protein solution through a capillary (with known dimensions) immersed in an aqueous bath at lower PH (500mM NaAc buffer with 200mM NaCl at pH 5). This set-up bio-mimetically simulate the decrease in pH found in the major ampullate gland[13].

The formation of the fibres is instantaneous they come in contact with the bath (Figure 9-1a). The fibres are collected on frames with a fixed rotation in air. This stretching procedure could emulate the pulling force used by spiders during the extrusion of the fibres[14].

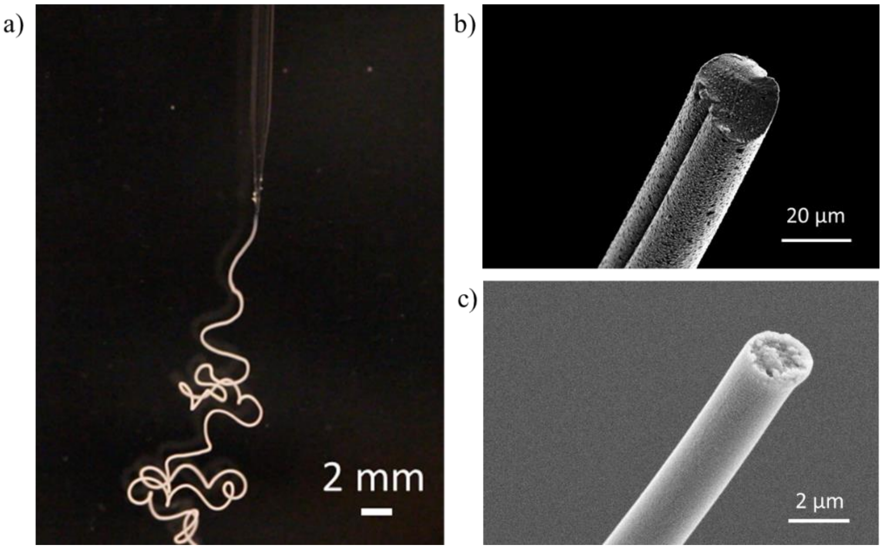

Figure 9-1: a) Spinning of the artificial spider silk in the low-ph bath. b) Fracture section of an artificial fibre silk and c) fracture section of the native spider silk.

The fibres are then dried under room conditions for one night. The use of recombinant proteins has the important advantage that it is possible to alter the amino acid sequence in order to tune the mechanical properties. Here, we succeeded in improving the fibres' mechanical properties by modifying the amino acids sequence and by altering the incubation time in the collection bath.

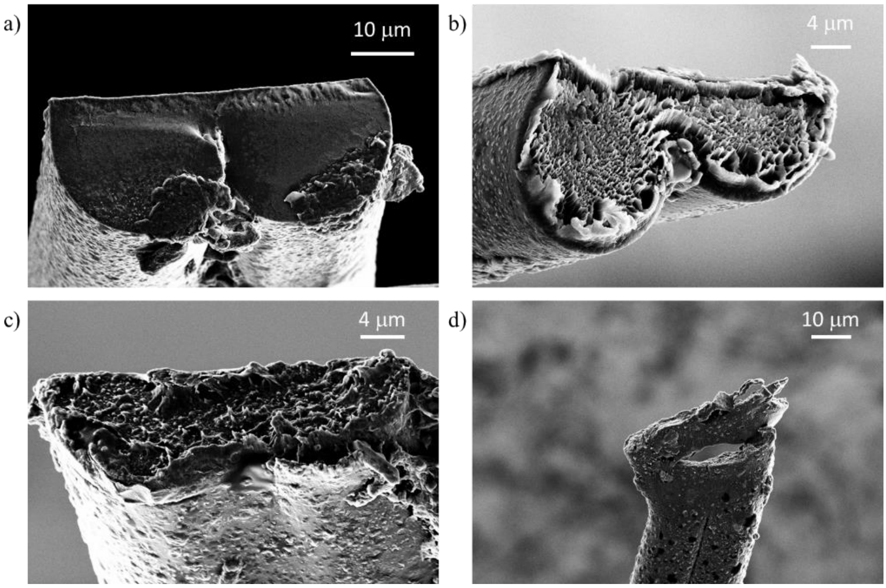

Figure 9-2: Different fracture sections of the artificial spider silk fibres. The dumbbell shape of the section makes difficult to estimate its area correctly.

The control artificial spider silk fibre used in the following experiments is named "NT2RepCT", which refers to the protein (around 33 kDa mw) that the fibres are made from. This construct consists of two terminal domains (NT and CT) and a central repetitive region (check Figure 3-8).

The amino acid sequence NT2RepCT is:
NT:
SHTTPWTNPGLAENFMNSFMQGLSSMPGFTASQLDDMSTIAQSM
VQSIQSLAAQGRTSPNKLQALNMAFASSMAEIAASEEGGGSLSTK
TSSIASAMSNAFLQTTGVVNQPFINEITQLVSMFAQAGMNDVSA
2Rep:
GNSGRGQGGYGQGSGGNAAAAAAAAAAAAAAAGQGGQGGYG
RQSQGAGSAAAAAAAAAAAAAAGSGQGGYGGQGQGGYGQSGN
S
CT:

TSGGYGYGTSAAAGAGVAAGSYAGAVNRLSSAEAASRVSSNIAA
IASGGASALPSVISNIYSGVVASGVSSNEALIQALLELLSALVHVLS
SASIGNVSSVGVDSTLNVVQDSVGQYVG.

The shape of the fibres' cross section was unfortunately not circular, as mainly occurs in the native ones, but dumbbell shaped (Figure 9-1b,c) and irregular (Figure 9-2). This peculiar aspect creates difficulties in the measurement of the fibres' cross-sectional area, since it is assumed to be circular. This led to an underestimation of the mechanical properties. Moreover, the data obtained on the fibres were not selected and this irregular shape led to a huge scattering of the data. We are currently working on trying to solve this problem.

Table 9-1: The effect of testing speed on the mechanical properties of the artificial fibres that we produced.

Testing speed (mm/min)	Nr. Fibres	Diameter (μm)	Strain at Break (mm/mm)	Strength (MPa)	Young's Modulus (GPa)	Toughness (MJ/m^3)
0.48	19	13.6 ± 1.4	0.03 ± 0.01	38 ± 12	1.3 ± 0.5	0.7 ± 0.4
3	17	13.8 ± 16	0.02 ± 0.01	40 ± 18	2.2 ± 1.1	0.5 ± 0.3
6	17	13.6 ± 2.0	0.03 ± 0.02	61 ± 29	2.9 ± 2.0	1.0 ± 0.7
12	18	12.5 ± 2.7	0.02 ± 0.01	55 ± 21	3.1 ± 1.3	0.7 ± 0.5

Table 9-2: The effect of the diameter on the mechanical properties in artificial fibres that we produced.

Sample Type	Nr. Fibres	Diameter (μm)	Strain at Break (mm/mm)	Strength (MPa)	Young's Modulus (GPa)	Toughness (MJ/m^3)
Small diameter	19	9 ± 2	0.03 ± 0.01	61 ± 23	2.9 ± 1.6	0.9 ± 0.5
Big diameter	19	22 ± 6	0.04 ± 0.02	48 ± 34	1.8 ± 0.9	1.1 ± 1.2

9.2. Mechanical properties

In order to evaluate the mechanical properties of the fibres samples were prepared following the procedure of Greco et al.[15]. The silk fibres were mounted with the support of double-sided tape on a paper frame with a square window of 1 cm. The used machine is an Instron 5943 tensile tester with a 5N load cell, which has a resolution of the 5% of the max load. As a standard and control extension rate, we used 1% per second with respect the gauge length (1 cm). The diameter, even if the fibres were not circular, was measured with the support of an optical microscope. In this way, we underestimated the mechanical properties of the artificial spider silk by dividing the force by the circular section (obtained with the diameter) in order to compute the engineering stress. The engineering strain was computed by dividing the displacement by the gauge length. All the mechanical properties were computed by following the description of the chapter 3 (introduction).

Tables 9-1 and 9-2 show the effect of the rates of extension and of the diameter on the mechanical properties. The fibres show a behaviour that is typical of the native spider silk, which is increased in the strength and rigidity if the fibre is pulled faster[16] (Table 9-1). This is related to the viscoelastic nature of spider silk, which tends to reduce the tensional state if it has time to relax[17]. The last two sets of samples (pulled at 6 and 12 mm/min) presented a non-significant difference in strength by ANOVA analysis (confidence level of 5%).

Interestingly, we did not notice any difference in mechanical properties if the fibres were spun in capillaries with different dimension (Table 9-2). Even if this conclusion is affected by the huge scattering of the data, we still believe that the difference is not sufficiently big to justify a specific dimension of the capillary. We then continued our work with the most convenient one for the specific type of fibre that we wanted to spin.

Even if we underestimated the mechanical properties of these fibres, it is obvious that they are not comparable to the ones of the native silks (see previous chapters).

This is possibly due to the fact that the spider silk spinning process is an extremely complex event, which involves several factors[18], and in our bio-inspired setup we only consider a few of these (shear forces and decrease in pH). For example, achieving protein with higher molecular weights is one of the way to possibly improve the mechanical properties of the fibres[19,20]. Unfortunately, dealing with big proteins is difficult in terms of keeping the solubility of the protein in water and the ratio costs-benefits of the entire process.

We thus needed to consider other aspects that can improve the mechanical properties of our fibres.

9.3. The problem of stability under different RH rates

If we consider the previous chapters, the possibility to use artificial spider silk for various purposes is certainly a huge opportunity.

The stability of the mechanical properties under different environmental conditions is crucial for commercial applications. For example, different humidity conditions are known to change the mechanical properties of spider silk[21]. This is not convenient for several applications (such as medical ones) where the material needs to be inserted in wet environment.

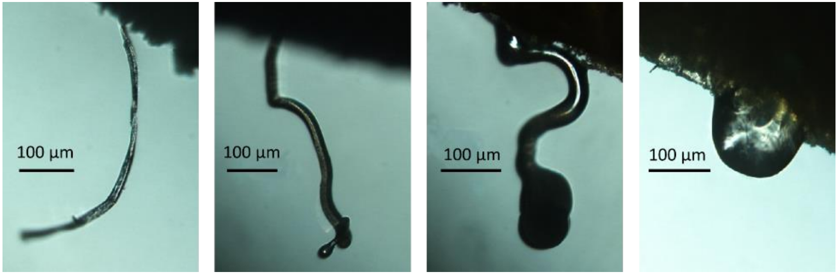

Figure 9-3: At 88% we observed that the fibres spun in the original setup started to dissolve.

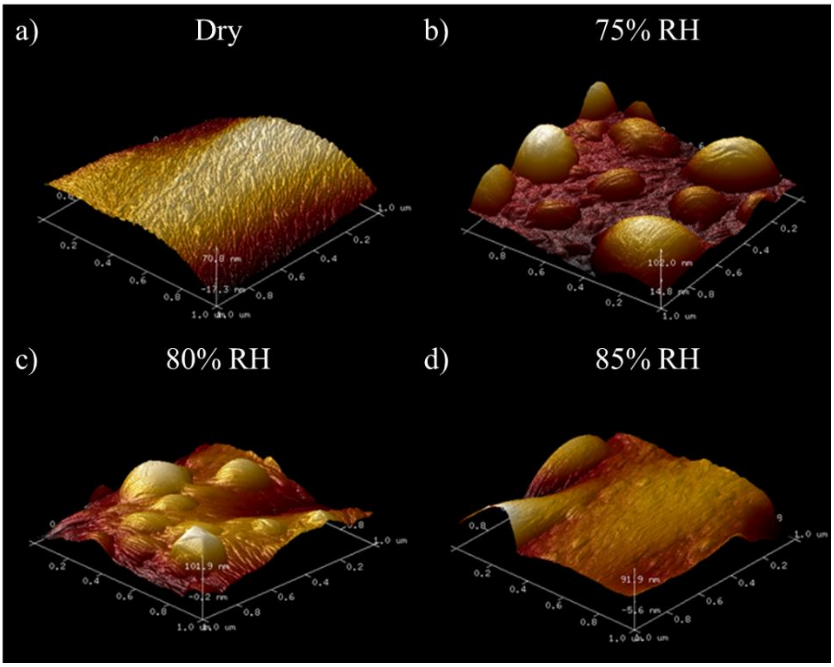

Figure 9-4: AFM images of the surface of the control fibres kept for 2 hours at different humidities. a) Dry fibres present a smooth surface. b-c) At 70% the fibres looked less smooth with the formation of bubble-like structures on the surface. d) At 85% the dissolution process starts to modifies the overall shape of the fibres.

On the contrary, for humidity sensor applications, the change of the mechanical properties could be an advantage. This is demonstrated by the recent works that have been published on the possibility to use native spider silk as basic material for developing sensors[22–24].

Even more drastic is when the fibre not only changes its mechanical properties, but also its morphology till the possibility of dissolving completely.

In our control fibres NT2RepCT we observed this phenomenon when these were kept in a humidity chamber at 88% RH for 2 hours (Figure 9-3). Interestingly, by analysing the fibres under AFM we recognize some bubble-like structures on the surfaces at humidity rates higher than 70% (Figure 9-4). These structures have been related to the starting of the dissolution process in native spider silk[25].

In order to solve this problem, we investigated the effect of the humidity on the artificial spider silk fibres.

9.4. Supercontraction

Before exploring the results regarding the effect of humidity in artificial spider silk it is necessary to introduce the effect of humidity on the native, i.e. major ampullate silk.

These effects can be defined through the supercontraction phenomenon. This was discovered in 1977[26] when native spider silk were kept in humid (or totally immerged in water) environment. Macroscopically, it is characterized by a shrinkage of the fibre length and an increase in the diameter, the extent of which depends on the species of spider[27]. In general, supercontraction occurs starting from 70% of relative humidity or higher. Coupled with the shortening of the fibres, a torsion induced by humidity has been recently observed in native spider silk[28].

Added to the morphological effects on the fibres, the mechanical properties of spider silk after supercontraction are also affected. The way in which these properties change depends on the way in which the fibre is treated.

If the fibre is immerged in water, this irreversibly plasticize it by decreasing the Young’s modulus and the strength, but increasing its deformability[29].

If the fibre is kept in a humid environment at fixed RH and restrained at both ends, on the other hand, a humid induced stress on the fibre occurs by shortening it. A small reduction in Young’s modulus is still observed. This process, interestingly, is demonstrated to be reversible creating the possibility to use spider silk as a muscle driven by humidity[30].

In terms of factors that affect this phenomenon, nowadays we know that if a fibre presents an higher tensional state the effect of water (supercontraction) is accelerated[31]. This is important if one considers the spinning of silk, which involves shear forces that may change (together with the tensional state of the fibre) if the spinning conditions are changed[32,33]. The higher is the tensional state, the bigger is the effect of water on the fibre.

Another important aspect to consider is the hydration rate of the fibre. If it is faster, higher stresses are generated in the fibre (up to 100 MPa)[34].

Even if the effects of supercontraction are well known in spider silk, its causes are still to be determined directly.

The most common and accepted hypothesis is that while water is diffusing in spider silk, a reorganization of hydrogen bonds occurs, changing the orientation of the amorphous region. The semi-crystals, however, seem to be unaffected by water[35,36]. Unfortunately, nobody still directly observed where this phenomenon exactly starts and what are the main structures involved.

The hypothesis that has guided scientists in these years is that the proline is the main cause of the supercontraction. This was hypothesized by observing that different content in proline leads to different response in term of supercontraction[37–39]. This was later partially confirmed by the fact that proline seems to have an higher mobility under humidity changes[40].

This hypothesis, however, has never been demonstrated directly, and there are facts suggesting that proline is not the only cause of supercontraction.

One of the strongest is the fact that regenerated *Bombyx mori* silk, which is mainly proline free, presents a contraction when exposed to water[41].

Another important evidence in favour of a non-proline involvement is the fact that under NMR spectroscopy only the peaks (in the spectra) of glycine, glutamine, serine and tyrosine are shifted after supercontraction[36]. An interesting paper based on Raman spectroscopy and molecular simulation proposed that tyrosine and arginine are the main amino acids residues involved in supercontraction[42]. The side chains of arginine and tyrosine are suggested to be involved in secondary structure transitions from extended in dry fibre state to coiled or helical structures in the wet state, leading to a contraction of the fibre. The transition is driven by water molecules that enter the fibre and break the intermolecular hydrogen bonds mediated by the side chains of these amino acid residues. Unfortunately, these findings were based on molecular simulation to a large extent, which makes the supercontraction phenomenon not fully understood. In order to make the situation clearer about the complexity of this phenomenon and the evolution of the knowledge in its regard, we invite the reader to refer to Table 9-3.

Table 9-3: The history of supercontraction.

Year	Paper	Type of study	Main Output

1977	Work[26]	Experimental: mechanical properties, morphology.	The discovery, MA silk contracts more than MiA silk.
1981	Work[27]	Experimental: mechanical properties, morphology	Supercontraction strongly depends on the species of spider.
1985	Work[43]	Experimental: mechanical properties, X-Rays	The first hypothesis that the change in the fibres occurs in the amorphous region.
1989	Vollrath et al.[44]	Experimental: mechanical properties	Fibre that entered in contact with water are plasticized in mechanical properties.
1992	Edmonds et al.[45]	Experimental: mechanical properties	Supercontraction is related to the mechanics of capture threads.
1992	Bonthrone et al.[46]	Experimental: NMR, mechanical properties	Extra elasticity is due to water induced mobility.
1997	Parkhe et al.[47]	Experimental: NMR, X-Rays, mechanical properties	The orientation of the amorphous region changes also in MiA,
1999	Grubb et al.[48]	Experimental: X-Rays, mechanical properties	There is a decrease in the order in the supercontracted fibres.
1999	Shao et al.[25]	Experimental: mechanical properties, morphology	More polar is the solvent, bigger is the effect on the fibres. First hydrogen bonds destruction hypothesis.
1999	Shao[49]	Experimental: mechanical properties, Raman spectroscopy	Raman spectroscopy seems not to be good for understanding supercontraction as long as the data shown a decrease in β-sheets.
2002	Bell et al.[50]	Experimental: mechanical properties	First time resolved analysis of the stress in supercontraction of spider silk. Supercontraction as a tool for re-tensioning of spider webs.
2003	Guinea and Peréz et al.[29,51]	Experimental: mechanical properties, morphology.	Supercontraction is irreversible and creates a ground state of the mechanical properties (affected then by everything). It starts around 70% RH.
2004	Elices et al.[52]	Experimental: mechanical properties, morphology	Definition of max supercontraction, which consists in the maximum contraction achieved in unrestrained or restrained fibres.
2004	Eles et al.[35]	Experimental: NMR	Reorientation of the chain (amorphous) is observed, which is a strong evidence of a change in hydrogen bonds.
2004	Holland et al.[36]	Experimental: NMR	β-sheets seem to not be intake by supercontraction. The modified peaks are those of Glycine, Glutammine, Serine and Tyrosine. Introduction of the concept that β-sheets can occur in different phases.
2005	Liu et al.[32]	Experimental: mechanical properties, morphology	More oriented chains induce more contraction, which means that different tensional states lead to different maximum supercontraction.
2005	Pérez-Rigueiro and Guinea et al.[33,53]	Experimental: mechanical properties and morphology	Supercontraction creates homogeneity in fibre's mechanical properties. Introduction of the alignment parameter as an indicator of supercontraction.
2008	Liu et al.[37]	Experimental: mechanical properties, morphology	The proline is involved in supercontraction and it is claimed to be the main cause.

2008	Savage et al.[38]	Experimental: mechanical properties, morphology, thermal analysis	The mobility of the proline in spider silk is easily modifiable.
2008	Savage et al.[39]	Experimental: birefringence, mechanical properties, morphology	The cause of the supercontraction could be the connection between proline and glycine. Hydrogen bonds are easier to break with the increase of the hydration rate.
2008	Plaza et al.[54]	Experimental: morphology, mechanical properties	Contraction due to water is observed also in *Bombyx mori* silk, which is almost proline free.
2009	Blackledge et al.[55]	Experimental: mechanical properties, morphology.	The change in mass, mechanical properties and shape is irreversible if the fibre is submerged.
2009	Agnarsson et al.[30]	Experimental: mechanical properties, morphology	Supercontraction can be used as a tool to lift object.
2009	Agnarsson[34]	Experimental: mechanical properties, morphology	Supercontraction forces are proportional to hydration rate. Faster is the process, higher is the generated stress in the fibre.
2010	Cecilia[56]	Experimental: mechanical properties, morphology, phylogenetic study	Supercontraction is predominant in orbweaver and it happens also in silks that do not present GPGXX motifs.
2010	Guinea[57]	Experimental: mechanical properties, morphology	Is the glue that makes the fibres elastomeric.
2011	Ene et al.[58]	Experimental: mechanical properties, FTIR, morphology	Supercontraction stress is formed in the amorphous region.
2011	Brown et al.[59]	Experimental: AFM, X-rays	The dimensions of the crystals seem not to change in supercontracted fibres with respect to the dry ones.
2011	Guan[60]	Experimental: mechanical properties, morphology, thermal analysis	Supercontraction is also induced by temperature, even if the main mechanisms are humidity induced.
2013	Boutry et al.[21]	Experimental: morphology, mechanical properties	Wet orb webs work better. Supercontraction affects the orb web efficiency.
2014	Shi et al.[40]	Experimental: morphology, NMR	Mobility of the proline is increased by the humidity.
2014	Jiang et al.[61]	Experimental: mechanical properties, morphology	Spider silk produced in an alternative way (extracting the silk solution from *Nephila inaurata* glands) still present supercontraction.
2015	Sampath et al.[62]	Experimental: morphology, X-rays	The crystals tend to recover the orientation after the drying process, while the amorphous region does not.
2016	Krasnov et al.[31]	Experimental + theoretical: Neutron diffusion	Higher is the tensional state of the fibre and higher is the velocity of diffusion of water molecules in it.
2017	Giesa et al.[42]	Experimental + theoretical: Raman spectroscopy	Proline is not the main mediator of supercontraction. Tyrosine and arginine are the main responsible. There is a reorganization of hydrogen bonds.
2018	Yazawa et al.[63]	Experimental: mechanical properties,	The skin layers of spider silk are not involved in supercontraction.

		supercontraction, FTIR, X-rays, NMR	
2019	Liu et al.[28]	Experimental + theoretical: mechanical properties, morphology	There is a torsion induced by humidity. The torsion is supposed to be caused by proline.
2019	Liu et al.[64]	Experimental: WGM resonator, morphology	Applications for spider silk induced by supercontraction
2019	Venkatesan et al.[65]	Experimental: mechanical properties, morphology	Artificial spider silk displays supercontraction.

In this context, the possibility to have a model to work with, i.e. artificial spider silk, could be crucial in understanding supercontraction. This is due to the fact that with a model many parameters (e.g. amino acid sequence) can be changed and then their effects directly observed.

Thus, in order to remove/reduce supercontraction in our artificial spider silk fibres we started investigating it, starting by the fact that the qualitative behaviour of our fibres is similar to the one of natural spider silk (as it has been observed recently[65]) and coupled with the fact that in our fibre there is no proline.

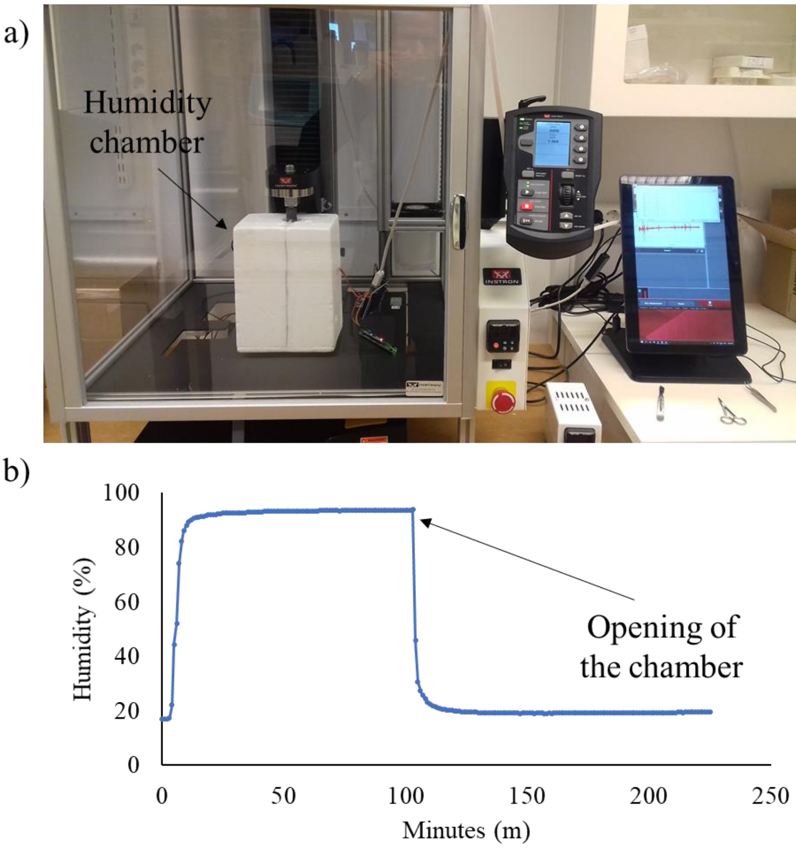

Figure 9-5: a) The climatic chamber coupled with the tensile tester and b) the plot of the humidity as a function of the time inside the chamber to verify its stability.

9.5. Supercontraction and the effect of humidity in artificial spider silk

Based on the hypothesis of Giesa et al.[42] we investigated supercontraction in the previous described control fibres (NT2RepCT) and in a mutant fibre where the tyrosine in the repetitive region was substituted with phenilalanine (Y substituted with F). This mutant, then, should have the following amino acid sequence in the repetitive region:
GNSGRGQGGFGQGSGGNAAAAAAAAAAAAAAAGQGGQGGFGR
QSQGAGSAAAAAAAAAAAAAAGSGQGGFGGQGQGGFGQSGS,
where the modification has been marked in red.

The mechanical properties of the control and the mutant fibres were the same in the dry state (Table 9-4).

To study the effect of humidity, we created a humidity chamber coupled with the mechanical tester as previously discussed (Figure 9-5). Representative stress-strain curves of the control fibres kept (at least 30 minutes) at different RH are depicted in Figure 9-6. The first aspect that can be noticed is the occurrence of the humidity effect in the interval of 60-70 % RH, coupled with the occurrence of a yielding point in the stress strain curves (Figure 9-6b). This particular aspect could be correlated with the fact that hydrated spider silk presents a higher degree of entropic energy (and thus more capability in deforming) in the initial elastic regime[39]. In particular, Keten et al.[66,67] proposed a nanomechanical model of spider silk where the yielding point occurs when the hydrogen bonds in the amorphous region break. Moreover, Savage et al.[68] proposed that hydrogen bonds energy decrease with the hydration of the fibres, leading to the premature occurrence of the yielding point with respect to the dry state. Then, an induced higher deformability can lead the fibre to reach the strain at which this additive entropic energy appears.

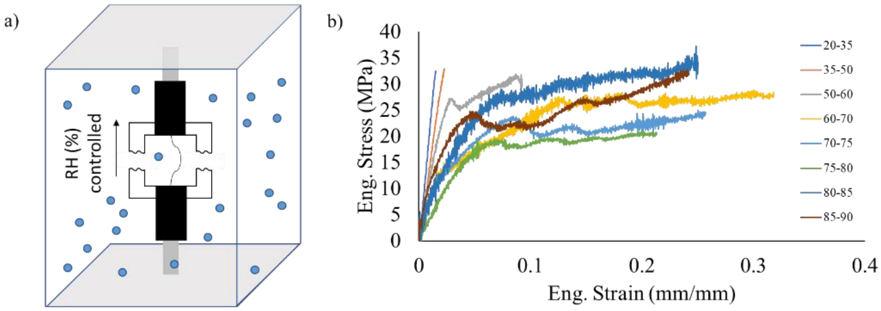

Figure 9-6: a) Schematic of the setup inside the climatic chamber and b) representative stress-strain curves of the control fibre at different humidity rates.

Figure 9-7 shows the mechanical properties of the mutant and the control fibres vs humidity rates. The increase in strain at break (Figure 9-7a), the small decrease in strength (Figure 9-7b), the decrease in Young's modulus (Figure 9-7c) and the subsequent increase in toughness (Figure 9-7d) are similar to those observed in native spider silk, with the exception of the toughness (here the silk of *Nephila* sp. has been taken as a control, Figure 9-8). The fibres were kept in a restrained configuration during the hydration at different humidity rates. This is important since it affects the mechanics of the fibres once they are dried. If they were restrained at both end, there is a recover in mechanical properties, which are equal to those of the dry fibres. This is consistent with what is normally observed in natural spider silk[55,69]. On the other hand, if the fibres were let free to contract with only one end restrained and then dried the situation is different. In particular, fibres kept at 86% (before they dissolve) had reduced strength and Young's modulus (Table 9-4).

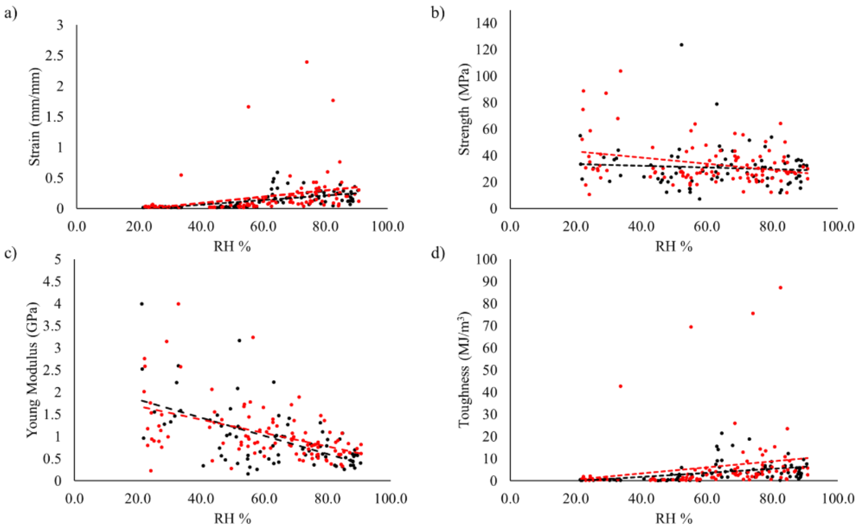

Figure 9-7: Mechanical properties vs humidity rates of the two types of fibres: control (black dots) and mutant (Red dots). a) Strain at break, b) strength, c) Young's modulus and d) toughness.

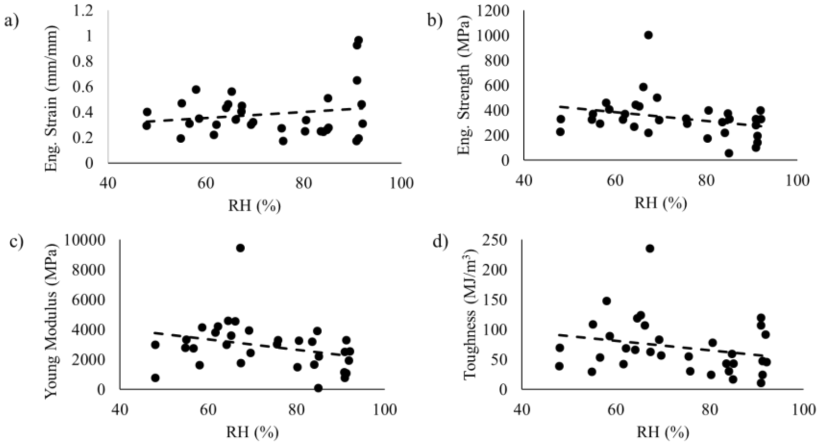

Figure 9-8: Mechanical properties vs humidity rates of the Nephila sp. silk. a) Strain at break, b) strength, c) Young's modulus and d) toughness.

The effect of humidity on our fibres occurs in a matter of minutes. We were able to observe the effect of humidity immediately when we immerged the fibres in a humid chamber with a saturated atmosphere (100% RH). This is true also for the opposite, in the sense that immediately after spinning, the fibres dried very fast. Luckily, this means that fibres that are tested immediately after spinning (freshly spun) present the same mechanical properties of the ones that are analysed few days or weeks later (Table 9-4).

Table 9-4: Mechanical properties of different artificial spider silk in different conditions.

Sample	Nr. Fibres	Diameter (mm)	Strain (mm/mm)	Strength (MPa)	Young's (GPa)	Toughness (MJ/m^3)
NT2RepCT	17	15 ± 2	0.02 ± 0.01	34 ± 10	2.0 ± 0.9	0.35 ± 0.12
NT2RepCT (Fresh spun)	16	20 ± 5	0.03 ± 0.01	36 ± 18	1.5 ± 0.8	0.63 ± 0.39
Mutant Dry	17	16 ± 5	0.03 ± 0.01	42 ± 23	1.4 ± 0.8	0.77 ± 0.54
NT2RepCT (dried after 86%)	9	18 ± 7	0.03 ± 0.01	26 ± 13	0.9 ± 0.6	0.40 ± 0.24
Mutant (dried after 86%)	13	19 ± 3	0.02 ± 0.02	22 ± 16	1.6 ± 1.1	0.29 ± 0.34

Thus, humidity seems to affect in the same way the mechanical properties of the mutant and control fibres, but differences supercontraction can be observed.

Giesa et al.[42] proposed that removing Tyrosine from the amino acid sequence would lead in a reduction of supercontraction.

In our mutant, we exchange tyrosine for phenylalanine in the repetitive region. The side chains of phenylalanine and tyrosine are similar, but the tyrosine side chain contains a hydroxyl group which makes it able to donate and accept hydrogen bonds. Thus, if hydrogen bonds mediated by tyrosine play a major role in supercontraction, replacing tyrosine for phenylalanine should have an effect on the supercontraction of the fibre. In fact, we were able to see a reduction in supercontraction in the mutant fibres. In Figure 9-9 it is possible to see the effect of humidity at different RH on the length and the diameter of the fibres is shown.

The mutant fibre presented a reduced supercontraction, suggesting the validity of the hypothesis. In particular, from the graphs it is clear that the supercontraction occurs at higher humidity. This was supported by AFM images of mutant fibres (Figure 9-10), where a change in the surface morphology occurred at higher humidity. Moreover, mutant fibres did not dissolve at 88%, but at 100%. Experiments to retrieve structural data (such as FTIR spectroscopy) are now ongoing to detect changes in the secondary structure.

We are, thus, on the right way to reduce the effect of water on artificial spider silk fibres, even if we are still looking for their improvement in mechanical properties. Moreover, our system can reveal the molecular events associated with supercontraction by studying the model that we are able to spin.

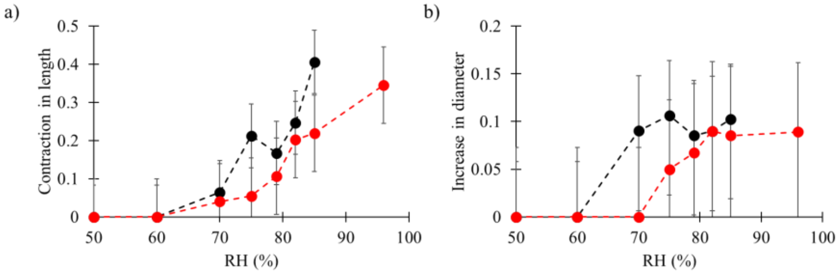

Figure 9-9: a) Contraction in length vs humidity rates of the two types of fibres: original (black dots) and mutant (red dots). b) Increase in diameter of the two types of fibres: original (black dots) and mutant (red dots).

9.6. How to improve the mechanical properties of the artificial spider silk?

As previously mentioned, the overall mechanical properties of our fibres do not correspond or are close to the ones of native spider silk (Figure 9-8).

In order to improve them, we explored the various aspects that are involved in our spinning setup. For example, we have to consider that in spinning of artificial spider silk both mechanical forces and chemistry play crucial roles, e.g. increasing the shear forces has been demonstrated to be a good tool to improve the strength of the fibres[33,70].

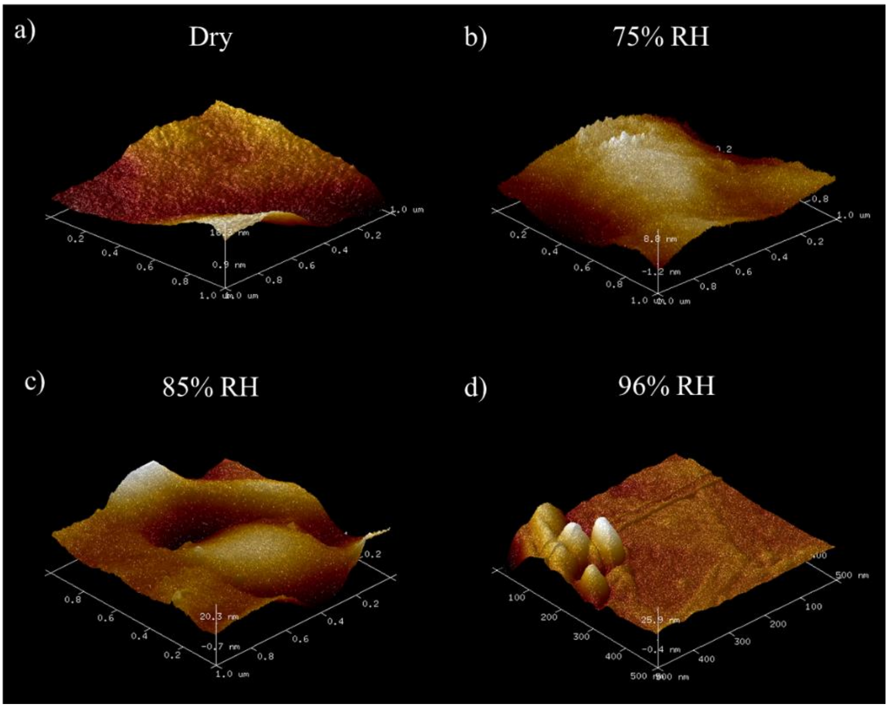

Figure 9-10: AFM images of the surface of the mutant fibres kept for 2 hours at different humidies. a-b) Dry fibres and those that were kept at 75% present a smooth surface. c) At 85% the fibres looked less smooth by with the formation of bubble-like structures on the surface. d) At 96% pillar-bubble-like structures appear, indicating that the fibre is dissolving.

Initially, we noticed that fibres that were kept longer in the spinning bath presented superior mechanical properties with respect the one that were immediately removed from it and consequently dried. In order to keep them in the bath, after the spinning we rolled them on to a plastic roller and kept the entire roller in the bath. We created different setups of fibres that were kept in the bath at different amount of time. After that, we collected the fibres from the roller and let them dry. The mechanical properties were tested as described above and the results are presented in Table 9-5. We performed this procedure for both the mutant and the control fibres (NT2RepCT).

Table 9-5: The mechanical properties of the fibres that were kept longer in the bath.

Sample	Inc. time (hr)	Nr. samples	Diameter (μm)	Strain at break (mm/mm)	Strength (MPa)	Young's modulus (GPa)	Toughness (MJ/m^3)	In water
Mutant	0	17	16 ± 5	0.03 ± 0.01	42 ± 23	1.4 ± 0.8	0.77 ± 0.54	Diss.
Control	0	10	15 ± 2.4	0.02 ± 0.01	34 ± 11	2.0 ± 0.9	0.35 ± 0.12	Diss.
Control	1	6	23 ± 10	0.14 ± 0.19	70 ± 44	2.3 ± 1.0	11 ± 20	Diss.
Control	2	5	15 ± 7	0.37 ± 0.56	80 ± 64	2.4 ± 1.7	40 ± 70	Diss.
Mutant	3	11	31 ± 15	0.11 ± 0.11	43 ± 23	1.6 ± 1.1	4.9 ± 7.8	Diss.
Control	3	8	29 ± 12	0.07 ± 0.05	38 ± 17	1.2 ± 0.5	1.1 ± 0.7	Diss.
Control	5	29	22 ± 6	0.05 ± 0.04	54 ± 36	1.9 ± 1.0	1.8 ± 2.5	Not diss.
Mutant	5	9	14 ± 11	0.39 ± 0.32	27 ± 18	0.8 ± 0.4	8.8 ± 10.4	Diss.
Control	5.5	19	22 ± 11	0.11 ± 0.13	48 ± 28	1.8 ± 1.1	4.9 ± 8.0	Not diss.
Mutant	5.5	1	9	0.79	32	0.7	21	Not diss.
Control	6	34	16 ± 8	0.33 ± 0.39	68 ± 30	2.4 ± 1.1	25 ± 34	Not diss.
Mutant	6	13	9 ± 3	0.26 ± 0.22	49 ± 34	1.8 ± 1.1	13 ± 21	Not diss.
Control	24	17	15 ± 5	0.15 ± 0.23	58 ± 31	2.3 ± 1.1	11 ± 22	Not diss.
Mutant	24	3	17 ± 4	0.03 ± 0.02	30 ± 28	1.3 ± 1.2	0.35 ± 0.31	Not diss.
Control	48	2	13 - 22	0.2	3-4	157-234	0.01-0.02	Not diss.
Mutant	48	10	23 ± 7	0.05 ± 0.03	8 ± 8	408 ± 610	0.18 ± 0.17	Not diss.

Since the handling of the fibres was high during the experiments, we noticed a huge scattering of the data, making hard to get any information (we did not exclude any data point).

We still are trying to understand the cause of this variability with the support of structural data, but it might be that the drying process (and then also the extraction of the fibres from the bath) causes irreversible changes in the fibres. Unfortunately, the shape of the fibres was not improved after the prolonged bath. In fact, the dumbbell shape persisted after this treatment (Figure 9-11). This led to an underestimation of the mechanical properties (especially the strength) for the same reasons as described above.

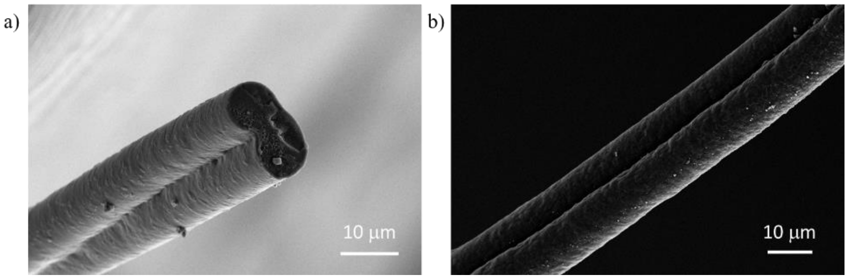

Figure 9-11: a) Fracture section of a fibre kept longer in the bath and b) its general shape.

The improvement of the mechanical properties was observed especially for the deformability of the fibres, which improved conspicuously even after 1 hour. The improvement of the strength was not big enough to justify this treatment, but this result could be obfuscated by the scattering. What is clear, however, is the fact that after 24 hours of incubation the fibres started to deteriorate the mechanical properties. What is interesting, on the other hand, is the fact that after 5 hours for the control and after 5.5 hours for the mutant, we obtained fibres that did not dissolve when immersed in water. This is certainly a good improvement in order to possibly apply these kinds of fibres in tissue engineering.

Finally, even if the ongoing work has to explain many features about the mechanical properties of artificial spider silk, we are happy about the preliminary results that we achieved in improving their mechanical efficiency.

9.7. References

1. Andrade, M.C.B. Female hunger can explain variation in cannibalistic behavior despite male sacrifice in redback spiders. Behav. Ecol. 1998, 9, 33–42.
2. Bilde, T.; Lubin, Y. The evolution of sociality in spiders. Adv. study Behav. 2007, 37.
3. Rising, A.; Johansson, J. Toward spinning artificial spider silk. Nat. Chem. Biol. 2015, 11, 309–315.
4. Fahnestock, S.R.; Bedzyk, L.A. Production of synthetic spider dragline silk protein in *Pichia pastoris*. Appl. Microbiol. Biotechnol. 1997, 47, 33–39.
5. Scheller, J.; Conrad, U. Production of Spider Silk Proteins in Transgenic Tobacco and Potato. Mol. Farming Plant-made Pharm. Tech. Proteins 2005, 19, 171–181.
6. Lazaris, A.; Arcidiacono, S.; Huang, Y.; Zhou, J.F.; Duguay, F.; Chretien, N.; Welsh, E.A.; Soares, J.W.; Karatzas, C.N. Spider silk fibers spun from soluble recombinant silk produced in mammalian cells. Science (80). 2002, 295, 472–476.
7. Fahnestock, S.R.; Irwin, S.L. Synthetic spider dragline silk proteins and their production in Escherichia coli. Appl. Microbiol. Biotechnol. 1997, 47, 23–32.
8. Xu, J.; Dong, Q.; Yu, Y.; Niu, B.; Ji, D.; Li, M.; Huang, Y.; Chen, X.; Tan, A. Mass spider silk production through targeted

gene replacement in *Bombyx mori*. Proc. Natl. Acad. Sci. 2018, 115, 8757–8762.

9. Oliveira, P.F.; Christiansen, D.; Ghazi, A.; Jones, J.; Lewis, R. V Large Scale Production of Spider Silk Protein in *E. coli*. 1, 8434, 2017
10. Edlund, A.M.; Jones, J.; Lewis, R.; Quinn, J.C. Economic feasibility and environmental impact of synthetic spider silk production from *Escherichia coli*. N. Biotechnol. 2018, 42, 12–18.
11. Astudillo, M.F.; Thalwitz, G.; Vollrath, F. Life cycle assessment of Indian silk. J. Clean. Prod. 2014, 81, 158–167.
12. Andersson, M.; Jia, Q.; Abella, A.; Lee, X.Y.; Landreh, M.; Purhonen, P.; Hebert, H.; Tenje, M.; Robinson, C. V.; Meng, Q.; et al. Biomimetic spinning of artificial spider silk from a chimeric minispidroin. Nat. Chem. Biol. 2017, 13, 262–264.
13. Andersson, M.; Chen, G.; Otikovs, M.; Landreh, M.; Nordling, K.; Kronqvist, N.; Westermark, P.; Jörnvall, H.; Knight, S.; Ridderstråle, Y.; et al. Carbonic Anhydrase Generates CO2and H+That Drive Spider Silk Formation Via Opposite Effects on the Terminal Domains. PLoS Biol. 2014, 12, 1–15.
14. Singh, K.; Maity, S.; Singha, M. Spinning and applications of spider silk. Text. Trends 2012, 55, 29–34.
15. Yang, Y.; Greco, G.; Maniglio, D.; Migliaresi, C.; Pugno, N.; Motta, A. Spider (*Linothele megatheloides*) and silkworm (*Bombyx mori*) silks: Comparative physical and biological evaluation. Mater. Sci. Eng. C 2019, 110197.
16. Denny, M.W. the Physical Properties of Spider'S Silk and Their Role in the Design of Orb-Webs. J. Exp. Biol. 1976, 65, 483–506.
17. Sanjeevi, R. A viscoelastic model for the mechanical properties of biological materials. J Biomech 1982, 15, 107–109.
18. Andersson, M.; Johansson, J.; Rising, A. Silk spinning in silkworms and spiders. Int. J. Mol. Sci. 2016, 17, 1–14.
19. Xia, X.-X.; Qian, Z.-G.; Ki, C.S.; Park, Y.H.; Kaplan, D.L.; Lee, S.Y. Native-sized recombinant spider silk protein produced in metabolically engineered *Escherichia coli* results in a strong fiber. Proc. Natl. Acad. Sci. 2010, 107, 14059–14063.
20. Bowen, C.H.; Dai, B.; Sargent, C.J.; Bai, W.; Ladiwala, P.; Feng, H.; Huang, W.; Kaplan, D.L.; Galazka, J.M.; Zhang, F. Recombinant Spidroins Fully Replicate Primary Mechanical

Properties of Natural Spider Silk. Biomacromolecules 2018, 19, 3853–3860.

21. Boutry, C.; Blackledge, T.A. Wet webs work better: humidity, supercontraction and the performance of spider orb webs. J. Exp. Biol. 2013, 216, 3606–3610.
22. Tow, K.H.; Chow, D.M.; Thévenaz, L.; Vollrath, F.; Ox, O. Weaving our way towards a new generation of fibre-optic chemical sensors based on spider silk.
23. Hey, K.; Chow, D.M.; Vollrath, F.; Dicaire, I.; Gheysens, T. Towards a new generation of fibre-optic chemical sensors based on spider silk threads. 2017, 10323, 1–4.
24. Hey Tow, K.; Chow, D.M.; Vollrath, F.; Dicaire, I.; Gheysens, T.; Thévenaz, L. Towards a novel "silky" way to detect chemical species using spider threads. 1st Int. Conf. Opt. Photonics Mater. NICE Opt. 2016, 1237021.
25. Shao, Z.; Vollrath, F. The effect of solvents on the contraction and mechanical properties of spider silk. Polymer (Guildf). 1999, 40, 1799–1806.
26. Work, R.W. Dimensions, Birefringences, and Force-Elongation Behavior of Major and Minor Ampullate Silk Fibers from Orb-Web-Spinning Spiders—The Effects of Wetting on these Properties. Text. Res. J. 1977, 47, 650–662.
27. Work, R. A comparative study of the supercontraction of major ampullate silk fibers of orb-web-building spiders (Araneae). J. Arachnol. 1981, 299–308.
28. Liu, D.; Tarakanova, A.; Hsu, C.C.; Yu, M.; Zheng, S.; Yu, L.; Liu, J.; He, Y.; Dunstan, D.J.; Buehler, M.J. Spider dragline silk as torsional actuator driven by humidity. Sci. Adv. 2019, 5, eaau9183.
29. Guinea, G. V.; Elices, M.; Pérez-Rigueiro, J.; Plaza, G. Self-tightening of spider silk fibers induced by moisture. Polymer (Guildf). 2003, 44, 5785–5788.
30. Agnarsson, I.; Dhinojwala, A.; Sahni, V.; Blackledge, T.A. Spider silk as a novel high performance biomimetic muscle driven by humidity. J. Exp. Biol. 2009, 212, 1990–1994.
31. Krasnov, I.; Seydel, T.; Greving, I.; Blankenburg, M.; Vollrath, F.; Müller, M. Strain-dependent fractional molecular diffusion in humid spider silk fibres. J. R. Soc. Interface 2016, 13, 20160506.
32. Liu, Y.; Shao, Z.; Vollrath, F. Relationships between supercontraction and mechanical properties of spider silk. Nat. Mater. 2005, 4, 901–905.

33. Perez-Rigueiro, J. The effect of spinning forces on spider silk properties. J. Exp. Biol. 2005, 208, 2633–2639.
34. Agnarsson, I.; Boutry, C.; Wong, S.C.; Baji, A.; Dhinojwala, A.; Sensenig, A.T.; Blackledge, T.A. Supercontraction forces in spider dragline silk depend on hydration rate. Zoology 2009, 112, 325–331.
35. Holland, G.P.; Lewis, R. V.; Yarger, J.L. WISE NMR Characterization of Nanoscale Heterogeneity and Mobility in Supercontracted Nephila clavipes Spider Dragline Silk. J. Am. Chem. Soc. 2004, 126, 5867–5872.
36. Eles, P.T.; Michal, C.A. Strain Dependent Local Phase Transitions Observed during Controlled Supercontraction Reveal Mechanisms in Spider Silk. Macromolecules 2004, 37, 1342–1345.
37. Liu, Y.; Sponner, A.; Porter, D.; Vollrath, F. Proline and processing of spider silks. Biomacromolecules 2008, 9, 116–121.
38. Savage, K.N.; Gosline, J.M. The role of proline in the elastic mechanism of hydrated spider silks. J. Exp. Biol. 2008, 211, 1948–1957.
39. Savage, K.N.; Gosline, J.M. The effect of proline on the network structure of major ampullate silks as inferred from their mechanical and optical properties. J. Exp. Biol. 2008, 211, 1937–1947.
40. Shi, X.; Yarger, J.L.; Holland, G.P. Elucidating proline dynamics in spider dragline silk fibre using 2H-13C HETCOR MAS NMR. Chem. Commun. 2014, 50, 4856–4859.
41. Pérez-rigueiro, J.; Madurga, R.; Gañán-calvo, A.M.; Elices, M.; Tasei, Y.; Nishimura, A.; Matsuda, H. Emergence of supercontraction in regenerated silkworm (*Bombyx mori*) silk fibers. Sci. Rep. 2019, 9, 1–14.
42. Giesa, T.; Schuetz, R.; Fratzl, P.; Buehler, M.J.; Masic, A. Unraveling the Molecular Requirements for Macroscopic Silk Supercontraction. ACS Nano 2017, 11, 9750–9758.
43. WORK, R.W. Viscoelastic behaviour and wet supercontraction of major ampullate silk fibres of certain orb-web-Building Spiders (Araneae). J. Exp. Biol. 1985, 118, 379 LP – 404.
44. Vollrath, F.; Edmonds, D.T. Modulation of the mechanical properties of spider silk by coating with water. Nature 1989, 340, 305–307.
45. Edmonds, D.T.; Vollrath, F. The Contribution of Atmospheric Water Vapour to the Formation and Efficiency of a Spider’s Capture Web. Proc. R. Soc. B Biol. Sci. 1992, 248, 145–148.

46. Bonthrone, K.M.; Vollrath, F.; Hunter, B.K.; Sanders, J.K.M. The elasticity of spiders' webs is due to water-induced mobility at a molecular level. Proc. R. Soc. Lond. B 1992, 248, 141–144.
47. Parkhe, A.D.; Seeley, S.K.; Gardner, K.; Thompson, L.; Lewis, R. V. Structural studies of spider silk proteins in the fiber. J. Mol. Recognit. 1997, 10, 1–6.
48. Grubb, D.T.; Ji, G. Molecular chain orientation in supercontracted and re-extended spider silk. Int. J. Biol. Macromol. 1999, 24, 203–210.
49. Shao, Z.; Vollrath, F. The effect of solvents on spider silk studied by mechanical testing and single-fibre Raman spectroscopy. Int. J. Biol. Macromol. 1999, 24, 295–300.
50. Bell, F.I.; McEwen, I.J.; Viney, C. Fibre science: Supercontraction stress in wet spider dragline. Nature 2002, 416, 37.
51. Pérez-Rigueiro, J.; Elices, M.; Guinea, G. V. Controlled supercontraction tailors the tensile behaviour of spider silk. Polymer (Guildf). 2003, 44, 3733–3736.
52. Elices, M.; Perez-Rigueiro, J.; Plaza, G. Recovery in Spider Silk Fibers. 2004, 20–24.
53. Guinea, G. V.; Elices, M.; Pérez-Rigueiro, J.; Plaza, G.R. Stretching of supercontracted fibers: a link between spinning and the variability of spider silk. J. Exp. Biol. 2005, 208, 25–30.
54. Plaza, G.R.; Corsini, P.; Pérez-Rigueiro, J.; Marsano, E.; Guinea, G. V.; Elices, M. Effect of Water on Bombyx mori Regenerated Silk Fibers and Its Application in Modifying Their Mechanical Properties. J. Polym. Sci. 2008, 109, 1793–1801.
55. Blackledge, T.A.; Boutry, C.; Wong, S.-C.; Baji, A.; Dhinojwala, A.; Sahni, V.; Agnarsson, I. How super is supercontraction? Persistent versus cyclic responses to humidity in spider dragline silk. J. Exp. Biol. 2009, 212, 1981–9.
56. Boutry, C.; Blackledge, T.A. Evolution of supercontraction in spider silk: structure-function relationship from tarantulas to orb-weavers. J. Exp. Biol. 2010, 213, 3505–3514.
57. Guinea, G. V.; Cerdeira, M.; Plaza, G.R.; Elices, M.; Pérez-Rigueiro, J. Recovery in viscid line fibers. Biomacromolecules 2010, 11, 1174–1179.
58. Ene, R.; Papadopoulos, P.; Kremer, F. Supercontraction in Nephila spider dragline silk - Relaxation into equilibrium state. Polymer (Guildf). 2011, 52, 6056–6060.
59. Brown, C.P.; MacLeod, J.; Amenitsch, H.; Cacho-Nerin, F.; Gill, H.S.; Price, A.J.; Traversa, E.; Licoccia, S.; Rosei, F. The critical

role of water in spider silk and its consequence for protein mechanics. Nanoscale 2011, 3, 3805–3811.

60. Guan, J.; Vollrath, F.; Porter, D. Two mechanisms for supercontraction in Nephila spider dragline silk. Biomacromolecules 2011, 12, 4030–4035.
61. Jiang, P.; Marí-Buyé, N.; Madurga, R.; Arroyo-Hernández, M.; Solanas, C.; Gañán, A.; Daza, R.; Plaza, G.R.; Guinea, G. V.; Elices, M.; et al. Spider silk gut: Development and characterization of a novel strong spider silk fiber. Sci. Rep. 2014, 4, 1–7.
62. Sampath, S.; Yarger, J.L. Structural hysteresis in dragline spider silks induced by supercontraction: An X-ray fiber micro-diffraction study. RSC Adv. 2015, 5, 1462–1473.
63. Yazawa, K.; Malay, A.D.; Masunaga, H.; Numata, K. Role of Skin Layers on Mechanical Properties and Supercontraction of Spider Dragline Silk Fiber. Macromol. Biosci. 2018, 19, 1–7.
64. Liu, Z.; Liu, W.; Hu, C.; Zhang, Y.; Yang, X.; Zhang, J.; Yang, J.; Yuan, L. Natural spider silk as a photonics component for humidity sensing. Opt. Express 2019, 27, 21946.
65. Venkatesan, H.; Chen, J.; Liu, H.; Kim, Y.; Na, S.; Wei Liu; Hu, J. Artificial spider silk is smart like natural one: having humidity-sensitive shape memory with superior recovery stress. Mater. Chem. Front. 2019, 3, 2472–2482.
66. Keten, S.; Xu, Z.; Ihle, B.; Buehler, M.J. Nanoconfinement controls stiffness, strength and mechanical toughness of Β-sheet crystals in silk. Nat. Mater. 2010, 9, 359–367.
67. Keten, S.; Buehler, M.J. Nanostructure and molecular mechanics of spider dragline silk protein assemblies. J. R. Soc. Interface 2010, 7, 1709–1721.
68. Savage, K.N.; Gosline, J.M. The effect of proline on the network structure of major ampullate silks as inferred from their mechanical and optical properties. J. Exp. Biol. 2008, 211, 1937–1947.
69. Agnarsson, I.; Dhinojwala, A.; Sahni, V.; Blackledge, T.A. Spider silk as a novel high performance biomimetic muscle driven by humidity. J. Exp. Biol. 2009, 212, 1990–1994.
70. Koeppel, A.; Laity, P.R.; Holland, C. Extensional flow behaviour and spinnability of native silk. Soft Matter 2018, 8838–8845.

10. CONCLUSIONS AND OUTLOOK

In the end of this thesis the reader might have noticed the potential uses of spider silks. The material itself is so fascinating that it has always played an important role in affecting our culture.

In chapter 4 the role of junctions in orb webs has been explained. These are necessary to improve the mechanical efficiency and robustness of the webs. For our perspective, these junctions could be an inspiration in design new fabrics with superior mechanical properties.

One of the features that contributes to the efficiency of these junctions is the piriform silk, which has been explored in chapter 5. Its remarkable mechanical properties, normally neglected in the models, are essential in the mechanics of the silk anchorages. These data could be used as informative for developing model and adhesives with high mechanical efficiency.

New spider silks are always interesting to be studied, as demonstrated in chapter 6. In this, we explore the biomedical potential of the silk of *Linothele megatheloides*, which presents better biological properties with respect to the more common silkworm silk.

In chapter 7, the potential uses of spider dragline silk as a support for bone tissue engineering have been presented. In particular, it has been shown that the mechanical properties of the obtained hybrid material (hydroxyapatite and spider silk) are still desirable, and are suitable for the purpose.

In chapter 8 we described the potential of a new technique used to developed biomedical films, which are made by silkworm silk. This technique could be used in spider silk technology, especially by considering the new emergent protocols to deal and treat recombinant spider silk solutions.

In order to scale spider silk, in chapter 9 we investigated the mechanical properties of artificial spider silk. We showed how these change at different humidity rates and how it is possible to reduce the effect of the humidity by modifying the primary structure of the spider silk protein. Moreover, we briefly explored the effect of prolonged incubation time (in the spinning bath) on the mechanical properties of artificial spider silk.

We think that the outputs of this work are good starting points on which we can build our future works on spider silks.

11. PERSONAL CONSIDERATION

I would like to finish this PhD thesis with its contextualization in my life. I think that these three years have been one of the most important part of my life. This is not because they represent the end of a prestigious academic recognition, but they have been the realization of one of my life's goals: working with spiders.

Since I was 5 years old (as far as evidences support me, Figure 11-1a), I was fascinated by spiders. The experience with them has consequently increased by exploring the scientific literature, improving my experience in breeding spiders in captivity. This led me to become an active and founder member of Aracnofilia (Italian Arachnological Society).

Figure 11-1: a) My 6th birthday's cake as the first evidence of my passion and b) my master's celebration cake.

As a consequence, my experience in connecting different topics from various scientific (and not) areas improved, when related to spiders. This is probably why I did my master thesis in physics on the mechanical properties of spider silk, thanks to the supervision of Nicola Pugno and Federico Montoncello (Figure 11-1b).

After started my PhD, during the first Silk Conference (Sheffield 2017, Figure 11-2a) I had the possibility to connect my passion with the outstanding works of many scientists around the world (some of them have contributed tremendously to my PhD). The variety of works, different in topics and methodologies, led me to understand the importance of exploration in spider silk science. Fortunately, I validated my guess in the Silk Conference in Trento (where I played a role in the local committee, Figure 11-2b) by meeting again the same people who inspired me so far.

And here my passion comes. Nowadays, my collection of spiders (more than 40 species and more than 300 animals) gives me the possibility to explore the huge variety of features of spiders, silk included.

My ability in handling spiders and my knowledge on their biology is essential for my work to scout unexplored area of the silk knowledge, giving me an interdisciplinary approach to the issue.

Although I have just made the first step in the spider silks research field, I am truly excited about what can possibly happen to me in the future, which I hope to be spider's involved.

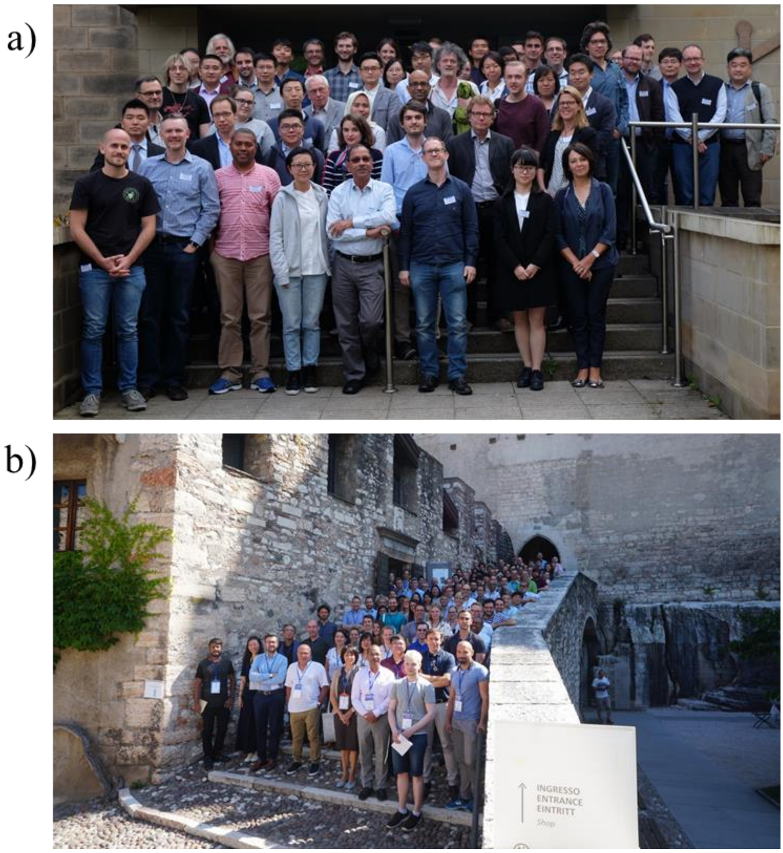

Figure 11-2: a) The first Silk Conference (2017, Sheffield) that I have attended; b) the last Silk Conference (2019, Trento) where I was a part of the local committee.

12. ACKNOWLEDGEMENTS

This work has seen many contributors. I had indeed the great opportunity to work with people who shown me their personal and professional values.

Above all, my supervisor Nicola and my colleague Fiorella. They thought me how to move properly in the academic environment (with a bunch of errors of mine) and how to improve myself by focusing on my skills and my personality. Moreover, this work and my experiences have been possible because of the funding availability of my supervisor.

I have to thank Anna Rising (and her beautiful family) for the hospitality. She has been the person who made me feel at home when I was very far from it. Because of this, I had the possibility to work productively and peacefully in Sweden.

My family and my friends have been important for the support. Among them, my cousin and mentor Nicola taught me wisely and guided me in this challenging path. My flatmate and friend Livia taught me a lot about English and helped me to correct some parts of this work.

I must, moreover, to acknowledge four special persons.

My mother, who cheers for me and supports me with her remarkable life’s example.

Carlo Maria Legittimo (president of Aracnofilia) for being my best friend and spiders’ mentor.

Mauro, my mountain’s friend. He thought me everything about mountains and bears. He offered me a way to escape from the exhausting life of the city and relax my mind. If I have finished these 3 years with the smile, it has been also because of him.

Virginia, the woman who literally changed my life and helped me to find my own equilibrium. If I am building something now, it is because she is the foundation of it.

13. APPENDIX

In this appendix are reported (with the relative permission) all the papers that have been not used as a base for the previous chapters, but that are important in the thesis contextualization.

A.

Materials Today: Proceedings 7 (2019) 418–425

DOI: https://doi.org/10.1016/j.matpr.2018.11.104

Being an author of the related paper, no special permission is required.

Fluid-structure interaction study of spider's hair flow-sensing system

Roberto Guarino[a], Gabriele Greco[a,b], Barbara Mazzolai[b], Nicola M. Pugno[a,c,d]

[a]Laboratory of Bio-Inspired & Graphene Nanomechanics, Department of Civil, Environmental and Mechanical Engineering, University of Trento, Via Mesiano 77, 38123 Trento, Italy

[b]Center for Micro-BioRobotics@SSSA, Istituto Italiano di Tecnologia, Viale Rinaldo Piaggio 34, 56025 Pontedera, Italy

[c]Ket Lab, Edoardo Amaldi Foundation, Italian Space Agency, Via del Politecnico snc, 00133 Rome, Italy

[b]School of Engineering and Materials Science, Queen Mary University of London, Mile End Road, London E1 4NS, United Kingdom

Abstract

In the present work we study the spider's hair flow-sensing system by using fluid-structure interaction (FSI) numerical simulations. We observe experimentally the morphology of *Theraphosa stirmi*'s hairs and characterize their mechanical properties through nanotensile tests. We then use the obtained information as input for the computational model. We study the effect of a varying air velocity and a varying hair spacing on the mechanical stresses and displacements. Our results can be of interest for the design of novel bio-inspired systems and structures for smart sensors and robotics.

1. Introduction

The ability of spiders in colonizing many habitats is also due to the fact that they interact efficiently with other animals for catching preys, escaping from predators and detecting potential partners also during the night. Spiders present a very complex and advanced sensing system based on tactile (or mechanical) [1-4], chemical [5,6] and air flow receptors [7-9] such as the hairs. These latter structures interact with the air velocity field and provide the spider with information regarding the surrounding environment [10,11], representing one of the most sensitive biosensors in Nature [12]. Since their extraordinary sensibility and efficiency, the interest in designing bio-inspired sensing systems and structures for soft robotics and high-tech applications has increased in the last decade [13-15].

Several numerical simulation works are available in the literature, but they are mainly related, for instance, to the engineering design and analysis of bio-inspired micro electro-mechanical systems (MEMS) (see, e.g., Ref. [16]). Numerical studies on the biological structures, in fact, are still poorly addressed and further investigations are needed in order to characterize the performance of spiders' hairs.

In this work, we employ fluid-structure interaction (FSI) simulations to study the behavior of spider's hairs in air. We investigate the effect of a varying flow velocity on the sensing capabilities, quantified in terms of displacements and von Mises stresses; and of a varying spacing of the hairs. The morphology of the hairs and their elastic properties are obtained experimentally, through Scanning Electron Microscopy (SEM), optical microscopy and nanotensile tests, and are used as inputs in the numerical simulations.

2. Materials and methods

2.1. Sample preparation

The hairs are obtained from an exoskeleton of Theraphosa stirmi kept under controlled feeding and environmental conditions. The tested samples are prepared following the same procedure reported by Blackledge et al. [17]. We stick the hair samples on a paper frame provided with a square window of 5 mm side. The hair sample is fixed on the paper frame with a double-sided tape coupled with a glue.

2.2. Morphology and mechanical properties

For the morphology characterization by SEM, we use a Zeiss Supra 40 (Carl Zeiss AG, Germany) at 2.30 kV. The metallization is made by using a sputtering machine Q150T (Quorum Technologies Ltd, UK) and the sputtering mode is Pt/Pd 80:20 for 5 minutes. In addition, we employ optical microscopy (Carl Zeiss AG, Germany) at 10x magnification for the extraction of an average value of the hair diameter.

For the mechanical characterization, we use a T150 UTM nanotensile machine (Agilent Technologies Inc., USA) with a 500 mN load cell. The displacement speed is 10 μm s-1 with the frequency load at 20 Hz. The declared sensitivity of the machine is 10 nN for the load and 1 Å for the displacement in the dynamic configuration.

2.3. Numerical simulations

The FSI simulations are carried out in COMSOL Multiphysics® [18]. We employ two-way coupling in order to have a comprehensive understanding of the interaction between fluid flow and mechanical displacements [19].

A single spider's hair is considered and it is approximated with a truncated cone of height L = 1000 μm, base diameter D_b = 30 μm and tip diameter D_t = 15 μm. The computational domain for the fluid flow is composed of a 3D box of width 100 μm and height 1200 μm, with inlet and outlet positioned 1000 μm before and after the hair, respectively. Moreover, a chitin of thickness h = 100 μm is considered below the hair. We assign linear elastic material properties, using a Young's modulus E = 600 MPa (i.e. in the order of the measured value), a Poisson's ratio v = 0.25 and a density ρ_h = 1425 kg m-3 (taken close to the respective values for chitin [20]). For the air, we consider its properties at 300 K, i.e. density ρ_a = 1.177 kg m-3 and dynamic viscosity μ_a = 1.85·10-5 kg m-1 s-1 [21]. A constant fluid velocity is imposed at the inlet and the domain is delimited by walls with full-slip boundary conditions. The whole domain is discretized with about 4.5·105 tetrahedral elements.

The inlet velocity is chosen from 0.1 to 1 m s^{-1}, which is in the range of the velocity field measured around flying insects [10]. The corresponding maximum von Mises stress $\sigma_{\max}$ and maximum displacement $\delta_{\max}$ is measured. An additional analysis is carried out on the hair spacing, considering two hairs on the same transversal coordinate, but positioned from 50 to 1000 μm from each other. In this case, the differences in $\sigma_{\max}$ and $\delta_{\max}$ are monitored, for a constant mean inlet velocity u_{avg} = 1 m s^{-1}.

3. Results

3.1. Morphology and mechanical properties

Fig. 1 shows the SEM images of different hair typologies found on the spiders' exoskeleton. We can observe a typical length from a few hundreds of μm to 1-2 mm and a variable diameter, with a tip size usually in the range 1-20 μm. The typical hair spacing is a few mm, i.e. in the order of the hair length. Usually, shorter hairs not involved in flow-sensing are also present on the spider's cuticle and are not shown here, for brevity.

The stress-strain curves extracted from the nanotensile test on different hairs are shown in Fig. A1. The mechanical properties of the hairs are intrinsically variable, because of their biological nature, and we have measured an initial Young's modulus in the range 500-800 MPa using linear regression, with a fracture strain in the order of 0.5 mm mm-1. In Fig. A2, we show a *Theraphosa stirmi* of the collection and an optical microscopy investigation. The average diameter of the hairs is around 30 μm.

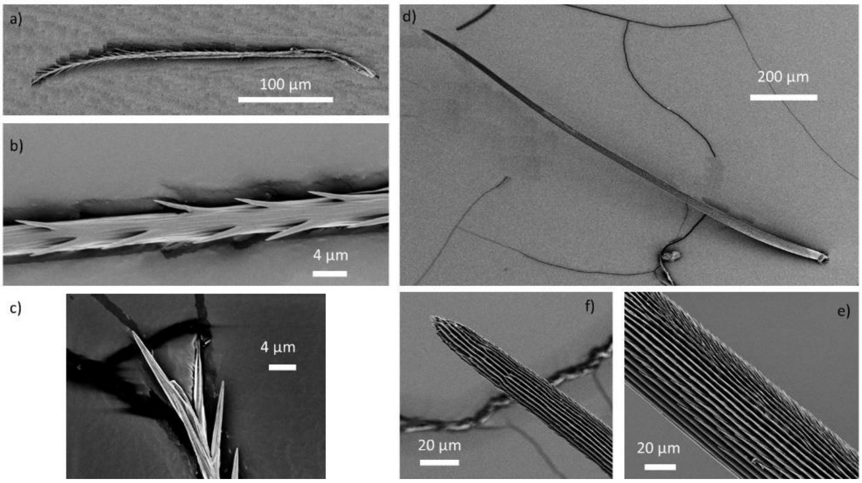

Figure 1: SEM morphology of different hairs found on the spider's exoskeleton.

3.2. Effect of a varying air flow

Fig. 2 shows the values of $\sigma_{\max}$ and $\delta_{\max}$ as function of the mean inlet velocity, as well as the von Mises stress distribution together with the qualitative flow streamlines. We can observe that both the stress and the displacement scale linearly with u_{avg}.

A rough estimation of the mechanical load can be obtained by considering a beam, here approximated as a cylinder with diameter $D_{avg} = \left(D_b + D_t\right)/2$, clamped at one end. We can assume that the fluid flow exerts a constant force per unit length, which, denoting by C_D the dimensionless drag coefficient, is given by:

$$f_D = \frac{1}{2}\rho_a C_D D_{avg} u_{avg}^2 \tag{1}$$

Neglecting the shear deformation, the displacement at the tip of the beam is given by:

$$\delta_{\max} \approx \frac{f_D L^4}{8EI} = \frac{4\rho_a C_D L^4}{\pi E D_{avg}^3} u_{avg}^2 \tag{2}$$

where we have inserted the expression of the maximum bending moment, equal to $f_D L^2/2$, and the moment of inertia of the section, i.e. $I = \pi D_{avg}^4/64$.

For a cylinder immersed in a laminar flow, for low Reynolds numbers Re and considering constant fluid properties, the drag coefficient depends on the flow velocity roughly as [22]:

$$C_D = C_D\left(u_{avg}\right) : Re^{-1} : u_{avg}^{-1} \qquad (3)$$

Therefore, inserting Eq. (3) into Eq. (2), we get the observed linear relationship between maximum hair displacement and average inlet velocity, i.e. $\delta_{max} : u_{avg}$. An analogous reasoning can be made on the von Mises stress, except for the fact that its expression is more complicated because it must include, together with the bending stress, also a shear term and the stresses deriving from the substrate. For simplicity, considering only the maximum bending stress $\sigma_{b,\max}$:

$$\sigma_{b,\max} \approx \frac{f_D L^2}{2EI}\frac{D_{avg}}{2} = \frac{8\rho_a C_D L^2}{\pi E D_{avg}^2} u_{avg}^2$$

(4)

and again, from Eq. (3), we get a law of the type $\sigma_{b,max} : u_{avg}$ as shown in Fig. 2.

In addition, we can fit the values of the maximum displacement with a law of the type $\delta_{\max} = K u_{avg}$, obtaining $K \approx 1.943 \cdot 10^{-6}$ s (R^2-value 0.9944). Consequently, the numerically-derived expression of the drag coefficient is:

$$C_D \approx 12.7 \, \mathrm{Re}^{-1}$$

(5)

which is in the same order of magnitude of the data available in the literature, e.g. for perfect spheres or cylinders [22]. This result, therefore, represents a good estimation of the aerodynamic performance of the spider’s hair at low Re, if considering the introduced approximation (i.e. cylindrical instead of conical geometry and rigid constraint) and the presence of the hair tip (i.e. finite-length body).

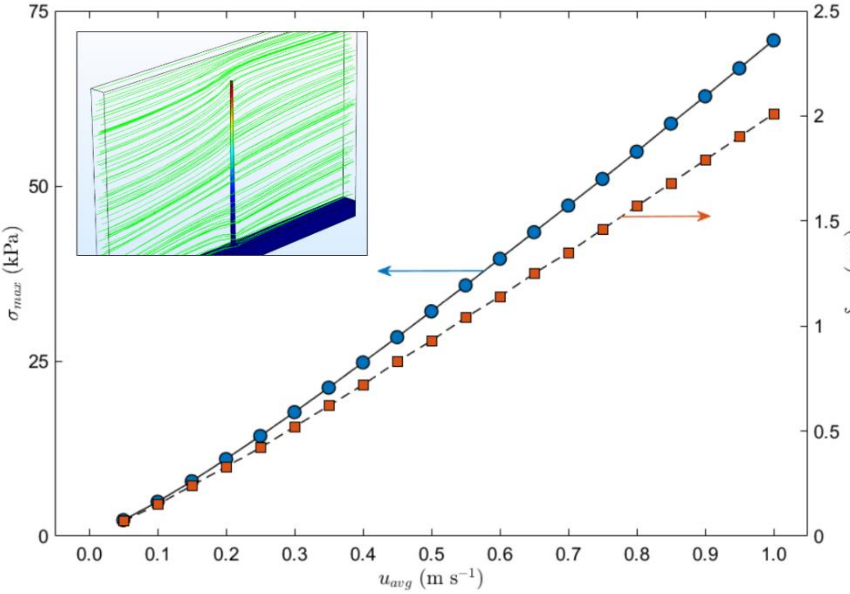

Figure 2: Maximum von Mises stress and maximum hair displacement as function of the mean inlet velocity. Inset: qualitative visualization of the displacement field of the structure and of the flow streamlines.

3.3 Effect of a varying hair spacing

The effect of the hair spacing, here denoted with Δ*s*, is quantified by monitoring the response of the second hair with respect to the first one. Specifically, we measure the variation of the maximum von Mises stress at a depth of 10 µm below the chitin surface, and of the maximum displacement at the hair tip. As shown in Fig. 3, for small values of Δ*s* the effect of the aerodynamic wake behind the first hair is to reduce the stresses and displacements to which the second hair is subjected. Only for a spacing higher than 1000 µm the variations $\Delta\sigma_{max}$ and $\Delta\delta_{max}$ are expected to fall below 5%.

These results suggest that the relative position of air flow-sensing hairs is probably dictated by the mutual interference. Therefore, the minimum distance between two hairs in the order of the hair length, is the optimal configuration to not affect the spider's sensing capabilities.

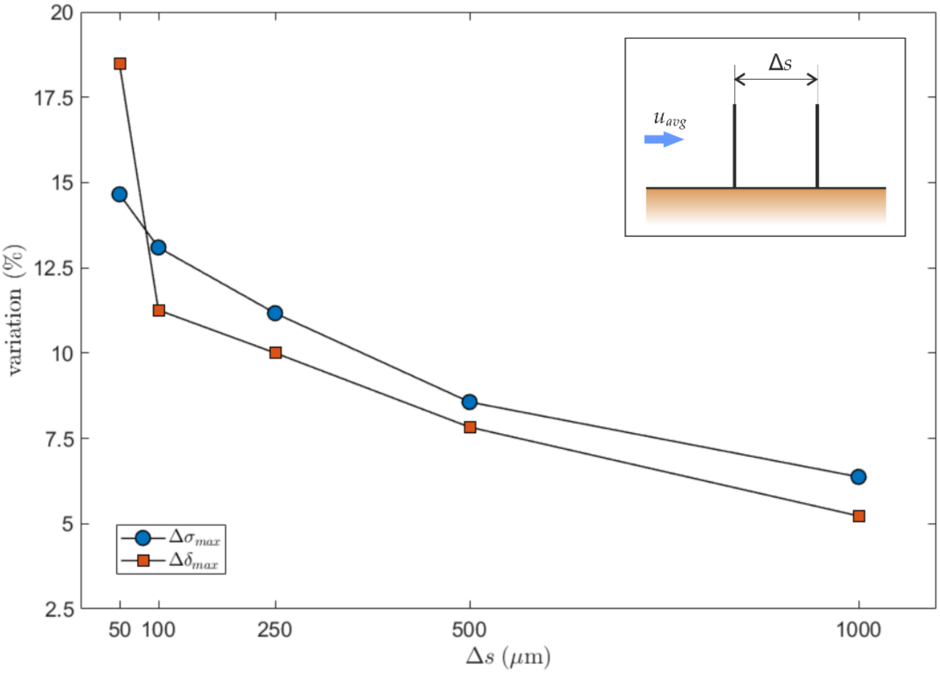

Figure 3: Difference on the maximum von Mises stress and the maximum displacement between the first and the second hair as function of the hair spacing. Inset: schematic view of the considered geometry.

4. Conclusions

We have used FSI numerical simulations to investigate the behavior of *Theraphosa stirmi*'s hairs under a fluid flow. We have extracted the morphology and the elastic properties of the hairs from experimental tests. The simulation study has allowed to compute the mechanical response of the hair under a varying flow velocity, suggesting a linear relationship between maximum displacement and mean inlet velocity, as well as between maximum von Mises stress and u_{avg}. In addition, we have considered the spacing between two hairs, showing that when the spacing is low the wake of the first hair affects the sensing capability of the second one. Therefore, this suggests that the optimal hair spacing in spiders might derive from fluid dynamic reasons and from the need of maximizing the sensing capabilities.

Acknowledgements

RG is supported by Bonfiglioli Riduttori SpA. NMP is supported by the European Commission under the Graphene Flagship Core 2 No. 785219 (WP14 “Polymer Composites”) and FET Proactive “Neurofibres” grant No. 732344.

References

1. R.F. Foelix, I.-W. Chu-Wang, Tissue Cell 5 (1973) 451-460.
2. J.T. Albert, O.C. Friedrich, H.-E. Dechant, F.G. Barth, J. Comp. Physiol. A 187 (2001) 303-312.
3. P. Fratzl, F.G. Barth, Nature 462 (2009) 442-448.
4. F.G. Barth, Curr. Opin. Neurobiol. 14 (2004) 415-422.
5. R.F. Foelix, J. Morphol. 132 (1970) 313-333.
6. R.F. Foelix, I.-W. Chu-Wang, Tissue Cell 5 (1973) 461-468.
7. B. Bathellier, F.G. Barth, J.T. Albert, J.A.C. Humphrey, J. Comp. Physiol. A 191 (2005) 733-746.
8. J.A.C. Humphrey, F.G. Barth, Adv. Insect Physiol. 34 (2007) 1-80.
9. A.-S. Ganske, G. Uhl, Arthtropod Struct. Dev. 47 (2018) 144-161.
10. C. Klopsch, H.C. Kuhlmann, F.G. Barth, J. R. Soc. Interface 9 (2012) 2591-2602.
11. C. Klopsch, H.C. Kuhlmann, F.G. Barth, J. R. Soc. Interface 10 (2013) 20120820.
12. F.G. Barth, Naturwissenschaften 87 (2000) 51-58.
13. M. Dijkstra, J.J. van Baar, R.J. Wiegerink, T.S.J. Lammerink, J.H. de Boer, G.J.M. Krijnen, J. Micromech. Microeng. 15 (2005) S132-S138.
14. G.J.M. Krijnen, M. Dijkstra, J.J. van Baar, S.S. Shankar, W.J. Kuipers, R.J.H. de Boer, D. Altpeter, T.S.J. Lammerink, R. Wiegerink, Nanotechnology 17 (2006) S84-S89.
15. J. Casas, T. Steinmann, G. Krijnen, J. R. Soc. Interface 7 (2010) 1487-1495.
16. B. Yang, D. Hu, L. Wu, Sensors 16 (2016) 1056.
17. T.A. Blackledge, J.E. Swindeman, C.Y. Hayashi, J. Exp. Biol. 208 (2005) 1937-1949.
18. COMSOL Multiphysics® v. 5.2a. www.comsol.com. COMSOL AB, Stockholm, Sweden.
19. F.-K. Benra, H.J. Dohmen, J. Pei, S. Schuster, B. Wan, J. Appl. Math. 2011 (2011) 853560.
20. H. Fabritius, C. Sachs, D. Raabe, S. Nikolov, M. Friák, J. Neugebauer, in: N.S. Gupta (Ed.), Chitin: Formation and Diagenesis, Springer Science+Business Media B.V., Dordrecht, 2011, pp. 35-60.
21. Dry Air Properties, Engineering ToolBox (2005) [online], https://www.engineeringtoolbox.com/dry-air-properties-d_973.html.
22. J.D. Anderson, Fundamentals of Aerodynamics, second ed., McGraw-Hill, New York, 1991.

Appendix A. Mechanical and optical characterization

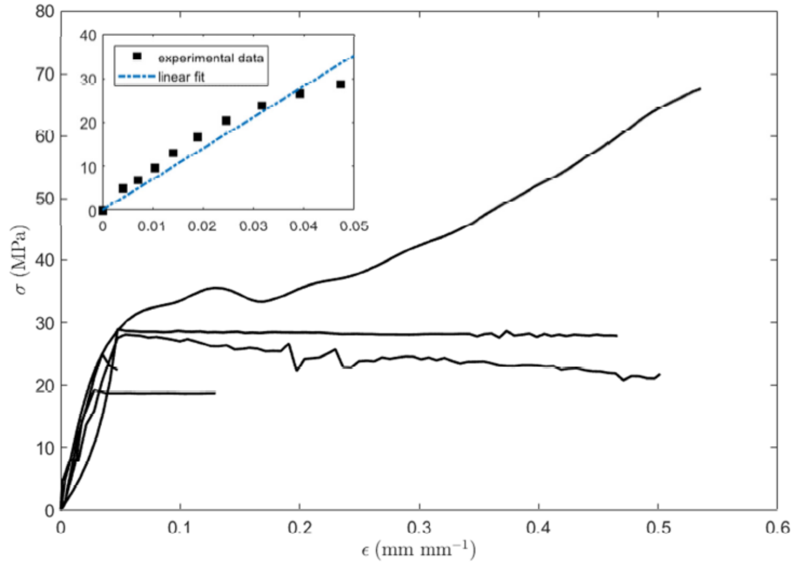

Figure A1. Example stress-strain curve of a Theraphosa stirmi's hair obtained through nanotensile test. Inset: linear fit on the first part of the curve, with extracted Young's modulus E ≈ 705.8 MPa (R^2-value = 0.921).

Figure A2: Left: a picture of a Theraphosa stirmi of the collection. Right: optical microscope image of a hair.

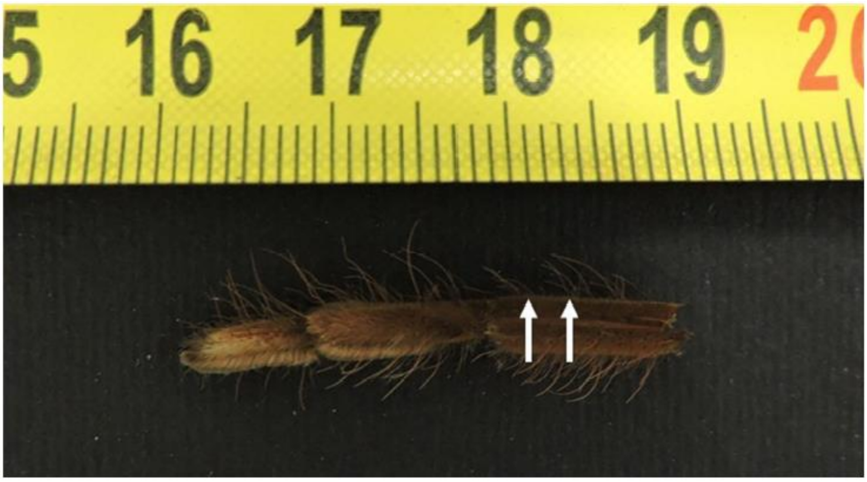

Figure 3: Pictures of a Theraphosa stirmi's leg with flow-sensing hairs and typical spacing in the order of the half-length of hair (white arrows).

B.

Materials, volume 12, Article number: 2797 (2019)

This paper was submitted on the 02 Juli 2019 and published on the 30 August 2019.

DOI: https://doi:10.3390/ma12172797

The Impact of Shear and Elongational Forces on Structural formation of Polyacrylonitrile/Carbon Nanotubes Composite Fibers during Wet Spinning Process

Hamideh Mirbaha[1,2], Parviz Nourpanah[1*], Paolo Scardi[3], Mirco D'incau[3], Gabriele Greco[2], Luca Valentini[4], Silvia Bittolo Bon[4], Shahram Arbab[5], and Nicola Pugno[2,6,7*]

[1] Department of Textile Engineering, Amirkabir University of Technology, 15875-4413 Tehran, Iran

[2] Laboratory of Bio-inspired & Graphene Nanomechanics, Department of Civil, Environmental and Mechanical Engineering, University of Trento, 38123 Trento, Italy

[3] Department of Civil, Environmental and Mechanical Engineering, University of Trento, 38123 Trento, Italy

[4] Civil and Environmental Engineering Department, University of Perugia and INSTM Research Unit, 05100 Terni, Italy

[5] Advanced Textile Materials and Technology Research Institute, Department of Textile Engineering, Amirkabir University of Technology, 15875-4413 Tehran, Iran

[6] School of Engineering and Materials Science, Queen Mary University of London, London E1 4NS, UK

[7] Ket-Lab, Edoardo Amaldi Foundation, 00133 Rome, Italy

* Correspondence: pnx@aut.ac.ir (P.N.); nicola.pugno@unitn.it (N.P.)

Abstract

Wet spinning of polyacrylonitrile/carbon nanotubes (PAN/CNT) composite fibers was studied and the effect of spinning conditions on structure and properties of as-spun fibers influenced by the presence of CNTs investigated. Unlike PAN fibers, shear force had a larger effect on crystalline structure and physical and mechanical properties of PAN/CNT composite fibers compared to the elongational force inside a coagulation bath. Under shear force CNTs induced nucleation of new crystals, whereas under elongational force nucleation of new crystals were hindered but the already formed crystals grew bigger. To our knowledge, this key effect has not been reported elsewhere. At different shear rates, strength, Young’s modulus and strain at break of PAN/CNT as-spun fibers were improved up to 20% compared to PAN fibers. Application of jet stretch had less influence on physical and mechanical properties of PAN/CNT fibers compared to PAN fibers. However, the improvement of interphase between polymer chains and CNTs as a result of chain orientation may have contributed to enhancement of Young’s modulus of jet stretched composite fibers.

Introduction

Carbon nanotubes (CNTs) have numerous applications due to their extraordinary properties, among which production of composite fibers based on polymer/CNT with ability to improve physical, mechanical, thermal, electrical and sound absorption properties can be noted [1–9]. Production of polyacrylonitrile (PAN)/CNT composite fibers with potential to be used as carbon fiber precursor and to improve mechanical properties of carbon fibers has attracted attention in recent years [6,10–13]. Since the parameters affecting structure formation during spinning process are diverse, successful production of PAN/CNT composite fibers with desired properties requires intensive research and correlation of the results. If production conditions are not controlled, CNTs may exist as aggregations, prohibiting orientation of polymers. Therefore, lower structural order, more defects and lack of crystalline interphase can be expected. In such conditions, exploiting desirable properties of CNTs inside fibers is not possible. There has been some research in recent years on PAN/CNT composite fibers, with a focus on the effect of different CNT types, content and post-processing on the structure and properties of final PAN/CNT fibers or their conversion to carbon fibers [1,6,10]. However, the structure formation of as-spun fibers in early stages of production in a coagulation bath has not been studied intensively and in detail. Understanding the effect of spinning conditions on the structure of as-spun fibers can give a bright image to design the wet spinning process more effectively. Thus, studying the structure formation of PAN/CNT composite fibers in early stages of production and the effects of different parameters in the spinning process is the focus of this paper.

The most important step in determination of fiber properties is the structure formation during the spinning process [14–16]. In the wet spinning process, polymer solution is extruded through a spinneret into a coagulation bath. The formed filaments are jet stretched by take-up rollers and then are subjected to washing, post-drawing and drying processes

[14,15,17]. When the spinning dope is passing through the spinneret, shear force is applied on polymer chains. Polymer chains are straightened under shear, leading to a decrease in internal friction of the spinning fluid [4,18]. The studies on melt spinning of polypropylene in the presence of CNTs show that the shear stress is also transferred to nanotubes, orientating them in the direction of shear flow [19]. When applied stress on CNTs exceeds a critical agglomeration strength, it can break the aggregations and separated nanotubes can orient more easily than their aggregations [19].

Improvement in orientation of polymer chains can be done by applying stretch on fibers in different production stages including jet stretch and drawing of as-spun fibers [20–22]. During the stretching process of solidifying spinning dope inside the coagulation bath—jet stretch stage-the rheological resistance is small making the orientation of macromolecules easier [4]. In the wet spinning process, jet stretch and shear stress coexist simultaneously and influence the structure formation and polymer chain orientation. Therefore, the necessity of detailed studies on the effect of these forces on the formation, development, and alignment of the structure and properties of the PAN/CNT as-spun fibers is evident. It is widely accepted that alignment of CNTs along fiber direction is important in order to take advantages of potential improvement in structure and properties of composite fibers [2]. Mai et al. [23] studied the effect of extension from take up rollers on the structure and properties of melt spun polyamide 66-multi walled CNTs (MWCNTs) composite fibers. They observe that high draw ratio not only can improve the dispersion of MWCNTs inside the polymer matrix, but also it can increase the orientation of fibers as well as interfacial adhesion between the matrix and MWCNTs, leading to improvement in mechanical properties of fibers. Mikolajczyk et al. [4] suggested that the presence of CNTs among polymers, similar to the softener effect, can facilitate the slippage of polymer chains and reduce the internal friction of the fluid. Many researchers have studied the effect of shear and elongation flows and their simultaneous impact on the structure formation and chain orientation of PAN fibers. However, the presence of CNTs among PAN can lead to different chain behavior under shear and elongational forces, which is not studied intensively and comprehensively.

Studying the effects of shear and elongational forces at different stages of fiber production, from spinning dope preparation to wet spinning and jet stretching on the structure evolution of as-spun PAN/CNT fibers can be a part of a road-map for controlling spinning parameters in order to improve the PAN/CNT fiber structure and properties. It can help to proceed on the route of improving the mechanical properties of PAN/CNT based carbon fibers. Accordingly, morphology, physical and mechanical properties and crystalline structure of as-spun PAN/CNT composite fibers at different stages of the wet spinning process have been studied in this paper. The effect of shear rates and jet stretch ratios on the fiber structure as well as the effect of the presence of CNTs on structure formation and evolution compared to PAN fibers have been investigated.

Methods

Materials, Ingredients, Synthesis

PAN powder with viscosity molecular weight of 112,000 g/mol containing comonomers of methyl acrylate and sodium methallyl sulfonate was obtained from Polyacryl Corp., Iran. Analysis grade dimethyl formamide (DMF) solvent, (Merck Co., Darmstadt, Germany) was used as received. Multi walled carbon nanotubes (MWCNTs) (Research Institute of Petroleum Industry, Tehran, Iran) with the average length of 10 micron, average diameter of 10–30 nanometers and purity over 95% were used.

Spinning Dope Preparation

For production of reference PAN fibers, PAN/DMF spinning dope was prepared from 20% w/v solution of PAN in DMF solvent. For production of PAN/CNT composite fibers, first 20% w/v solution of PAN in DMF was prepared. Then a suspension of CNT in 400 mL of DMF solvent was prepared with a concentration of 0.75 wt% of CNT in proportion to the polymer weight. The concentration of 0.75% for CNT was chosen based on the literature and the optimization experiments regarding the dispersion of CNTs in a polymer solution. For the purpose of dispersion of CNT in DMF, a UP200S ultrasonic homogenizer (Hielscher Ultrasonics GmbH, Teltow, Germany) was utilized for 30 minutes. Then the polymer solution was gradually introduced to the dispersion under shear force applied from a mechanical stirrer until a homogenous solution was obtained. The ultrasonication process was again continued for 15 minutes. According to Zhao et al. [24], polymers can permeate into bundles of CNTs through ultrasonication and prevent the van derWaals adherence between one CNT and other CNT bundles. As a result, a thicker bundle of CNTs is divided into thinner sub-bundles and even up to single nanotubes. Zhao et al. [24] also observed higher stability of CNT dispersion when the polymer exists in the solution during ultrasonication. After ultrasonication, the extra solvent was evaporated under shear force and heat until the PAN/CNT/DMF solution with a concentration of 20% PAN and 0.75% CNT was obtained.

Wet Spinning

Composite PAN/CNT and reference PAN fibers were wet spun using a laboratory spinning machine. Figure 1 shows a schematic diagram of the wet spinning machine used in the present work. The spinning dope was pumped at different speeds to a one-hole spinneret with a diameter of 200 microns using a metering pump and then was extruded into a coagulation bath containing water as nonsolvent at a temperature of 20 °C. The freely spun fibers were obtained by taking fibers directly out of the coagulation bath and then washing and drying at room temperature. The coagulated fibers at different jet stretch ratios, (2, 2.5, 3 and 3.5) were collected at the take-up rollers by changing the velocity of the take-up rollers for the same extrusion velocity of the spinning solution. Jet stretch ratios are defined as take-up velocity of the coagulated fiber to the extrusion velocity of the spinning solution. The collected fiber samples were soaked in and washed thoroughly with water and finally, they were allowed to dry naturally in air.

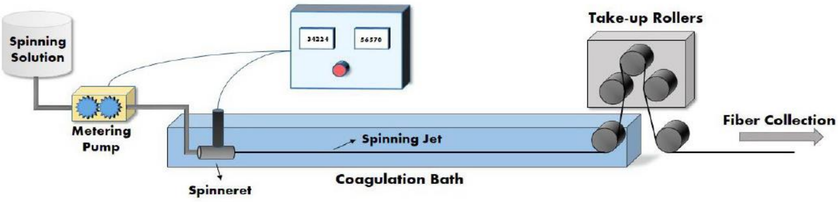

Figure 4: Schematic diagram of the wet spinning machine used in the present work.

In Table 1, denotation and different conditions for the production of reference PAN and composite PAN/CNT fibers are listed. In the fiber denotation, P and PC stand for PAN and PAN/CNT, respectively. The first numbers are equivalent shear rates inside the spinneret ($s^{-1} \times 10^{-3}$) as listed in Table 1. The second numbers of 2, 2.5, 3 and 3.5 coming after the letter D are the jet stretch ratios applied on fibers inside the coagulation bath. The fiber codes without a second number are freely spun fibers. The equivalent shear rate inside the spinneret ($\gamma°$) in unit of inverse seconds (s^{-1}) is calculated as [18]:

$$\gamma° = \frac{32Q}{\pi D^3} \quad (1)$$

where Q is volumetric flow rate and D is the diameter of the spinneret hole. This equation simply assumes that the polymer dope is Newtonian and it is in fully developed flow.

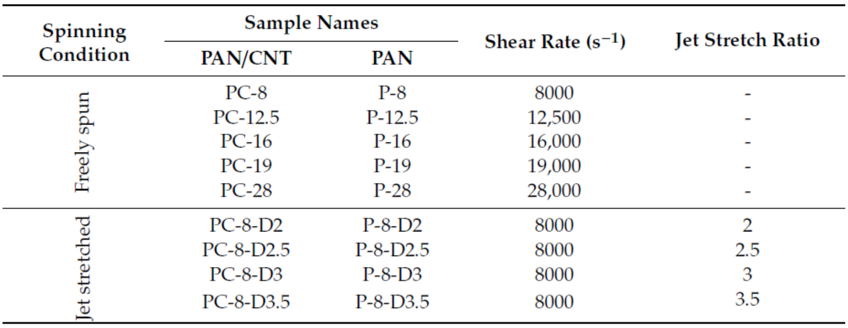

Spinning Condition	Sample Names		Shear Rate (s^{-1})	Jet Stretch Ratio
	PAN/CNT	PAN		
Freely spun	PC-8	P-8	8000	-
	PC-12.5	P-12.5	12,500	-
	PC-16	P-16	16,000	-
	PC-19	P-19	19,000	-
	PC-28	P-28	28,000	-
Jet stretched	PC-8-D2	P-8-D2	8000	2
	PC-8-D2.5	P-8-D2.5	8000	2.5
	PC-8-D3	P-8-D3	8000	3
	PC-8-D3.5	P-8-D3.5	8000	3.5

Table 5: Denotation and production conditions of polyacrylonitrile (PAN) and PAN/carbon nanotube (CNT) fibers.

Fiber Characterization

The fiber diameter was measured at numerous points along fiber length using a Microphot FXA optical microscope (Nikon, Tokyo, Japan) at magnification of 50x. To estimate the die swell ratio, spinning dope was extruded to a coagulation bath freely without applying jet stretch and the diameter of fiber cross section was measured by Microphot FX microscope (Nikon, Tokyo, Japan). The die swell ratio was obtained from dividing this diameter by the diameter of the spinneret hole [16,25]. The linear density was calculated by measuring the mass of different lengths of fibers with a GR-200 balance (A and D Balance, Tokyo, Japan). The average values of linear density were reported in the unit of tex (weight in grams of 1000 meters of fibers). The overall porosity of fibers was estimated by measuring the mass (via weight) and calculating the volume of fibers at numerous one-meter long replicates of fibers [26]:

$$Overall\ porosity(\%) = \left(\frac{\pi R^2 L - m\rho^{-1}}{\pi R^2 L}\right) \times 100 \quad (2)$$

where R, L, m and ρ are radius, length, mass of fibers and density of polymer, respectively.

The glass transition temperature (T_g) of selected fibers was measured using a DSC Q200 (TA Instruments, FC, USA) with dynamic scans between 60 °C and 160 °C at a heating rate of 2 °C/min. The microscopic images of Pt coated cross sections of fibers at magnifications of 500x and 7000x were obtained using a SUPRA^{TM} 40 VP Field Emission Scanning Electron Microscope (FESEM) (Zeiss, Oberkochen, Germany) at 2 kV. The images at magnification of 150,000x were captured using a MIRA3 FESEM (Tescan, Brno, Czech Republic) at 15 kV. The intact cross sections of fibers were obtained by cutting the samples in liquid nitrogen.

The crystalline structure of PAN and PAN/CNT fibers was studied using an X-ray diffractometer (Panalytical X'Pert MRD, Malvern, United Kingdom) operated at 40 kV and 40 mA using Co K-α radiation (wavelength: 1.790 Angstrom). Bundles of fibers were placed on the sample holder. The scanning range of 10°–48° (2θ) with a scanning step of 0.15 and counting time of 25 s/step was used. To extract data from XRD patterns, the peak resolving method in Origin 2017 software (OriginLab, Massachusetts, USA) based on three Lorenz functions was utilized to get the best fit for the experimental diffraction curve. The intense peak at $2\theta \sim 17°$ was used to calculate the crystalline parameters. The plane spacing (d) was calculated from Bragg's formula and lateral crystal size (L_c) was obtained using Scherrer equation [25,27]:

$$L_c = \frac{K\lambda}{\beta \cos(\theta)} \qquad (3)$$

where K is a constant with value of 0.89 and β is the full width at half maximum intensity (FWHM).

Among different methods for the calculation of relative degree of crystallinity, the Gupta–Singhal method was more reasonable and repeatable for the samples of this research. Therefore, this method was used here [28]:

$$Cristallinty(\%) = \frac{A_{crystal}}{A_{total}} \times 100 \qquad (4)$$

where $A_{crystal}$ is the area of crystalline peaks and A_{total} is the total area of diffraction over the entire measurement range after the background subtraction.

Mechanical properties of PAN and PAN/CNT single filaments were measured using a Universal testing machine MIDI 10 (Messphysik Materials testing GmbH, Fürstenfeld, Austria) using a 10 N load cell. The distance between two grips was 1 cm and the elongation rate was 0.1 mm/s (based on standard D3822). Each mechanical property was reported as the average value of at least 10 test results, and the standard deviation and coefficient of variation (CV%) were calculated. It needs to be mentioned that diversity of data between different repeats of a sample was low. Breaking tenacity was calculated from dividing the load at break by linear density of fibers. Tex was used as linear density that is defined as the mass in grams of 1000 meters of fibers. The Young's modulus (cN/tex) was obtained from the initial slope of the specific stress–strain curve. The toughness was calculated from the area under the tenacity–strain curve up to the failure point.

The electrical properties were measured using Keithley 4200-SCS having two probes with 25 mm distance (Keithley semiconductor characterization system, OH, Unites States). The electrical conductivity σ (S/cm) was calculated as [29]:

$$\sigma = \frac{IL}{VA} \quad (5)$$

where I, L, V and A are electrical current, sample length, voltage and fiber cross section area, respectively.

Results and Discussion

Jet Swell Ratio

When spinning dope is extruded freely from a spinneret into a coagulation bath, radial expansion of the thread takes place, resulting in a loss of orientation of polymer chains. This phenomenon that is called jet swell is a result of viscoelasticity of polymer solutions. It happens because of the energy storage from shear forces applied on spinning dope during its entrance and exit from the spinneret hole [16,19,25,30]. In Figure 2, the die swell ratio as a function of shear rate for PAN and PAN/CNT fibers is shown. With an increase in shear rate the jet swell ratio increases.

The jet swell ratio of PAN/CNT fibers is less than PAN fibers. As a result, polymer chains in composite fibers can preserve their orientation along the fiber direction better. Choi et al. [30] also observed lower jet swell with addition of CNT to PAN fibers. It seems that presence of CNTs inside PAN solution, decreases the elastic recovery of PAN chains, affects the chain mobility and reduces the internal friction [30]. In addition, the decrease in jet swell ratio of a PAN solution in presence of CNTs may indicate the formation of an interphase between polymer and nanotubes.

When spinning dope is extruded to a coagulation bath under certain tension applied by jet stretch, the jet swell can be limited or eliminated [16,25]. Having a clear understanding of the jet swell effect, it is necessary to optimize jet stretch ratio to obtain proper fiber structure. Considering the estimated values for jet swell ratio at shear rate of 8000 s^{-1} (Figure 2), a jet stretch ratio of about two is required to overcome the jet swell of PAN fibers and to obtain a fiber with diameter of 200 microns (the same as the spinneret hole diameter). For PAN/CNT composite fibers, this ratio is about 1.4, due to the role of CNTs in reducing the jet swell effect. Thus, CNTs help to overcome jet swell at lower jet stretch ratios. Therefore, at jet stretch ratio of two and higher used in this research, the jet swell effect in both PAN and PAN/CNT fibers was eliminated and the diameter of fibers was less than the spinneret hole diameter. In addition, due to lower jet swell ratio in PAN/CNT composite fibers, the stretching force applied on polymer chains at the same jet stretch ratio was higher than PAN fibers. This could possibly lead to higher chain orientation in PAN/CNT fibers. Materials 2019, 12, x FOR PEER REVIEW 6 of 23 stretch ratios. Therefore, at jet stretch ratio of two and higher used in this research, the jet swell effect in both PAN and PAN/CNT fibers was eliminated and the diameter of fibers was less than the spinneret hole diameter. In addition, due to lower jet swell ratio in PAN/CNT composite fibers, the stretching force applied on polymer chains at the same jet stretch ratio was higher than PAN fibers. This could possibly lead to higher chain orientation in PAN/CNT fibers.

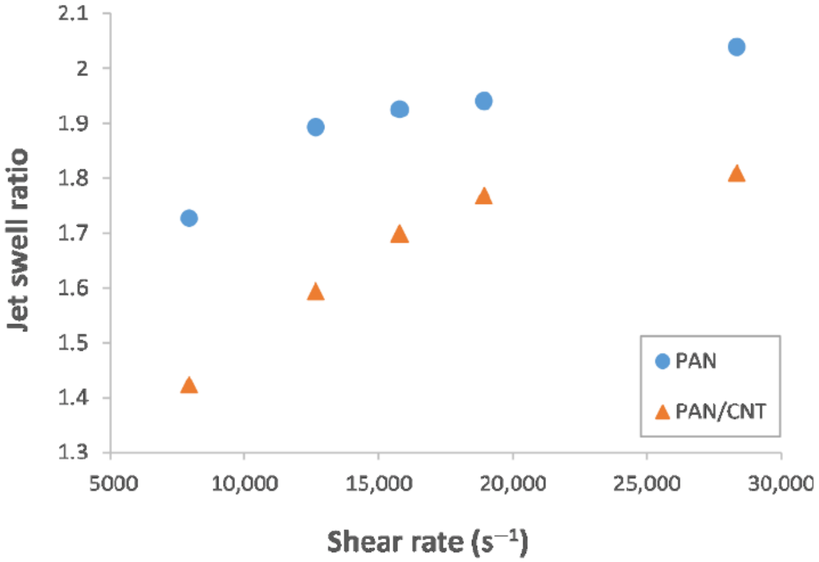

Figure 6: Jet swell ratio of PAN and PAN/CNT fibers at different shear rates.

Physical properties

The average diameter, linear density and overall porosity of PAN and PAN/CNT fibers at different shear rates and jet stretch ratios are reported in Table 2.

Shear Rate Effect

With an increase in the shear rate, the diameter and linear density of PAN and PAN/CNT fibers increased (Table 2). The presence of CNTs among PAN chains slightly decreased the fiber diameter. This was attributed to smaller jet swell ratio in the presence of CNTs (Figure 2) [30]. The diameter of PAN/CNT fibers at different shear rates was about 9%–19% lower than corresponding PAN fibers, whereas the linear density is about

33%–48% less than PAN fibers. Since linear density is the mass per unit length of fibers, this significant discrepancy in the diameter and linear density between PAN and PAN/CNT fibers showed that a structure with higher porosity is formed in PAN/CNT fibers. The pores can be the origin for fiber fracture, with an important effect on mechanical strength of fibers [31]. The calculated overall porosity of fibers at different shear rates in Table 2 also confirmed that the presence of CNTs among polymer chains led to higher porosity of structure. Apparently, CNTs and their aggregations inside spinning dope can act as a hindrance for compactness of structure. Addition of CNTs to PAN fibers led to an increase in T_g. Mahfuz et al. [32] also observed about 5 °C increase in T_g due to addition of CNTs to nylon filaments. This increase in T_g might be due to restrictions in mobility of PAN chains, possibly as a result of formation of a strong interface between PAN and CNTs or crystallization of structure in the vicinity of CNTs [33,34].

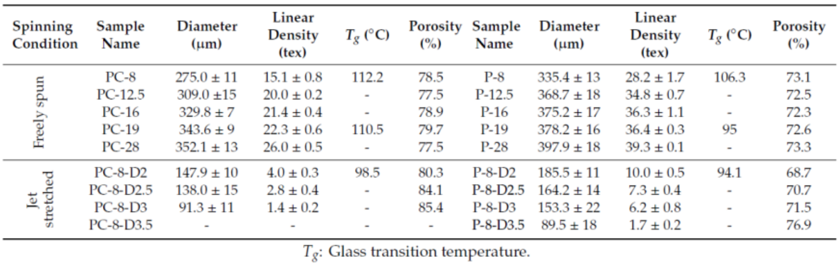

Spinning Condition	Sample Name	Diameter (μm)	Linear Density (tex)	T_g (°C)	Porosity (%)	Sample Name	Diameter (μm)	Linear Density (tex)	T_g (°C)	Porosity (%)
Freely spun	PC-8	275.0 ± 11	15.1 ± 0.8	112.2	78.5	P-8	335.4 ± 13	28.2 ± 1.7	106.3	73.1
	PC-12.5	309.0 ±15	20.0 ± 0.2	-	77.5	P-12.5	368.7 ± 18	34.8 ± 0.7	-	72.5
	PC-16	329.8 ± 7	21.4 ± 0.4	-	78.9	P-16	375.2 ± 17	36.3 ± 1.1	-	72.3
	PC-19	343.6 ± 9	22.3 ± 0.6	110.5	79.7	P-19	378.2 ± 16	36.4 ± 0.3	95	72.6
	PC-28	352.1 ± 13	26.0 ± 0.5	-	77.5	P-28	397.9 ± 18	39.3 ± 0.1	-	73.3
Jet stretched	PC-8-D2	147.9 ± 10	4.0 ± 0.3	98.5	80.3	P-8-D2	185.5 ± 11	10.0 ± 0.5	94.1	68.7
	PC-8-D2.5	138.0 ± 15	2.8 ± 0.4	-	84.1	P-8-D2.5	164.2 ± 14	7.3 ± 0.4	-	70.7
	PC-8-D3	91.3 ± 11	1.4 ± 0.2	-	85.4	P-8-D3	153.3 ± 22	6.2 ± 0.8	-	71.5
	PC-8-D3.5	-	-	-	-	P-8-D3.5	89.5 ± 18	1.7 ± 0.2	-	76.9

T_g: Glass transition temperature.

Table 2: Physical properties of PAN and PAN/CNT fibers at different spinning conditions.

Jet Stretch Effect

When jet stretch was applied on fibers inside the coagulation bath, the diameter and linear density of PAN and PAN/CNT as-spun fibers decreased considerably (Table 2). Diameter and linear density of PAN/CNT fibers were less than PAN fibers at different jet stretch ratios. The tolerance of PAN/CNT composite fibers against jet stretch was less than PAN, as they could not tolerate a high jet stretch ratio of 3.5. It may be a result of higher stretch forces exerted on polymers due to lower jet swell ratios. In addition, slippage of polymer chains over each other due to lower internal friction in composite fibers may have led to filament breakage during stretching. In addition, presence of nano-additives may have reduced the filament ability to distort in the drawing stage [35].

For both PAN and PAN/CNT fibers, increasing the jet stretch ratio resulted in an increase in overall porosity. For reference PAN fibers, applying jet stretch up to a ratio of three decreased the overall porosity compared to corresponding freely spun fibers. This could be due to alignment of polymer chains and fibrils in a more oriented and compact form, thus with fewer pores and voids, as well as radial shrinkage and diameter reduction. Inside a coagulation bath the movement of structural sections of fibers is easier compared to coagulated fibers since fibers are not yet completely solidified. Thus a more compact structure can be formed by stretching. In addition, applying jet stretch reduces the time that fibers remain in a coagulation bath. As a result, the available time for pore growth decreases. The presence of CNTs, however, had different influence on this behavior. Since jet stretch ratios were apparently higher than optimum values for PAN/CNT composite fibers, slippage of polymers over each other and creation of defects and voids in structure resulted in higher overall porosity compared to freely spun fibers even at a jet stretch ratio of two. CNTs may act like impurities among polymer chains, reducing the structural integrity at jet stretch ratios of two and higher. As a result, the tolerance of PAN/CNT fibers against stretch forces inside coagulation bath was less than PAN fibers. For jet stretched fibers, T_g of PAN/CNT fibers was also higher than neat PAN fibers (Table 2). This was due to lower mobility of PAN chains in the presence of CNTs, which may suggest the formation of an interphase between nanotubes and polymers.

Morphology and Microscopic Structure

Shear Rate Effect

The FESEM images from cross section and internal morphology of PAN and PAN/CNT fibers spun at different shear rates are shown in Figure 3. No big morphological differences between PAN and PAN/CNT fibers could be observed. In general, the structure of fibers consisted of loose fibrils and finger like hollow pores in the radial direction of fibers. Formation of this structure is due to counter diffusion of solvent/nonsolvent and phase separation during coagulation [16]. The channels formed during counter diffusion of solvent/nonsolvent and the areas occupied by the liquid phase are responsible for formation of voids in fibrillar structure [16]. As the shear rate increased, the fibrillar parts and internal surfaces of finger-like voids became looser as a result of bigger jet swell (Figure 2).

The outer surface of fibers—as it can be seen in Figure 3—were fairly smooth without grooves due to negligible stretching force inside the coagulation bath.

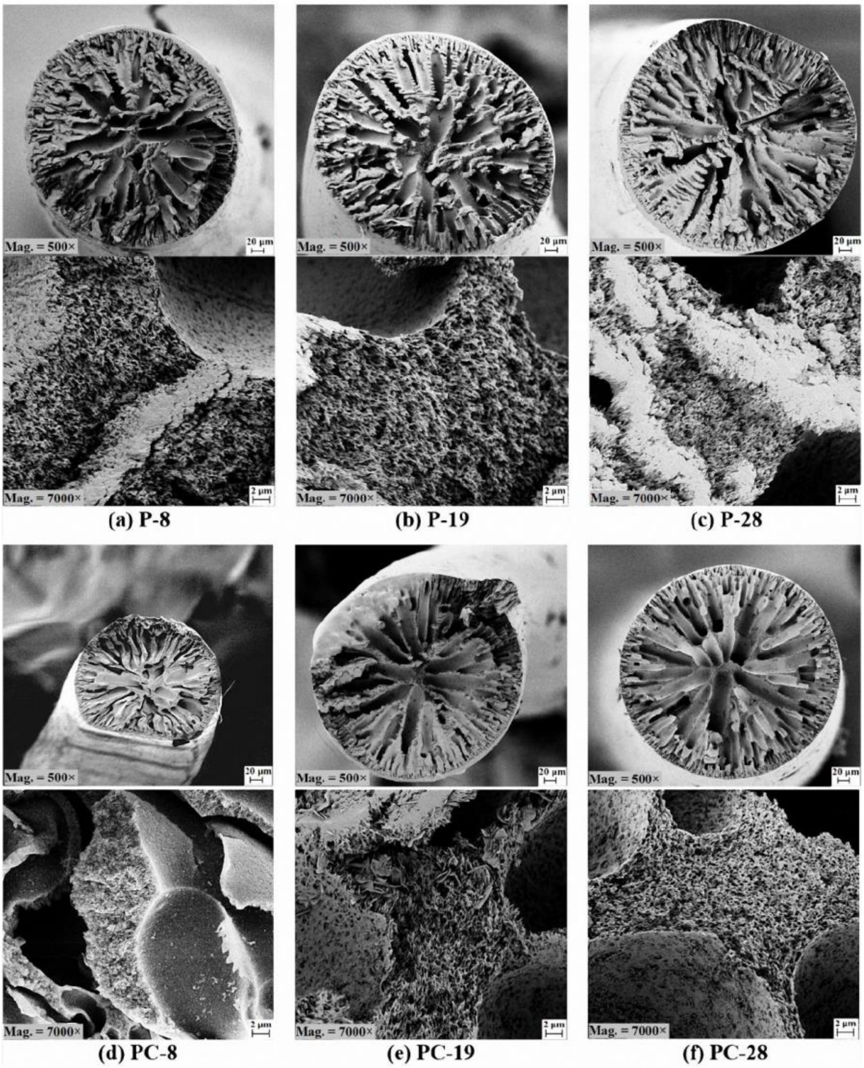

(a) P-8 (b) P-19 (c) P-28

(d) PC-8 (e) PC-19 (f) PC-28

Figure 3: FESEM images from cross section and internal morphology of PAN and PAN/CNT fibersspun with different shear rates at magnifications of 500x and 7000x.

Jet Stretch Effect

The effect of jet stretch on cross section shape and morphology of PAN and PAN/CNT fibers is shown in Figure 4. A significant decrease in fiber diameter by applying jet stretch was observed. Jet stretch ratio of two and higher changed the cross-section shape of PAN/CNT fibers from circular to an irregular shrunken form with numerous deep surface grooves. It confirmed that even a jet stretch ratio of two was higher than the optimum value for production of PAN/CNT composite fibers. However, the cross-section shape of PAN fibers was still circular at jet stretch ratios of 2 and

2.5. Deviation of cross-section shape from circular has an influence on the physical and mechanical properties of fibers [15,36]. The stress distribution is uniform in fibers with circular cross section, leading to improvement in mechanical strength [15,36], whereas fibers with non-circular cross section cannot tolerate high stretches in the following production stages due to stress concentration.

The outer surface of PAN reference fibers were smooth and without grooves at a jet stretch ratio of two, whereas fine grooves appeared on the surface at jet stretch ratio of 2.5. Surface grooves were caused by elongational forces applied on fibers inside the coagulation bath. The number and depth of these grooves grew with jet stretch ratio. For PAN/CNT composite fibers, however, the deep surface grooves could be observed even at jet stretch ratio of two, again confirming that PAN/CNT fibers were less tolerant for jet stretch compared to PAN fibers. Probably, the presence of CNTs prevented proper integration of structure under stretch. A jet stretch ratio of two and higher led to disintegration of structure and internal damages in PAN/CNT fibers. In addition, the reduction of internal friction in the presence of CNTs could lead to slippage of polymer chains over each other at high stretch ratios, creating damages in fibers structure. These damages grew with jet stretch ratio, where at jet stretch ratio of 3.5 filament self-breakage did not allow for fiber production.

In comparison with freely spun fibers, the pores in cross-section of jet stretched PANand PAN/CNT fibers were smaller and narrower. The residence time of filaments in the coagulation bath was shortened by jet stretch, reducing the available time for nucleation and growth of voids, resulting in fibers with lower porosity [37,38]. Arbab et al. [37,39] has also observed more compact structure with smaller voids by increasing the jet stretch ratio in wet spinning of PAN fibers. In addition, the applied tension on fibers during jet stretch makes the fiber thread thinner, limits the mobility of polymer parts, and hinders the counter-diffusion of solvent/nonsolvent. Thus formation of big voids is avoidable to some extent. On the other hand, the already formed bigger voids can be stretched and shrunk when the thread thinning is taking place during stretching [16]. The calculated overall porosity of PAN fibers up to a jet stretch ratio of three in Table 2, also confirmed this argument. On the other hand, the overall porosity of PAN/CNT composite fibers increased by applying a jet stretch ratio of two and higher (Table 2). This could be a result of the presence of CNTs among polymer chains. In addition, the jet stretch ratios over the tolerance limit of PAN/CNT fibers caused structural defects and voids in the fibers. This observation confirmed the necessity of applying lower jet stretch ratios on PAN/CNT fibers compared to PAN fibers. When jet stretch ratio was very high (three for PAN/CNT fibers, 3 and 3.5 for PAN fibers), bigger voids were again obvious in the cross-section of fibers, confirming the damages to structure.

It was not possible to identify CNTs even at magnifications as high as 150,000x (Figure 4h). This could result from similar appearance of CNT individuals and their bundles with fibrillar form of porous as-spun PAN. Considering the smoother surface of CNTs compared to PAN fibrils, it could be deduced that CNTs may have been wrapped by polymer chains and an interphase might have been formed between PAN and CNT.

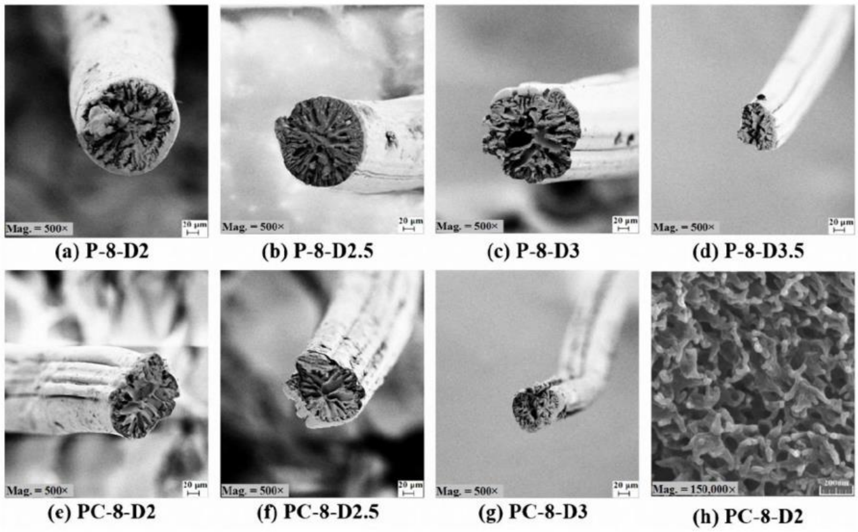

(a) P-8-D2 (b) P-8-D2.5 (c) P-8-D3 (d) P-8-D3.5

(e) PC-8-D2 (f) PC-8-D2.5 (g) PC-8-D3 (h) PC-8-D2

Figure 4: (a-g) FESEM images of PAN and PAN/CNT fibers spun at different jet stretch ratios at magnification of 500x (h) Internal morphology of PC-8-D2 fibers at magnification of 150000x.

Crystalline Structure of Fibers

The supramolecular structure of coagulated as-spun fibers—i.e., crystallinity, crystallite size and crystal orientation—is directly related to mechanical properties of final fibers [28]. Therefore, it is important to study crystalline structure to understand the mechanical properties of fibers.

Shear Rate Effect

The effect of shear rate on X-ray diffraction patterns of PAN and PAN/CNT fibers are depicted in Figure 5. The data extracted from the XRD patterns after peak resolving are listed in Table 3. The intense peak at 2θ~17° was attributed to the diffraction from crystalline portion and the wide scattered diffraction at 2θ between 25°–30° was attributed to amorphous portions of fibers [28]. From XRD patterns it could be deduced that crystalline structure of PAN and PAN/CNT fibers was the same. Mai et al. [23] also observed the same crystal structure for PA66 fibers and their composites with MWCNT.

Spinning Condition	Sample Name	Angle (2θ)	FWHM (2θ)	d (A)	L_c (nm)	L_c/d	C%	Sample Name	Angle (2θ)	FWHM (2θ)	d (A)	L_c (nm)	L_c/d	C%
Freely spun	PC-8	17.09	3.07	5.185	2.593	5.00	13.01	P-8	17.02	3.10	5.206	2.562	4.92	13.51
	PC-12.5	16.85	2.39	5.256	3.319	6.31	34.83	P-12.5	17.01	2.3	5.209	3.357	6.44	28.02
	PC-19	16.85	2.38	5.257	3.332	6.34	36.44	P-19	16.88	2.11	5.248	3.769	7.18	30.34
	PC-28	16.90	2.39	5.252	3.330	6.34	35.53	P-28	16.94	2.18	5.229	3.649	6.98	34.07
Jet stretched	PC-8-D2	16.93	2.19	5.233	3.626	6.93	34.14	P-8-D2	16.91	2.32	5.240	3.428	6.54	53.90
	PC-8-D2.5	16.76	2.10	5.286	3.781	7.15	36.51	P-8-D2.5	16.82	2.29	5.266	3.476	6.60	54.56
	PC-8-D3	17.00	2.06	5.210	3.849	7.39	38.55	P-8-D3	16.85	2.22	5.257	3.572	6.79	54.80

d: d-spacing

Table 3: Crystalline parameters of PAN and PAN/CNT fibers after peak resolving.

The intensity of diffraction peak at 2θ~17° for PAN/CNT fibers spun at shear rate of 8000 s^{-1} is very weak, indicating very low crystallinity degree (Figure 5a). The data extracted from XRD patterns of PAN/CNT fibers in Table 3 also shows large FWHM, small crystallite sizes (L_c) and low crystallinity (C%). This peak for PAN fibers spun at shear rate of 8000 s^{-1} (P-8) was very wide, which made it very difficult to resolve to crystalline and amorphous portions (Figure 5b). This wide peak apparently indicates that amorphous phase was dominant in fibers. Therefore, the data obtained from this curve was not fully reliable and could only be used for comparison. However, it was clear that the crystallinity was low and the crystallite size was very small.

Increasing the shear force on polymers can nucleate new crystals [23,40]. In addition, it can increase the alignment of polymers along the spinning direction [4,41], so they would have more possibility to be attached to crystal nuclei. Both reasons can develop the crystalline phase, resulting in crystallite size and crystallinity improvements. According to Table 3, the peak width for both PAN and PAN/CNT fibers was decreased with an increase in the shear rate, indicating the growth of crystals and increase of crystallite size (Figure 6). L_c/d, which is a measure of average layers in crystallites [27], also grew with the shear rate, in which d stands for d-spacing of (*hkl*) reflections. This trend is shown schematically in Figure 7.

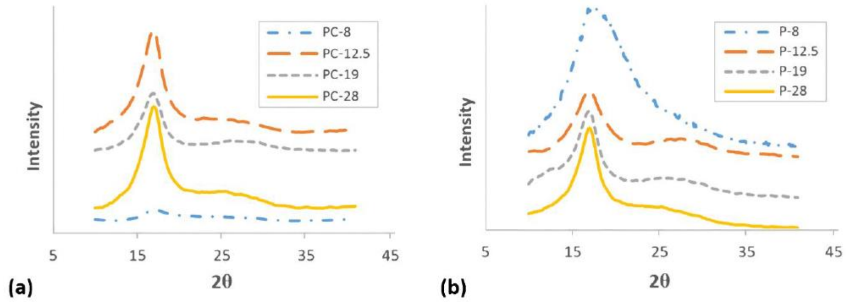

Figure 5: XRD patterns of fibers spun at different shear rates. (a) PAN/CNT fibers, (b) PAN fibers.

At shear rate of 28,000 s^{-1}, the highest shear force was applied on polymer chains leading to nucleation of crystals and the increase in crystallinity of PAN fibers to 34% (Table 3 and Figure 6). However, smaller crystallite size (L_c: 3.649 nm) compared to shear rate of 19,000 s^{-1} (L_c: 3.769 nm) showed that higher than optimal value of shear force probably caused the slippage of polymer chains over each other along the flow direction of spinning dope. Consequently, the possibility of attachment of chains to crystalline phase was less and the crystallite size was smaller. The average number of crystalline layers of PAN fibers spun at shear rate of 28,000 s^{-1} (i.e., 6.98) was also less than that of shear rate of 19,000 s^{-1} (i.e., 7.18). At lower shear rates, the possibility of nucleation of crystals was less, while the nucleated crystals were bigger due to attachment of more chains to the crystalline phase.

On the other hand, both crystallite size and crystallinity were decreased in PAN/CNT composite fibers spun at shear rate of 28,000 s^{-1} (L_c: 3.330 nm, C%: 35.53%) (Table 3, Figure 6). The presence of CNTs changed the response of polymer chains to shear force during the spinning process. It was easily recognizable by naked eyes that the viscosity of PAN/CNT spinning dope was less than PAN spinning dope. Mikolajczyk et al. [4] also reported the reduction in internal friction of PAN solution with addition of CNTs. At high shear rate of 28,000 s^{-1}, the slippage of polymer chains in spinning dope with lower viscosity hindered the crystal growth and crystallinity enhancement.

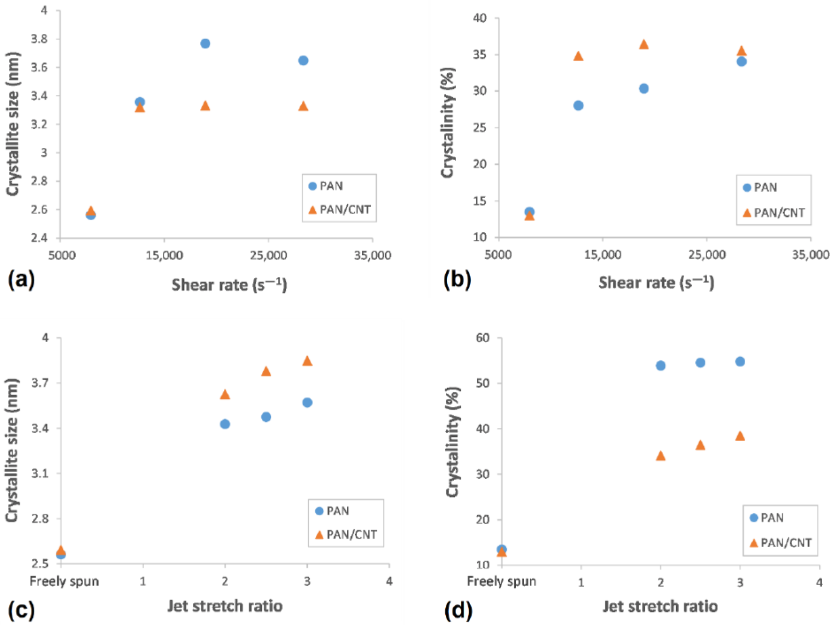

Figure 6: (a) The crystallite size and (b) crystallinity of PAN and PAN/CNT fibers as a function of shear rate, (c) The crystallite size and (d) crystallinity of PAN and PAN/CNT fibers as a function of and jet stretch ratio.

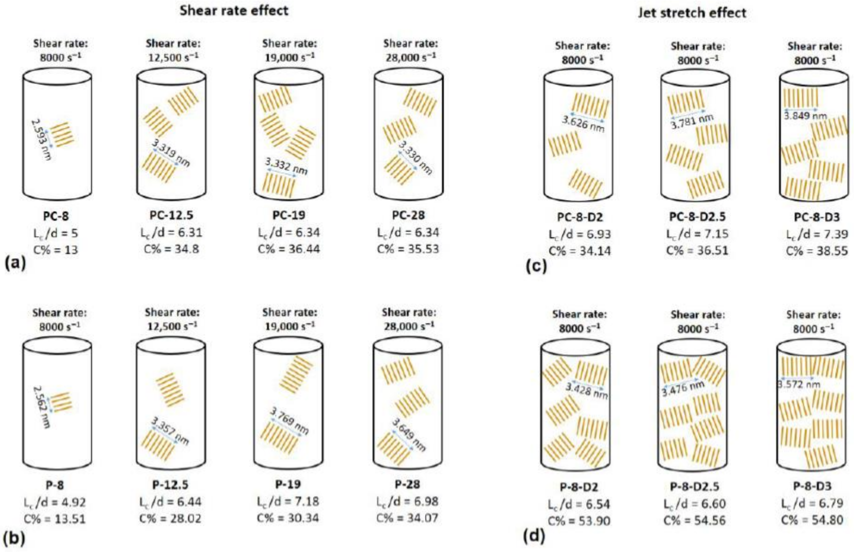

Figure 7: A schematic showing the changes in crystalline parameters of PAN and PAN/CNT fibers at different spinning conditions (a) PAN/CNT fibers at different shear rates, (b) PAN fibers at different shear rates, (c) PAN/CNT fibers at different jet stretch ratios, (d) PAN fibers at different jet stretch ratios.

Comparison of crystalline parameters of PAN and PAN/CNT fibers at different shear rates in Table 3 and Figure 6 revealed that PAN/CNT fibers had higher crystallinity but smaller crystallites with less crystalline layers. The higher crystallinity of PAN/CNT fibers also led to lower mobility of polymer chains compared to neat PAN fibers, resulting in higher Tg values (Table 2). The increase in crystallinity can have a big effect on mechanical properties of PAN/CNT fibers, which is beyond the direct reinforcement resulted from load transfer [14]. The crystallite sizes of PAN and PAN/CNT fibers were almost identical up to the shear rate of 12,500 s^{-1}. At higher shear rates, the crystallite sizes of PAN fibers exceeded those of PAN/CNT fibers. In the presence of CNTs, the nucleation of crystals under shear force was increased. Possibly the CNTs acted as nuclei for formation of new crystals with smaller size [23,40,42]. Polymer chains can interact with CNTs and nucleate on their surface [23,40]. Chae et al. [43] observed that CNTs are surrounded by a graphitic layer after carbonization of PAN/CNT fibers at low temperatures of 1100 °C. Formation of this graphitic layer can be indicative of ability of CNTs to act as templates for orientation and crystallization of polymer chains [43]. In the absence of CNTs in PAN reference fibers, however, fewer number of new crystals were formed, whereas the formed crystals grew more under shear force compared to PAN/CNT fibers. In the other words, shear force was more beneficial for nucleation of new crystals in PAN/CNT composite fibers and for growth of formed crystals in PAN reference fibers.

The extended-polymer chain conformation is the most desired structure for formation of fibers with high modulus and strength [40]. To induce extended chain crystallization, extensional force that is usually applied to polymer solution through shear flow is required [40]. Zhang et al. [40] observed that in PAN/single-walled CNT fibers with high concentration of PAN that has been under shear force, an interface in form of fibril-like crystals with extended chain is formed. Considering the production methods used in this research, i.e., applying shear force on PAN/CNT solution during preparation of spinning dope as well as during the passing of the spinning dope through the spinneret, could nucleate new crystals. Consequently, higher crystallinity in PAN/CNT fibers could be obtained compared to PAN fibers. The possible mechanism for the effect of shear force on crystal nucleation and crystallite size growth is shown in Figure 8a,b.

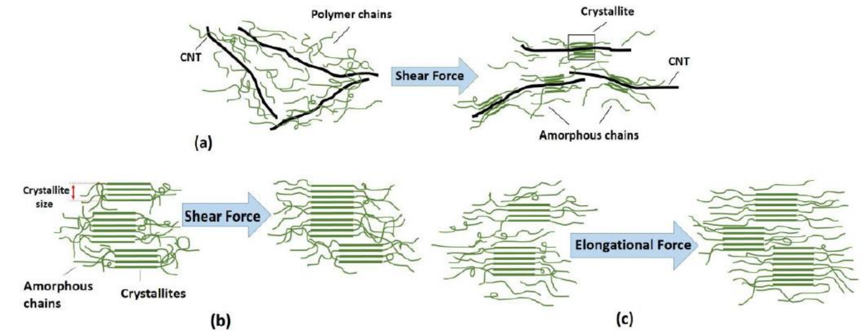

Figure 8: Schematics showing (a) possible mechanism for the effect of shear force on the interface between polymer and CNT, (b) the effect of shear force on crystallite size of PAN and PAN/CNT fibers, (c) the effect of elongational force on crystallite size and crystallinity of PAN fibers.

Jet Stretch Effect

In Figure 9, the XRD patterns of PAN and PAN/CNT fibers spun under different jet stretch ratios are shown. The data extracted from these patterns after peak resolving are listed in Table 3. Applying jet stretch on fibers and increasing its ratio up to three decreased the width of crystalline peak at 2θ~17° for both PAN and PAN/CNT fibers. The crystallite size and crystallinity of jet stretched fibers were considerably higher than freely spun fibers at the same shear rate of 8000 s^{-1}. The elongational force from application of jet stretch inside the coagulation bath increased the orientation of polymer chains along the fiber direction. Therefore, more polymer chains were placed in proper position to join the crystalline phase. Consequently, crystallite size and crystallinity increased (Table 3, Figure 6).

When comparing crystal parameters of PAN and PAN/CNT fibers that were jet stretched inside the coagulation bath, it became obvious that the presence of CNTs was beneficial for the growth of crystallite size, whereas it had less effect on crystallinity improvement compared to PAN reference fibers. Namely, when jet stretch was applied on fibers in the coagulation bath, PAN/CNT fibers had fewer but bigger crystals compared to PAN reference fibers, in which the crystals were greater in number but in smaller sizes. Chai et al. [1] also observed bigger crystallite size and lower crystallinity of PAN fibers in presence of MWCNT. It showed the ability of PAN chains to nucleate new crystals under elongational force, compared to PAN/CNT fibers. CNTs apparently act as deterrent for nucleation of new crystals under high elongational force. The high jet stretch ratios applied in this research, may lead to overstretching of polymer chains in composite fibers and their slippage over each other, thus hindering the nucleation and formation of new crystals. However, polymer chains in

PAN/CNT fibers could join the already formed crystals under elongational force, due to orientation of polymers along fiber direction. Overall, it is clear that CNTs had a different impact on crystalline structure of fibers under shear and elongational forces. Under shear force, CNTs induced nucleation of new crystals, whereas under elongational force nucleation of new crystals were hindered but the already formed crystals had grown bigger. To our knowledge, this key effect has not been studied and reported elsewhere.

Comparison of crystalline parameters of jet stretched and freely spun reference PAN fibers revealed that crystallinity of jet stretched fibers spun at shear rate of 8000 s^{-1} was considerably higher than fibers freely spun at highest shear rate of 28,000 s^{-1} (Table 3). However, the crystallite sizes of jet stretched fibers were not bigger than freely spun fibers at high shear rates of 19,000 and 28,000 s^{-1}. These results showed the stronger effect of shear force on growth of crystallites and the bigger effect of elongational force on the crystallinity of PAN reference fibers. Probably under shear force, the crystallites in PAN fibers had the ability to join each other, whereas under elongational force polymer chains in amorphous phase were stretched and oriented along fiber direction, being more able to join the crystalline phase. This mechanism is schematically represented in Figure 8b,c.

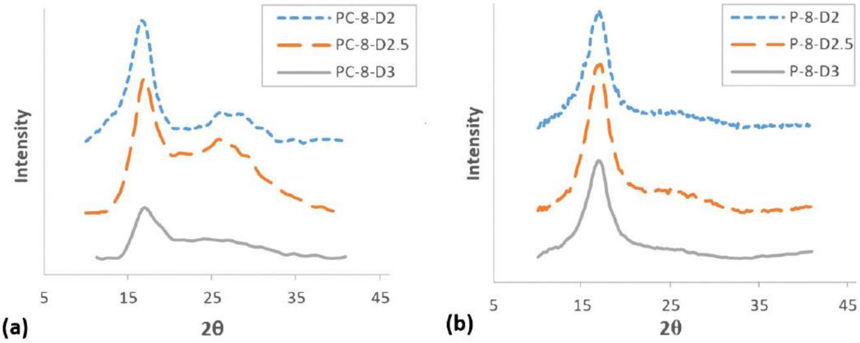

*Figure 9: XRD patterns of fibers spun at di_erent jet stretch ratios. (**a**) PAN/CNT, (**b**) PAN.*

Unlike PAN fibers, the differences between crystallinity of PAN/CNT fibers freely spun at different shear rates or under jet stretch were not considerable (Table 3). Again, unlike PAN fibers, applying jet stretch on PAN/CNT fibers increased crystallite size compared to PAN/CNT fibers freely spun at different shear rates. This was because of the stronger effect of shear force on crystallinity of PAN/CNT composite fibers compared to elongational force. It may have resulted from the effect of CNTs and their bundles on hindering the extension and orientation of polymer chains under jet stretch inside the coagulation bath. It may have also been due to the minor effect of high jet stretch ratios used in this research on crystallinity of PAN/CNT fibers. As it was reported in Section 3.3.2 (Figure 4), jet stretch ratios used in this research were higher than tolerance limit of PAN/CNT fibers, causing damages to fiber structure and deviation of cross-section shape from regular circular form. The high porosity of jet stretched PAN/CNT fibers (Table 2) can also be a confirmation on slippage of chains over each other at high jet stretch ratios or prevention of long CNTs from free mobility and alignment of polymer chains, creating voids in the structure.

Mechanical Properties

Mechanical properties of PAN and PAN/CNT as-spun fibers at different conditions of shear and jet stretch are reported in Table 4. The tenacity–strain curves for PAN and PAN/CNT fibers spun at different shear rates and jet stretch ratios are presented in Figure 10. It needs to be mentioned that to study the effect of spinning parameters on the structure and properties of first fiber-form product obtained in the coagulation bath, the properties reported here were related to as-spun fibers. The post-drawing stage—as an important stage in improvement of fiber properties—was not performed on the reported fibers and is the focus of our ongoing research. The results of post drawing stage on the structure and properties of PAN/CNT fibers are to be presented in other research papers.

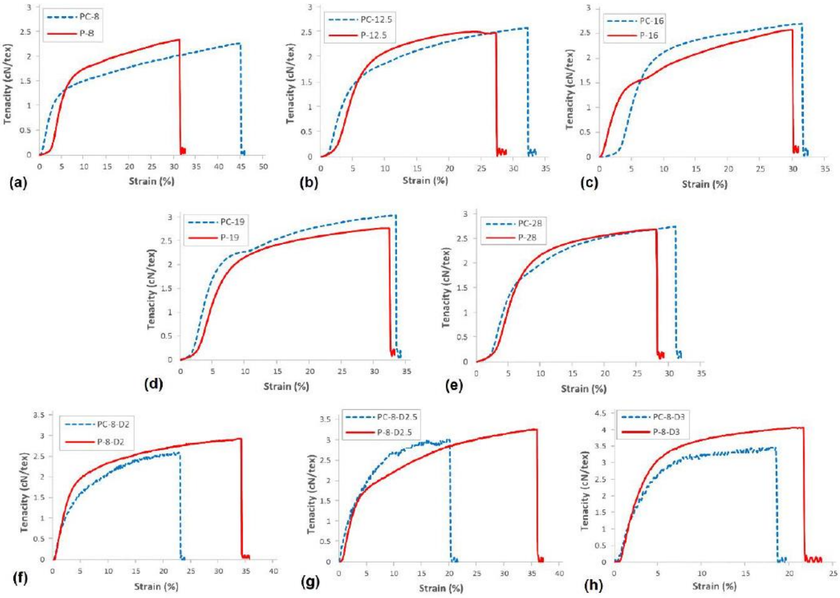

Figure 7 The tenacity–strain curves of PAN and PAN/CNT fibers spun at different shear rates and jet stretch ratios. (a) At shear rate of 8000 s^{-1}, (b) At shear rate of 12,500 s^{-1}, (c)

At shear rate of 16,000 s^{-1}, (d) At shear rate of 19,000 s^{-1}, (e) At shear rate of 28,000 s^{-1}, (f) At jet stretch ratio of 2, (g) At jet stretch ratio of 2.5, (h) At jet stretch ratio of 3.

Shear Rate Effect

If jet stretch was not applied on fibers, the orientation of polymer chains that was improved inside the spinneret was almost lost after exiting from the spinneret. As a result, the improvement in mechanical strength with increase in shear rate was not considerable (Table 4). Considering the results obtained from XRD patterns in Section 3.4.1, the crystals nucleated under shear force remained in the fibers after exiting the spinneret. These crystals may be responsible for minor improvement in mechanical properties of fibers with shear rate. The highest mechanical strength for both PAN and PAN/CNT fibers were obtained at shear rate of 19,000 s^{-1} and the strength decreases at shear rate of 28,000 s^{-1}. The fiber strength not only is influenced by orientation of macromolecules inside fibers, but also depends on intact molecular structure with fewer voids and defects and higher crystallinity [44,45]. It seems that the diminution of mechanical strength of PAN and PAN/CNT fibers at shear rate of 28,000 s^{-1} was a result of application of shear rates higher than optimum values. One of its consequences was higher jet swell (Figure 2) and eventually loss of orientation and mechanical properties of fibers. In addition, at higher shear rates the revolution of metering pump was faster, increasing the possibility of formation of bubbles inside the spinning dope while passing through the pump and spinning path. These bubbles can remain in the fiber as defects and act as a source of fiber failure under stretching force [31]. Furthermore, the slippage of polymer chains over each other at very high shear forces, which leads to smaller crystallite sizes and lower crystallinity, might be another reason for lower mechanical strength of fibers.

The presence of CNTs affects the mechanical properties of PAN fibers by changing the structure parameters such as orientation, crystallinity and crystallite size. Fei et al. [9] observed the improvement in mechanical compressive strength of polystyrene composite foams by addition of MWCNTs, which was gradually improved by increasing the MWCNT wt% up to 1%. Comparison of mechanical strength of PAN and PAN/CNT fibers spun at different shear rates showed that even having the higher porosity (Table 2), the strength of freely spun PAN/CNT fiber improved up to 20% compared of corresponding PAN fibers. This was a result of the reinforcing role of CNTs in the structure, suggesting the formation of an interphase between polymer and CNTs. It also showed the possibility of nucleation of new crystals templated by CNTs and enhancement of fiber crystallinity (Table 3). Moreover, due to reduction of elastic recovery of PAN chains in the presence of CNTs, PAN/CNT fibers can retain their orientation better, resulting in a decrease in the number of entanglements in the structure of as-spun fibers [30].

Similar to mechanical strength, Young’s modulus of PAN and PAN/CNT fibers did not have regular incremental or decreasing trend with shear rate (Table 4). Young’s modulus is influenced by crystallinity of structure, perfection of crystallites, alignment of crystals along fiber direction and orientation of polymer chains [46]. The most important factor in orientation of polymer chains and crystals in fibers is application of elongational force. In the absence of elongational force in freely spun fibers, the formed crystals under shear did not have proper orientation along fiber direction. Thus, the change in Young’s modulus of PAN and PAN/CNT fibers with shear rate was not significant.

The comparison between PAN and PAN/CNT fibers spun at different shear rates in Table 4 showed that the Young’s modulus of PAN/CNT as-spun fibers at all shear rates was up to 25% higher than that of PAN fibers. Due to the presence of CNTs, the crystalline structure of composite fibers has been improved through CNT templated crystallization. Possibly an interphase has been formed between CNTs and polymer chains leading to an improvement in stress transfer from soft polymer matrix to stiff CNTs. Consequently, Young’s modulus of as-spun PAN/CNT composite fibers was improved compared to PAN fibers even in the absence of elongational force in the coagulation bath, when orientation of polymers and crystals was not noticeable.

The presence of CNTs in PAN fibers increased the strain at break of freely spun PAN/CNT composite fibers compared to PAN fibers (Table 4). The improvement in mechanical properties of composite fibers resulted from interaction between CNTs and PAN matrix. The conventional reinforcements for composites usually improve the modulus and strength at the expense of strain at break [1]. CNTs as reinforcements for PAN fibers, however, could improve strength, modulus and strain at break simultaneously, thus resulting in higher toughness up to 18% (Table 4), as Chae et al. [1] also reported in their research.

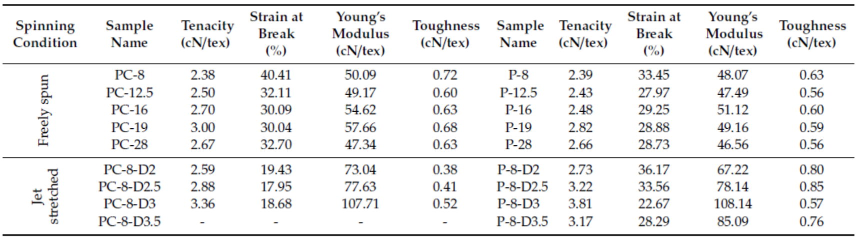

Spinning Condition	Sample Name	Tenacity (cN/tex)	Strain at Break (%)	Young’s Modulus (cN/tex)	Toughness (cN/tex)	Sample Name	Tenacity (cN/tex)	Strain at Break (%)	Young’s Modulus (cN/tex)	Toughness (cN/tex)
Freely spun	PC-8	2.38	40.41	50.09	0.72	P-8	2.39	33.45	48.07	0.63
	PC-12.5	2.50	32.11	49.17	0.60	P-12.5	2.43	27.97	47.49	0.56
	PC-16	2.70	30.09	54.62	0.63	P-16	2.48	29.25	51.12	0.60
	PC-19	3.00	30.04	57.66	0.68	P-19	2.82	28.88	49.16	0.59
	PC-28	2.67	32.70	47.34	0.63	P-28	2.66	28.73	46.56	0.56
Jet stretched	PC-8-D2	2.59	19.43	73.04	0.38	P-8-D2	2.73	36.17	67.22	0.80
	PC-8-D2.5	2.88	17.95	77.63	0.41	P-8-D2.5	3.22	33.56	78.14	0.85
	PC-8-D3	3.36	18.68	107.71	0.52	P-8-D3	3.81	22.67	108.14	0.57
	PC-8-D3.5	-	-	-	-	P-8-D3.5	3.17	28.29	85.09	0.76

Table 4: Mechanical properties of PAN and PAN/CNT fibers at different shear rates and jet stretch ratios.

Jet Stretch Effect

According to Table 4 and Figure 11, applying jet stretch to PAN and PAN/CNT fibers spun at shear rate of 8000 s^{-1} improved the strength of fibers compared to corresponding freely spun fibers. The elongational force applied on filaments inside the coagulation bath can open the random coils in polymer chains. It can reduce or eliminate the jet swell, enhancing the chain alignment and orientation, increasing the compactness of structure and eventually improving the crystallinity and mechanical properties of fibers. Internal micro-voids can become smaller as well [25,41]. The biggest improvement in mechanical strength, which was about 40% for PAN/CNT fibers and 60% for PAN fibers compared to corresponding freely spun fibers, was achieved at a jet stretch ratio of three. Investigation of crystalline structure of PAN fibers also showed the highest crystallinity and crystallite size at a jet stretch ratio of three. At a jet stretch ratio of 3.5, the strength of PAN fibers was reduced, showing that this jet stretch ratio was higher than tolerance limit of polymer chains, causing chain rupture and damages to structure. It could be seen from appearance of PAN fibers spun at jet stretch ratio of 3.5 that fibers split at many spots along the length of fibers. FESEM images also showed deep grooves on the surface of these fibers resulting from high stretching forces (Figure 4). The sudden porosity increase at this jet stretch ratio (Table 2) was another reason for the reduction in mechanical properties of PAN fibers at a jet stretch ratio of 3.5.

Although the jet stretch ratios of two and higher improved the mechanical properties of PAN/CNT fibers compared to freely spun fibers at the same shear rate, it could be seen that higher shear rates had bigger influence on tensile strength (Table 4). These results confirm again that the optimal jet stretch ratios for PAN and PAN/CNT fibers were different. To the best of our knowledge, these results have not been reported elsewhere, since most research has focused on final PAN/CNT fibers than the early structure of as-spun PAN/CNT fibers. This understanding can be useful for designing the spinning process of composite fibers. The stretch ratios applied in this research were not optimized for improving the structure of PAN/CNT as-spun fibers as it was expected, due to the different focus of this study.

Comparison of PAN and PAN/CNT fibers at different jet stretch ratios showed that the strength of jet stretched PAN/CNT as-spun fibers was about 5%–12% less than corresponding PAN fibers (Table 4, Figure 11). Applying jet stretch improved orientation and mechanical strength of PAN fibers more than PAN/CNT fibers due to following reasons: 1. Jet stretch ratios applied on PAN/CNT fibers were higher than optimum value. Due to lower viscosity of PAN/CNT spinning dope, the jet stretch ratio must be less than PAN fibers to increase the orientation of polymer chains without slippage of structural units over each other. 2. The cross-section shape of jet stretched PAN/CNT fibers changed from circular to an irregular form (Figure 4), which is in general not beneficial for mechanical properties of fibers due to stress concentration. 3. The presence of CNTs and their possible bundles and aggregations as well as the formed interface between CNTs and polymer chains, will probably reduce the free movement of polymers under stretching force, hindering the crystallinity enhancement and increasing the fiber porosity. Although increasing the jet stretch ratio seems economically beneficial and increases the production speed, one should take into account the differences in tolerance limit of PAN and PAN/CNT fibers for jet stretch, when designing the production line. Overall, it seems that lower jet stretch ratios were required for production of PAN/CNT fibers to retain and increase orientation, improve crystalline structure and crystal orientation, decrease the porosity and increase the mechanical strength without damaging the fiber structure.

Application and increasing the jet stretch ratio increased the Young's modulus of PAN and PAN/CNT as-spun fibers significantly. The highest Young's modulus was obtained at a jet stretch ratio of three for both PAN and PAN/CNT fibers. As it was already mentioned in Section 3.4.2, the crystallinity was also the highest at jet stretch ratio of three (Table 3). Although the application of jet stretch did not improve the crystallinity of PAN/CNT fibers considerably compared to freely spun composite fibers at high shear rates, the Young's modulus was still significantly higher than freely spun fibers. This revealed the importance of chain orientation for improvement of Young's modulus. When chain orientation is increased, more primary chemical bonds are distributed along the fiber direction to tolerate the applied force, leading to an improvement in mechanical properties of fibers. For PAN fibers, Young's modulus decreased significantly at a jet stretch ratio of 3.5. It confirmed that this stretch ratio was higher than the bearing limit of polymer chains, causing damages to structure, as confirmed in FESEM images in Figure 4.

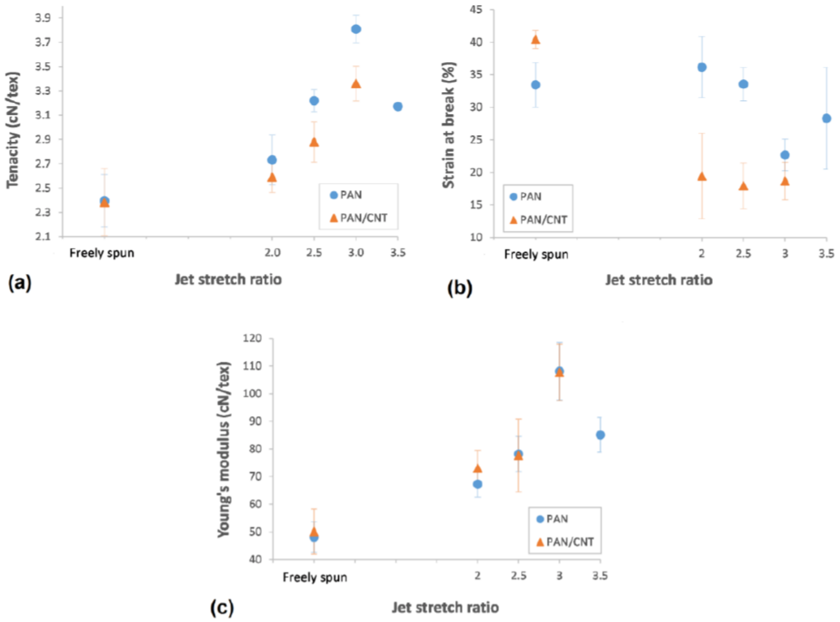

Figure 8 (a) Tenacity, (b) strain at break and (c) Young's modulus of PAN and PAN/CNT fibers as a function of jet stretch ratio.

Comparison of Young's modulus of PAN and PAN/CNT fibers at different jet stretch ratios showed that despite significantly lower crystallinity (Table 3), lower tensile strength (Table 4) and higher porosity (Table 2) of jet stretched PAN/CNT fibers compared to PAN fibers, Young's modulus of PAN/CNT as-spun fibers at jet stretch ratio of two was about 10% higher than PAN fibers. At higher jet stretch ratios, Young's modulus of PAN/CNT fibers was almost the same as PAN fibers. For jet stretched fibers, multi walled CNTs have bigger effect on Young's modulus than on tensile strength. Some researchers have shown that the development of crystalline interface between polymer and CNTs can improve the stress transfer between matrix and these CNTs [12,47]. It seems that applying jet stretch strengthened the interface between polymer and CNTs by increasing the orientation of polymers and CNTs along the fiber direction, leading to improvement in Young's modulus of PAN/CNT fibers. However, applying jet stretch ratios higher than optimum values for composite fibers prevented maximum reinforcing capabilities of CNTs inside polymer structure from being obtained.

Electrical Properties

Shear Rate Effect

Electrical conductivity of PAN and PAN/CNT composite fibers as a function of shear rate and jet stretch ratio is illustrated in Figure 12. The electrical conductivity of neat PANfiber was 1.80 x 10^{-7} S/cm. The electrical conductivity of composite fibers containing CNTs was increased up to about two times compared to PAN fibers. With an increase in shear rate, the electrical conductivity of PAN/CNT fibers decreased. When the shear rate increased, the fibers became thicker (Table 2). This thickening happened while the same percentage of CNTs existed inside fibers. As a result, the distance between CNTs became bigger and they had fewer connections with each other, which was deterrent for electrical conductivity of fibers. In addition, jet swell ratio was bigger at higher shear rates (Figure 2), resulting in bigger loss of orientation for polymers and CNTs. Therefore, CNTs might have been placed more randomly in the fibers instead of being aligned in fiber direction. This was unbeneficial for the transmittance of current along fibers and was considered another reason for lower conductivity of fibers at higher shear rates. Moreover, high porosity and the presence of macro voids in fibers could have prevented percolation between CNT's and reduced the current transmit through them.

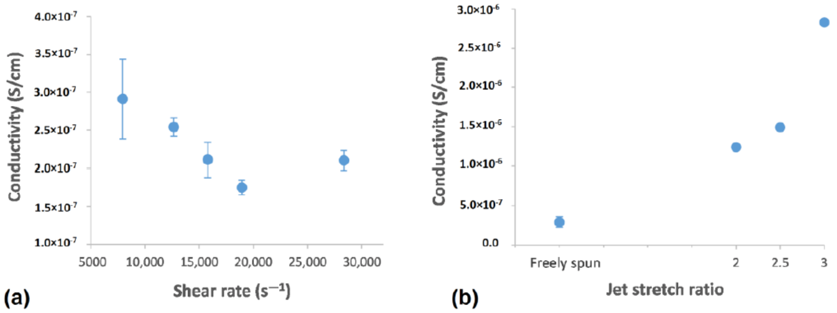

Figure 9: Electrical conductivity of PAN/CNT fibers as a function of (a) shear rate and (b) jet stretch ratio.

Jet Stretch Effect

Applying jet stretch on coagulating filament increased the electrical conductivity significantly (Figure 12b). This sudden increase was indicative of higher orientation of polymer chains and CNTs due to stretching force, which also improved the mechanical properties of fibers (Table 4). The highest electrical conductivity was obtained at a jet stretch ratio of three. The mechanical properties was also the highest at a jet stretch ratio of three. The results of mechanical and electrical properties confirmed that with an increase in polymer chain orientation at a jet stretch ratio of three, the CNTs were also oriented along fiber direction, increasing the current transmit through them, leading to higher electrical conductivity.

Conclusions

Wet spinning of PAN and PAN/CNT fibers was studied and the effect of different shear and stretching conditions on the structural, mechanical and electrical properties of as-spun fibers was investigated. The results showed different effects of CNTs on crystalline structure of fibers under shear and elongational forces. CNTs caused nucleation of new crystals under shear force, whereas under elongational force nucleation of crystals were hindered but the already formed crystals grew bigger. To our knowledge, this key effect has not been studied and reported elsewhere. In the absence of CNTs in PAN fibers, shear force influenced the crystal growth more, whereas the elongational force rather affected the crystallinity. At different shear rates, mechanical strength, Young’s modulus and strain at break of freely spun PAN/CNT fibers improved up to 20% compared to PAN fibers due to possible formation of interface between polymer and CNTs. At different jet stretch ratios, the presence of CNTs rather influenced the Young’s modulus than mechanical strength. Despite lower crystallinity and much higher porosity of composite fibers than PAN reference fibers at different jet stretch ratios, high Young’s modulus can still be obtained in PAN/CNT fibers. Microscopic observations and porosity estimation showed that the tolerance of PAN/CNT fibers for jet stretch inside a coagulation bath was less than PAN fibers. Understanding the effect of shear and elongational forces during spinning process on the structure and properties of PAN/CNT as-spun fibers can help to design the production line carefully, in order to obtain better physical and mechanical properties in final PAN/CNT precursor fibers.

Author Contributions: Conceptualization, H.M., P.N., S.A., N.P.; methodology, H.M., P.S., M.D., L.V., S.B.B., S.A., N.P..; software, H.M., M.D., G.G., S.B.B.; validation, P.S., L.V., N.P.; formal analysis, H.M., G.G., M.D., S.B.B.; investigation, H.M., M.D., S.B.B.; resources, P.N., P.S., L.V., S.A., N.P.; data curation, H.M.; writing—original draft preparation, H.M.; writing—review and editing, H.M., L.V., N.P.; supervision, P.N., L.V., S.A., N.P.; project administration, P.N., S.A., N.P.; funding acquisition, P.N., N.P.

Funding: N.M.P. was funded by European Commission under the Graphene Flagship Core 2, grant number. 785219 (WP14, “Composites”), the Future and Emerging Technologies (FET) Proactive (“Neurofibres”) grant number. 732344 as well as by the Italian Ministry of Education, University and Research (MIUR) under the “Departments of Excellence” grant L.232/2016, the ARS01-01384- PROSCAN and the PRIN-20177TTP3S grants.

Conflicts of Interest: The authors declare no conflict of interest. The funders had no role in the design of the study; in the collection, analyses, or interpretation of data; in the writing of the manuscript, or in the decision to publish the results.

References

1. Chae, H.G.; Sreekumar, T.V.; Uchida, T.; Kumar, S. A comparison of reinforcement effciency of various types of carbon nanotubes in polyacrylonitrile fiber. Polymer 2005, 46, 10925–10935. [CrossRef]
2. Dintcheva, N.T.; Arrigo, R.; Nasillo, G.; Caponetti, E.; Mantia, F.P.L. On the role of extensional flow in morphology and property modifications of MWCNT/Polyamide-based fibers. Macromol. Mate. Eng. 2011, 296, 645–657. [CrossRef]
3. Hameed, A.; Islam, M.; Ahmad, I.; Mahmood, N.; Saeed, S.; Javed, H. Thermal and mechanical properties of carbon nanotube epoxy nanocomposites reinforced with pristine and functionalized multiwalled carbon nanotubes. Polym. Compos. 2015, 36, 1891–1898. [CrossRef]
4. Mikolajczyk, T.; Szparaga, G.; Bogun, M.; Fraczek-Szczypta, A.; Blazewicz, S. Effect of spinning conditions on the mechanical properties of polyacrylonitrile fibers modified with carbon nanotubes. J. Appl. Polym. Sci. 2010, 115, 3628–3635. [CrossRef]
5. Li, Y.H.; Yu, Y.X.; Liu, Y.D.; Lu, C. Interphase development in polyacrylonitrile/SWNT nano-composite and its effect on cyclization and carbonization for tuning carbon structures. ACS Appl. Nano Mater. 2018, 1, 3105–3113. [CrossRef]
6. Liu, Y.D.; Chae, H.G.; Kumar, S. Gel-spun carbon nanotubes/polyacrylonitrile composite fibers. Part I: Effect of carbon nanotubes on stabilization. Carbon 2011, 49, 4466–4476. [CrossRef]
7. Li, Y.; Gora, A.; Anariba, F.; Baji, A. Enhanced Tensile Strength and Electrical Conductivity of Electrospun Polyacrylonitrile Yarns Via Post-Treatment. Polymer Compos. 2018, 40, 1702–1707. [CrossRef]
8. Li, T.T.; Zhao, G.Q.;Wang, G. Effect of preparation methods on electrical and electromagnetic interference shielding properties of PMMA/MWCNT nanocomposites. Polym. Compos. 2018, 40, E1786–E1800. [CrossRef]
9. Fei, Y.P.; Fang, W.; Zhong, M.Q. Extrusion foaming of lightweight polystyrene composite foams with controllable

cellular structure for sound absorption application. Polymers 2019, 11, 106. [CrossRef]

10. Jain, R.; Minus, M.L.; Chae, H.G.; Kumar, S. Processing, Structure, and Properties of PAN/MWNT Composite Fibers. Macromol. Mater. Eng. 2010, 295, 742–749. [CrossRef]
11. Liu, Y.D.; Choi, Y.H.; Chae, H.G.; Gulgunje, P.; Kumar, S. Temperature dependent tensile behavior of gel-spun polyacrylonitrile and polyacrylonitrile/carbon nanotube composite fibers. Polymers 2013, 54, 4003–4009. [CrossRef]
12. Newcomb, B.A.; Chae, H.G.; Gulgunje, P.V. Stress transfer in polyacrylonitrile/carbon nanotube composite fibers. Polymers 2014, 55, 2734–2743. [CrossRef]
13. Sahin, K.; Fasanella, N.A.; Chasiotis, I. High strength micron size carbon fibers from polyacrylonitrile-carbon nanotube precursors. Carbon 2014, 77, 442–453. [CrossRef]
14. Jestin, S.; Poulin, P. Wet spinning of CNT-based fibers. In Nanotube Superfiber Materials, Changing Engineering Design; Schulz, M.J., Shanov, V.N., Yin, Z., Eds.; William Andrew Applied Science: Oxford, UK, 2014; pp. 167–209.
15. Chen, J.; Ge, H.; Liu, H.; Li, G.; Wang, C. The coagulation process of nascent fibers in PAN wet spinning. J. Wuhan Univ. Technol. 2010, 25, 200–205. [CrossRef]
16. Qin, O.Y.; Chen, Y.S.; Zhang, N.; Mo, G.M.; Li, D.H.; Yan, Q. Effect of jet swell and jet stretch on the structure of wet-spun polyacrylonitrile fiber. J. Macromol. Sci. Part B: Phys. 2011, 50, 2417–2427.
17. Wilms, C.; Seide, G.; Gries, T. The relationship between process technology, structure development and fibre properties in modern carbon fibre production. Chem. Eng. Trans. 2013, 32, 1609–1614.
18. Sulong, A.B.; Park, J. Alignment of multi-walled carbon nanotubes in a polyethylene matrix by extrusion shear flow: Mechanical properties enhancement. J. Compos. Mater. 2010, 45, 931–941. [CrossRef]
19. Kang, D.W.; Ryu, S.H. Orientation of carbon nanotubes in polypropylene melt. Polym Inter. 2013, 62, 152–157. [CrossRef]
20. Lian, F.; Liu, J.; Ma, Z.; Liang, J. Stretching-induced deformation of polyacrylonitrile chains both in quasicrystals and in amorphous regions during the in situ thermal modification of fibers prior to oxidative stabilization. Carbon 2012, 50, 488–499. [CrossRef]
21. Andreoli, C.; Freti, F. Man-made fibers, Reference books of Textile Techologies; Fondazione ACIMIT: MiIan, Italy, 2004; pp. 1–71.

22. Arbab, S.; Nourpanah, P.; Mohammadi, N.; Zeinolebadi, A. Exploring the effects of non-solvent concentration, jet-stretching and hot-drawing on microstructure formation of poly (acrylonitrile) fibers during wet-spinning. J. Polym. Res. 2011, 18, 1343–1351. [CrossRef]
23. Mai, F.; Pan, D.D.; Gao, X. Extension-induced mechanical reinforcement in melt-spun fibers of polyamide 66/multiwalled carbon nanotube composites. Polym. Inter. 2011, 60, 1646–1654. [CrossRef]
24. Zhao, L.P.; Gao, L. Stability of multi-walled carbon nanotubes dispersion with copolymer in ethanol. Colloids Surf. A 2003, 224, 127–134. [CrossRef]
25. Ji, B.;Wang, Ch.;Wang, Y. Effect of jet stretch on polyacrylonitrile as-spun fiber formation. J. Appl. Polym. Sci. 2007, 103, 3348–3352. [CrossRef]
26. Arbab, S.; Mohammadi, N.; Noorpanah, P. Designing Index of void structure and tensile modulus in wet-spun poly (acrylonitrile) proto-fibres. Part II: synergistic effect of dope non-solvent concentration and jet draw ratio. Iran. Polym. J. 2008, 17, 227–235.
27. Gong, Y.; Du, R.; Mo, G.; Xing, X.Q.; Lu, C.X.; Wu, Z. In-situ microstructural changes of polyacrylonitrile based fibers with stretching deformation. Polymer. 2014, 55, 4270–4280. [CrossRef]
28. Qin, O.Y.; Chen, Y.S.;Wang, X.F.; Ma, H.B.; Li, D.H.; Yang, J. Supramolecular structure of highly oriented wet-spun polyacrylonitrile fibers used in the preparation of high-performance carbon fibers. J. Polym. Res. 2015, 22, 229.
29. Arbab, S.; Teimoury, A.; Mirbaha, H.; Adolphe, D.C.; Noroozi, B.; Nourpanah, P. Optimum stabilization processing parameters for polyacrylonitrile-based carbon nanofibers and their di erence with carbon (micro) fibers. Polym. Degrad. Stab. 2017, 142, 198–208. [CrossRef]
30. Choi, Y.H. Polyacrylonitrile/carbon nanotube composite fibers: Effect of various processing parameters on fiber structure and properties. PhD Thesis, Georgia Institute of Technology, North Avenue, Atlanta, GA, USA, 15 November 2010.
31. Ji, M.; Wang, Ch.; Bai, Y.; Yu, M.; Wang, Y. Structural evolution of polyacrylonitrile precursor fibers during preoxidation and carbonization. Polym. Bull. 2007, 59, 527–536. [CrossRef]

32. Mahfuz, H.; Adnan, A.; Rangari, V.K. Enhancement of strength and stiffness of Nylon 6 filaments through carbon nanotubes reinforcement. Appl. Phys. Lett. 2006, 88, 083119. [CrossRef]
33. Zhang, X. Fundamentals of Fiber Science; DEStech Publications, Inc.: Lancaster, PA, USA, 2014.
34. Fan, X.X.; Ren, H.H.; Yan, Y. Poly (amino acid)/carbon nanotube nanocomposites with enhanced thermal, electrical, and mechanical properties. Polym. Compos. 2018, 39, E1939–E1949. [CrossRef]
35. Bogun, M.; Rabiej, S. The Influence of fiber dormation conditions on the structure and properties of nanocomposite alginate fibers containing tricalcium phosphate or montmorillonite. Polym. Compos. 2010, 31, 1321–1331.
36. Chen, J.; Wang, Ch.; Ge, H.; Bai, Y.; Wang, Y. Effect of coagulation temperature on the properties of poly (acrylonitrile-itaconic acid) fibers in wet spinning. J. Polym. Res. 2007, 14, 223–228. [CrossRef]
37. Arbab, S.; Mohammadi, N.; Noorpanah, P. The synergistic effect of dope concentration and jet-drawing on structure development of wet-spun poly (acrylonitrile). e-Polymers 2008, 80, 1–11.
38. Ismail, A.F.; Rahman, M.A.; Mustafa, A.; Matsuura, T. The effect of processing conditions on a polyacrylonitrile fiber produced using a solvent-free coagulation process. Mater. Sci. Eng. A. 2008, 485, 251–257. [CrossRef]
39. Arbab, S.; Noorpanah, P.; Mohammadi, N.; Zeinolebadi, A. Simultaneous effects of polymer concentration, jet-stretching, and hot-drawing on microstructural development of wet-spun poly(acrylonitrile) fibers. Polym. Bull. 2011, 66, 1267–1280. [CrossRef]
40. Zhang, Y.Y.; Song, K.N.; Meng, J.S.; Minus, M.L. Tailoring polyacrylonitrile interfacial morphological structure by crystallization in the presence of single-wall carbon nanotubes. ACS Appl. Mater. Interfaces. 2013, 5, 807–814. [CrossRef]
41. Cao, C.; Chung, T.; Chen, S.; Dong, Z.; Jiang, S. The study of elongation and shear rates in spinning process and its effect on gas separation performance of poly (ether sulfone) (PES) hollow fiber membrane. Chem. Eng. Sci. 2004, 59, 1053. [CrossRef]
42. Minus, M.L.; Chae, H.G.; Kumar, S. Polyethylene crystallization nucleated by carbon nanotubes under Shear. ACS Appl. Mater. Interfaces. 2012, 4, 326–330. [CrossRef]

43. Chae, H.G.; Minus, M.L.; Rasheed, A.; Kumar, S. Stabilization and carbonization of gel spun polyacrylonitrile/single wall carbon nanotube composite fibers. Polymers 2007, 48, 3781–3789. [CrossRef]
44. An, N.; Xu, Q.; Xu, L.;Wu, S. Orientation structure and mechanical properties of polyacrylonitrile precursors. Adv. Mater. Res. 2006, 11–12, 383–386. [CrossRef]
45. Sedghi, A.; Farsani, R.E.; Shokuhfar, A. The effect of commercial polyacrylonitrile fibers characterizations on the produced carbon fibers properties. J. Mater. Processing Technol. 2008, 198, 60–67. [CrossRef]
46. Huang, X. Fabrication and properties of carbon fibers. Materials 2009, 2, 2369–2403. [CrossRef]
47. Lin, Y.J.; Che, J.J.; Pu, S.Q.; Wang, K. Structural origins of mechanical strengthening in poly (phenylene sulfide) multiwalled carbon nanotube nanocomposites obtained via hot-stretching. Polym. Compos. 2019, 40, E589–E598. [CrossRef]

C.

Entomata 2017, 5, 10-13

This paper is here reprinted with permission in the English version.

Bioinspired engineering from Beetles and Spiders

Lakshminath Kundanati[1], Gabriele Greco[1] and Nicola M. Pugno[1]

1Laboratory of Bio-inpsired and Graphene nanomechanics

Department of Civil, Environmental and Mechanical Engineering,

University of Trento, Italy, 38123

Insects and Arachnids are the most successful group of organisms on earth because of their ability to adapt and survive in various environments because of their body size, ability to fly, find and breakdown food, prevent damage and protect themselves using their exoskeleton, and most importantly reproduce successfully. Engineers and scientists are inspired from insects to develop novel drilling mechanisms, hydrophobic surfaces for harvesting fog, dry adhesives and robots that can navigate through difficult terrains (Menon et al., 2006; Parker and Lawrence, 2001; Armour et al., 2007; Akerboom et al., 2015). For example, wasp ovipositors and mosquito mouthparts have become a source of inspiration for surgical probes and needles, to reduce force and improve manoeuvrability (Kundanati and Gundiah, 2014; Schneider et al., 2009; Yang and Zahn, 2004). Insect exoskeleton provides protection with a variety of mechanical specializations (Vincent and Wegst, 2004), which has led to the development of composite material for engineering applications. Stag beetle (Lucanus cervus) is species involve in fearsome battles and experience falls from tree branches. Thus, using stag beetle (Figure 1A) as a model system, we are trying to understand elytra structure-property relations with the aim building novel bioinspired composites (Figure 1B). We also aim to gain understanding of mechanics involved in wing-folding and unfolding, which can be source of inspiration of deployable structures (Figure 1C). Spider fangs are made of hierarchical structure with multiscale gradients that are precisely designed and they play an important role in prey capture (Politi et al., 2012). We plan to investigate structure-property of spider fangs and also study biomechanics of fang piercing to investigate the role of shape in biting mechanics (Figure 1D). Modelling studies have been carried out on various bioinspired designs for understanding fracture behaviour which improves our understanding of biological materials (Signetti and Pugno, 2015).

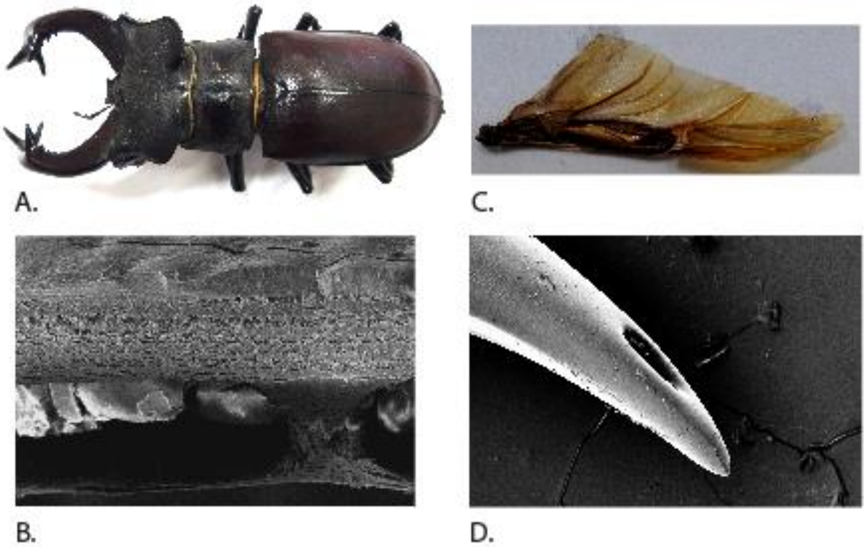

Figure 10 A) Stag beetle specimen B) wing of the stag beetle C) cross-section elytra D) spider fang with venom injecting canal (Zoropsis spinimana)

Silk is produced by insects for building traps and cocoons for protection, is processed, fabricated and genetically engineered for intended use in various medical applications (Kluge et al., 2008; Kundanati et al., 2016; Mandal et al., 2009; Vasconcelos et al., 2012). Spider silk has inspired development of toughness increasing mechanisms using simple knots (Pantano et al., 2016). Currently, we are carrying out in depth structural and mechanical characterization of different kinds of silk from various species (Figure 2A-B) to understand the variations and fabricate the bioinspired counterparts. For example, silk used for anchorage plays a very different role in holding the whole web together (Figure 2C). Insects also serve as a source of inspiration for developing materials with better adhesion. A recent analytical study based on insects like flies and spiders, showed that the strength of attachment depends on length of attaching surface (Varenberg et al., 2010). Such studies led to understanding frictional response of bioinspired adhesive using elastomeric micro-fibrils for guiding the future development of such adhesive systems (Piccardo et al., 2013). So, we are also examining the adhesive structures on the legs of spiders (Figure 2D) and adhesion based friction elements present on the abdominal casing (Figure 2E), for developing ideas to fabricate fibrous adhesive structures.

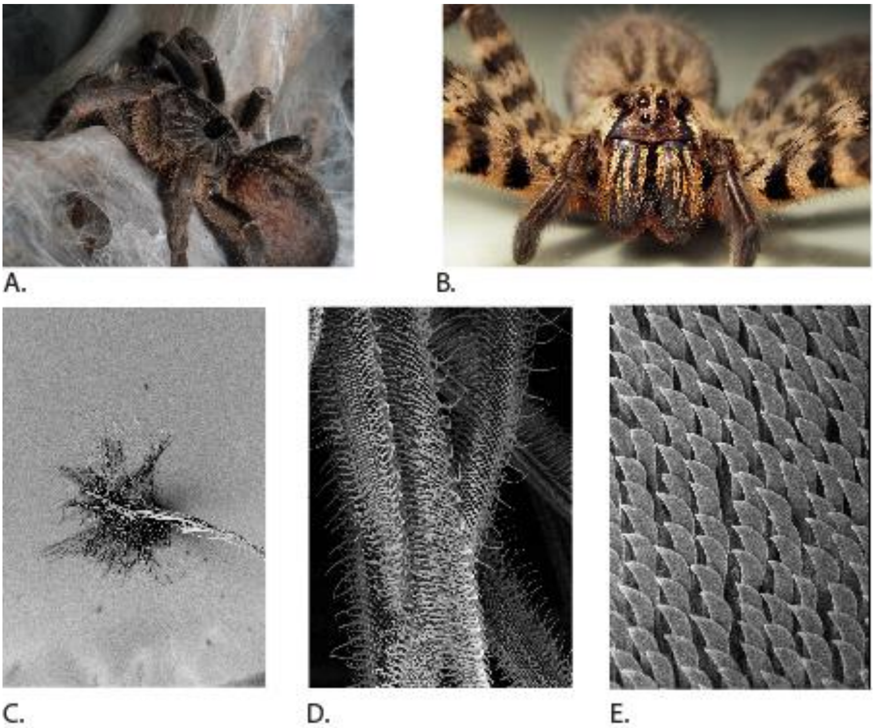

Figure 11 A) Ceratogyrus marshalli B) Cupiennius salei , scanning electron micrographs of C) anchorage of a web (Cupiennius salei) D) fine hairs on spiders leg (Cupiennius salei) E) hairy structures on the abdominal rim.

Acknowledgements

We would like to thank Enrico Simeon for the picture of *Cupiennius salei* and Nicola Angeli for help with SEM imaging.

References

1. Kluge, J. a, Rabotyagova, O., Leisk, G. G. and Kaplan, D. L. (2008). Spider silks and their applications. Trends Biotechnol. 26, 244–51.
2. Kundanati, L. and Gundiah, N. (2014). Biomechanics of substrate boring by fig wasps. J. Exp. Biol. 217, 1946–54.
3. Kundanati, L., Singh, S., Mandal, B., Murthy, T., Gundiah, N. and Pugno, N. (2016). Fabrication and Mechanical Characterization of Hydrogel Infused Network Silk Scaffolds. Int. J. Mol. Sci. 17, 1631.
4. Mandal, B. B., Kapoor, S. and Kundu, S. C. (2009). Silk fibroin/polyacrylamide semi-interpenetrating network hydrogels for controlled drug release. Biomaterials 30, 2826–36.

5. Pantano, M. F., Berardo, A. and Pugno, N. M. (2016). Tightening slip knots in raw and degummed silk to increase toughness without losing strength. Sci. Rep. 6, 18222.
6. Piccardo, M., Chateauminois, A., Fretigny, C., Pugno, N. M. and Sitti, M. (2013). Contact compliance effects in the frictional response of bioinspired fibrillar adhesives. J. R. Soc. Interface 10, 20130182.
7. Politi, Y., Priewasser, M., Pippel, E., Zaslansky, P., Hartmann, J., Siegel, S., Li, C., Barth, F. G. and Fratzl, P. (2012). A spider's fang: How to design an injection needle using chitin-based composite material. Adv. Funct. Mater. 22, 2519–2528.
8. Schneider, A., Frasson, L., Parittotokkaporn, T., Rodriguez y Baena, F. M., Davies, B. L. and Huq, S. E. (2009). Biomimetic microtexturing for neurosurgical probe surfaces to influence tribological characteristics during tissue penetration. Microelectron. Eng. 86, 1515–1517.
9. Signetti, S. and Pugno, N. M. (2015). Frontiers in Modeling and Design of Bio-Inspired Armors. Front. Mater. 2, 2014–2016.
10. Varenberg, M., Pugno, N. M. and Gorb, S. N. (2010). Spatulate structures in biological fibrillar adhesion. Soft Matter 6, 3269.
11. Vasconcelos, A., Gomes, A. C. and Cavaco-Paulo, A. (2012). Novel silk fibroin/elastin wound dressings. Acta Biomater. 8, 3049–60.
12. Yang, M. and Zahn, J. D. (2004). Communications & Therapeutic Micro and Nanotechnology Section : Microneedle Insertion Force Reduction Using Vibratory Actuation. Biomed. Microdevices 177–182.

D.

This paper has been submitted to the journal “Bioinspiration & Biomimetic” and is now under the second phase of revision.

The role of hairs in the adhesion of octopus suckers: a hierarchical peeling approach

Gabriele Greco [1, 2]; Federico Bosia[3], Francesca Tramacere [2]; Barbara Mazzolai[2] and Nicola M. Pugno [1, 4, 5*]

[1] Laboratory of Bio-Inspired & Graphene Nanomechanics, Department of Civil, Environmental and Mechanical Engineering, University of Trento, Via Mesiano, 77, 38123 Trento, Italy
[2] Center for Micro-BioRobotics@SSSA, Istituto Italiano di Tecnologia, Viale Rinaldo Piaggio 34, I-56025 Pontedera, Italy
[3] Department of Applied Science and Technology, Politecnico di Torino, Corso Duca degli Abruzzi 24, 10129, Torino, Italy
[4]School of Engineering and Materials Science, Queen Mary University of London, Mile End Road, E1 4NS London, United Kingdom
[5]Ket-Lab, Edoardo Amaldi Foundation, Via del Politecnico snc, 00133 Rome, Italy
*Corresponding author: nicola.pugno@unitn.it

Abstract

The *Octopus vulgaris* is able to generate a remarkable pressure difference in its suckers to adhere to surfaces, exploiting the adhesion of two internal membranes. On the other hand, clingfish use suction cups with a bed of microfibrils or “micropapillae”, which are tiny soft protuberances that line the cup perimeter, to better adhere to rough rock surfaces. These structures are a precious source of inspiration for designing innovative suction cups, but a complete mechanical description of their attachment process is still lacking. In this paper, we exploit the recent discovery of the presence of hairs in the acetabulum roof of octopus suction cups to revise the current model for its adhesion to the acetabulum wall. We show how this additional feature, which can be considered an example of a hierarchical structure, can lead to an increase of adhesive strength, based on the analysis of the cases of a simple tape and an axisymmetrical membrane. Using peeling theory, we discuss in both cases the influence of hierarchical structure and the resulting variation of contact angles on the adhesive energy, highlight how an increase in number of hierarchical levels contributes to its increase, with a corresponding improvement in functionality for the octopus suckers.

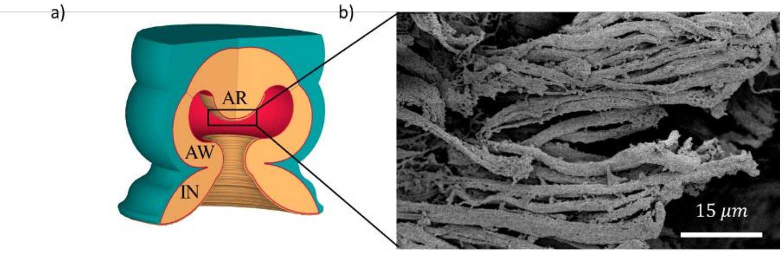

Figure 1: a) Schematic of the octopus' sucker: Acetabular Roof (AR), Acetabular Wall (AW) and Infundibulum (IN). b) Hairs present on the surface of the AR that is attached to the AW during adhesion.

Introduction

The octopus is one of the most intelligent animals that lives on Earth. It uses its suckers to perform many functions ([1], [2]). In particular, octopus suckers are able to generate a maximum pressure difference of about 0.27 MPa that can be reached in a few milliseconds [3]. Other animals, such as clingfish, exploit suction cups to adhere to rough surfaces underwater [4]. For this reason, these structures represent a remarkable source of inspiration for designing artificial suction cups or adhesives ([5]–[8]). To develop these artificial devices, the full understanding of the adhesion process and the capability to model it correctly is crucial. In the past, octopus suckers and their interaction with the substrate have been studied by analyzing their arrangement [9], their structure and mechanical properties ([10]–[12]) and their morphology [13]. Their adhesion is achieved exploiting the pressure difference between the external environment, the acetabulum cavity and the infundimbulum cavity (Fig. 1a)[11]. To maintain this pressure difference, the acetabulum roof and the acetabulum wall must remain in full contact. As in other bioadhesion problems, peeling theory has been adopted to describe how these two parts of the octopus suckers delaminate [14]. The first elastic approach developed in the literature in this respect was the Kendall model [15], which describes the peeling of a thin elastic tape from a rigid substrate. The main physical quantity that governs the attachment, or the detachment, of the tape is the surface energy γ, which is defined as the energy required to generate a unit area of interface (for a certain crack speed), with Mode I (opening) primary separation mode. In the Kendall model, the force necessary to detach the membrane can be determined by adopting an energy-based criterion, imposing the Griffith's balance between the elastic energy, the adhesive energy and the work of the applied load [16]. The peeling force relative to a tape pulled at an angle θ, is thus:

$$F = Etw\left(\cos\theta - 1 + \sqrt{(1-\cos\theta)^2 + \frac{2\gamma}{Et}}\right) \qquad (1)$$

where E is the Young's modulus of the tape, t its thickness and w its width. Introducing $\hat{F} = \frac{F}{Etw}$ and $\hat{\gamma} = \frac{\gamma}{Et}$, the relation can be written in non-dimensional form:

$$\hat{F} = cos\,\theta - 1 + \sqrt{(1 - cos\,\theta)^2 + 2\hat{\gamma}} \qquad (2)$$

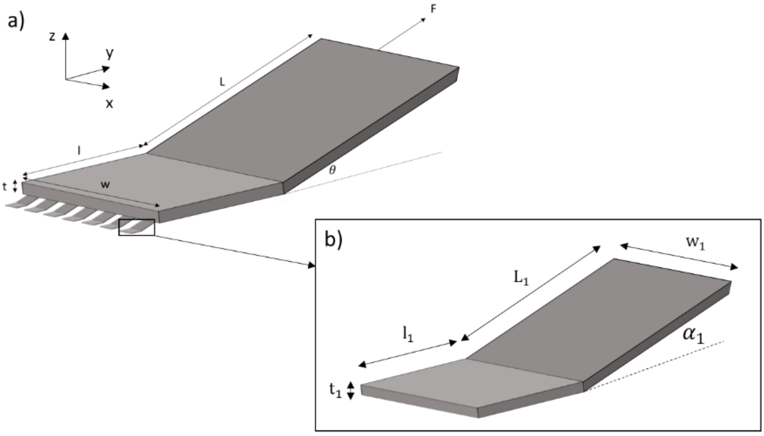

Figure 2: a) Schematic of the peeling of an elastic tape equipped with hairs; b) schematic of a single second -level tape (hair).

Starting from this approach, a series of more refined models were developed in order to describe various biological mechanisms of adhesion. Among these, the theory of multiple peeling was introduced to model a system of numerous tapes loaded by a single force at a common point [17]. This was used in complex adhesive systems, e.g. to describe the adhesive behaviour of spider web anchors [18],[19],[20]. Moreover, a so-called "hierarchical shear lag model" was introduced to model hierarchical contact splitting occurring in biological adhesive structures such as gecko pads [21], [22]. These works showed that hierarchical structuring of the surface also leads to the reduction of stress concentrations and the appearance of multiple separate peeling fronts, with a resulting increase in adhesive capabilities. These examples indicate the possibility of exploiting various types of structures present in nature for enhanced adhesion in artificial adhesives.

The recent discovery of the presence of hairs in the acetabulum roof of the octopus' suckers [23] (Fig. 1) suggests a revision of the model outlined in Tramacere et al. [13]. In particular, the peeling model therein can be improved by adding the additional effect due to the presence of hairs on the flat membrane. This work therefore aims to model the peeling process of a membrane equipped with hierarchical hairs, i.e. to analyse how the hairs affect the peeling force. To do this, we apply Yao's approach [24] to the geometry of an axisymmetric membrane, formulating a modified expression for the work of adhesion as a function of the surface energy in a hierarchical structure and deriving the corresponding detachment force of the membrane.

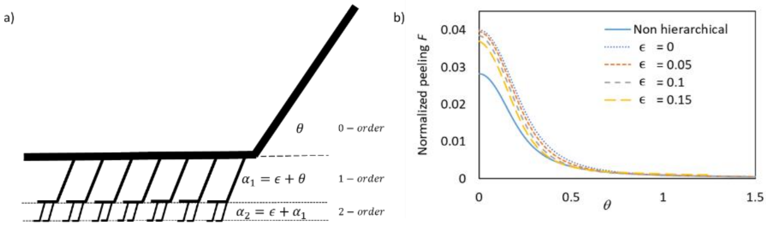

Figure 3: a) Schematic of hierarchical levels up to the second order. b) Normalized peeling force vs. peeling angle (Eq. (7)) for different ϵ *parameter values and* $\hat{\gamma}=4\cdot 10^{-4}$.

2. Theoretical model

2.1 Hierarchical tape with hairs

We analyse a simple tape with hairs at the interface with the substrate, as shown schematically in Fig. 2, which we define as "hierarchical", meaning that its adhesive properties depend on structures present at two (or more) different size scales. As a first approximation, hairs are considered to be of the same material of the tape (an incompressible soft material with $\nu = 0.5$). Furthermore, they are modelled as flat tapes of thickness t_1, width w_1 detached length L_1 and contact length l_1. The distance between two adjacent hairs is ρ along both x and y directions, so that $N = lw/\rho^2$ is the total number of hairs. The hairs form an angle α_1 with the substrate that is considered to be constant, and whose relation to the tape contact angle θ is discussed below. During the attachment and detachment phases, we do not consider bunching effects of the hairs and possible variation effects in the section of the tape. Equation (1) is valid for a simple tape without hairs. The presence of hairs on the tape surface results in an increase of the equivalent surface energy, since there is additional elastic energy stored in the hairs themselves that is “dissipated” as kinetic energy released after detachment ([22], [25]). Thus, Eq. (1) remains valid and modifying the surface energy term to

$$\gamma' = \gamma + \gamma_H \qquad (3)$$

where γ' is the total surface energy, γ the surface energy of the flat tape and γ_H the equivalent surface energy due to the additional elastic energy stored in the hairs. Since all hairs are assumed identical, γ_H can be considered homogeneous over the whole contact surface, and can be evaluated as:

$$\gamma_H = \frac{l_1 + L_1}{2Ew_1^2 t_1 l_1} \; P_1^2 \qquad (4)$$

whereP_1 is the detachment force of a single hair. Using Eq. (1) to compute P_1 , we obtain:

$$\gamma_H = \frac{Et_1}{2}\left(1 + \frac{L_1}{l_1}\right)\left(\cos\alpha_1 - 1 + \sqrt{(1-\cos\alpha_1)^2 + \frac{2\gamma}{Et_1}}\right)^2 \qquad (5)$$

We can now write Eq. (3) in non-dimensional form:

$$\widehat{\gamma'} = \hat{\gamma} + \frac{\gamma_H}{Et} = \hat{\gamma} + \frac{t_1}{2t}\left(1 + \frac{L_1}{l_1}\right)\left(\cos\alpha_1 - 1 + \sqrt{(1-\cos\alpha_1)^2 + \frac{2t}{t_1}\hat{\gamma}}\right)^2 \qquad (6)$$

Substituting this expression for the surface energy in Eq. (2), we obtain the modified non-dimensional pull-off force as:

$$\hat{F} = cos\,\theta - 1 + \sqrt{(1 - cos\,\theta)^2 + 2\hat{\gamma} + \kappa_1\left(\cos\alpha_1 - 1 + \sqrt{(1-\cos\alpha_1)^2 + \lambda_1\hat{\gamma}}\right)^2} \qquad (7)$$

Where $\kappa_1 = \frac{t_1}{2t}\left(1 + \frac{L_1}{l_1}\right)$ and $\lambda_1 = \frac{2t}{t_1}$. Equation (7) thus represents the dimensionless force necessary to detach a rectangular tape equipped with hairs. Notice that the area fraction, i.e. the ratio between the contact areas of the tape with/without hairs, respectively, is usually considered close to 1, i.e., the presence of hairs does not entail a reduction/increase of the contact area[22]. To illustrate the resulting behavior, we plot the peeling force $\hat{F}$ in Fig. 3b for various angles ϵ, having chosen the following parameters: $\hat{\gamma}$= $4{\cdot}10^{-4}$, $w = 10^{-2}m,\ l = 10^{-2}m,\ t = 10^{-3}m,$ $w_1 = 10^{-5}m,\ \ l_1 = 10^{-5}m,\ \ L_1 = 10^{-5}m,\ \ t_1 = 10^{-5}m.$ As expected, the presence of a hierarchical structure, i.e. of hairs, contributes to an increase of the adhesive properties of the tape for all peeling angles due to the additional stored elastic energy, which is dissipated during delamination, with an increased effect for small angles. The peeling force decreases only slightly for increasing ϵ values. For θ = 0, and α_1 = 0, the tape is sheared parallel to the surface, and the additional dissipated energy due to the contribution of the hairs is maximum. Conversely, their decreasing effect when the peeling angle increases and tends to *π/2* is consistent with the qualitative behavior observed in biological adhesion, where the peeling force needs to be maximized mainly for small peeling angles, while facilitated detachment is required at larger angles, to achieve the ON/OFF mechanism necessary, e.g. for motion in animals like geckos or insects like beetles.

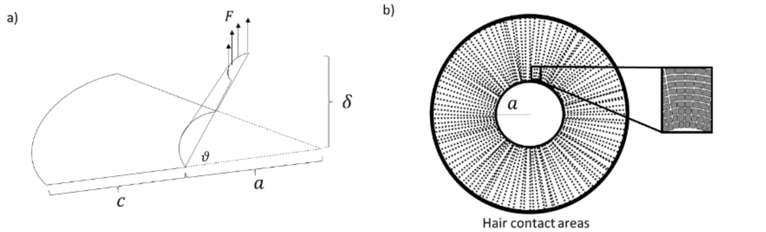

Figure 4: a) Schematic of the peeling of an axisymmetric membrane and b) schematic the contact region between the hairs of the axisymmetric membrane and the substrate.

2.2. Hierarchical axisymmetric membrane

The detachment of a single octopus' sucker can be treated as the peeling of an axisymmetric membrane [13], treated by Afferrante et al. [26], and schematically illustrated in Fig. 4a. The non-dimensional force necessary to detach the membrane is

$$\hat{F} = \left(\frac{32}{27}\right)^{\frac{1}{4}} (\hat{\gamma})^{\frac{3}{4}}(1+\hat{a}) \qquad (8)$$

where $\hat{F}$ and $\hat{a}$ are the dimensionless vertical load and detached radius, respectively. Equation (8) predicts a linearly increasing peeling force with the membrane detached radius $\hat{a}$, i.e. an adhesive membrane can ideally bear an arbitrary load, provided it is large enough. In this case, the modification of γ due to the presence of hairs should be also considered. By inserting Eq. (6) in Eq. (8) we obtain the non-dimensional force necessary to detach the axisymmetric membrane equipped with hairs, although in this case the latter are assumed to be radially distributed, as shown in Fig. 4b. Making the same assumptions as in the previous Section, we obtain the detachment force of the axisymmetric membrane as:

$$\hat{F} = \left(\frac{32}{27}\right)^{\frac{1}{4}} \left(\hat{\gamma} + \kappa_1 \left(\cos\alpha_1 - 1 + \sqrt{(1-\cos\alpha_1)^2 + \lambda_1\hat{\gamma}}\right)^2\right)^{3\backslash 4} (1+\hat{a}) \qquad (9)$$

The role of the hairs for the axisymmetric membrane can be visualized in Fig. 5. In this case, we plot the peeling force versus the detached radius $\hat{a}$ for $\hat{\gamma}$ = 4·10^{-4}, and various values of α_1. The dependence is linear, but again, the presence of a hierarchical structure implies a considerable increase in the adhesive properties of the membrane for a given detached radius. The influence of the hairs on the peeling force decreases as the angle increases, but the $\hat{F}$ vs. $\hat{a}$ curves remain considerably larger than that relative to non-hierarchical case, even for large angles, e.g. α_1 = 0.4. This is again consistent with the qualitative behavior observed in biological adhesion, where the peeling force needs to be maximized mainly for small peeling angles.

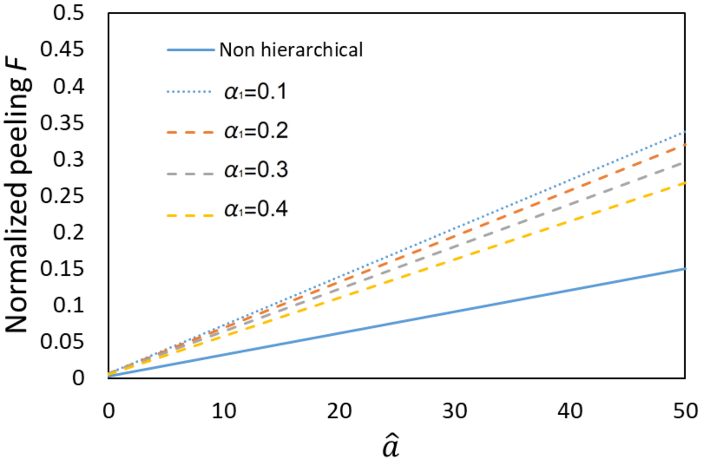

Figure 5: Peeling force for an axisymmetric membrane vs. detached radius â (Eq. (9)) for different α_1 values ($\hat{\gamma}$ = 4·10^{-4}).

2.3 Additional levels of hierarchy

The previous model can be extended to additional levels of hierarchy, as illustrated schematically in Fig. 3a. In this case, Eq. (3) can be extended as follows:

$$\gamma' = \gamma + \gamma_1 + \gamma_2 + \cdots + \gamma_n \qquad (10)$$

where γ_1 coincides with the previously introduced γ_H. The total force necessary to detach this type of tape/membrane can be computed as previously, by recursively adding the terms relative to the appropriate hierarchical level. For example, the second level of hierarchy can be described by adding to $\hat{\gamma}_1$ another term of the form

$$\hat{\gamma}_2 = \kappa_2 \left(cos\, \alpha_2 - 1 + \sqrt{(1 - cos\, \alpha_2)^2 + \lambda_2 \hat{\gamma}} \right)^2 \qquad (11)$$

where κ_2 , λ_2 and α_2 are analogous to the first level parameters κ_1, λ_1 and α_1, respectively. Analogous expressions can be written for i > 2. In order to compute the κ_i and λ_i and α_i parameters, it is necessary to consider the geometry (i.e. geometry and contact angles at the various hierarchical levels) of the new system. The approach outlined in the previous sections can then be adopted to determine higher order surface energy values γ_i to the adhesive energy due to the additional hierarchical levels, and the corresponding peeling force. Given the small bending stiffness of the tapes at the various hierarchical levels, the angle variations from one hierarchical level to the next are in all cases small. Therefore, the corrections decrease in magnitude for an increasing number of levels, i.e. the adhesive energy and force values do not diverge. This can be seen in results illustrated in Fig. 6. Here, we consider as previously a perturbation ϵ on the contact angle from one level to the next, and assume for simplicity that the perturbation is of the same order for each level, i.e. $\cos\alpha_{i+1} = \cos(\alpha_i + \epsilon)$, $\forall i$. Thus, an increase of the hierarchical level also implies an increase in the overall perturbation on the initial peeling angle θ. Figures 6a and 6b show the effect of an increasing number of hierarchical levels for the $\hat{F}$ vs. θ and $\hat{F}$ vs. $\hat{a}$ plots in the case of a hierarchical tape and a hierarchical axisymmetric membrane, respectively. For 3 levels of hierarchy, at θ = 0.1 the adhesive force is increased by approximately 6 times with respect to the non-hierarchical case. It is apparent that the main increase takes place for the first hierarchical levels, as is clearly visible in Figs. 6c and 6d, where $\hat{F}$ is plotted as a function of the number of hierarchical levels for fixed θ and $\hat{a}$ values, again in the case of a hierarchical tape and a hierarchical axisymmetric membrane, respectively. This is consistent with observations on biological adhesive structures found in nature, such as beetle legs or gecko toes [16][27], which typically display 2 or 3 levels of hierarchy. In the case of octopus's sucker membranes, hairs appear to be present at most at three levels of hierarchy.

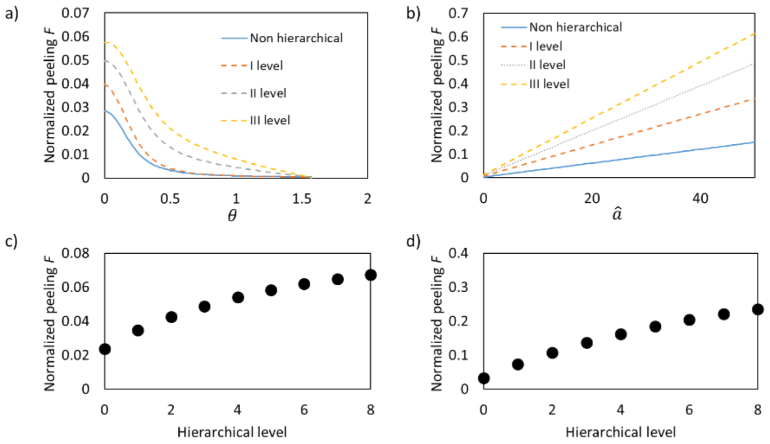

Figure 6: a) Normalized peeling force vs. peeling angle for increasing hierarchical levels in the case of a simple tape ($\varepsilon = 0.05$); b) Normalized peeling force vs normalized detached radius for increasing hierarchical levels in the case of an axisymmetric membrane ($\varepsilon = 0.05$ and $\theta = 0.1$). c) Normalized peeling force as a function of number of hierarchical levels in the case of a simple tape ($\epsilon = 0.05$ and $\theta = 0.1$). d) Normalized peeling force as a function of number of hierarchical levels in the case of an axisymmetric membrane ($\epsilon = 0.05$, $\hat{a} = 10$).

Conclusions

Understanding of the effect of a layer of hairs on the adhesive properties of octopus' suckers is important for the design of artificial suction cups with improved adhesion for various applications, such as smart-skin attachable skin patches [28] or biorobotic adhesive discs [29]. Here, we have evaluated the effect of hierarchical structure, i.e. the presence of hairs, on the adhesion and detachment of a simple tape and of an axisymmetric membrane, in order to gain insight into the adhesion mechanism of octopus' suckers (in particular the detachment of the acetabulum roof from the acetabulum wall). The model is based on a number of simplifying assumptions, e.g. that there is no hair bunching and that the peeling angle does not vary significantly between structures at one hierarchical level and those at the next.

Results for the simple tape case indicate that the presence of hairs can improve the adhesive properties by more than 30% at small peeling angles, with the effect decreasing for larger angles. This is consistent with observations on biological adhesion, where typically adhesive forces need to be enhanced at small peeling angles. The main parameter determining this increase is the initial detached length of the hairs, which has an upper limit in lengths for which there is an onset of bunching effects. The detachment force for an axisymmetric membrane also increases in the presence of hierarchical structuring. We show that the model can be easily extended to the analysis to multiple levels of hierarchy. Here, results indicate that the first hierarchical levels are the ones that contribute more to an increase in adhesive force. In terms of convergence, we find that after the third level of hierarchy there is no longer a significant change in peeling force.

This paper provides a possible explanation for the role of the hairs in octopus' suckers, correctly accounting for their role in determining the ON/OFF behavior during adhesion. Currently, further studies are under way to evaluate other possible functions of these hairs (e.g. sensing) that could be fundamental to the octopus functionality. Our work can also help the design of artificial suction cups by providing a model that predicts the potential benefits of a hierarchical surface in terms of improved and angle-dependent adhesive properties.

Acknowledgements

F.B. is supported by H2020 FET Proactive "Neurofibres" grant No. 732344, by the project “Metapp” (n. CSTO160004) funded by Fondazione San Paolo, and by the Italian Ministry of Education, University and Research (MIUR), under the “"Departments of Excellence”" grant L. 232/2016. NMP is supported by the European Commission under the Graphene Flagship Core 2 Grant no. 785219 (WP14 “Composites”) and FET Proactive “Neurofibres” Grant no. 732344 as well as by the Italian Ministry of Education, University and Research (MIUR) under the “Departments of Excellence” Grant L.232/2016, the ARS01-01384-PROSCAN Grant and the PRIN-20177TTP3S. This work was carried out within the COST Action CA15216 “European Network of Bioadhesion Expertise: Fundamental Knowledge to Inspire Advanced Bonding Technologies”.

References

1. L. A. Fuiman, C. M. Young, A. J. Gooday, and S. E. Shumway, Advances in Marine Biology. London, 2014.
2. J. B. W. Roland C. Anderson, Jennifer A. Mather, Octopus The Ocean’s Intelligente Invertebrate. Portland, 2010.
3. A. M. Smith, “Cephalopod sucker design and the physical limits to negative pressure,” J. Exp. Biol., vol. 199, no. Pt 4, pp. 949–58, 1996.

4. J. A. Sandoval, S. Jadhav, H. Quan, D. D. Deheyn, and M. T. Tolley, “Reversible adhesion to rough surfaces both in and out of water, inspired by the clingfish suction disc,” Bioinspir. Biomim., vol. 14, no. 6, 2019.
5. F. Tramacere, M. Follador, N. M. Pugno, and B. Mazzolai, “Octopus-like suction cups: From natural to artificial solutions,” Bioinspiration and Biomimetics, vol. 10, no. 3, pp. 1–8, 2015.
6. M. Follador et al., “Octopus-inspired innovative suction cups,” Lect. Notes Comput. Sci. (including Subser. Lect. Notes Artif. Intell. Lect. Notes Bioinformatics), vol. 8064 LNAI, pp. 368–370, 2013.
7. S. Baik, D. W. Kim, Y. Park, T. J. Lee, S. Ho Bhang, and C. Pang, “A wet-tolerant adhesive patch inspired by protuberances in suction cups of octopi,” Nature, vol. 546, no. 7658, pp. 396–400, 2017.
8. S. Sareh et al., “Anchoring like octopus: biologically inspired soft artificial sucker,” J. R. Soc. Interface, vol. 14, no. 135, p. 20170395, 2017.
9. F. Tramacere, L. Beccai, M. J. Kuba, and B. Mazzolai, “Octopus Suckers Identification Code (OSIC),” Mar. Freshw. Behav. Physiol., vol. 46, no. 6, pp. 447–453, 2013.
10. F. Tramacere, L. Beccai, M. Kuba, A. Gozzi, A. Bifone, and B. Mazzolai, “The Morphology and Adhesion Mechanism of Octopus vulgaris Suckers,” PLoS One, vol. 8, no. 6, 2013.
11. W. M. Kier, “The Structure and Adhesive Mechanism of Octopus Suckers,” Integr. Comp. Biol., vol. 42, no. 6, pp. 1146–1153, 2002.
12. F. Tramacere, A. Kovalev, T. Kleinteich, S. N. Gorb, and B. Mazzolai, “Structure and mechanical properties of Octopus vulgaris suckers,” J. R. Soc. Interface, vol. 11, no. 91, pp. 20130816–20130816, 2013.
13. F. Tramacere, N. M. Pugno, M. J. Kuba, B. Mazzolai, F. Tramacere, and B. Mazzolai, “Unveiling the morphology of the acetabulum in octopus suckers and its role in attachment,” J. R. Soc. Interface, vol. 5, pp. 1–5, 2015.
14. A. J. Kinloch, Adhesion and Adhesives. Heildeberg, 1987.
15. K. Kendall, “Thin-Film Peeling - The Elastic Term,” J. Phys. D. Appl. Phys., vol. 8, pp. 1449–1452, 1975.

16. M. Varenberg, N. M. Pugno, and S. N. Gorb, “Spatulate structures in biological fibrillar adhesion,” Soft Matter, vol. 6, no. 14, p. 3269, 2010.
17. N. M. Pugno, “The theory of multiple peeling,” Int. J. Fract., vol. 171, no. 2, pp. 185–193, 2011.
18. J. O. Wolff, I. Grawe, M. Wirth, A. Karstedt, and S. N. Gorb, “Spider’s super-glue: Thread anchors are composite adhesives with synergistic hierarchical organization,” Soft Matter, 2015.
19. J. O. Wolff and M. E. Herberstein, “Three-dimensional printing spiders: Back-and-forth glue application yields silk anchorages with high pull-off resistance under varying loading situations,” J. R. Soc. Interface, 2017.
20. L. Brely, F. Bosia, and N. M. Pugno, “Numerical implementation of multiple peeling theory and its application to spider web anchorages.,” Interface Focus, vol. 5, no. 1, p. 20140051, 2015.
21. H. Gao, X. Wang, H. Yao, S. Gorb, and E. Arzt, “Mechanics of hierarchical adhesion structures of geckos,” Mech. Mater., vol. 37, no. 2-3 SPEC. ISS., pp. 275–285, 2005.
22. L. Brely, F. Bosia, and N. M. Pugno, “Emergence of the interplay between hierarchy and contact splitting in biological adhesion highlighted through a hierarchical shear lag model,” Soft Matter, vol. 14, pp. 5509–5518, 2018.
23. F. Tramacere, E. Appel, B. Mazzolai, and S. N. Gorb, “Hairy suckers: The surface microstructure and its possible functional significance in the octopus vulgaris sucker,” Beilstein J. Nanotechnol., vol. 5, no. 1, pp. 561–565, 2014.
24. H. Yao and H. Gao, “Reprint of ‘Multi-scale cohesive laws in hierarchical materials’ [In. J. Solids Struct. 44 (2007) 8177-8193],” Int. J. Solids Struct., vol. 45, no. 13, pp. 3627–3643, 2008.
25. B. Chen, P. Wu, and H. Gao, “Hierarchical modelling of attachment and detachment mechanisms of gecko toe adhesion,” Proc. R. Soc. A Math. Phys. Eng. Sci., vol. 464, no. 2094, pp. 1639–1652, 2008.
26. L. Afferrante, G. Carbone, G. Demelio, and N. Pugno, “Adhesion of elastic thin films: Double peeling of tapes

versus axisymmetric peeling of membranes," Tribol. Lett., vol. 52, no. 3, pp. 439–447, 2013.

27. E. Arzt, S. Gorb, and R. Spolenak, "From micro to nano contacts in biological attachment devices," Proc. Natl. Acad. Sci. U. S. A., 2003.
28. S. Baik, J. Kim, H. J. Lee, T. H. Lee, and C. Pang, "Highly Adaptable and Biocompatible Octopus-Like Adhesive Patches with Meniscus-Controlled Unfoldable 3D Microtips for Underwater Surface and Hairy Skin," Adv. Sci., 2018.
29. Y. Wang et al., "A biorobotic adhesive disc for underwater hitchhiking inspired by the remora suckerfish," Sci. Robot., 2017.

Spider silks are biological materials that have inspired the humankind since its beginning. From raising the interest of ancient philosophers to the practical outcomes in the societies, spider silks have always been part of our culture and, thus, of our scientific development. They are protein-based materials with exceptional mechanical and biological properties that from liquid solutions passes to the solid fibres once extruded from the body of the spiders.

Spider silks have deeply been investigated in these decades for their possible outcomes in biomedical technology as a supporting material for drugs delivery or tissues regeneration.

Furthermore, spiders build webs with the support of different types of silks to create mechanically efficient structures, which are currently under investigation as models for metamaterials and fabrics with superior mechanical properties. This diversity in materials and structures makes spider silks scientific outcomes potentially infinite.

In this work, we present some of the outputs of these three years of PhD. We explored the properties of the native material across different aspects (different species and glands) and trying to find possible derived applications (tissue engineering). Then we explored the mechanical behaviour of the natural structures (such as orb webs or attachment discs) coupled with their biological functions.

In order to develop to an industrial level this material, we tried to understand and improve the physical properties of artificial spider silk, which helps also in understanding the ones of the native materials.

Gabriele Greco obtained his master's degree in Physics from the University of Ferrara, Italy. He is a founding member of Aracnofilia (Italian Association of Arachnology) and a professional graduated sommelier. His research activity is focused on spider silk and spiders biomechanics, whose outputs have been published in international peer reviewed journals. As a reviewer, he has worked for the Journal of Experimental Biology and Journal of Applied Polymer Science.